Iwate University

Professor Hiroyuki Fujishiro

Research Achievements
（1990 ~ 2022）

March 2022

目 次

※添付の DVD には全てのデータ、論文ファイル、動画等が掲載されている。

１．代表的研究の概略

１．酸化物超電導体の熱的性質（熱伝導率、熱拡散率、音速、熱膨張、熱起電力）に関する研究

1993 年に能登宏七教授と共同で He 冷凍機を用いた低温における熱伝導率の完全自動測定装置を開発し、様々な条件で作製した酸化物超伝導体の熱伝導率を測定し、フォノン散乱機構の解明を行った。さらに、オリジナルな熱拡散率測定法、ストレインゲージを用いた熱膨張測定法、熱起電力測定法、2 次元熱伝導率測定法、接触熱抵抗測定法等を開発した。10 T までの磁場中における超電導線材や超電導バルク材の熱物性の測定を系統的に行った。超電導バルク材に関する一連の研究は、文部省の岩手県地域結集型共同研究事業「生活・地域への磁気活用技術の開発」(1999~2004)で実施され、研究成果は論文発表すると共に、データベースを構築して Web 公開を継続して行っている。

２．Mn, Co 系酸化物の熱的、電気的特性に関する研究

1997 年頃から、超巨大磁気抵抗(CMR)効果を示す様々な Mn 系酸化物($RE_{1-x}AE_xMnO_3$)や、大きな熱起電力を有し熱電変換材料への応用が期待される Co 系酸化物($RE_{1-x}AE_xCoO_3$)の作製及び、熱的、電気的特性の研究を実施した。磁性転移付近における熱的散乱の変化や、磁場中熱伝導率測定、音速測定（東北大金属材料研究所深瀬研究室との共同研究）を行い、論文発表を行った。これらの研究の一部はチェコ科学アカデミー物理学研究所の J. Hejtmanek 博士と共同で実施した。

３．Co 系酸化物$(Pr_{1-y}Y_y)_{1-x}Ca_xCoO_3$の特異な金属絶縁体転移に関する研究

2005 年頃から、特異な金属絶縁体転移を示す Co 系酸化物$(Pr_{1-y}Y_y)_{1-x}Ca_xCoO_3$ (PYCCO)に注目し、焼結体試料作製と電気的、熱的測定等を行った。2011 年からは Pr イオンの転移点近傍での価数変化を測定するため、SPring-8 での XAFS 測定を行い、Pr イオン価数変化と関係する転移メカニズムを明らかにした。さらに 2015 年から、レーザ蒸着法（PLD 法）による PYCCO 単結晶薄膜を作製し（東北大金属材料研究所後藤研究室との共同研究）、多結晶に対する結果との比較検討を行った。一連の研究はチェコ科学アカデミー物理学研究所の J. Hejtmanek 博士と共同で実施した。

４．超電導バルク材のパルス着磁法の実験的研究

2002 年頃から、文部省の岩手県地域結集型共同研究事業(1999~2004)の中で、安価で簡便な着磁法であるパルス着磁法(PFM)により REBaCuO 系超電導バルク材の着磁研究を実験的に行い、特に着磁時の温度測定の重要性に注目して研究を実施した。実験結果の蓄積から、2005 年に温度上昇を低減した Modified Multi-Pulse Technique with Stepwise Cooling (MMPSC)法を提案し、直径 45 mm の GdBaCuO バルク表面で PFM 法では世界最高となる 5.2 T の捕捉磁場を実現した。この記録は現在も破られていない。現在でも PFM 法による捕捉磁場の向上の手法として、MMPSC 法（又は Two-step MPSC 法）が一般に用いられている。さらに、MgB_2 バルクに対しても PFM 法を用いて捕捉磁場の向上を目指した。その結果、2016 年に単一パルスにより 1.1 T を達成し、さらに 2019 年には MgB_2 バルク、Cu 板、軟磁鉄ヨークの複合体に複数パルス磁場印加により 1.6 T の世界最高の捕捉磁場を実現した。これらの一連の研究は、 (株)イムラ材料開発研究所（現：(株)イムラジャパン）、(株)新日本製鐵（現：(株)日本製鉄）、理化学研究所及び、イタリア EDISON S.p.A., R&D Division の Giovanni Giunchi 博士及び、英国ケンブリッジ大学 Mark D. Ainslie 博士との共同研究で実施した。

５．超電導バルク材の着磁現象のシミュレーション

実験による検討は限られたパラメータを変化させるに過ぎず、実験結果の再現や新たなパルス着磁法の提案を行うために、2010 年頃から有限要素法を用いた PFM の電磁気的、熱的シミュレーションを行った。シミュレーションの結果は PFM 現象を理解する上で非常に重要であることを明らかにした。さらに応力解析に関するシミュレーションを追加し、超電導バルクの着磁時の破壊を回避するための機械的補強法の提案を行った。実験とシミュレーションを併用した着磁プロセスの研究は他の研究機関では行われて居らず、多くの論文の出版と国際会議での招待講演が行われた。これらの一連の研究は、英国ケンブリッジ大学 Mark D. Ainslie 博士との共同研究で実施した。

６．新しい超電導バルク磁石の提案と実証

これまでの超伝導バルクの着磁に関する実験とシミュレーションの多くの蓄積から、全く新しいバルク磁石装置を２件提案し特許出願を行った。１つは 2017 年に発明した着磁磁場よりも大きな捕捉磁場を持続的に発生するハイブリッド型超伝導バルク磁石レンズ(HTFML: Hybrid Trapped Field Magnet Lens)であり、実際に GdBaCuO バルクレンズと GdBaCuO バルク円筒を用いて，着磁磁場 7 T で 9.8 T の捕捉磁場を持続的に発生することを実験で確認した。もう一つは 2020 年に発明した HTFML よりも非常に大きな勾配磁場を発生する新しいタイプのバルク磁石（HG-TFM: High Gradient Trapped Field Magnet）である。HG-TFM は着磁磁場 8.5 T で着磁した結果, 磁気力場 $B_z dB_z/dz$ = 1930 T^2/m が実現し、この擬似微小重力環境において反磁性体である金属ビスマスや水滴の浮上を確認した。HG-TFM　は今後、地上で擬似微小重力環境の実現を可能にし、ライフサイエンス分野への応用展開が可能である。これらの一連の研究は、大学院生の高橋圭太君（現：学習院大学助教）と英国ケンブリッジ大学 Mark D. Ainslie 博士との共同研究で実施した。

７．新しい酸化物系熱電変換材料に関する研究

これまで蓄積してきた酸化物試料作製と熱伝導率や熱起電力等の熱物性測定の経験を生かし、2003 年頃から様々な新しい酸化物材料の熱電変換特性を検討した。具体的に検討した材料は、$RE_{1-x}AE_xCoO_3$ 系（チェコ科学アカデミー物理学研究所の J. Hejtmanek 博士と共同研究)、CuO 系、TiO_2 系、In_2O_3-SnO_2 系、BiCuSeO 系（東北大金属材料研究所後藤研究室との共同研究)、Li_yCoO_2 系、Na_yCoO_2 系、SnSe 単結晶薄膜（東北大金属材料研究所後藤研究室との共同研究）などである。各材料の熱電材料としてのポテンシャルを明らかにした。

２．学術論文 291 編

A. Mn, Co 酸化物の熱物性（熱伝導率、熱拡散率、熱膨張、音速、熱起電力） 49 編

(A-1) M. Ikebe, H. Fujishiro and Y. Konno, “Anomalous Phonon-Spin Scattering in $La_{1-X}Sr_XMnO_3$”,
J. Phys. Soc. Jpn. **67** (1998) pp. 1083-1085 (No. 51 paper)

(A-2) H. Fujishiro, M. Ikebe and Y. Konno, “Phase Transition to Antiferromagnetic State in $La_{1-X}Sr_XMnO_3$ ($X \geq 0.5$)”,
J. Phys. Soc. Jpn. **67** (1998) pp. 1799-1800 (No. 52 paper)

(A-3) H. Fujishiro, T. Fukase and M. Ikebe, “Charge Ordering and Sound Velocity Anomaly in $La_{1-X}Sr_XMnO_3$ ($X \geq 0.5$)”,
J. Phys. Soc. Jpn. **67** (1998) pp. 2582-2585 (No. 53 paper)

(A-4) H. Fujishiro and M. Ikebe, “Two-level-like anomalous phonon scattering in $La_{1-X}Sr_XMnO_3$ and $La_{2-X}Sr_XCuO_4$”,
Physica B **263-264** (1999) pp. 691-694 (No. 56 paper)

(A-5) H. Fujishiro, T. Fukase, M. Ikebe and T. Kikuchi, “Sound Velocity Anomaly at around X~1/8 in $La_{1-X}Ca_XMnO_3$”,
J. Phys. Soc. Jpn. **68** (1999) pp. 1469-1472 (No. 57 paper)

(A-6) H. Fujishiro, M. Ikebe, T. Kikuchi and H. Ozawa, “First-order-like ferromagnetic transition in $(La_{1-y}Pr_y)_{1-x}(Ca_{1-z}Sr_z)_xMnO_3$ (X~0.25)”,
Physica B **281&282** (2000) pp. 491-493 (No. 65 paper)

(A-7) M. Ikebe, H. Fujishiro and S. Sugawara, “An evidence for strong phonon-conduction electron interaction from thermal transport anomaly in $Nd_{0.50}Sr_{0.50}MnO_3$”,
Physica B **281&282** (2000) pp. 496-497 (No. 66 paper)

(A-8) H. Fujishiro, M. Ikebe, S. Ohshiden and K. Noto, “Canted Antiferromagnetic Order and Large Magnetoresistance in $La_{1-X}Ca_XMnO_3$, $Pr_{1-X}Ca_XMnO_3$ and other $RE_{1-X}AE_XMnO_3$ Manganese Oxides (X~0.9)”,
J. Phys. Soc. Jpn. **69** (2000) pp. 1865-1871 (No. 69 paper)

(A-9) H. Fujishiro, S. Ohshiden and M. Ikebe, “Thermal Transport Anomaly Associated with Weak Ferromagnetism in $CaMnO_3$”,
J. Phys. Soc. Jpn. **69** (2000) pp. 2082-2086 (No. 70 paper)

(A-10) H. Fujishiro, T. Fukase and M. Ikebe, “Anomalous Lattice Softening at X=0.19 and 0.82 in $La_{1-X}Ca_XMnO_3$”,
J. Phys. Soc. Jpn. **70** (2001) pp. 628-631 (No. 73 paper)

(A-11) M. Ikebe, H. Fujishiro, S. Kanoh and T. Mikami, “Characteristic Phonon Scattering Enhancement Correlated with Magnetic and Charge Orders in $La_{1-X}Sr_XMnO_3$ ($X > 0.50$)”,
phys. stat. sol. (b) **225** (2001) pp. 135-143 (No. 74 paper)

(A-12) H. Fujishiro, S. Kanoh, H. Yamazaki and M. Ikebe, “Enhanced Phonon Heat Conduction Correlated with Induced Ferromagnetic Metallic Phase in $Pr_{0.65}Ca_{0.35}(Mn_{1-Z}Co_Z)O_3$”,
J. Phys. Soc. Jpn. **70** (2001) pp. 2616-2621 (No. 75 paper)

(A-13) Y. Moritomo, T. Akimoto, H. Fujishiro and A. Nakamura, “Specific heat of $La_{1-X}Sr_XMnO_3$ (X~0.5): Comparison between three- and two-dimensional metallic states”,
Phys. Rev. B **64** (2001) pp. 064401-1~4 (No. 77 paper)

(A-14) H. Fujishiro, “Thermal conductivity anomalies around antiferromagnetic order in $La_{0.50}Sr_{0.50}MnO_3$ and $Nd_{0.50}Sr_{0.50}MnO_3$ crystals”,
Physica B **307** (2001) pp. 57-63 (No. 78 paper)

(A-15) H. Fujishiro, S. Kanoh and M. Ikebe, "Heat Transport Enhancement in Ferromagnetic Metallic Phase of $La_{1-X}Ba_XMnO_3$",
J. Phys. Soc. Jpn. **71** (2002) Suppl. pp. 142-144 (No. 79 paper)

(A-16) M. Ikebe, H. Fujishiro, H. Yamazaki and S. Kanoh, "Stabilization of Ferrromagnetic Metallic Phase and Anomalous Magnetotransport in $Pr_{1-X}Ca_X(Mn_{1-Z}Co_Z)O_3$",
J. Phys. Soc. Jpn. **71** (2002) Suppl. pp. 145-147 (No. 80 paper)

(A-17) H. Fujishiro, M. Ikebe, T. Akashi and T. Goto, "Thermal diffusivity of $La_{1-X}Ca_XMnO_3$ up to 1200 K",
Physica B **316-317** (2002) pp.261-264 (No. 81 paper)

(A-18) M. Ikebe, H. Fujishiro, and M. Numano, "Effect of oxygen content variation on phonon heat transport in $La_{0.75}Ca_{0.25}MnO_{3+\delta}$",
Physica B **316-317** (2002) pp. 265-268 (No. 82 paper)

(A-19) H. Fujishiro, S. Sugawara and M. Ikebe, "Anomalous phonon transport enhancement at first-order ferromagnetic transition in $(Gd,Sm,Nd)_{0.55}Sr_{0.45}MnO_3$",
Physica B 316-317 (2002) pp.331-334 (No. 83 paper)

(A-20) H. FUJISHIRO, M. IKEBE, S. KANOH AND H. OZAWA, "THERMAL TRANSPORT IN FERROMAGNETIC $La_{1-X}AE_XMnO_3$ WITH LARGE DIVALENT IONS",
ACTA PHYSICA POLONICA B **34** (2003) pp. 823-826 (No. 87 paper)

(A-21) M. IKEBE, H. FUJISHIRO AND H. OZAWA, "EFFECT OF A-SITE CATION SIZE MISMATCH ON FIRST-ORDER-LIKE FERROMAGNETIC TRANSITION IN PEROVSKITE MANGANITES",
ACTA PHYSICA POLONICA B **34** (2003) pp. 827-830 (No. 88 paper)

(A-22) K. Suzuki, H. Fujishiro, Y. Kashiwada, Y. Fujine and M. Ikebe, "Magnetic, electrical and thermal properties of $La_{0.80}Sr_{0.20}(Mn_yCo_{1-y})O_3$",
Physica B **329-333** (2003) pp.922-923 (No. 91 paper)

(A-23) Y. Kashiwada, H. Fujishiro and M. Ikebe, "Thermal conductivity of $Pr_{0.65}(Ca_{1-Z}Sr_Z)_{0.35}MnO_3$ under applied field",
Physica B **329-333** (2003) pp. 924-925 (No. 92 paper)

(A-24) Y. Watanabe, K. Takahashi, S. Awaji, K. Watanabe. H. Fujishiro and M. Ikebe, "Temperature and Magnetic Field Dependence of the Coexistent Phases in $La_{1-X}Ca_XMnO_3$ (X=0.47, 0.49),
J. Phys. Soc. Jpn. **72** (2003) pp. 817-821 (No. 96 paper)

(A-25) Y. Fujine, H. Fujishiro, K. Suzuki, Y. Kashiwada and M. Ikebe, "Magnetism and thermoelectricity in $La_{0.8}Sr_{0.2}Co_{1-Z}M_ZO_3$ (M: 3d transition metal)",
J. Mag. Mag. Mat. **272-276** (2004) pp. 104-105 (No. 98 paper)

(A-26) H. Fujishiro, Y. Fujine, Y. Mita and M. Ikebe, "Thermal conductivity and magnetism in $(Ca_{1-X}Sr_X)MnO_3$",
J. Mag. Mag. Mat. **272-276** (2004) pp. 1796-1797 (No. 99 paper)

(A-27) M. Ikebe, H. Fujishiro, S. Kanoh and H. Yamazaki, "Lattice effect on ferromagnetic-metal phase transition in $Pr_{0.65}Ca_{0.35}(Mn_{1-Z}Co_Z)O_3$ and $Pr_{0.65}Ca_{0.35}(Mn_{1-Z}Cr_Z)O_3$",
J. Mag. Mag. Mat. **272-276** (2004) pp. 1798-1799 (No. 100 paper)

(A-28) J. Hejtmanek, Z. Jirak, K. Knizek, M. Marysko, M. Veverka and H. Fujishiro, "Magnetism, structure and transport of $Y_{1-X}Ca_XCoO_3$ and $La_{1-X}Ba_XCoO_3$",
J. Mag. Mag. Mat. **272-276** (2004) pp. e283-e284 (No. 101 paper)

(A-29) M. Ikebe, H. Fujishiro, T. Kumagai, A. Fujiwara and Y. Obi, "Magic d-electron number of doped ions for occurrence of ferromagnetic metal phase in $Pr_{0.65}Ca_{0.35}Mn_{0.96}A_{0.04}O_3$",
Physica B **359-361** (2005) pp. 1294-1296 (No. 110 paper)

(A-30) Y. Fujine, H. Fujishiro, Y. Kashiwada, J. Hejtmanek and M. Ikebe, "Anomalous phonon scattering by Jahn-Teller active Co intermediate spins in $LaCoO_3$ and doped $LaCoO_3$",
Physica B **359-361** (2005) pp. 1360-1362 (No. 111 paper)

(A-31) M. Ikebe, H. Fujishiro, S. Kanoh and T. Fukase, "Anomalies in Sound Velocity and Thermal Expansion Related to Charge Order and Ferromagnetic Transitions in $Pr_{0.65}Ca_{0.35}(Mn_{1-Z}Co_Z)O_3$",
Physica B **378-380** (2006) pp. 534-535 (No. 123 paper)

(A-32) H. Fujishiro, M. Ikebe, T. Kikuchi and T. Fukase, "Anomalous Sound Velocity Behavior of $La_{1-X}Ca_XMnO_3$ (X~0.48) in Applied Field",
Physica B **378-380** (2006) pp. 518-519 (No. 124 paper)

(A-33) Y. Kashiwada, H. Fujishiro, Y. Fujine, M. Ikebe and J. Hejtmanek, "Metal-Insulator Transition and Phonon Scattering Mechanisms in $La_{1-X}Sr_XCoO_3$",
Physica B **378-380** (2006) pp. 529-531 (No. 125 paper)

(A-34) H. Fujishiro and M. Ikebe, "Thermal Conductivity Anomaly in $La_{0.52}Ca_{0.48}MnO_3$ under Applied Field",
Physica B **378-380** (2006) pp. 499-500 (No. 128 paper)

(A-35) H. Fujishiro, T. Naito, Y. Kashiwada and Y. Fujine, "Thermal conductivity anomalies of $RECoO_3$ related with spin-state transition",
J. Phys. Soc. Jpn. **77** (2008) 084603 (5 pages) (No. 149 paper)

(A-36) T. Naito, M. Sumomozawa, H. Sasaki and H. Fujishiro, "Thermal Conductivity of $(Pr_{1-x}RE_x)_{0.7}Ca_{0.3}CoO_3$ (RE=Sm, Gd) around Metal-Insulator – Spin-state Transition",
J. Phys. Conf. Series **150** (2009) 022062 (4 pages) (No. 155 paper)

(A-37) T. Naito, H. Sasaki and H. Fujishiro, "Simultaneous metal-insulator and spin-state transition in $(Pr_{1-y}RE_y)_{1-x}Ca_xCoO_3$ (RE=Nd, Sm, Gd, and Y)",
J. Phys. Soc. Jpn. **79** (2010) 034710 (5 pages) (No. 166 paper)

(A-38) T. Naito, H. Sasaki, H. Fujishiro and M. Yoshizawa, "Elastic and Thermal Transport Properties of $(Pr_{1-y}Gd_y)_{0.7}Ca_{0.3}CoO_3$ at Metal Insulator Transition",
J. Phys. Conf. Series **200** (2010) 012137 (4 pages) (No. 167 paper)

(A-39) J. Hejtmanek, E. Santava, K. Knizek, M. Marysko, Z. Jirak, T. Naito, H. Sasaki, and H. Fujishiro, "Metal-insulator transition and the Pr^{3+}/Pr^{4+} valence shift in $(Pr_{1-y}Y_y)_{0.7}Ca_{0.3}CoO_3$",
Phys. Rev. B **82** (2010) 165107 (7 pages) (No. 175 paper)

(A-40) M. Marysko, Z. Jirak, K. Knizek, P. Novak, J. Hejtmanek, T. Naito, H. Sasaki, and H. Fujishiro, "Thermally and field-driven spin-state transitions in $(Pr_{1-y}Y_y)_{0.7}Ca_{0.3}CoO_3$"
J. Appl. Phys. **109** (2011) 07E127 (3 pages) (No. 178 paper)

(A-41) H. Fujishiro, T. Naito, S. Ogawa, K. Nitta, J. Hejtmanek, K. Knizek and Z. Jirak, "Valence shift of Pr ion from 3+ to 4+ in $(Pr_{1-y}Y_y)_{0.7}Ca_{0.3}CoO_3$ estimated by X-ray absorption spectroscopy",
J. Phys. Soc. Jpn. **81** (2012) 064709 (5 pages) (No. 189 paper)

(A-42) H. Fujishiro, T. Naito, D. Takeda, N. Yoshida, T. Watanabe, K. Nitta, J. Hejtmanek, K. Knizek and Z. Jirak, "Simultaneous valence shift of Pr and Tb ions at the spin-state transition in $(Pr_{1-y}Tb_y)_{0.7}Ca_{0.3}CoO_3$",
Phys. Rev. B **87** (2013) 155153 (7 pages) (No. 203 paper)

(A-43) J. Hejtmánek, Z. Jirák, O. Kaman, K. Knížek, E. Santava, K. Nitta, T. Naito, and H. Fujishiro, "Phase transition in $Pr_{0.5}Ca_{0.5}CoO_3$ and related cobaltites",
The European Physical Journal B **86** (2013) 305 (8 pages) (No. 204 paper)

(A-44) Z. Jirak, J. Hejtmanek, K. Knizek, M. Marysko, P. Novak, E. Santava, T. Naito and H. Fujishiro, "Ground state properties of the mixed-valence cobaltites $Nd_{0.7}Sr_{0.3}CoO_3$, $Nd_{0.7}Ca_{0.3}CoO_3$ and $Pr_{0.7}Ca_{0.3}CoO_3$",
J. Phys. Condensed Mater **25** (2013) 216006 (12 pages) (No. 208 paper)

(A-45) K. Knizek, J. Hejtmanek, M. Marysko, P. Novak, E. Santava, Z. Jirak, T. Naito, H. Fujishiro and C. R. dela Cruz, "Spin-state crossover and low-temperature magnetic state in yttrium doped $Pr_{0.7}Ca_{0.3}CoO_3$",
Phys. Rev. B **88** (2013) 224412 (8 pages) (No. 209 paper)

(A-46) Z. Jirak, J. Hejtmanek, K. Knizek, P. Novak, E. Santava, and H. Fujishiro, "Magnetism of perovskite cobaltites with Kramers rare-earth ions",
J. Appl. Phys. **115** (2014) 17E118 (3 pages) (No. 210 paper)

(A-47) T. Naito, H. Fujishiro, T. Nishizaki, N. Kobayashi, J. Hejtmanek, K. Knizek and Z. Jirak, "Suppression of the metal-insulator transition by magnetic field in $(Pr_{1-y}Y_y)_{0.7}Ca_{0.}3CoO_3$ (y = 0.0625)",
J. Appl. Phys. **115** (2014) 233914 (5 pages) (No. 213 paper)

(A-48) Y. Noda, H. Fujishiro, T. Naito, A. Ito, T. Goto, J. Hejtmanek and Z. Jirak, "Electrical resistivity anomaly in $(Pr_{1-y}M_y)_{1-x}Ca_xCoO_3$ epitaxial films (M = Y, Gd) fabricated by pulsed laser deposition",
AIP Advances **6** (2016) 025318 (9 pages) (No. 232 paper)

(A-49) H. Fujishiro, Y. Noda, K. Akuzawa, T. Naito, A. Ito, T. Goto, M. Marysko, Z. Jirak, J. Hejtmanek and K. Nitta, "Electrical resistivity anomaly, valence shift of Pr ion and magnetic behavior in epitaxial $(Pr_{1-y}Y_y)_{1-x}Ca_xCoO_3$ thin films under compressive strain",
J. Appl. Phys. **121** (2017) 115104 (8 pages) (DOI: 10.1063/1.4978747）(No. 246 paper)

B. 酸化物超電導体の熱物性（熱伝導率、熱拡散率、熱起電力） 30 編

(B-1) M. Ikebe, H. Fujishiro, T. Naito, K. Noto, S. Kohayashi and S. Yoshizawa, "Thermal conductivity of YBCO(123) and YBCO(211) mixed crystals prepared by MMTG",
Cryogenics **34** (1994) pp. 57-61 (No. 14 paper)

(B-2) M. Ikebe, H. Fujishiro, T. Naito and K. Noto, "Simultaneous Measurement of Thermal Diffusivity and Conductivity Applied to Bi-2223 Ceramic Superconductors",
J. Phys. Soc. Jpn. **63** (1994) pp. 3107-3114 (No. 16 paper)

(B-3) M. Matsukawa, K. Noto, H. Fujishiro, T. Todate, K. Mori, Y. Yamada and M. Ishihara, "THERMAL TRANSPORT AND SCATTERING MECHANISMS IN BPSCCO HIGH-T_c SUPERCONDUCTORS",
Physica B **194-196** (1994) pp. 2217-2218 (No. 17 paper)

(B-4) M. Matsukawa, F. Tatezaki, K. Noto, H. Fujishiro, K. Michishita and Y. Kubo, "Thermal conductivity of Ag-doped Bi-2212 superconducting materials prepared by the floating method",
Cryogenics **34** (1994) pp. 685-688 (No. 23 paper)

(B-5) H. Fujishiro, M. Ikebe, T. Naito, K. Noto, S. Kohayashi and S. Yoshizawa, "Anisotropic Thermal Diffusivity and Conductivity of YBCO(123) and YBCO(211) Mixed Crystals I",
Jpn. J. Appl. Phys. **33** (1994) pp. 4965-4970 (No. 24 paper)

(B-6) H. Fujishiro, M. Ikebe, T. Naito and K. Noto, "Phonon Thermal Diffusivity and Conductivity of Oxygen Deficient $YBa_2Cu_3O_7$",
Physica C **235-240** (1994) pp. 825-826 (No. 26 paper)

(B-7) H. Ogasawara, M. Matsukawa, K. Noto, H. Sato, H. Fujishiro, Y. Kashiwaba, S. Fujinuma, K. Mori and Y. Hidaka, "In-plane thermal conductivity of $Ln_{2-x}Ce_xCuO_{4-y}$ single crystals (Ln = Nd and Pr) with the T'-phase structure",
Physica C **235-240** (1994) pp. 1399-1400 (No. 27 paper)

(B-8) H. Fujishiro, M. Ikebe, T. Naito, M. Matsukawa, K. Noto, I. Shigaki, K. Shibutani, S. Hayashi and R. Ogawa, "Thermal Conductivity of Bi-2212 Single Crystals Prepared by TSFZ Method",
Physica C **235-240**(1994) pp. 1533-1534 (No. 28 paper)

(B-9) M. Ikebe, H. Fujishiro, T. Naito, M. Matsukawa and K. Noto, "Anisotropic Thermal Diffusivity and Conductivity of YBCO(123) and YBCO(211) Mixed Crystals II",
Jpn. J. Appl. Phys. **33** (1994) pp. 6157-6159 (No. 30 paper)

(B-10) H. Fujishiro, M. Ikebe, M. Yagi, M. Matsukawa, H. Ogasawara and K. Noto, "Thermal Conductivity and Diffusivity of $Nd_{2-X}Ce_XCuO_4$",
Physica B **219&220** (1996) pp. 163-165 (No. 32 paper)

(B-11) H. Fujishiro, M. Ikebe, K. Nakasato and K. Noto, "Influence of Cu site impurities on the thermal conductivity of $YBa_2Cu_3O_{7-\delta}$",
Physica C **263** (1996) pp. 305-308 (No. 33 paper)

(B-12) M. Ikebe, H. Fujishiro, K. Nakasato and K. Noto, "Thermal conductivity of $REBa_2Cu_3O_7$ (RE = Y, Dy, Sm, Nd) superconductors",
Physica C **263** (1996) pp. 309-312 (No. 34 paper)

(B-13) H. Fujishiro, K. Nakasato, S. Takahashi and M. Ikebe, "Effect of Y-site and Ba-site Substitution on Thermal Properties of $YBa_2Cu_3O_{7-\delta}$",
Czech. J. Phys. **46** (1996) Suppl. S3, pp. 1207-1208 (No. 38 paper)

(B-14) M. Ikebe, H. Fujishiro, Y. Obi, H. Fujimori and K. Noto, "Transport and Thermal Properties of Amorphous Mn-Y Alloys",
Czech. J. Phys. **46** (1996) Suppl. S4, pp. 2241-2242 (No. 39 paper)

(B-15) H. Fujishiro, M. Ikebe, M. Yagi, K. Nakasato, Y. Shibazaki and T. Fukase, "Thermal Conductivity and Phonon Scattering Mechanisms in $La_{2-X}M_XCuO_4$",
J. Low Temp. Phys. **105** (1996) pp. 981-986 (No. 41 paper)

(B-16) M. Ikebe, H. Fujishiro, M. Yagi and T. Fukase, "Effect of annealing on thermal and electrical transport in $Nd_{1.85}Ce_{0.15}CuO_4$",
Superlattices and Microstructures **21** (1997) pp. 357-362 (No. 44 paper)

(B-17) M. Ikebe, H. Fujishiro and K. Nakasato, "Energy Gap Symmetry and Thermal Conductivity of $YBa_2Cu_3O_7$",
J. Low Temp. Phys. **107** (1997) pp. 467-472 (No. 46 paper)

(B-18) H. Fujishiro, M. Ikebe, Y. Konno and T. Fukase, "Sound Velocity Anomaly Associated with Polaron Ordering in $La_{1-X}Sr_XMnO_3$",
J. Phys. Soc. Jpn. **66** (1997) pp. 3703-3705 (No. 48 paper)

(B-19) M. Ikebe, H. Fujishiro, K. Nakasato, T. Mikami, T. Naito and T. Fukase, "Thermal Transport in 90 K- and 60 K-phase $YBa_2Cu_3O_{7-\delta}$ High-T_c Oxides",
phys. stat. sol. (b) **209** (1998) pp. 413-426 (No. 54 paper)

(B-20) M. Ikebe and H. Fujishiro, "Enhanced phonon scattering due to 3d-transition metal substitution for Cu in $YBa_2Cu_3O_{7-\delta}$",
Physica B **263-264** (1999) pp. 636-639 (No. 55 paper)

(B-21) H. Fujishiro, M. Ikebe and Y. Shibazaki, "Enhanced Phonon Scattering below T_c Caused by Zn and Ni Substitution in $La_{1.85}Sr_{0.15}CuO_4$",
J. Low Temp. Phys. **117** (1999) pp. 1181-1185 (No. 59 paper)

(B-22) M. Ikebe, H. Fujishiro and K. Noto, "ANISOTROPIC Ag CONTRIBUTION TO TRANSPORT PHENOMENA IN Ag-$Bi_2Sr_2CaCu_2O_y$ BULK CRYSTAL",
Advances in Science and Technology **23** (1999) pp. 421-428 (No. 60 paper)

(B-23) H. Fujishiro, M. Ikebe and Y. Shibazaki, "THERMAL CONDUCTIVITY OF T*-PHASE $(Nd_{1-x-y}Ce_xSr_y)_2CuO_4$ OXIDE SUPERCONDUCTORS",
Advances in Science and Technology **23** (1999) pp. 429-436 (No. 61 paper)

(B-24) H. Fujishiro, M. Ikebe and T. Fukase, "ULTRASONIC AND PHONON THERMAL TRANSPORT STUDIES ON $YBa_2Cu_3O_{7-\delta}$ OXIDE SUPERCONDUCTORS",
Advances in Science and Technology **23** (1999) pp. 437-444 (No. 62 paper)

(B-25) M. Ikebe and H. Fujishiro, "Heat transport in T*-phase $(Nd_{1-x-y}Ce_xSr_y)_2CuO_4$ superconductors",
Physica B **284-288** (2000) pp. 1007-1008 (No. 68 paper)

(B-26) H. Fujishiro, M. Ikebe and T. Takahashi, "Preparation of $RuSr_2GdCu_2O_8$ Compounds with Enhanced Superconducting Transition Temperature",
J. Low Temp. Phys., Vol. **131**, (2003) pp. 589-593 (No. 90 paper)

(B-27) T. Naito, K. Sato, D. Yamaguchi and H. Fujishiro, "Vortex Pinning Properties of $(Y_{1-X}La_X)$-Ba-Cu-O and $(Y_{1-X}Pr_X)$-Ba-Cu-O Superconducting Bulks",
Physica C **469** (2009) pp. 1218-1230 (No. 163 paper)

(B-28) T. Naito, S. Ohata, T. Konno and H. Fujishiro, “La-site Substitution Effect by Ce Ion on Carrier Concentration and Structural Phase Transition in $La_{2-x}Sr_xCuO_4$”,
Physica C **470** (2010) pp. S261-S262 (No. 176 paper)

(B-29) T. Naito, D. Yamaguchi and H. Fujishiro, “Anisotropic Thermal Conductivity of RE_2CuO_4 (RE = Pr, Nd, and Sm) Single Crystals Grown by TSFZ Method”,
Chinese Journal of Physics (CJP) **49** (2011) pp. 331-334 (No. 177 paper)

(B-30) T. Naito, Y. Ueno and H. Fujishiro, “Relationship between structural phase transition and carrier concentration in $La_{2-x-y}Sr_xR_yCuO_4$ (R = Ce or Tb)”,
Physica C **471** (2011) pp. 690-692 (No. 184 paper)

C. 超伝導線材、シース合金材料の熱物性　13 編

(C-1) H. Fujishiro, M. Ikebe, K. Noto, T. Sasaoka, K. Nomura, “Thermal and electrical properties of Ag-Au and Ag-Cu Alloy tapes for the metal stabilizer of oxide superconductors”,
Cryogenics **33** (1993) pp. 1086-1090 (No. 13 paper)

(C-2) T. Sasaoka, K. Nomura, J. Sato, S. Kuma, H. Fujishiro, M. Ikebe and K. Noto, “Characteristics of Ag-Au alloy sheathed Bi-Pb-Sr-Ca-Cu-O superconducting tapes for current leads”,
Appl. Phys. Lett. **64** (1994) pp. 1304-1305 (No. 18 paper)

(C-3) H. Fujishiro, M. Ikebe, K. Noto, M. Matsukawa, T. Sasaoka, K. Nomura, J. Sato and S. Kuma, “Low Thermal Conductive Bi-2223 Tapes Sheathed with Ag-Au Alloys”,
IEEE Trans. Mag. **30** (1994) pp. 1645-1650 (No. 21 paper)

(C-4) T. Naito, H. Fujishiro, Y. Yamada, “Thermal conductivity and thermal dilatation of Bi2223 sheathed tape”,
IEEE Trans. Appl. Supercond. **19** (2009) pp. 3034-3036 (No. 159 paper)

(C-5) T. Naito, H. Fujishiro and Y. Yamada, “Thermal conductivity of single and multi-stacked DI-BSCCO tapes”,
Cryogenics **49** (2009) pp. 429-432 (No. 161 paper)

(C-6) T. Naito, H. Fujishiro and Y. Yamada, “Thermal conductivity of DI-BISCCO tapes with stacked or sandwiched structure”,
J. Phys. Conf. Series **234** (2010) 022025 (No. 169 paper)

(C-7) T. Naito, H. Fujishiro and Y. Yamada, “Anisotropic thermal transport in double-pancake coil wound with DI-BISCCO tape”,
Physica C **470** (2010) pp. 1397-1400 (No. 172 paper)

(C-8) T. Naito, H. Fujishiro, H. Okamoto, H. Hayashi, Y. Gosho, N. Fujiwara and Y. Shiohara, “Thermal conductivity of YBCO coated conductors fabricated by IBAD-PLD method”,
Supercond. Sci. Technol. **23** (2010) 105013 (4 pages) (No. 173 paper)

(C-9) T. Naito, H. Fujishiro, H. Okamoto, H. Hayashi, Y. Gosho, N. Fujiwara, Y. Shiohara, “Thermal conductivity of YBCO coated conductors reinforced by metal tape”,
IEEE Trans. Appl. Supercond. **21** (2011) pp. 3037-3040 (No. 181 paper)

(C-10) T. Naito, H. Fujishiro and J. Fujikami, “Anisotropic thermal conductivity of silver sheathed Bi2223 superconducting tape “,
IEEE Trans. Appl. Supercond. **21** (2011) pp. 2828-2831 (No. 182 paper)

(C-11) T. Naito, H. Fujishiro, Y. Yamamura, K. Saito, H. Okamoto, H. Hayashi, Y. Gosho, T. Ohkuma, and Y. Shiohara, “Specific heat and thermal diffusivity of YBCO coated conductors”,
Physics Procedia, **36** (2012) pp. 1609-1613 (No. 196 paper)

(C-12) T. Naito, H. Fujishiro, G. Osabe and J. Fujigami, “Anisotropic thermal transport in Bi2223/Ag superconducting tape with sandwiched structure”,
Physica C **484** (2012) pp. 159-162 (No. 199 paper)

(C-13) Tomoyuki Naito, Hiroyuki Fujishiro, and Yuichi Yamada, “Thermal conductivity and dilatation of a Bi-2223/Ag (DI-BISCCO) superconducting wire laminated with Ni-alloy tapes”,
IEEE Trans. Appl. Supercond. **28** (2018) 6400404 (DOI: 10.1109/TASC.2018.2796382) (No. 259 paper)

D. 熱物性測定技術の開発（熱拡散率測定、2 次元熱伝導率測定、接触熱抵抗測定） 6 編

(D-1) 藤代博之、内藤智之、池部　学、能登宏七、「低温における熱拡散率と熱伝導率の同一セッティング測定」、
低温工学 **28** (1993) pp. 533-539 (No. 10 paper)

(D-2) 藤代博之、池部　学、内藤智之、能登宏七、「Bi 系酸化物超伝導体の同一セッティングによる熱拡散率、熱伝導率測定」、
低温工学 **28** (1993) pp. 582-587 (No. 11 paper)

(D-3) 保原夏朗、松川倫明、松浦伸悌、藤代博之、能登宏七、「ヘリウム冷凍機を用いた熱伝導率の完全自動測定」、
低温工学 **28** (1993) pp. 688-692 (No. 12 paper)

(D-4) H. Fujishiro, M. Ikebe, K. Nakasato and T. Naito, “Proposal of Three Terminal Method for Low Temperature Thermal Diffusivity Measurement”,
Czech. J. Phys. **46** (1996) Suppl. S5, pp. 2761-2762 (No. 40 paper)

(D-5) H. Fujishiro, T. Okamoto, M. Ikebe and K. Hirose, “A New Method for Simultaneous Determination of Anisotropic Thermal Conductivities Based on Two-Dimensional Analyses”,
Jpn. J. Appl. Phys. **40** (2001) pp. 388-392 (No. 71 paper)

(D-6) H. Fujishiro, T. Okamoto and K. Hirose, “Thermal contact resistance between high-T_c superconductor and copper”,
Physica C **357-360** (2001) pp. 785-788 (No. 76 paper)

E. REBaCuO 系超電導バルクの熱物性　12 編

(E-1) H. Fujishiro and S. Kohayashi, “Thermal Conductivity, Thermal Diffusivity and Thermoelectric Power of Sm-Based Bulk Superconductors”,
IEEE Trans. Appl. Supercond. **12** (2002) pp. 1124-1127 (No. 84 paper)

(E-2) 藤代博之、池部　学、能登宏七、手嶋英一、澤村　充、「GdBaCuO 系バルク超伝導体の熱的性質—YBaCuO 系との比較—」,
低温工学 **37** (2002) pp. 659-664 (No. 85 paper)

(E-3) 手嶋英一、平野芳生、藤代博之、「0.5 T - 77 K で動作可能な 250A 級 Y 系高温超電導バルク電流リード」,
低温工学 **37** (2002) pp. 718-725 (No. 86 paper)

(E-4) H. Fujishiro, M. Ikebe, S. Kohayashi, K. Noto and K. Yokoyama, “Additional effect of Ag and 211 phase on thermal expansion of REBaCuO bulk superconductor (RE = Sm, Y),
Cryogenics **43** (2003) pp. 477-481 (No. 89 paper)

(E-5) H. Fujishiro, H. Teshima, M. Ikebe and K. Noto, “Thermal conductivity of YBaCuO bulk superconductors under applied field: effect of content and size of Y211 phase”,
Physica C **392-396** (2003) P1, pp. 171-174 (No. 94 paper)

(E-6) K. Noto, T. Oka, K. Yokoyama, K. Katagiri, H. Fujishiro, H. Okada, H. Nakazawa, M. Muralidhar and M. Murakami, “Thermal and mechanical properties of high T_c bulk superconductors and their applications”,
Physica C **392-396** (2003) pp. 677-683 (No. 95 paper)

(E-7) H. Fujishiro, K. Katagiri, A. Murakami, Y. Yoshino and K. Noto, “Database for thermal and mechanical properties of REBaCuO bulks”,
Physica C **426-431** (2005) pp. 699-704 (No. 121 paper)

(E-8) H. Fujishiro, S. Nariki and M. Murakami, “Thermal Conductivity and Thermoelectric Power of DyBaCuO Bulk Superconductor”,
Supercond. Sci. Technol. **19** (2006) pp. S447-S450 (No. 130 paper)

(E-9) H. Fujishiro, M. Ikebe, H. Teshima and H. Hirano, “Low-Thermal-Conductive DyBaCuO Bulk Superconductor for Current Lead Application”,
IEEE Trans. Appl. Supercond. **16** (2006) pp. 1080-1083 (No. 133 paper)

(E-10) T. Naito, H. Fujishiro, K. Iida, S. Nariki and M. Murakami, “Thermal Conductivity of Er-Ba-Cu-O and Ho-Ba-Cu-O superconducting bulks”,
Supercond. Sci. Technol. **21** (2008) 085001 (4 pages) (No. 148 paper)

(E-11) T. Naito, H. Fujishiro, K. Iida and M. Murakami, “Anisotropic Thermal Conductivity of Er-Ba-Cu-O Bulk Superconductors”,
Physica C **468** (2008) pp. 1428-1430 (No. 152 paper)

(E-12) T. Naito, D. Furuta, T. Arayashiki, H. Fujishiro, Y. Yanagi and Y. Itoh, “Position dependence of irreversibility line on thin plate Gd-Ba-Cu-O bulk superconductor”,
Physics Procedia **27** (2012) pp. 168-171 (No. 191 paper)

F. REBaCuO 系超電導バルク磁石の開発　59 編

(F-1) H. Fujishiro, T. Oka, K. Yokoyama and K. Noto, “Time evolution and spatial distribution of temperature in YBCO bulk superconductor after pulse field magnetizing”,
Supercond. Sci. Technol. **16** (2003) pp. 809-814 (No. 97 paper)

(F-2) H. Fujishiro, K. Yokoyama, T. Oka and K. Noto, “Temperature rise in an Sm-based bulk superconductor after applying iterative pulse fields”,
Supercond. Sci. Technol. **17** (2004) pp. 51-57 (No. 103 paper)

(F-3) H. Fujishiro, T. Oka, K. Yokoyama, M. Kaneyama and K. Noto, “Flux Motion Studies by Means of Temperature Measurement in Magnetizing Processes for HTSC Bulks”,
IEEE Trans. Applied Supercond. **14** (2004) pp. 1054-1057 (No. 104 paper)

(F-4) H. Fujishiro, K. Yokoyama, M. Kaneyama, T. Oka and K. Noto, “Estimation of generated heat in pulse field magnetizing for SmBaCuO bulk superconductor”,
Physica C **412-414** (2004) pp. 646-650 (No. 105 paper)

(F-5) K. Yokoyama, M. Kaneyama, T. Oka, H. Fujishiro and K. Noto, “Temperature measurement of RE123 bulk superconductors on magnetizing process”,
Physica C **412-414** (2004) pp. 688-694 (No. 106 paper)

(F-6) H. Fujishiro, M. Kaneyama, K. Yokoyama, T. Oka and K. Noto, “Generated heat during pulse field magnetizing for REBaCuO (RE = Gd, Sm, Y) bulk superconductors with different pinning ability”,
Supercond. Sci. Technol. **18** (2005) pp. 158-165 (No. 109 paper)

(F-7) H. Fujishiro, K. Yokoyama, M. Kaneyama, T. Oka and K. Noto, “Effect of Metal Ring Setting Outside HTSC Bulk Disk on Trapped Field and Temperature Rise in Pulse Filed Magnetizing”,
IEEE Trans. Appl. Supercond. **15** (2005) pp. 3762-3765 (No. 112 paper)

(F-8) H. Fujishiro, M. Kaneyama, K. Yokoyama, T. Oka and K. Noto, “Rise-Time Elongation Effects on Trapped Field and Temperature Rise in Pulse Field Magnetization for High Temperature Superconducting Bulk”,
Jpn. J. Appl. Phys. **44** (2005) pp. 4919-4925 (No. 115 paper)

(F-9) 金山雅彦、藤代博之、横山和哉、岡　徹雄、能登宏七、「20-40 K における Sm-Ba-Cu-O バルクに対するパルス着磁による捕捉磁場と発熱解析」、
低温工学 **40** (2005) pp. 231-237 (No. 116 paper)

(F-10) H. Fujishiro, M. Kaneyama, T. Tateiwa and T. Oka, “Record High Trapped Field by Pulse Field Magnetization Using GdBaCuO Bulk Superconductor”,
Jpn. J. Appl. Phys. **44** (2005) pp. L1221-L1224 (No. 118 paper)

(F-11) H. Fujishiro, K. Yokoyama, M. Kaneyama, M. Ikebe, T. Oka and K. Noto, “Approach from temperature measurement to trapped field enhancement in HTSC bulks by pulse field magnetizing”,
Physica C **426-431** (2005) pp. 594-601 (No. 119 paper)

(F-12) K. Yokoyama, M. Kaneyama, H. Fujishiro, T. Oka and K. Noto, “Temperature rise and trapped field in a GdBaCuO bulk superconductor cooled down to 10 K after applying pulse magnetic field”,
Physica C **426-431** (2005) pp. 671-675 (No. 120 paper)

(F-13) T. Oka, K. Yokoyama, H. Fujishiro, M. Kaneyama and K. Noto, “Temperature changes in a melt-processed YBCO superconductor activated by field cooling magnetizing process”,
Physica C **426-431** (2005) pp. 794-799 (No. 122 paper)

(F-14) H. Fujishiro, M. Kaneyama, T. Tateiwa and T. Oka, “Trapped Field over 4 Tesla on GdBaCuO Bulk by Pulse Field Method and Magnetizing Mechanism”,
J. Phys.: Conf. Series **43** (2006) pp. 405-408 (No. 126 paper)

(F-15) H. Fujishiro, S. Kawaguchi, M. Kaneyama, A. Fujiwara, T. Tateiwa and T. Oka, “Heat Propagation Analysis in HTSC Bulks during Pulse Field Magnetization”,
Supercond. Sci. Technol. **19** (2006) S540-S544 (No. 131 paper)

(F-16) H. Fujishiro, A. Fujiwara, T. Tateiwa, T. Oka and H. Hayashi, “New Type Superconducting Bulk Magnet by Pulse Field Magnetization with Usable Surface on Both-sides in Open Space”,
IEEE Trans. Appl. Supercond. **16** (2006) 1080-1083 (No. 132 paper)

(F-17) Hiroyuki Fujishiro, Tatsuya Tateiwa, Atsushi Fujiwara, Tetsuo Oka and Hidemi Hayashi, “Higher trapped field over 5 Tesla on HTSC bulk by modified pulse field magnetizing”,
Physica C **445-448** (2006) pp. 334-338 (No. 134 paper)

(F-18) A. Fujiwara, T. Tateiwa, H. Fujishiro, H. Hayashi, T. Nagafuchi and T. Oka, “Development of five aligned superconducting bulk magnets by pulse field magnetizing”,
Physica C **445-448** (2006) pp. 399-402 (No. 135 paper)

(F-19) 藤原　篤、立岩達也、藤代博之、林　秀美、永渕尚志、岡　徹雄、「パルス着磁による ab 面方向冷却型超伝導バルク磁石の伝熱解析---*c* 軸方向冷却との比較 ---」
低温工学 **41** (2006) pp. 390-396 (No. 136 paper)

(F-20) H. Fujishiro, T. Tateiwa, T. Hiyama, Y. Sazuka and T. Oka, “Enhancement of Trapped Field and Total Trapped Flux on High Temperature Bulk Superconductor by a New Pulse-Field Magnetization Method”,
Jpn. J. Appl. Phys. **46** (2007) pp. 4108-4112 (No. 140 paper)

(F-21) H. Fujishiro, T. Tateiwa, K. Kakehata, T. Hiyama and T. Naito, “Trapped Field and Temperature Rise on ϕ65 mm GdBaCuO Bulk by Pulse Field Magnetization”,
Supercond. Sci. Technol. **20** (2007) pp. 1009-1014 (No. 141 paper)

(F-22) H. Fujishiro, T. Hiyama, T. Tateiwa, Y. Yanagi and T. Oka, “Importance of initial M-shaped trapped field profile using a two-step pulse field magnetization (MMPSC) method”,
Physica C **463-465** (2007) pp. 394-397 (No. 142 paper)

(F-23) T. Tateiwa, Y. Sazuka, H. Fujishiro, H. Hayashi, T. Nagafuchi and T. Oka, “Trapped field and temperature rise in rectangular shaped HTSC bulk magnetized by pulse fields”,
Physica C **463-465** (2007) pp. 398-401 (No. 143 paper)

(F-24) K. Yokoyama, T. Oka, H. Fujishiro, “Evaluation of Current Distribution of Bulk Superconductors Magnetized by Pulsed Field”
Physica C **463-465** (2007) pp. 410-414 (No. 144 paper)

(F-25) T. Oka, K. Yokoyama, H. Fujishiro and K. Noto, “Temperature Rise in Melt-Textured Large Grain Superconducting Bulk Magnets during Magnetizing Processes”,
Physica C **460-462** (2007) pp. 748-749 (No. 145 paper)

(F-26) K. Yokoyama, T. Oka, H. Fujishiro and K. Noto, “Numerical Analysis of Bulk Superconducting Magnet Magnetized by Pulsed-Field Considering a Partial Difference of Superconducting Characteristics”,
IEEE Trans. Appl. Supercond. **18** (2008) pp. 1545-1548 (No. 146 paper)

(F-27) K. Kajikawa, R. Yokoo, K. Tomachi, K. Enpuku, K. Funaki, H. Hayashi and H. Fujishiro, “Numerical Evaluation of Pulsed Field Magnetization in a Bulk Superconductor Using Energy Minimization Technique”, *IEEE Trans. Appl. Supercond.* **18** (2008) pp. 1557-1560 (No. 147 paper)

(F-28) T. Hiyama, H. Fujishiro, T. Tateiwa, T. Naito, H. Hayashi and K. Tone, “Trapped Field Enhancement of Five-aligned Superconducting Bulk Magnetized by Pulse Field for Magnetic Separation” *Physica C* **468** (2008) pp. 1469-1472 (No. 150 paper)

(F-29) H. Fujishiro, T. Tateiwa, K. Kakehata, T. Hiyama, T. Naito and Y. Yanagi, “Trapped field characteristics on ϕ65 mm GdBaCuO bulk by modified multi-pulse technique with stepwise cooling (MMPSC)”, *Physica C* **468** (2008) pp. 1477-1480 (No. 151 paper)

(F-30) K. Kajikawa, R. Yokoo, K. Tomachi, K. Enpuku, K. Funaki, H. Hayashi and H. Fujishiro, “Finite element analysis of pulse field magnetization process in a cylindrical bulk superconductor”, *Physica C* **468** (2008) pp. 1494-1497 (No. 153 paper)

(F-31) H. Fujishiro, T. Hiyama, T. Naito, T. Tateiwa and Y. Yanagi, “Possible explanation for trapped field enhancement on REBaCuO bulk by modified multi-pulse technique with stepwise cooling (MMPSC)”, *Materials Science and Engineering B*, **151** (2008) pp. 95-100 (No. 154 paper)

(F-32) T. Oka, K. Yokoyama, H. Fujishiro and K. Noto, “Thermal Behavior and Field-Trapping Property of Melt-Textured Superconducting Bulk Magnets Activated by Quasi-Static Magnetic Fields” *J. Phys. Conf. Series* **150** (2009) 052195 (4 pages) (No. 156 paper)

(F-33) T. Oka, K. Yokoyama, H. Fujishiro and K. Noto, “Thermal and Magnetic Behaviors of Melt-Textured Superconducting Bulk Magnet in Zero-Field Cooling Magnetizing Process”, *Supercond. Sci. Technol.* **22** (2009) 065014 (8 pages) (No. 157 paper)

(F-34) H. Fujishiro, T. Hiyama, T. Miura, T. Naito, S. Nariki, N. Sakai, I. Hirabayashi, “Pulsed Field Magnetization for GdBaCuO Bulk with Stronger Pinning Characteristics”, *IEEE Trans. Appl. Supercond.* **19** (2009) pp. 3545-3548 (No. 158 paper)

(F-35) H. Fujishiro, T. Hiyama, T. Naito, Y. Yanagi and Y. Itoh, “Enhancement of trapped field and total trapped flux on GdBaCuO bulk by MMPSC-IMRA method”, *Supercond. Sci. Technol.* **22** (2009) 095006 (6 pages) (No. 160 paper)

(F-36) H. Fujishiro, K. Kakehata, T. Naito, Y. Yanagi and Y. Itoh, “Enhancement of total trapped fluxes on ϕ65 mm GdBaCuO bulk by multi-pulse techniques”, *Physica C* **469** (2009) pp. 1250-1253 (No. 162 paper)

(F-37) 岡　徹雄，横山和哉，藤代博之，能登宏七、「準静的磁場による磁化過程における溶融超伝導バルク磁石の温度変化と磁場特性」、 *低温工学* **44** (2009) pp. 587-593 (No. 164 paper)

(F-38) H. Fujishiro, T. Naito, K. Kakehata, Y. Yanagi and Y. Itoh, “Estimation of temperature rise from trapped field gradient on superconducting bulk magnetized by multi-pulse technique”, *Supercond. Sci. Technol.* **23** (2010) 025013 (6 pages) (No. 165 paper)

(F-39) H. Fujishiro, T. Naito, T. Miura and H. Hayashi, “Highly efficient magnetic separation using five-aligned superconducting bulk magnet”, *J. Phys. Conf. Series* **234** (2010) 032015 (6 pages) (No. 168 paper)

(F-40) H. Fujishiro, K. Kakehata, D. Furuta and T. Naito, “Temperature measurements in small holes drilled in HTSC bulk during pulsed field magnetization”, *Physica C* **470** (2010) pp. 1181-1184 (No. 170 paper)

(F-41) H. Fujishiro, D. Furuta, T. Naito, K. Yaegashi and N. Yoshimoto, “Large and spatial magnetic field modulation using superconducting bulk magnet and silicon steel”, *Physica C* **470** (2010) pp. 1856-1859 (No. 171 paper)

(F-42) H. Fujishiro, T. Naito, D. Furuta, T. Arayashiki, Y. Yanagi and Y. Itoh, “Direct J_c measurements and trapped field profiles using an identical superconducting bulk”, *Supercond. Sci. Technol.* **24** (2011) 105003 (6 pages) (No. 183 paper)

(F-43) H. Fujishiro, T. Handa, T. Naito, N. Kikuchi, "J_c distribution measurement and analysis on superconducting bulk using "Magnetoscan" method",
Physica C **471** (2011) pp. 893-896 (No. 185 paper)

(F-44) T. Oka, H. Seki, T. Kimura, D. Mimura, S. Fukui, J. Ogawa, T. Sato, M. Ooizumi, H. Fujishiro, H. Hayashi, K. Yokoyama and C. Stiehler, "Magnetic Separation Technique for Ground Water by Five HTS Melt-Processed Bulk Magnets Arranged in a Line",
Physica C **471** (2011) pp. 1506-1560 (No. 187 paper)

(F-45) H. Fujishiro, T. Arayashiki, T. Tamura, T. Naito, H. Teshima and M. Morita, "Trapped field profiles on square-shaped GdBaCuO bulks with different arrangement of growth sector boundaries",
Jpn. J. Appl. Phys. **51** (2012) 093005 (5 pages) (No. 192 paper)

(F-46) Hidekazu Teshima, Mitsuru Morita, Takahiro Arayashiki , Tomoyuki Naito and Hiroyuki Fujishiro, "10 T Class Trapped Field Properties of a Large Gd-Ba-Cu-O Bulk Superconductor",
Physics Procedia **45** (2013) pp. 61-64 (No. 206 paper)

(F-47) H. Mochizuki, H. Fujishiro, T. Naito, Y. Itoh, Y. Yanagi, and T. Nakamura, "Trapped Field Characteristics and Fracture Behavior of REBaCuO Bulk Ring During Pulsed Field Magnetization",
IEEE Trans. Appl. Supercond. **26** (2016) 6800205 (No. 231 paper)

(F-48) K Takahashi, H Fujishiro, M. D. Ainslie and T Naito, "Pulsed field magnetizing characteristics of rectangular-shaped GdBaCuO bulk using split- and solenoid-type coils",
IEEE Trans. Appl. Supercond. **27** (2017) 6800205 (6 pages) (DOI: 10.1109/TASC.2016.2625764) (No. 241 paper)

(F-49) T. Naito, H. Mochizuki, H. Fujishiro and H. Teshima, "Trapped magnetic-field properties of prototype for Gd-Ba-Cu-O/MgB_2 hybrid-type superconducting bulk magnet",
Supercond. Sci. Technol. **29** (2016) 034005 (8 pages) (DOI: 10.1088/0953-2048/29/3/034005) (No. 242 paper)

(F-50) K. Takahashi, M. D. Ainslie, H. Fujishiro, T. Naito, Y-H. Shi, and D. A. Cardwell, "Trapped field properties of a Y-Ba-Cu-O bulk using pulsed field magnetization with a split coil with iron yokes of various geometries and magnetic properties",
Physica C, **536** (2017) pp. 1-10 (DOI: 10.1016/j.physc.2017.03.005) (No. 247 paper)

(F-51) K. Takahashi, H. Fujishiro, T. Naito, Y. Yanagi, Y. Itoh and T. Nakamura, "Fracture behavior by magnetic stress in EuBaCuO superconducting ring bulk reinforced by a stainless steel during field-cooled magnetization",
Supercond. Sci. Technol. **30** (2017) 115006 (9 pages) (No. 250 paper)

(F-52) K. Takahashi, S. Namba, H. Fujishiro, T. Naito, Y. Yanagi, Y. Itoh, T. Nakamura; "Thermal and magnetic strain measurements on REBaCuO ring bulk reinforced by metal ring during field-cooled magnetization",
Supercond. Sci. Technol. **32** (2019) 015007 (9 pages) (DOI: 10.1088/1361-6668/aaee01) (No. 261paper)

(F-53) Tatsuya Hirano, Keita Takahashi, Fumiya Shimoyashiki, Hiroyuki Fujishiro, Tomoyuki Naito, and Mark D. Ainslie, "Influence of $J_c(B, T)$ Characteristics on the Pulsed Field Magnetization of REBaCuO Disk Bulks",
IEEE Trans. Appl. Supercond. **29** (2019) 8000705 (5 pages) (DOI: 10.1109/TASC.2018.2872819) (No. 263 paper)

(F-54) T. Hirano, H. Fujishiro, T. Naito, M. D. Ainslie and Y-H. Shi, "Flux dynamics and thermal behavior of a Gd-Ba-Cu-O bulk magnetized by single- and multi-pulse techniques using split-type coil",
IEEE Trans. Appl. Supercond. **29** (2019) 6801705 (5 pages) (DOI: 10.1109/TASC.2019.2900979) (No. 266 paper)

(F-55) F. Shimoyashiki, H. Fujishiro, T. Naito, and M. D. Ainslie, "Trapped field properties of GdBaCuO superconducting bulk with various diameters magnetized by pulsed field using identical split coil",
IEEE Trans. Appl. Supercond. **29** (2019) 6802405 (5 pages) (DOI: 10.1109/TASC.2019.2901349) (No. 269 paper)

(F-56) Sora Namba, Hiroyuki Fujishiro, Tomoyuki Naito, Mark D Ainslie and Kai Y Huang, “Electromagnetic strain measurements and bidirectional mechanical stress estimation for a REBaCuO ring bulk reinforced by a metal ring during field-cooled magnetization”
Supercond. Sci. Technol. **32** (2019) 125011 (10 pages) (DOI: 10.1088/1361-6668/ab4a8b) (No. 270 paper)

(F-57) T. Naito, H. Fujishiro and S. Awaji, “Field-cooled magnetization of Y-Ba-Cu-O superconducting bulk pair reinforced by full metal encapsulation under high magnetic fields up to 22 T”,
J. Appl. Phys. **126** (2019) 243901 (8 pages) (DOI: 10.1063/1.5124010) (No. 272 paper)

(F-58) D. K. Namburi, K. Takahashi, T. Hirano, T. Kamada, H. Fujishiro, Y-H. Shi, D. A. Cardwell, J. H. Durrell and M. D. Ainslie, “Pulsed-field magnetisation of Y-Ba-Cu-O bulk superconductors fabricated by the infiltration growth technique”,
Supercond. Sci. Technol. **33** (2020) 115012 (12 pages) (DOI: 10.1088/1361-6668/abb590) (No. 282 paper)

(F-59) Motoki Shinden, D. K. Namburi, Keita Takahashi, Hiroyuki Fujishiro, and Mark D. Ainslie, “Pulsed Field Magnetization of GdBaCuO Superconducting Bulks with High Magnetization Efficiency Using a Split-Type Coil with Soft Iron Yoke”,
to be published in IEEE Trans. Appl. Supercond. (2022) (No. 287 paper)

G. 超電導バルク磁石の着磁シミュレーション　32 編

(G-1) H. Fujishiro and T. Naito, “Simulation of temperature and magnetic field distribution in superconducting bulk during pulsed field magnetization”,
Supercond. Sci. Technol. **23** (2010) 105021 (8 pages) (No. 174 paper)

(G-2) H. Fujishiro, T. Naito and M. Oyama, “Mechanism of magnetic flux trapping on superconducting bulk magnetized by pulsed field using a vortex-type coil”,
Supercond. Sci. Technol. **24** (2011) 075015 (7 pages) (No. 179 paper)

(G-3) H. Fujishiro, T. Naito and D. Furuta, “Analysis of temperature and magnetic field distribution in superconducting bulk during pulsed field magnetization”,
IEEE Trans. Appl. Supercond. **21** (2011) pp. 2723-2726 (No. 180 paper)

(G-4) H. Fujishiro, T. Naito, M. Oyama, “Simulation of flux dynamics in a superconducting bulk magnetized by multi-pulse technique”,
Physica C **471** (2011) pp. 889-892 (No. 186 paper)

(G-5) H. Fujishiro, T. Naito and M. Oyama, “Size effect of magnetizing solenoid coil for pulsed field magnetization on the trapped field on superconducting bulk”,
IEEE Trans. Appl. Supercond. **22** (2012) 4700204 (4 pages) (No. 193 paper)

(G-6) H. Fujishiro, T. Naito and M. Oyama, “Three-dimensional simulation of magnetic flux dynamics and temperature rise in HTSC bulk during pulsed field magnetization”,
Physics Procedia **36** (2012) pp. 687-692 (No. 195 paper)

(G-7) H. Fujishiro, T. Naito, M. Oyama, T. Arayashiki, T. Tamura, T. Sasaki and G. Giunchi, “Numerical simulation of trapped field and temperature rise in MgB_2 bulks magnetized by pulsed field”,
IEEE Trans. Appl. Supercond. **23** (2013) 6800804 (4 pages) (No. 205 paper)

(G-8) M. D. Ainslie, H. Fujishiro, T. Ujiie, J. Zou, A. Dennis, Y.-H. Shi and D. A. Cardwell, “Modeling and comparison of trapped fields in (RE)BCO bulk superconductors for activation using pulsed field magnetization”,
Supercond. Sci. Technol. **27** (2014) 065008 (9 pages) (No. 211 paper)

(G-9) H. Fujishiro, T. Naito and T. Yoshida, “Numerical simulation of trapped field on MgB2 bulk disk magnetized by field cooling”,
Supercond. Sci. Technol. **27** (2014) 065019 (7 pages) (No. 212 paper)

(G-10) M. D. Ainslie, H. Fujishiro, “Modelling of bulk superconductor magnetization”,
Supercond. Sci. Technol. **28** (2015) 053002 (20 pages) (Topical Review Paper) (No. 219 paper)

(G-11) J. Zou, M. D. Ainslie, H. Fujishiro, A. G. Bhagurkar, T. Naito, N. Hari Babu, J-F. Fagnard, P. Vanderbemden, A. Yamamoto, “Numerical modeling and comparison of MgB_2 bulks fabricated by HIP and infiltration growth magnetized by field cooling”,
Supercond. Sci. Technol. **28** (2015) 075009 (9 pages) (No. 223 paper)

(G-12) H. Fujishiro, Y. Itoh, Y. Yanagi and T. Nakamura, “Drastic improvement of the trapped field homogeneity in a superconducting hollow bulk by the insertion of a high-J_c superconducting cylinder for NMR bulk magnets”,
Supercond. Sci. Technol. **28** (2015) 095018 (8 pages) (No. 226 paper)

(G-13) M. D. Ainslie, J. Zou, H. Mochizuki, H. Fujishiro, Y-H. Shi, A. R. Dennis and D. A. Cardwell, “Pulsed field magnetization of 0°-0° and 45°-45° bridge-seeded Y-Ba-Cu-O bulk superconductors”
Supercond. Sci. Technol. **28** (2015) 125002 (14 pages) (No. 228 paper)

(G-14) Mark Douglas Ainslie, Hidehiko Mochizuki, Hiroyuki Fujishiro, Wei Zhai, Yun-hua Shi, Anthony Dennis, David Anthony Cardwell, “Pulsed field magnetization of single grain YBCO processed from graded precursor powders”,
IEEE Trans. Appl. Supercond. **26** (2016) 6800104 (4 pages) (No. 231-2 paper)

(G-15) M D Ainslie, H Fujishiro, H Mochizuki, K Takahashi, Y-H Shi, D K Namburi, J Zou, D Zhou, A R Dennis and D A Cardwell, “Enhanced trapped field performance of bulk high-temperature superconductors using split coil, pulsed field magnetization with an iron yoke”
Supercond. Sci. Technol. **29** (2016) 074003 (16 pages) (No. 233 paper)

(G-16) M. D. Ainslie, D. Zhou, H. Fujishiro, K. Takahashi, Y-H. Shi and J. H. Durrell, “Flux jump-assisted pulsed field magnetization of high-J_c bulk high-temperature superconductors”,
Supercond. Sci. Technol. **29** (2016) 124004 (9 pages) (No. 238 paper)

(G-17) 藤代博之、柳　陽介、伊藤佳孝、仲村高志、「超電導各層円筒内挿による NMR 用超電導バルクの捕捉磁場均一化のシミュレーション解析　—円筒の位置、長さ、形状の影響—」、
低温工学 **52** (2017) pp. 33-37 (DOI: 10.2221/jcsj.52.33) (No. 244 paper)

(G-18) M. D. Ainslie, H. Fujishiro, K. Takahashi, Y-H. Shi, D. A. Cardwell, “Pulsed field magnetization of bridge-seeded, bulk YBCO using solenoid and split coils”,
IEEE Trans. Appl. Supercond. **27** (2017) 6801105 (5 pages) (DOI: 10.1109/TASC.2017.2667621) (No. 245 paper)

(G-19) H. Fujishiro, M. D. Ainslie, K. Takahashi, T. Naito, Y. Yanagi, Y. Itoh and T. Nakamura, “Simulation studies of mechanical stresses in REBaCuO superconducting ring bulks with infinite and finite height reinforced by metal ring during field-cooled magnetization”,
Supercond. Sci. Technol. **30**, 085008 (2017) (12 pages) (DOI: 10.1088/1361-6668/aa76a2) (No. 249 paper)

(G-20) Mark D. Ainslie, Akiyasu Yamamoto, Hiroyuki Fujishiro, Jeremy D. Weiss and Eric E. Hellstrom, “Numerical modelling of iron-pnictide bulk superconductor magnetization”,
Supercond. Sci. Technol. **30** (2017) 105009 (7 pages) (No. 251 paper)

(G-21) Mark D Ainslie, Jan Srpcic, Hiroyuki Fujishiro, Difan Zhou, Keita Takahashi, Fernando Perez, David A Cardwell, John H Durrell, “Towards optimization of multi-pulse, multi-temperature pulsed field magnetization of bulk high-temperature superconductors”,
IEEE Trans. Appl. Supercond. **28** (2018) 6800207 (7 pages) (DOI: 10.1109/TASC.2017.2788924) (No. 255 paper)

(G-22) K. Takahashi, H. Fujishiro, T. Naito, Y. Yanagi, Y. Itoh and T. Nakamura, “Numerical simulation of electromagnetic and thermal hoop stresses in REBaCuO superconducting ring and disk bulks reinforced by stainless steel ring with various thicknesses during field-cooled magnetization”,
IEEE Trans. Appl. Supercond. **28** (2018) 6800705 (5 pages) (DOI: 10.1109/TASC.2018.2799578) (No. 256 paper)

(G-23) H. Fujishiro, K. Takahashi, T. Naito, Y. Yanagi, Y. Itoh and T. Nakamura, “A new proposal of mechanical reinforcement structures to annular REBaCuO bulk magnet for compact and cryogen-free NMR spectrometer”,
Physica C **550** (2018) pp. 52-56 (DOI: 10.1016/j.physc.2018.04.012) (No. 258 paper)

(G-24) M. D. Ainslie, K. Y. Huang, H. Fujishiro, J. Chaddock, K. Takahashi, S. Namba, D. A. Cardwell and J. H. Durrell, “Numerical modelling of mechanical stresses in bulk superconductor magnets with and without mechanical reinforcement”
Supercond. Sci. Technol. **32** (2019) 034002 (17 pages) (DOI: 10.1088/1361-6668/aaf851) (No. 262 paper)

(G-25) H. Fujishiro, T. Naito and S. Awaji, “Proposal of effective mechanical reinforcement structure for REBaCuO disk bulk pair by full metal encapsulation to achieve higher trapped field over 20 T”,
Supercond. Sci. Technol. **32** (2019) 045005 (9 pages) (DOI: 10.1088/1361-6668/ab0017) (No. 264 paper)

(G-26) H. Fujishiro, K. Takahashi, T. Naito, Y. Itoh, Y. Yanagi, T. Nakamura and M. D. Ainslie, “Influence of Inner Diameter and Height of Ring-shaped REBaCuO Bulks on Electromagnetic and Mechanical Properties during Field-cooled Magnetization”,
IEEE Trans. Appl. Supercond. (2019) **29** 6801206 (6 pages) (DOI: 10.1109/TASC.2019.2896782) (No. 267 paper)

(G-27) H. Fujishiro, T. Naito, Y. Yanagi, Y. Itoh and T. Nakamura, “Promising effects of a new hat structure and double metal ring for mechanical reinforcement of REBaCuO ring-shaped bulk during field-cooled magnetization at 10 T without fracture”,
Supercond. Sci. Technol. **32** (2019) 065001 (12 pages) (DOI: 10.1088/1361-6668/ab0bed) (No. 268 paper)

(G-28) T. Hirano, H. Fujishiro, T. Naito and M. D Ainslie, “Numerical simulation of flux jump behavior in REBaCuO ring bulks with an inhomogeneous Jc profile during pulsed field magnetization”,
Supercond. Sci. Technol. **33** (2020) 044003 (11 pages) (DOI: 10.1088/1361-6668/ab7297) (No. 273 paper)

(G-29) F. Shimoyashiki, H. Fujishiro, T. Hirano, T. Naito and M. D. Ainslie, "Simulation of mechanical stress in REBaCuO disk bulk magnetized by pulsed-field",
J. Phys. Conf. Series **1559** (2020) 012029 (7 pages) (DOI: 10.1088/1742-6596/1559/1/012029) (No. 277 paper)

(G-30) T. Hirano, H. Fujishiro, T. Naito and M. Ainslie, “Simulation of mechanical stresses in reinforced REBaCuO ring bulks during pulsed-field magnetization”,
J. Phys. Conf. Series 1**559** (2020) 012027 (9 pages) (DOI: 10.1088/1742-6596/1559/1/012027) (No. 279 paper)

(G-31) V. Cientanni, M. D. Ainslie, H. Fujishiro, K. Takahashi, “Modelling higher trapped fields by pulsed field magnetisation of composite bulk MgB_2 superconducting rings”,
Supercond. Sci. Technol. **34** (2021) 114003 (13 pages) (DOI: 10.1088/1361-6668/ac2621) (No. 286 paper)

(G-32) Motoki Shinden, Hiroyuki Fujishiro, Keita Takahashi and Mark D Ainslie, “Possibility of mechanical fracture of superconducting ring bulks due to thermal stress induced by local heat generation during pulsed-field magnetization”,
to be published in Supercond. Sci. Technol. (2022) (No. 288 paper)

H. ハイブリッド型超電導バルク磁石の開発　10 編

(H-1) K. Takahashi, H. Fujishiro and M. D. Ainslie, “A new concept of hybrid trapped field magnet lens (HTFML)”,
Supercond. Sci. Technol. **31** (2018) 044005 (9 pages) (DOI: 10.1088/1361-6668/aaae94) (No. 257 paper)

(H-2) S. Namba, H. Fujishiro, M. D. Ainslie, K. Takahashi, T. Naito, Devendra K. Namburi, and Difan Zhou, “Design optimization of a hybrid trapped field magnet lens (HTFML)”
IEEE Trans. Appl. Supercond. **29** (2019) 6801605 (5 pages) (DOI: 10.1109/TASC.2019.2899255) (No. 265 paper)

(H-3) Sora Namba, Hiroyuki Fujishiro, Tomoyuki Naito, Mark D Ainslie, Keita Takahashi, “Experimental realization of a Hybrid Trapped Field Magnet Lens (HTFML) using a GdBaCuO magnetic lens and MgB_2 bulk cylinder”,
Supercond. Sci. Technol. Letter **32** (2019) 12LT03 (7 pages) (DOI: 10.1088/1361-6668/ab5048) (No. 271 paper)

(H-4) K. Takahashi, H. Fujishiro and M. D. Ainslie, " Simulation study for magnetic levitation in pure water exploiting the ultra-high magnetic field gradient product of a Hybrid Trapped Field Magnet Lens (HTFML)",
J. Appl. Phys. **127** (2020) 185106 (DOI: 10.1063/5.0005356) (11 pages) (No. 274 paper)

(H-5) Sora Namba, Hiroyuki Fujishiro, Tatsuya Hirano, Tomoyuki Naito and Mark D Ainslie, "Optimized performance of an all-REBaCuO hybrid trapped field magnet lens (HTFML)",
Physica C **575** (2020) 1353690 (8 pages) (DOI: 10.1016/j.physc.2020.1353690) (No. 275 paper)

(H-6) S. Namba, H. Fujishiro, T. Naito, M. D. Ainslie and D. Zhou, “Realisation of Hybrid Trapped Field Magnetic Lens (HTFML) consisting of REBCO bulk lens and REBCO bulk cylinder at 77 K”,
J. Phys. Conf. Series **1559** (2020) 012079 (9 pages) (DOI: 10.1088/1742-6596/1559/1/012079) (No. 278 paper)

(H-7) Motoki Shinden, Sora Namba, Tatsuya Hirano, Hiroyuki Fujishiro, Tomoyuki Naito, and Mark D. Ainslie, "Numerical Simulation of a Hybrid Trapped Field Magnet Lens (HTFML) Magnetized by Pulsed Fields",
J. Phys. Conf. Series **1590** (2020) 012048 (8 pages) (DOI: 10.1088/1742-6596/1590/1/012048) (No. 280 paper)

(H-8) K. Takahashi, H. Fujishiro and M. D. Ainslie, “A conceptual study of a high gradient trapped field magnet (HG-TFM) providing toward a quasi-zero gravity space on Earth”,
Supercond. Sci. Technol. **34** (2021) 035001 (13 pages) (DOI: 10.1088/1361-6668/abd386) (No. 283 paper)

(H-9) K. Takahashi, H. Fujishiro, S. Namba and M. D. Ainslie, “Experimental realization of an all-(RE)BaCuO hybrid trapped field magnet lens generating a 9.8 T concentrated magnetic field from a 7 T external field”,
Supercond. Sci. Technol. **34** (2021) 05LT02 (9 pages) (DOI: 10.1088/1361-6668/abeb01) (No. 284 paper)

(H-10) K. Takahashi, H. Fujishiro and M. D. Ainslie, “Validation of a quasi-microgravity space exploiting a high-gradient trapped field magnet (HG-TFM) as a desktop-type magnetic field source”,
to be published in Supercond. Sci. Technol. (2022) (No. 290 paper)

I. MgB_2超電導バルク磁石の開発　29 編

(I-1) T. Naito, T. Sasaki and H. Fujishiro, “Trapped magnetic field and vortex pinning properties of MgB_2 superconducting bulk fabricated by a capsule method”,
Supercond. Sci. Technol. **25** (2012) 095012 (6 pages) (No. 190 paper)

(I-2) T. Naito, T. Sasaki and H. Fujishiro, “A proposal of new fabricating technique of large MgB_2 bulk by a capsule method”,
IEEE Trans. Appl. Supercond. **22** (2012) 4401703 (4 pages) (No. 194 paper)

(I-3) H. Fujishiro, T. Tamura, T. Arayashiki, M. Oyama, T. Sasaki, T. Naito, G. Giunchi and A. Albisetti, “Pulsed field magnetization of large MgB_2 bulk fabricated by reactive liquid Mg infiltration”
Jpn. J. Appl. Phys. **51** (2012) 103005 (5 pages) (No. 197 paper)

(I-4) H. Fujishiro, T. Naito, T. Sasaki, T. Arayashiki, “Trapped field and temperature rise in MgB_2 bulks magnetized by pulsed field”,
Proc. ICEC24-ICMC2012 (2013) pp. 571-574 (No. 200 paper)

(I-5) T. Sasaki, T. Naito and H. Fujishiro, “Trapped field and critical density of MgB_2 bulk fabricated by a capsule method “,
Proc. ICEC24-ICMC2012 (2013) pp. 575-578 (No. 201 paper)

(I-6) T. Sasaki, T. Naito and H. Fujishiro, “Trapped magnetic field of dense MgB_2 bulks fabricated under high pressure”,
Physics Procedia **45** (2013) pp. 93-96 (No. 207 paper)

(I-7) H. Fujishiro, T Ujiie, T Naito, A Figini Albisetti and G Giunchi, “Trapped magnetic field between double stacked MgB_2 bulks magnetized by pulsed field”,
J. Phys. Conf. Series **507** (2014) 032016 (4 pages) (No. 214 paper)

(I-8) T. Ujiie, T. Naito, H. Fujishiro, A. Figini Albisetti and G. Giunchi, “Shielding and trapped field properties of large MgB_2 bulk”,
Physics Procedia **58** (2014) pp. 306-309 (No. 215 paper)

(I-9) H. Fujishiro, T. Naito, T. Ujiie, A. Figini Albisetti and G. Giunchi, “Trapped field and flux dynamics in MgB_2 superconducting bulks magnetized by pulsed field”,
Physics Procedia **58** (2014) pp. 286-289 (No. 216 paper)

(I-10) A. Murakami, H. Teshima, T. Naito, H. Fujishiro, T. Kudo, “Mechanical properties of MgB_2 bulks”,
Physics Procedia **58** (2014) pp. 98-101 (No. 217 paper)

(I-11) T. Yoshida, T. Naito and H. Fujishiro, “Effects of sintering condition on the trapped magnetic field properties for MgB_2 bulks fabricated by in-situ capsule method”,
Physics Procedia **58** (2014) pp. 106-109 (No. 218 paper)

(I-12) H. Fujishiro, T. Naito, T. Ujiie, T. Mochizuki, T. Yoshida, “Recent progress of MgB_2 bulk magnet magnetized by pulsed field”,
IEEE Trans. Appl. Supercond. **25** (2015) 6800104 (4 pages) (No. 221 paper)

(I-13) T. Yoshida, T. Naito and H. Fujishiro, “Development of 4 T class MgB_2 bulk magnets doped by Ti”,
IEEE Trans. Appl. Supercond. **25** (2015) 6801204 (4 pages) (No. 222 paper)

(I-14) T. Naito, T. Yoshida and H. Fujishiro, “Ti-doping effects on magnetic properties of dense MgB_2 bulk superconductors”,
Supercond. Sci. Technol. **28** (2015) 095008 (8 pages) (No. 224 paper)

(I-15) T. Naito, T. Yoshida and H. Fujishiro, “Trapped magnetic field properties of MgB_2 bulks doped with Ti”,
Physics Procedia **67** (2015) pp. 958-962 (No. 225 paper)

(I-16) H. Mochizuki, H. Fujishiro, T. Naito, A Figini Albisetti and G. Giunchi, “Trapped field properties of concentric circle MgB_2 bulk composite magnetized by pulsed field and field cooling”
Supercond. Sci. Technol. **28** (2015) 105004 (7 pages) (No. 227 paper)

(I-17) T. Naito, T. Yoshida, H. Mochizuki, H. Fujishiro, R. Basu and A. Szpunar, “Vortex Pinning Properties of Dense Ti-doped MgB_2 Bulks Sintered at Different Temperature”,
IEEE Trans. Appl. Supercond. **26** (2016) 6800805 (5 pages) (No. 229 paper)

(I-18) H. Fujishiro, H. Mochizuki, M. D. Ainslie and T. Naito, “Trapped field of 1.1 Tesla without flux jumps on high-J_c MgB_2 bulk during pulsed field magnetization using split coil with soft iron yoke”,
Supercond. Sci. Technol. **29** (2016) 084001 (10 pages) (No. 234 paper)

(I-19) T. Naito, A. Ogino and H. Fujishiro, “Potential ability of 3 T-class trapped field on MgB_2 bulk surface synthesized by the infiltration-capsule method”,
Supercond. Sci. Technol. **29** (2016) 115003 (6 pages) (No. 235 paper)

(I-20) H. Fujishiro, H. Mochizuki, T. Naito, M. D. Ainslie and G. Giunchi, “Flux jumps in high-J_c MgB_2 bulks during pulsed field magnetization”,
Supercond. Sci. Technol. **29** (2016) 034006 (7 pages) (No. 237 paper)

(I-21) H. Fujishiro, K. Takahashi, M.D. Ainslie, H. Mochizuki and T. Naito, “Suppression of flux jumps and enhancement of trapped field on high-J_c MgB_2 bulk using split-type coil with soft iron yoke during pulsed field magnetization”,
IEEE Trans. Appl. Supercond. **27** (2017) 6800404 (4 pages) (DOI: 10.1109/TASC.2016.2637363) (No. 239 paper)

(I-22) A. Ogino, T. Naito, and H. Fujishiro, “Optimization of infiltration and reaction process for the fabrication of strong MgB_2 bulk magnets”,
IEEE Trans. Appl. Supercond. **27** (2017) 6800905 (5 pages) (DOI: 10.1109/TASC.2016.2643500) (No. 240 paper)

(I-23) T. Naito, Y. Endo and H. Fujishiro, “Enhancement of vortex pinning properties on ex-situ MgB_2 bulks using ball-milling and spark plasma sintering processes: the dimensional change in grain boundary pinning”,
Supercond. Sci. Technol. **30** (2017) 095007 (8 pages) (No. 248 paper)

(I-24) Y. Takahashi, T. Naito, and H. Fujishiro, “Vortex pinning properties and microstructure of MgB_2 heavily doped with titanium group elements”,
Supercond. Sci. Technol. **30** (2017) 125006 (6 pages) (DOI: 10.1088/1361-6668/aa91ed) (No. 253 paper)

(I-25) Tatsuya Hirano, Yuhei Takahashi, Sora Namba, Tomoyuki Naito and Hiroyuki Fujishiro, “A record-high trapped field of 1.61 T in MgB_2 bulk comprised of copper plates and soft iron yoke cylinder using pulsed-field magnetization”,
Supercond. Sci. Technol. **33** (2020) 085002 (10 pages) (DOI: 10.1088/1361-6668/ab9542) (No. 276 paper)

(I-26) Tomoyuki Naito, Arata Ogino, Hiroyuki Fujishiro, Satoshi Awaji, “Effects of Carbon Doping on Trapped Magnetic Field of MgB2 Bulk Prepared by in-situ Hot Isostatic Pressing Method’,
IEEE Trans. Appl. Supercond. **30** (2020) 6800406 (6 pages) (DOI: 10.1109/TASC.2020.2985355) (No. 281 paper)

(I-27) Muralidhar Miryala, Sai Srikanth Arvapalli, Naomichi Sakai, Masato Murakami, Hidehiko Mochizuki, Tomoyuki Naito, Hiroyuki Fujshiro, Milos Jirsa, Akira Murakami, and Jacques Noudem, “Complex Pulse Magnetization Process and Mechanical Properties of Spark Plasma Sintered Bulk MgB_2”,
Materials Science & Engineering B **273** (2021) 115390 (10 pages) (DOI: 10.1016/j.mseb.2021.115390) (No. 285 paper)

(I-28) Y. Takahashi, T. Naito and H. Fujshiro, “Trapped field properties of MgB_2 bulks prepared via an in-situ infiltration-reaction process using refined boron powders”,
to be published in IEEE Trans. Appl. Supercond. (2022) (No. 289 paper)

(I-29) Y. Takahashi, T. Naito and H. Fujshiro, “Critical current properties of an ex-situ MgB_2/TiB_2 sample fabricated by spark plasma sintering using MgB_2 powder containing TiB_2”,
Submitted to Physica C (2022) (No. 291 paper)

J. 熱電変換材料の開発 10 編

(J-1) H. Fujishiro, K. Kusaka, M. Ikebe, H. Ogasawara and K. Noto, “Possibility of Ag_2O+$YBa_2Cu_3O_{7-X}$ ceramics for low temperature thermoelectric refrigeration”,
Cryogenics **34** (1994) Suppl. ICEC-15, pp. 231-234 (No. 25 paper)

(J-2) N. Yoshida, T. Naito and H. Fujishiro, “Thermoelectric Properties of Li-Doped CuO”,
Jpn. J. Appl. Phys. **52** (2013) 031102 (5 pages) (No. 198 paper)

(J-3) N. Yoshida, T. Naito and H. Fujishiro, “Thermoelectric properties of Li-doped $Cu_{0.95-x}M_{0.05}Li_xO$ (M=Mn, Ni, Zn)”,
MRS Online Proceedings **1490** (2013) pp. 69-73 (No. 202 paper)

(J-4) Y.-C. Lai, H.-J. Tsai, C.-I. Hung, H. Fujishiro, T. Naito, W.-K. Hsu, “Carbon nanotubes enhanced Seebeck coefficient and power factor of rutile TiO_2”,
Phys. Chem. Chem. Phys. **17** (2015) pp. 8120-8124 (No. 220 paper)

(J-5) R. Abe, H. Fujishiro and T. Naito, “Substitution effect of tetravalent and pentavalent elements on thermoelectric properties in In_2O_3-SnO_2 system”,
Trans. Mat. Res. Soc. Jpn. **41** (2016) pp. 101-108 (No. 229 paper)

(J-6) Shu Mizuno, Mamoru Ishizawa, Hiroyuki Fujishiro, Tomoyuki Naito, Hirokazu Katsui and Takashi Goto, "Ball milling effects for induced carriers and reduced grain size on thermoelectric properties in $Bi_{1-x}Sr_xCuSeO$ (x = 0, 0.1)",
Jpn. J. Appl. Phys. **55** (2016) 115801 (7 pages) (No. 236 paper)

(J-7) Shu Mizuno, Hiroyuki Fujishiro, Mamoru Ishizawa, Tomoyuki Naito, Hirokazu Katsui and Takashi Goto, "Thermoelectric properties of $LiCo_{1-x}M_xO_2$ (M=Cu, Mg, Ni, Zn) and comparison to Li_yCoO_2 and Na_yCoO_2 systems",
Jpn. J. Appl. Phys. **56** (2017) 021101 (6 pages) (DOI: 10.7567/JJAP.56.021101) (No. 243 paper)

(J-8) Takamitsu Hara, Hiroyuki Fujishiro, Tomoyuki Naito, Akihiko Ito and Takashi Goto, "Optimized growth condition of SnSe epitaxial films grown by pulsed laser deposition",
Jpn. J. Appl. Phys. **56** (2017) 125503 (6 pages) (DOI: 10.7567/JJAP.56.125503) (No. 252 paper)

(J-9) Mamoru Ishizawa, Hiroyuki Fujishiro, Tomoyuki Naito, Akihiko Ito and Takashi Goto, "Crystal orientation, crystallinity, and thermoelectric properties of $Bi_{0.9}Sr_{0.1}CuSeO$ epitaxial films grown by pulsed laser deposition",
Jpn. J. Appl. Phys. **57** (2018) 025502 (7papers) (DOI: 10.7567/JJAP.57.025502) (No. 254 paper)

(J-10) Mamoru Ishizawa, Yuki Yasuzato, Hiroyuki Fujishiro, Tomoyuki Naito, Hirokazu Katsui and Takashi Goto, "Oxidation states and thermoelectric properties of BiCuSeO bulks fabricated under Bi or Se deficiencies in the nominal composition",
J. Appl. Phys. **123** (2018) 245104 (9 pages) (DOI: 10.1063/1.5034499) (No. 260 paper)

K. 高分子材料、磁性蓄冷材、その他の熱物性　9 編

(K-1) H. Fujishiro, M. Ikebe, T. Kashima and A. Yamanaka, "Thermal Conductivity and Diffusivity of High-Strength Polymer Fibers",
Jpn. J. Appl. Phys. **36** (1997) pp. 5633-5637 (No. 47 paper)

(K-2) H. Fujishiro, M. Ikebe, T. Kashima and A. Yamanaka, "Drawing Effect on Thermal Properties of High-Strength Polyethylene Fibers",
Jpn. J. Appl. Phys. **37** (1998) pp. 1994-1995 (No. 50 paper)

(K-3) A. Yamanaka, T. Kitagawa, M. Tsutsumi, T. Kashima, H. Fujishiro, K. Ema, Y. Izumi and S. Nishijima, "Thermal Strain of High Strength Polyethylene Fiber in Low Temperature",
J. Appl. Polym. Sci. **93** (2004) pp. 2918-2925 (No. 107 paper)

(K-4) A. Yamanaka, H. Fujishiro, T. Kashima, T. Kitagawa, K. Ema, Y. Izumi, M. Ikebe and S. Nishijima, "Thermal Conductivity of High Strength Polyethylene Fiber in Low Temperature",
J. Polym. Sci., Part B **43** (2005) pp. 1495-1503 (No. 114 paper)

(K-5) A. Yamanaka, M. Yoshikawa, S. Abe, M. Tsutsumi, T. Oohazama, T. Kitagawa, H. Fujishiro, K. Ema, Y. Izumi, S. Nishijima, "Effects of Vaper-Phase-Formaldehyde Treatments on Thermal Conductivity and Diffusivity of Ramie Fibers in the Range of Low Temperature",
J. Polym. Sci., Part B **43** (2005) pp. 2754-2766 (No. 117 paper)

(K-6) A. Yamanaka, S. Abe, M. Tsutsumi, T. Kitagawa, H. Fujishiro, K. Ema, Y. Izumi and S. Nishijima, "Thermal Conductivity of Ramie Fiber Drawn in Water in Low Temperature",
J. Appl. Polym. Sci. **100** (2006) pp. 2196-2202 (No. 127 paper)

(K-7) A. Yamanaka, Y. Izumi, T. Kitagawa, T. Terada, H. Hirahata, K. Ema, H. Fujishiro and S. Nishijima, "The Radiation Effect on Thermal Strain of High Strength Ultra-High-Molecular-Weight Polyethylene Fiber by γ-Rays,
J. Appl. Polymer Sci. **101** (2006) pp. 2619-2626 (No. 129 paper)

(K-8) A. Yamanaka, Y. Izumi, T. Terada, K. Ema, M. Tsutsumi, M. Nakamura, T. Oohazama, T. Kitagawa, H. Fujishiro, S. Abe and S. Nishijima, “Radiation Effect on the Thermal Conductivity and Diffusivity of Ramie Fiber in a Range of Low Temperatures by γ-Rays”,
J. Appl. Polymer Sci. **101** (2006) pp. 5007-5018 (No. 137 paper)

(K-9) A. Yamanaka, Y. Izumi, T. Kitagawa, T. Terada, H. Hirahata, K. Ema, H. Fujishiro and S. Nishijima, “The Effect of γ-Irradiation on Thermal Strain of High Strength Polyethylene Fiber at Low Temperature”,
J. Appl. Polym. Sci. **102** (2006) pp. 204-209 (No. 138 paper)

L. パーコレーション伝導、熱伝導率のモデル解析　4 編

(L-1) M. Ikebe, H. Fujishiro, M. Matsukawa, F. Tatezaki, H. Ogasawara, K. Noto, K. Michishita and Y. Kubo, “A Model Analysis of the Thermal Conductivity of Ag-doped Bi-Sr-Ca-Cu-O Superconducting Oxide”,
Jpn. J. Appl. Phys. **33** (1994) pp. 2004-2007 (No. 20 paper)

(L-2) H. Fujishiro, M. Ikebe, Y. Minato, H. Ogasawara and K. Noto, “Model analyses of thermal conductivity and purity of doped Ag in Ag+$YBa_2Cu_3O_7$”,
Superlattices and Microstructures **21** (1997) pp. 349-352 (No. 43 paper)

(L-3) M. Ikebe and H. Fujishiro, “TRANSPORT AND THERMOELECTRIC PROPERTIES OF $YBa_2Cu_3O_{7-\delta}$-Ag PERCOLATION SYSTEM”,
Advances in Science and Technology **23** (1999) pp. 445-452 (No. 63 paper)

(L-4) M. Ikebe and H. Fujishiro, “Percolation Analyses on Transport Properties of $YBa_2Cu_3O_{7-\delta}$-Ag System,
J. Low Temp. Phys. **117** (1999) pp. 1289-1293 (No. 64 paper)

M. 多層膜超伝導体の研究　18 編

(M-1) M. Ikebe, Y. Obi, H. Fujishiro and H. Fujimori, “A Study of the Flux Pinning Anisotropy in Nb/Al_2O_3 Superconducting Multilayers”,
Jpn. J. Appl. Phys. **32** (1993) pp. 55-59 (No. 7 paper)

(M-2) Y. Obi, M. Ikebe, H. Fujishiro and H. Fujimori, “Pinning Mechanism Studies on the Nb /Ag Superconducting Multilayer”,
Jpn. J. Appl. Phys. **32** (1993) pp. 1952-1955 (No. 8 paper)

(M-3) M. Ikebe, Y. Obi, H. Fujishiro and H. Fujimori, “Dimensional Crossover in the Nb/Al_2O_3 Josephson-Coupled Multilayers”,
J. Phys. Soc. Jpn. **62** (1993) pp. 3680-3685 (No. 9 paper)

(M-4) Y. Obi, M. Ikebe, H. Fujishiro, S. Takahashi and H. Fujimori, “Superconducting Properties of NbTi Based Multilayers”,
J. Low Temp. Phys. **96** (1994) pp. 1-18 (No. 22 paper)

(M-5) Y. Obi, M. Ikebe, H. Fujishiro and H. Fujimori, “Anomalous T_c behavior in NbTi/Nb superconducting multilayers”,
Physica C **235-240** (1994) pp. 2561-2562 (No. 29 paper)

(M-6) M. Ikebe, T. Naito, H. Fujishiro, K. Noto, N. Kobayashi and K. Mori, “Lattice thermal conductivity of Nb-based alloy superconductors and phonon scattering by electrons”,
Physica B **219&220** (1996) pp. 80-82 (No. 31 paper)

(M-7) M. Ikebe, Y. Obi, H. Fujishiro and H. Fujimori, “Flux Pinning and Dimensionality of Superconductivity in Multilayers”,
Czech. J. Phys. **46** (1996) Suppl. S2, pp. 719-720 (No. 37 paper)

(M-8) M. Ikebe, H. Fujishiro, Y. Obi, H. Fujimori and Y. Kamiguchi, “Pauli Paramagnetic Effect and Parallel Critical Field of Nb/Al_2O_3 Multilayers”,
Superlattices and Microstructures **21** (1997) Suppl. A. pp. 153-156 (No. 42 paper)

(M-9) Y. Obi, H. Fujimori, M. Ikebe and H. Fujishiro, “Flux pinning in NbTi-based multilayers”, *Superlattices and Microstructures* **21** (1997) pp. 423-426 (No. 45 paper)

(M-10) M. Ikebe, H. Fujishiro and H. Iwasaki, “Magnetic structure and dipolar interaction in antiferromagnetic superconductor BCT-$ErRh_4B_4$”, *J. Mag. Mag. Mater.* **177-181** (1998) pp. 549-550 (No. 49 paper)

(M-11) M. Ikebe, H. Fujishiro, Y. Obi, H. Fujimori and S. Morohashi, “On anomalous temperature dependence of $H_{c2\perp}$ in natural and artificial layer superconductors”, *Physica C* **317-318** (1999) pp. 142-148 (No. 58 paper)

(M-12) Y. Obi, M. Ikebe, H. Fujishiro and H. Fujimori, “Flux pinning characteristics in NbTi/Nb superconductor/superconductor multilayers”, *Physica B* **284-288** (2000) pp. 857-858 (No. 67 paper)

(M-13) Y. Obi, M. Ikebe, H. Fujishiro, K. Takanaka and H. Fujimori, “Synthetic Analyses of T_c and H_{c2} of NbTi/Nb Superconductor/Superconductor Superlattice”, *phys. stat. sol. (b)* **223** (2001) pp. 799-809 (No. 72 paper)

(M-14) Y. Obi, M. Ikebe and H. Fujishiro, “Pauli paramagnetic effect and spin-orbit scattering time in Nb/Al_2O_3 superconducting multilayers”, *Physica B* **329-333** (2003) pp.1423-1424 (No. 93 paper)

(M-15) Y. Obi, H. Fujishiro and M. Ikebe, “Evidence for zero and π phase from superconducting transition temperature in Nb/Co superconducting multilayers”, *J. Mag. Mag. Mat.* **272-276** (2004) pp. e1087-e1088 (No. 102 paper)

(M-16) Y. Obi, M. Ikebe and H. Fujishiro, “Repulsive Flux Pinning Force in NbTi/Nb Superconductor/Superconductor Multilayers”, *J. Low Temp. Phys.* 137 (2004) pp. 125-137 (No. 108 paper)

(M-17) Y. Obi, M. Ikebe and H. Fujishiro, “Evidence for Zero- and π-Phase Order Parameters of Superconducting Nb/Co Tri- and Pentalayers from the Oscillatory Behavior of the Transition Temperature”, *Phys. Rev. Lett.* 94 (2005) pp. 057008-1–4 (No. 113 paper)

(M-18) Y. Obi, M. Ikebe and H. Fujishiro, “Analyses of the pinning mechanism for the superconductor/normal-metal and superconductor/superconductor multilayers”, *J. Superconductivity and Novel Magnetism* **19** (2006) pp. 117-123 (No. 139 paper)

N. Si, GaAs, ZnSe などの半導体材料に関する研究　11 編

(N-1) H. Fujishiro and S. Furukawa, “GROWTH MODEL OF HYDROGENATED MICROCRYSTALLINE SILICON PREPARED BY RF SPUTTERING IN PURE HYDROGEN”, *Solid State Commun.* **73** (1990) pp. 835-838 (No. 1 paper)

(N-2) 藤代博之、古川昌司、山崎義武、「水素プラズマスパッター法による微結晶 Si:H の成長モデル」、*日本化学会誌* **1990-5** (1990) pp.495-498 (No. 2 paper)

(N-3) F. Sakurai, H. Fujishiro, K. Suto and J. Nishizawa, “ZnSe epitaxial growth by the temperature difference method under controlled vapor pressure (TDM-CVP) using Se solvent,” *J. Cryst. Growth* **112** (1991) pp. 153-159 (No. 3 paper)

(N-4) H. Fujishiro and S. Furukawa, “Dependence of microcrystal size on hydrogen gas pressure in silicon-based alloys prepared by reactive laser ablation”, *J. Phys.: Condens. Matter* **3** (1991) pp. 7539-7543 (No. 4 paper)

(N-5) S. Furukawa, M. Obana, M. Tamura and H. Fujishiro, “ORIENTATION OF ONE-DIMENSIONAL SILICON BACKBONE IN TERNARY Si:C:H FILMS PREPARED BY EVAPORATION OF ORGANOPOLYSILANE”,
Solid State Commun. **84** (1992) pp. 475-478 (No. 5 paper)

(N-6) S. Furukawa, M. Nagatomo, H. Kokuhata, K. Takeuchi, H. Fujishiro and M. Tamura, “Effects of iodine doping on electrical and optical properties of ternary Si:C:H films prepared by evaporation of organopolysilane”,
J. Phys.: Condens. Matter **4** (1992) pp. 8357-8362 (No. 6 paper)

(N-7) H. Fujishiro, S. Furukawa, I. Takahashi and T. Kuwashima, “Structure and Electrical Properties of Low-Pressure-Plasma-Sprayed Silicon-Based Materials”,
J. Ceram. Soc. Jpn. **102** (1994) pp. 1-4 (No. 15 paper)

(N-8) J. Nishizawa, M. Motozawa, Y. Oyama, K. Dezaki, H. Fujishiro and K. Suto, “Photocapacitance Measurement on Intentionally Undoped n-type $Ga_{0.9}Al_{0.1}As$ Grown by Stoichiometry Control Method”,
Jpn. J. Appl. Phys. **33** (1994) pp. 1753-1758 (No. 19 paper)

(N-9) M. Ikebe, M. Matsukawa, H, Fujishiro, N. Yoshimoto, M. Yoshizawa and K. Noto, “Thermal Conductivity in the *ab*-Plane of the Organic Conductor α-$(BEDT\text{-}TTF)_2I_3$”,
J. Phys. Soc. Jpn. **65** (1996) pp. 651-651 (No. 35 paper)

(N-10) D. H. Yoon, I. Agung, H. Fujishiro and M. Yoshizawa, “Exact Observation of Oxygen Radicals by Voltage Locked Loop Method for the Application to Molecular Beam Epitaxial Growth”,
Materials Transactions, JIM **37** (1996) pp. 898-901 (No. 36 paper)

(N-11) Abdusalam Ismayil, Taichi Nakamura, Ryosuke Kamiya, Mitsuteru Nakamura, Yoshiki Nakanishi, Tomoyuki Naito, Hiroyuki Fujishiro, Takao Watanabe, Gaku Sawada, Masahiro Toita, Katsuhiko Takegahara, and Masahito Yoshizawa, “Effect of Carrier Doping on Physical Properties of A-Site Ordered Perovskite $CaCu_3Ti_4O_{12}$”,
J. Phys. Soc. Jpn. **80** (2011) SA113 (No. 188 paper)

O. 博士学位論文

(O-1) 藤代博之：「蒸気圧制御下における相図の研究」東北大学（工第 987 号）

３．代表的論文リスト 10 編

1. (D-1) 藤代博之、内藤智之、池部　学、能登宏七、「低温における熱拡散率と熱伝導率の同一セッティング測定」、
   低温工学 **28** (1993) pp. 533-539 (No. 10 paper)
2. (F-17) Hiroyuki Fujishiro, Tatsuya Tateiwa, Atsushi Fujiwara, Tetsuo Oka and Hidemi Hayashi, “Higher trapped field over 5 Tesla on HTSC bulk by modified pulse field magnetizing”,
   Physica C **445-448** (2006) pp. 334-338 (No. 134 paper)
3. (G-1) H. Fujishiro and T. Naito, “Simulation of temperature and magnetic field distribution in superconducting bulk during pulsed field magnetization”,
   Supercond. Sci. Technol. **23** (2010) 105021 (8 pages) (No. 174 paper)
4. (A-41) H. Fujishiro, T. Naito, S. Ogawa, K. Nitta, J. Hejtmanek, K. Knizek and Z. Jirak, “Valence shift of Pr ion from 3+ to 4+ in $(Pr_{1-y}Y_y)_{0.7}Ca_{0.3}CoO_3$ estimated by X-ray absorption spectroscopy”,
   J. Phys. Soc. Jpn. **81** (2012) 064709 (5 pages) (No. 189 paper)
5. (A-48) Y. Noda, H. Fujishiro, T. Naito, A. Ito, T. Goto, J. Hejtmanek and Z. Jirak, “Electrical resistivity anomaly in $(Pr_{1-y}M_y)_{1-x}Ca_xCoO_3$ epitaxial films (M = Y, Gd) fabricated by pulsed laser deposition”,
   AIP Advances **6** (2016) 025318 (9 pages) (No. 232 paper)
6. (H-1) K. Takahashi, H. Fujishiro and M. D. Ainslie, “A new concept of hybrid trapped field magnet lens (HTFML)”,
   Supercond. Sci. Technol. **31** (2018) 044005 (9 pages) (No. 257 paper)
7. (H-3) Sora Namba, Hiroyuki Fujishiro, Tomoyuki Naito, Mark D Ainslie, Keita Takahashi, “Experimental realization of a Hybrid Trapped Field Magnet Lens (HTFML) using a GdBaCuO magnetic lens and MgB_2 bulk cylinder”,
   Supercond. Sci. Technol. Letter **32** (2019) 12LT03 (7 pages) (No. 271 paper)
8. (I-25) Tatsuya Hirano, Yuhei Takahashi, Sora Namba, Tomoyuki Naito and Hiroyuki Fujishiro, “A record-high trapped field of 1.61 T in MgB_2 bulk comprised of copper plates and soft iron yoke cylinder using pulsed-field magnetization”,
   Supercond. Sci. Technol. **33** (2020) 085002 (10 pages) (No. 276 paper)
9. (H-8) K. Takahashi, H. Fujishiro and M. D. Ainslie, “A conceptual study of a high gradient trapped field magnet (HG-TFM) providing toward a quasi-zero gravity space on Earth”,
   Supercond. Sci. Technol. **34** (2021) 035001 (13 pages) (No. 283 paper)
10. (H-9) K. Takahashi, H. Fujishiro, S. Namba and M. D. Ainslie, “Experimental realization of an all-(RE)BaCuO hybrid trapped field magnet lens generating a 9.8 T concentrated magnetic field from a 7 T external field”,
    Supercond. Sci. Technol. **34** (2021) 05LT02 (9 pages) (No. 284 paper)

４．研究論文の分析、概要

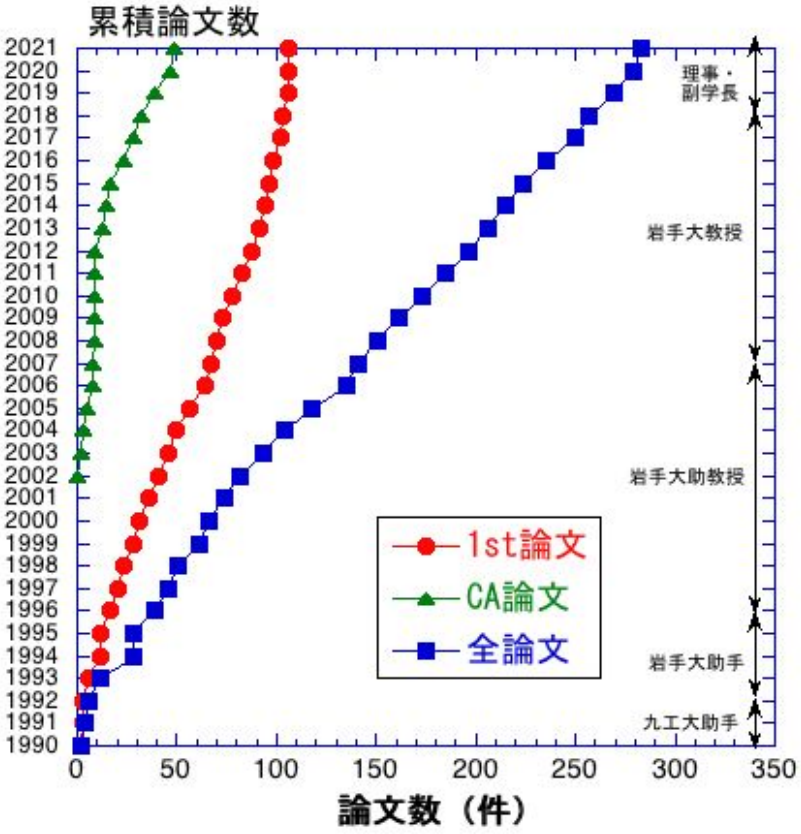
累積論文数
2021
2020
2019
2018
2017
2016
2015
2014
2013
2012
2011
2010
2009
2008
2007
2006
2005
2004
2003
2002
2001
2000
1999
1998
1997
1996
1995
1994
1993
1992
1991
1990
理事・
副学長
岩手大教授
岩手大助教授
岩手大助手
九工大助手
1st論文
CA論文
全論文
0
50
100
150
200
250
300
350
論文数（件）

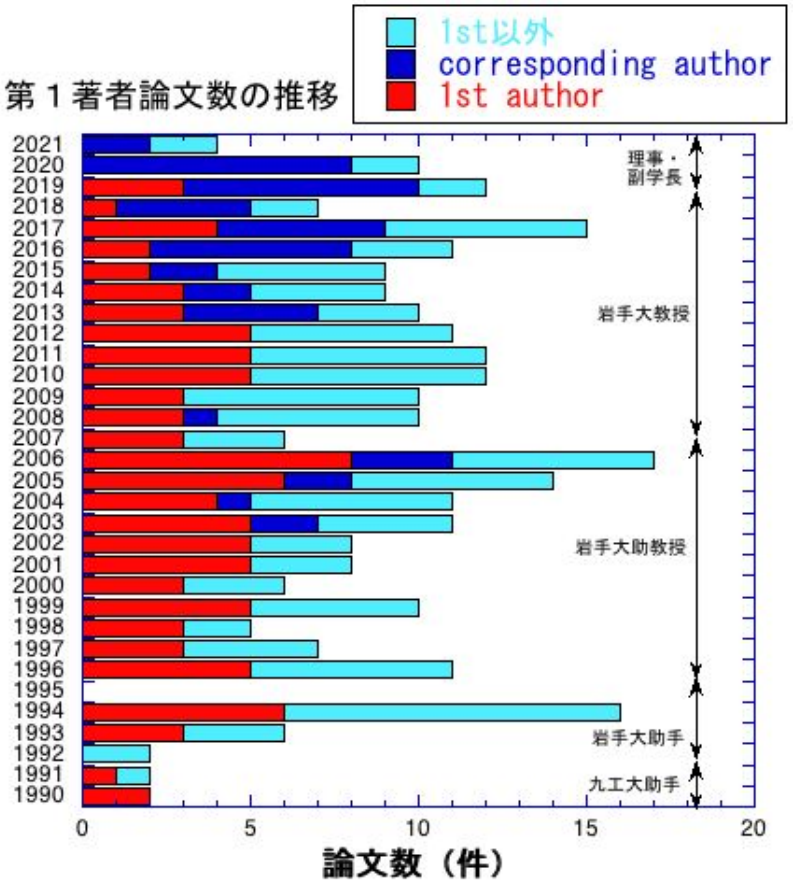
第１著者論文数の推移
1st以外
corresponding author
1st author
2021
2020
2019
2018
2017
2016
2015
2014
2013
2012
2011
2010
2009
2008
2007
2006
2005
2004
2003
2002
2001
2000
1999
1998
1997
1996
1995
1994
1993
1992
1991
1990
理事・
副学長
岩手大教授
岩手大助教授
岩手大助手
九工大助手
0
5
10
15
20
論文数（件）

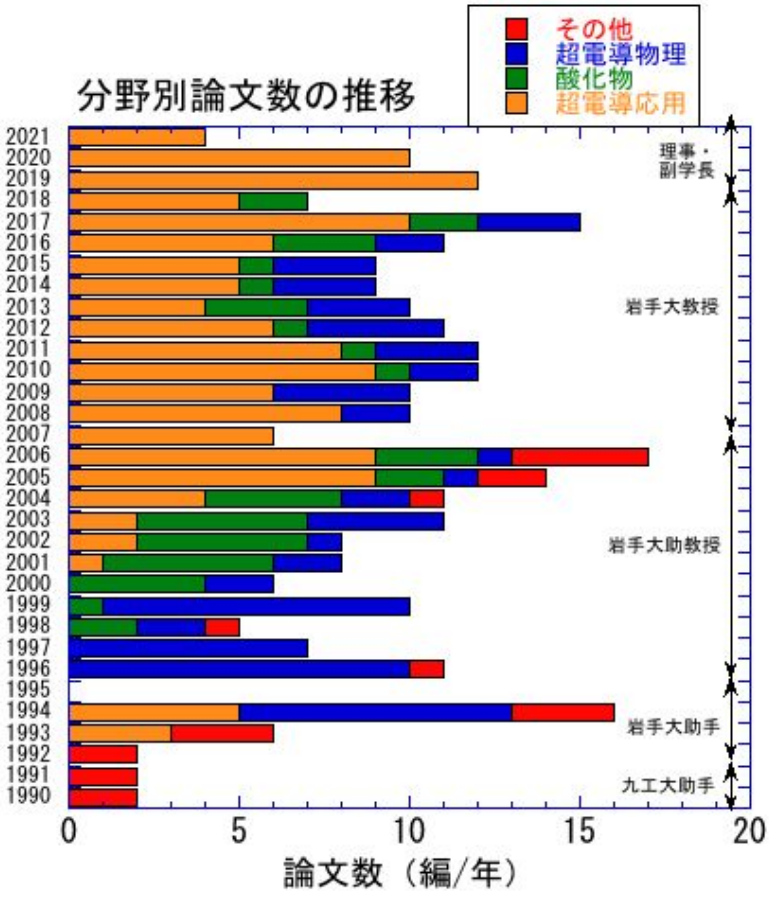
分野別論文数の推移
その他
超電導物理
酸化物
超電導応用
理事・副学長
岩手大教授
岩手大助教授
岩手大助手
九工大助手
2021
2020
2019
2018
2017
2016
2015
2014
2013
2012
2011
2010
2009
2008
2007
2006
2005
2004
2003
2002
2001
2000
1999
1998
1997
1996
1995
1994
1993
1992
1991
1990
0
5
10
15
20
論文数（編/年）

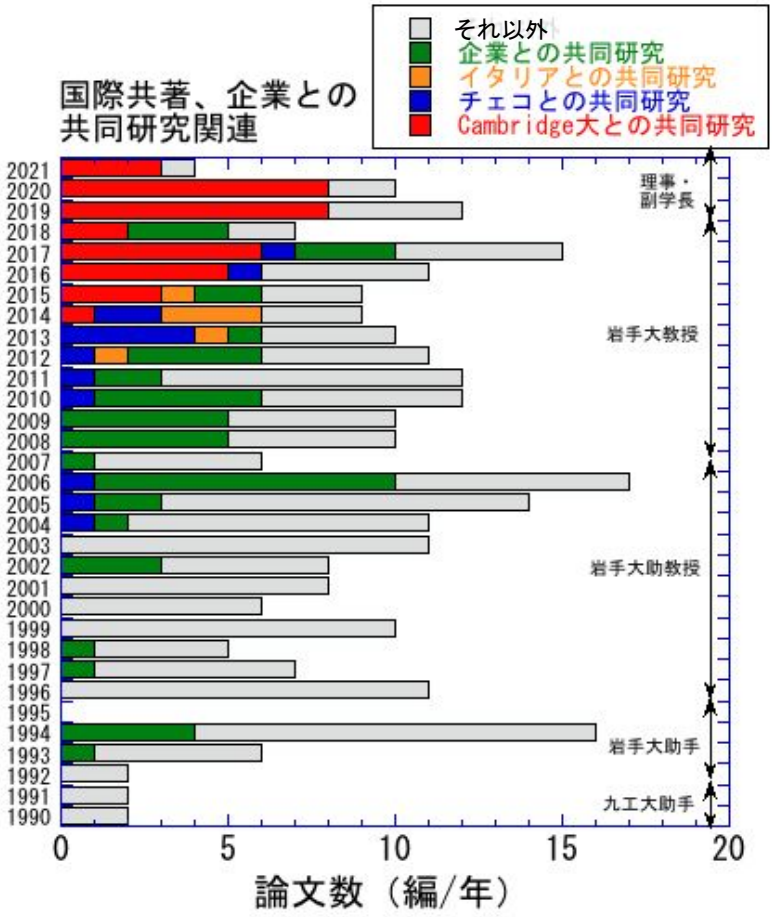
国際共著、企業との共同研究関連
それ以外
企業との共同研究
イタリアとの共同研究
チェコとの共同研究
Cambridge大との共同研究
理事・副学長
岩手大教授
岩手大助教授
岩手大助手
九工大助手
2021
2020
2019
2018
2017
2016
2015
2014
2013
2012
2011
2010
2009
2008
2007
2006
2005
2004
2003
2002
2001
2000
1999
1998
1997
1996
1995
1994
1993
1992
1991
1990
0
5
10
15
20
論文数（編/年）

Scopusによる分析（2021.12.1現在）

出版物別の文献数

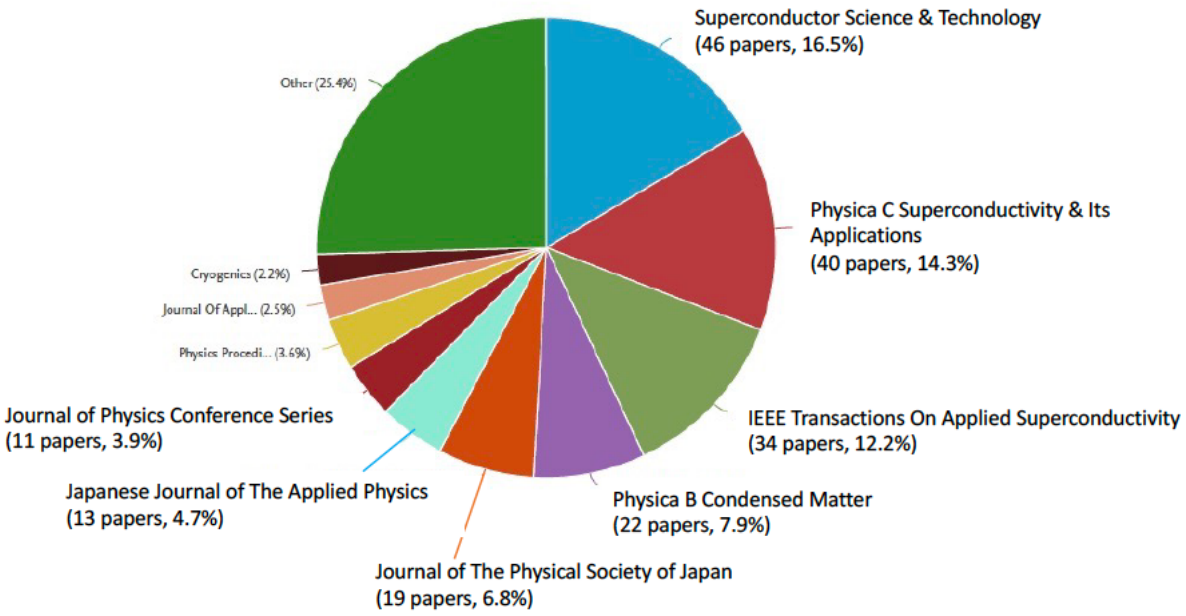

分野別の文献数

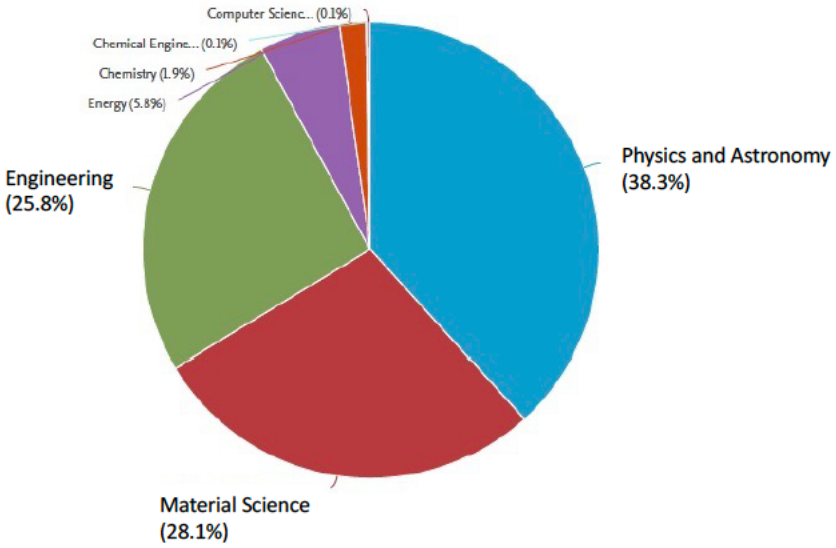

文献タイプ別の文献数

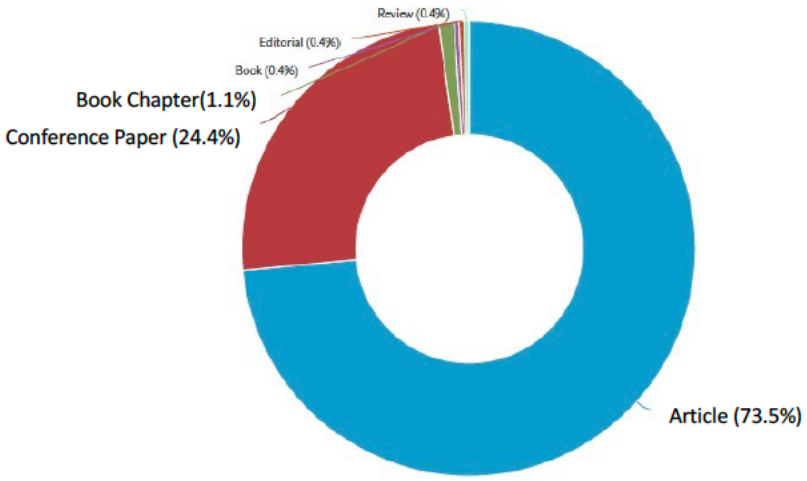

引用された文献

		文献	被引用数	<2006	2006	2007	2008	2009	2010	2011	2012	2013	2014	2015	2016	2017	2018	2019	2020	2021	小計	>2021	合計
			Total	552	90	90	80	86	86	85	158	95	116	175	214	259	202	286	359	216	2597	0	3149
F-17 paper	☐	1 Higher trapped field over 5 T on HTSC bulk by modified pulse...	2006			8	6	8	5	9	14	9	8	9	11	14	15	17	12	6	151		151
G-10 paper	☐	2 Modelling of bulk superconductor magnetization	2015											6	15	24	15	26	32	19	137		137
G-8 paper	☐	3 Modelling and comparison of trapped fields in (RE)BCO bulk s...	2014										1	11	13	15	7	14	13	15	89		89
A-3 paper	☐	4 Charge Ordering and Sound Velocity Anomaly in La_{1-x}	1998	25	2		1	7	1	1	5	1	5	4	2	5	1	8	2	4	49		74
G-1 paper	☐	5 Simulation of temperature and magnetic field distribution in...	2010							5	9	2	6	8	6	9	9	8	4	5	71		71
K-1 paper	☐	6 Thermal conductivity and diffusivity of high-strength polyme...	1997	15	3	1	1	4	2		5	4	3	2	2	3	5	6	5	3	49		64
B-2 paper	☐	7 Simultaneous Measurement of Thermal Diffusivity and Conducti...	1994	45	3		1	5	3	1	1	1	1		1			1	1		19		64
I-1 paper	☐	8 Trapped magnetic field and vortex pinning properties of MgB ...	2012								1	4	10	12	8	9	5	5	6	2	62		62
A-2 paper	☐	9 Phase Transition to Antiferromagnetic State in La_{1}	1998	39	3	4	1	3		1	2			1	1		2		1	1	20		59
A-39 paper	☐	10 Metal-Insulator transition and the Pr^{3+}-Pr^{4+}...	2010							5	5	8	10	5	4	7	2	5	3	2	56		56

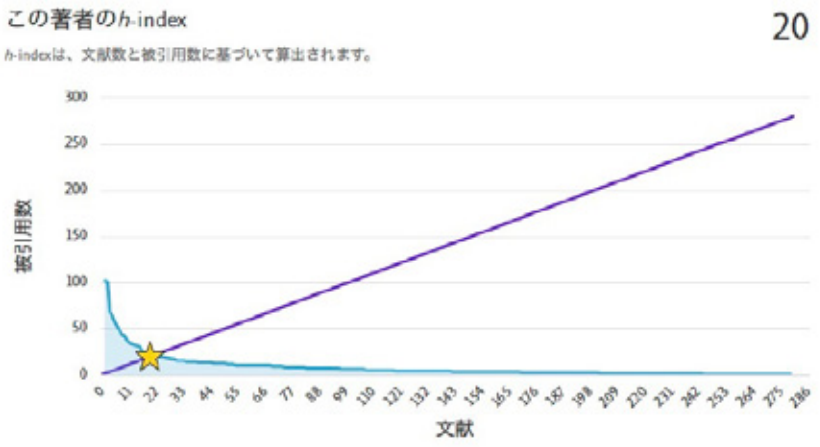

主な学術雑誌の論文の件数とインパクトファクター(IF)

雑誌名	論文数	IF (2022.2.10 現在)
Superconductor Science and Technology	46	3.219
Physica C: Superconductivity & Its applications	40	1.241
IEEE Trans. Appl. Supercond.	34	1.704
Physica B: Condensed Matter	22	2.436
J. Physical Society of Japan	19	1.828
Japanese Journal of Applied Physics	13	1.480
Journal Physics Conference Series	11	0.547
J. Low Temp. Physics	7	1.570
J. Mag. Mag. Matter	6	2.993
J. Applied Physics	6	2.546
Cryogenics	6	2.226
Physical Review B	3	4.036

主な共著者との論文の件数

共著者	共著論文数
Tomoyuki Naito	130
Manabu Ikebe	90
Mark D Ainslie	37
Keita Takahashi	24
Tetsuo Oka	28
Yousuke Yanagi	17
Jiri Hejtmanek	13

５．国際会議発表論文

(Koku-1) H. Fujishiro, K. Kusaka, M. Ikebe and K. Noto, “Use of Bi-2223 Superconducting Tapes Sheathed with Ag-Au Alloys for a Passive Thermoelement”,
Proceedings of the 12th International Conference on Thermoelectrics (XII ICT) Editied by K. Matsuura, (Yokohama, Japan, Nov. 9-11, 1993) pp. 169-174, 1993

(Koku-2) H. Fujishiro, M. Ikebe, H. Ogasawara, K. Noto, K. Michishita and Y. Kubo, “Anisotropic Transport Properties of Ag-Bi2212 Prepared by Floating Zone Method”,
Proceedings of the 9th US-Japan Workshop on High-Field Superconducting Materials, Wires and Conductors and Standard Procedures for High-Field Superconducting Wires Testing, (Kyoto, Japan, March 13-15, 1995) pp. 61-64, 1995

(Koku-3) T. Sasaoka, K. Nomura, J. Sato, M. Seido, H. Kumakura, K. Togano, H. Maeda, J. Shimoyama, H. Fujishiro, M. Ikebe and K. Noto, “Bi-System Oxide Superconducting Tapes Based on Silver-Alloy for Power Current Leads”,
Proceedings of International Symposium on Superconductivity (ISS’92) pp. 729-731, 1993

(Koku-4) H. Fujishiro and M. Ikebe, “Heat Transport Anomalies around Ferromagnetic and Charge-order Transitions in $La_{1-X}Ca_XMnO_3$”,
Proceedings of International Symposium on Physics in Local Lattice Distortions (Physics in Local Lattice Distortions, edited by H. Oyanagi and A. Bianconi (American Institute of Physics) (Tsukuba, Japan, July 23-26, 2000) pp. 433-436, 2001

(Koku-5) H. Nakane, S. Yamazaki, H. Fujishiro, T. Yamaguchi, S. Yoshizawa, T. Numazawa and M. Okamura, “Low Temperature Properties of HoSb, DySb and GdSb”,
Proceedings of the 11th International Cryocooler Conference (Colorado, USA, 2000.6.20-22), pp451-457, 2000

(Koku-6) H. Nakane, S. Yamazaki, H. Fujishiro, S. Yoshizawa, T. Numazawa and M. Okamura, “Low Temperature Properties of Rare-Earth and Sb Compounds”,
Proceedings of the Sixth Joint Sino-Japanese Seminar on Cryocooler and its Applications (JSJS-6) (Lanzhou, China, 2000. 8.20-24) pp. 137-142, 2000

(Koku-7) H. Nakane, S. Nishijima, H. Fujishiro, T. Yamaguchi, S. Yoshizawa and S. Yamazaki, “THERMAL PROPERTIES OF EPOXY RESINS AT CRYOGENIC TEMPERATURES”,
Advanced in Cryogenic Engineering (Proceedings of the International Cryogenic Materials Conference – ICMC), Vol.48, pp.211-217, 2002

(Koku-8) H. Fujishiro, Y. Fujine, J. Hejtmanek, D. Sedmidubsky, A. Maignan and C. Martin, “Search for p-type oxide thermoelectrics –cobaltites—“,
Proceedings of 21th International Conference on Thermoelectrics (ICT ’03) IEEE, (La Grande-Motte, France, August 17-21, 2003), pp. 192-195, 2004 No.83

(Koku-9) H. Fujishiro, Y. Fujine, Y. Kashiwada, M. Ikebe and J. Hejtmanek, “Enhanced Thermoelectric Properties at X~0.1 in $La_{1-X}Sr_XCoO_3$ and $La_{1-X}Sr_X(Co_{1-Y}M_Y)O_3$ (M = Cr, Co)”, No.82
Proceedings of 21th International Conference on Thermoelectrics (ICT ’03) IEEE, (La Grande-Motte, France, August 17-21, 2003), pp. 235-238, 2004

(Koku-10) H. Fujishiro, Y. Suzuki, Y. Fujine and M. Ikebe, “Size Effect of A-site Cation on n-type Thermoelectric Properties in $CaMnO_3$-based System”,
Proceedings of 22th International Conference on Thermoelectrics (ICT ’04) IEEE, (Adelaide, Australia, July 24-29, 2004), 2005

(Koku-11) H. Fujishiro, Y. Fujine, M. Ikebe and J. Hejtmanek, “Influence of Co-site Substitution on Thermoelectric Properties in $La_{1-X}Sr_XCoO_3$”,
Proceedings of 22th International Conference on Thermoelectrics (ICT ’04) IEEE, (Adelaide, Australia, July 24-29, 2004), 2005

(Koku-12) Y.-H. Lee, T. Koyanagi and H. Fujishiro, “Transport Properties of Bi-Sb Sintered Alloys Prepared by Spark Plasma Sintering”,
Proceedings of 22th International Conference on Thermoelectrics (ICT ’04) IEEE, (Adelaide, Australia, July 24-29, 2004), 2005

６．著書

(Book-1) “Superconductivity –Recent Developments and New Production Technologies—“, Edited by Muralidhar Miryala, Nova Publishers Inc., New York (ISBN: 978-1-62257-137-6), Chapter 12, “Pulsed Field Magnetization on Superconducting Bulk and the Applications as a Strong Magnet” pp. 241-257（分担執筆）2012

(Book-2) “Research, Fabrication and Applications Bi-2223 HTS Wires” Edited by Kenichi Sato, World Scientific Series in Applications of Superconductivity and Related Phenomena, Vol. 1, (ISSN 2424-8533), Chapter 1.7, “Thermal Properties of Bi-2223 Wires” pp. 73-103（分担執筆）2016

(Book-3) “Numerical Modelling of Bulk Superconductor Magnetization”, Mark Ainslie and Hiroyuki Fujishiro, IOP Publishing, Bristol, UK (ISBN: 978-0-7503-1332-2) 2020

７．解説、総説、新聞記事

(kai-1) 能登宏七、松川倫明、藤代博之、「固体物性解析技術—超伝導測定法—」まてりあ, Vol. 36, No. 4, pp. 330-336, 1997

(kai-2) 「安価な強力磁石開発」《岩手日報 2005,8.28 朝刊 1 面掲載》

(kai-3) 藤代博之、「超強力なバルク超伝導磁石の開発と産業応用」《2006 年：岩手大学工学部同窓会誌（北杜）「研究の窓」寄稿》

(kai-4) 藤代博之「バルク超電導体のパルス着磁技術の動向と熱物性データベース」《2006 年：電気学会研究会 ASC-07-06》

(kai-5) 藤代博之、「パルス着磁法による５Ｔを越える超伝導バルク磁石の実現」《2007 年：まぐね vol. 2 pp. 28-34》

(kai-6) 藤代博之、「超伝導バルク磁石装置と産業応用」《2007 年：化学工業 vol.58, no.6, pp. 423-427》

(kai-7) 藤代博之、「バルク超電導体の着磁現象」《2011 年：低温工学・超伝導学会誌 vol. 46, pp. 81-88 解説》

(kai-8) 藤代博之、「地方支部活動の必要性（東北・北海道支部支部長に就任して）」《2019 年：低温工学・超伝導学会誌サロン, Vol. 54 p. 492》

(kai-9) 藤代博之、高橋圭太、「擬似微小重力環境を実現するハイブリッド超電導バルク磁石装置の開発と磁気浮上応用」《2021 年：化学工業 vol. 72, no.12, pp. 781-785》

(Kai-10) 内藤智之、藤代博之、「MgB_2 超伝導バルク磁石の現状と展望」《2021 年：低温工学・超伝導学会誌 vol. 56, pp. 309-316 テーマ解説》

８．特許出願、取得

(Pat-1) 「バルク超伝導体の熱的安定化方法」
出願日および出願番号：2003 年 4 月 16 日 （特願 2003-112116）（特開 2004-319797）
発明者：藤代博之、岡　徹雄、横山和哉
出願人：科学技術振興事業団、アイシン精機㈱

(Pat-2) 「バルク超伝導体の熱的安定化方法」
出願日および出願番号：2003 年 4 月 16 日 （特願 2003-112117）（特開 2004-319798）
発明者：藤代博之、岡　徹雄、横山和哉
出願人：科学技術振興事業団、アイシン精機㈱

(Pat-3) 「バルク超伝導体の着磁方法」
出願日および出願番号：2004 年 3 月 31 日 （特願 2004-106330）（特開 2005-294471）
発明者：藤代博之、岡　徹雄、横山和哉
出願人：科学技術振興事業団、アイシン精機㈱

(Pat-4) 「断熱性セルロース繊維」
出願日および出願番号：2005 年 5 月 20 日 （特願 2005-147738）（特開 2006-322115）
発明者：山中淳彦、安倍俊三、堤　正幸、大峡岳志、吉川雅敏、西嶋茂宏、泉　佳信、寺田　隆哉、藤代博之
出願人：東洋紡績㈱

(Pat-5) 「熱伝導性セルロース繊維」
出願日および出願番号：2005 年 5 月 20 日 （特願 2005-147739）（特開 2006-322116）
発明者：山中淳彦、安倍俊三、堤　正幸、大峡岳志、吉川雅敏、西嶋茂宏、泉　佳信、寺田　隆哉、藤代博之
出願人：東洋紡績㈱

(Pat-6) 「バルク超伝導体のパルス着磁方法及び超伝導磁石装置」
出願日および出願番号：2005 年 5 月 30 日 (特願 2005-156956)（特開 2006-332499）
発明者：藤代博之、金山雅彦、岡　徹雄
出願人：岩手大学、アイシン精機㈱

(Pat-7) 「薄膜の製造方法」
出願日：2007.9.19 (特願 2007-242624)
発明者：吉本則之、藤代博之、小川　智
特許権者：国立大学法人岩手大学
登録日：2013.5.24 (特許第５２３４２９号)

(Pat-8) 「磁場中有機単結晶薄膜作成法及び作成装置」
出願日：2010.3.1 (特願 2010-044727)
発明者：吉本則之、荒木俊行、藤代博之
特許権者：国立大学法人岩手大学
登録日：2014.8.8 (特許第５５９０６５９号)

(Pat-9) 「有機半導体材料並びに有機半導体装置及びその製造方法」
出願日：2010.8.18 (特願 2010-182792)
発明者：小川　智、吉本則之、藤代博之
特許権者：国立大学法人岩手大学
登録日：2015.4.10 (特許第５７２５４９４号)

(Pat-10)「超電導磁場発生素子」

出願日：2017/5/23（特願 2017-101661）（特開 2018-198245）

発明者：柳　陽介、伊藤佳孝、藤代博之、内藤智之

特許権者：株式会社アイシン

登録日：2021.10.5 (特許第６９５５１９２号)

(Pat-11)「ハイブリッド型超電導バルク磁石装置」

出願日：2018/1/17（特願 2018-005677）（特開 2019-125710）

特許査定：2021/12/17

発明者：藤代博之、髙橋圭太

特許権者：国立大学法人岩手大学

登録日：2022/1/11 (特許第７００６２９１号)

(Pat-12)「ハイブリッド型超電導バルク磁石装置とその着磁方法」

出願日：2019/11/28（特願 2019-214998）（特開 2021-86927）

発明者：藤代博之

出願人：国立大学法人岩手大学

(Pat-13)「高磁気勾配型超電導バルク磁石装置」

出願日：2020/10/28、（特願 2020-180228）

発明者：髙橋圭太、藤代博之

出願人：国立大学法人岩手大学

９．表彰、受賞

(Hyo-1) 低温工学協会褒賞、優良発表賞：「REBaCuO バルク超伝導体の熱的性質(RE=Dy, Gd, Ho, Nd)」（平成 17 年）

(Hyo-2) Top Cited Article 2005-2010 (Physica C: Superconductivity and its Applications", ELSEVIER, Hiroyuki Fujishiro, Tatsuya Tateiwa, Atsushi Fujiwara, Tetsuo Oka and Hidemi Hayashi "Higher trapped field over 5 Tesla on HTSC bulk by modified pulse field magnetizing", *Physica C* 445-448 (2006) pp. 334-338

(Hyo-3) Superconductor Science and Technology (SUST)誌 30th anniversary collection として選定される。 "Modelling of bulk superconductor magnetization", M D Ainslie and H Fujishiro 2015 *Supercond. Sci. Technol.* 28 053002

(Hyo-4) IOP (Institute of Physics Publishing: 英国物理学会出版)誌の trusted reviewer として選定される。2020 年

１０．国際会議出席発表（本人発表分）

（★：招待講演、☆：口頭発表、△：short oral+poster、□：poster）

Year	海外で開催された国際会議及び、講演	国内で開催された国際会議	
1993 (H5)	★MT-13(Victoria, Canada) (9.21-27) “Low Thermal Conductive Bi-2223 Tapes Sheathed with Ag-Au Alloys”	△ICT12 (Yokohama) (11.9-11) “Use of Bi2223 Superconducting Tapes Sheathed with Ag-Au Alloys for a Passive Thermoelement”	
1994 (H6)	□15th ICEC (Genova, Italy) (6.7-10) “Possibility of Ag_2O+$YB_{a2}Cu_3O_{7-X}$ ceramics for low temperature thermoelectric refrigeration” □M2S (Grenoble, France) (7.7-11) “Thermal Conductivity of Bi-2212 Single Crystals Prepared by TSFZ Method” “Phonon Thermal Diffusivity and Conductivity of Oxygen Deficient $YBa_2Cu_3O_7$”	☆Jpn.-US workshop (Kyoto)	
1995 (H7)		□Phonons'95 (Sapporo) “Thermal Conductivity and Diffusivity of $Nd_{2-X}Ce_XCuO_4$”	
1996 (H8)	☆WTC'96 (Budapest, Hungary) (7.7-10) “Model analyses of thermal conductivity and purity of doped Ag in Ag+$YBa_2Cu_3O_7$” □MOS'96 (Karlsruhe, Germany) (8.1-7) “Thermal conductivity and phonon scattering mechanisms in $La_{1-x}M_xCuO_4$” □LT21 (Prague, Czech) (8.8-14) “Effect of Y-site and Ba-site Substitution on Thermal Properties of $YBa_2Cu_3O_{7-d}$” “Proposal of Three Terminal Method for Low Temperature Thermal Diffusivity Measurement”		
1997 (H9)	□ICM'97 (Cairns, Australia) (7.27-8.1) “Thermal conductivity and phonon scattering of $La_{1-X}Sr_XMnO_3$”		
1998 (H10)	□CIMTEC'98 (Florence, Italy) (6.18-28) “THERMAL CONDUCTIVITY OF T*-PHASE $(Nd_{1-x-y}Ce_xSr_y)_2CuO_4$ OXIDE SUPERCONDUCTORS” “ULTRASONIC AND PHONON THERMAL TRANSPORT STUDIES ON $YBa_2Cu_3O_{7-d}$ OXIDE SUPERCONDUCTORS” ☆Phonons'98 (Lancaster, England) (7.26-31) “Two-level-like anomalous phonon scattering in $La_{1-X}Sr_XMnO_3$ and $La_{2-X}Sr_XCuO_4$”		
1999 (H11)	□MOS'99 (Stockholm, Sweden) (7.28-8.2) “Enhanced Phonon Scattering below T_c Caused by Zn and Ni Substitution in $La_{1.85}Sr_{0.15}CuO_4$”	□SCES'99 (Nagano) (8.24-27) First-order-like ferromagnetic transition in $(La_{1-y}Pr_y)_{1-x}(Ca_{1-z}Sr_z)_xMnO_3$ (X~0.25)”	

	□LT22 (Helsinki, Finland) (8.4-11) Sound Velocity Anomaly Related to Charge Ordering in $La_{1-x}Ca_xMnO_3$"		
2000 (H12)		☆JARCAT Workshop (Kyoto) (5.31) "Sound Velocity Anomalies Related to Charge Ordered Transition in $La_{1-x}Ca_xMnO_3$ ($0<x<1$)" △LLD2k (Tsukuba) (7.23-26) "Heat Transport Anomalies around Ferromagnetic and Charge-order Transitions in $La_{1-x}Ca_xMnO_3$" □ISS2000 (Tokyo) (10.14) "Thermal contact resistance between high-T_c superconductor and copper"	
2001 (H13)	□Phonons2001 (Dartmouth, USA) (8.12-17) "Thermal diffusivity of $La_{1-X}Ca_XMnO_3$ up to 1200 K" □MT-17 (Genova, Swiss) (9.24-27) "Thermal Conductivity, Thermal Diffusivity and Thermoelectric Power of Sm-Based Bulk Superconductors"	☆IMR workshop (Sendai) (5.22) "Charge/Orbital Order Fluctuation and Lattice Softening in $La_{1-x}Ca_xMnO_3$" △Orbital2001 (Sendai) (9.11-13) "Heat Transport Enhancement in Ferromagnetic Metallic Phase of $La_{1-X}Ba_XMnO_3$"	
2002 (H14)	□SCES'02 (Kraków, Poland) (7.8-15) "THERMAL TRANSPORT IN FERROMAGNETIC $La_{1-X}AE_XMnO_3$ WITH LARGE DIVALENT IONS" ★チェコ科学アカデミー講演(7.16)	□LT23 (Hiroshima) (August) "Co Site Substitution Effect on Thermoelectric Properties in $Na(Co_{1-X}M_X)_2O_4$ (M=Ni, Fe, Mn, Cu)" □ISS2002 (Yokohama) "Thermal conductivity of YBaCuO bulk superconductors under applied field: effect of content and size of Y211 phase"	
2003 (H15)	**文部省短期在外研究員（チェコ科学アカデミー）(2003.7.26~9.26)** □ICM'03 (Roma, Italy) (7.27-31) "Thermal conductivity and magnetism in $(Ca_{1-X}Sr_X)MnO_3$" ☆ICT2003 (La Grande-Motte, France) (8.17-21) "Search for p-type Oxide Thermoelectrics – Cobaltites" "Enhanced Thermoelectric Properties at X~0.1 in $La_{1-X}Sr_XCoO_3$ and $La_{1-X}Sr_X(Co_{1-Y}M_Y)O_3$ (M=Cr, Cu)"	☆MT-18 (Morioka) (10.21) "Flux Motion Studies by means of Temperature Measurement in Magnetizing Processes for HTSC Bulks" ☆ISS2003 (Tsukuba) (10.27) "Estimation of generated heat in pulse field magnetizing for SmBaCuO bulk superconductor"	
2004 (H16)	□ICT2004 (Adelaide, Australia) (7.24-31) "Influence of Co-site Substitution on Thermoelectric Properties in $La_{1-x}Sr_xCoO_3$" "Size Effect of A-site Cation on n-type Thermoelectric Properties in $CaMnO_3$-based System"	★ISS2004 (Niigata) (11.16) "Approach from temperature measurement to trapped field enhancement in HTSC bulks by pulse field magnetizing" "Database for thermal and mechanical properties of REBaCuO bulks"	

	□ASC2004 (Jacksonville, U.S.A) (10.2-11) “Effect of Metal Ring Setting outside HTSC Bulk Disk on Trapped Field and Temperature Rise in Pulse Field Magnetizing”		
2005 (H17)	□SCES’05 (Wien, Austria) (7.28-31) “Anomalous Sound Velocity Behavior of $La_{1-X}Ca_XMnO_3$ (X~0.48) in Applied Field” “Thermal Conductivity Anomaly in $La_{0.52}Ca_{0.48}MnO_3$ under Applied Field” □EUCAS2005 (Wien, Austria) (9.12-15) “Trapped Field over 4 Tesla on GdBaCuO Bulk by Pulse Field Method and Magnetizing Mechanis □MT19 (Genova, Italy) (9.19-23) “Low-Thermal-Conductive DyBaCuO Bulk Superconductor for Current Lead Application” ★チェコ科学アカデミー講演(9.11)	☆PASREG (Tokyo University of Marine Science and Technology）(10.20) “Thermal Conductivity and Thermoelectric Power of DyBaCuO Bulk Superconductor” ☆ISS2005 (Tsukuba) (10.24-26) “Higher trapped field over 5 Tesla on HTSC bulk by modified pulse field magnetizing”	
2006 (H18)		☆ISS2006 (Nagoya) (10.30-11.2) “Importance of initial ‘‘M-shaped’’ trapped field profile in a two-stage pulse field magnetization (MMPSC) method”	
2007 (H19)	☆6th PASREG (Cambridge, England) (9.11-18) “Possible Explanation for Trapped Field Enhancement on REBaCuO Bulk by Modified Multi-pulse Technique with Stepwise Cooling (MMPSC)”	□ISS2007 (Tsukuba) (11.5-7) “Trapped field characteristics on f 65 mm GdBaCuO bulk by modified multi-pulse technique with stepwise cooling (MMPSC)”	
2008 (H20)	☆ASC2008 (Chicago, USA) (8.17-23) “Pulsed Field Magnetization for GdBaCuO Bulk with Stronger Pinning Characteristics”	□ISS2008 (Tsukuba) (10.27-29) “Enhancement of total trapped fluxes on f65 mm GdBaCuO bulk by multi-pulse techniques”	
2009 (H21)	□EUCAS2009 (Dresden, Germany) (9.12-20) “Highly efficient magnetic separation using five-aligned superconducting bulk magnet” ★チェコ科学アカデミー講演 (9.20) “Recent research progresses of Cobaltites and Manganites in Iwate”	☆ISS2009 (Tsukuba) (11.1-3) “Temperature measurements in small holes drilled in superconducting bulk during pulsed field magnetization”	
2010 (H22)	□ASC2010 (Washington DC, USA) (8.1-10) “Analysis of Temperature and Magnetic Field Distribution in Superconducting Bulk during Pulsed Field Magnetization”	□ISS2010 (Tsukuba) (10.31-11.2) “Simulation of flux dynamics in a superconducting bulk magnetized by multi-pulse”	
2011 (H23)	□EUCAS2011 (Den Hague, The Netherland) (9.17-25) “Three-dimensional simulation of magnetic flux dynamics and temperature rise in HTSC bulk during pulsed field magnetization” ★チェコ科学アカデミー講演 (9.17)		

2012 (H24)	☆ASC2012 (Portland, USA) (10.9-13) “Numerical Simulation of Trapped Field and Temperature Rise in MgB_2 Bulks Magnetized by Pulsed Field” ★大連理工大講演(6.12-13)	□ICEC24-ICMC2012 (Fukuoka) (5.14-18) “Trapped field and temperature rise in MgB_2 bulks magnetized by pulsed field”	
2013 (H25)	□EUCAS2013 (Genova, Italy) (9.15-20) “Trapped magnetic field between double stacked MgB_2 bulks magnetized by pulsed field” ★チェコ科学アカデミー講演(9.22) “Recent research progresses of Cobaltites and Manganites in Iwate”	☆ISS2013 (Tokyo) (11.19) “Trapped field and flux dynamics in MgB_2 superconducting bulks magnetized by pulsed field”	
2014 (H26)	☆ASC2014 (Charlotte, USA) (8.9-18) “Recent progress of MgB_2 bulk magnets magnetized by pulsed field” ★Saskatchewan 大講演 (12.1-3)	☆IU-MRS (Fukuoka) (8.28-31) “Characteristics and trapped field of REBaCuO and MgB_2 superconducting bulks”	
2015 (H27)	☆UK-Japan workshop (Cambridge, England) (4.11-19) “Magnetizing process and trapped field of REBaCuO and MgB_2 superconducting bulks” ★PASREG2015 (Liege, Belgium) (9.1-5) “Pulsed field magnetization for (RE)BCO and MgB_2 superconducting bulks and their applications” □MT25 (Seoul, South Korea) (10.18-22) “Trapped field homogeneity in NMR superconducting bulk magnet by the insertion of high-J_c HTS cylinder with various positions, lengths and shapes”		
2016 (H28)	☆ASC2016 (Denver, USA) (9.4-11) “Trapped Field Enhancement of a Thin, High-J_c MgB_2 Bulk without Flux Jumps using Pulsed Field Magnetization with a Split-type Coil with a Soft Iron Yoke”		
2017 (H29)	□MT25 (Amsterdam, The Netherland) (8.26-9.2) “New proposal of mechanical reinforcement structures to annular REBaCuO bulk magnet for compact and cryogen-free NMR spectrometer”	★PASREG2017 (Tokyo) (12.11-12) “Mechanical Reinforcement of REBaCuO Bulk during Field-Cooled Magnetization -- Road to Achieve Trapped Field Higher than 20 Tesla –"	
2018 (H30)	★Cambridge 大での招待講演(4.11-13) “Recent research progresses in Iwate” ☆ASC2018 (Seattle, USA) (10.28-11.2) “Influence of Inner Diameter and Height of Ring-shaped REBaCuO Bulks on Trapped Field and Mechanical Stress during Field-cooled Magnetization”	★ISS2018 (Tsukuba) (12.12-14) “Mechanical reinforcement of REBaCuO bulk during field-cooled magnetization to achieve higher trapped field without fracture”	

2019 (R1)	★PASREG2019 (Prague, Czech) (8.27-30) “A new mechanical reinforcement structure for REBaCuO bulks during field-cooled magnetization to achieve higher trapped fields without fracture” ★EUCAS2019 (Glasgow, England) (9.1-5) “A Hybrid Trapped Field Magnet Lens (HTFML): concept and realization”	★ISS2019 (Kyoto) (12.3-5) “A Hybrid Trapped Field Magnet Lens (HTFML): concept and experimental realization”	
2020 (R2)			
2021 (R3)	★PASREG (Shanghai, China: WEB) (11.11-13) “A Hybrid Trapped Field Magnet Lens (HTFML): concept and validation”		

西暦	元号	年齢	所属・職位	海外開催の国際会議発表	国内開催の国際会議発表	招待講演数
1990	H2	34	九州工大助手	0	0	0
1991	H3	35	岩手大助手	0	0	0
1992	H4	36		0	0	0
1993	H5	37	岩手大助教授	1(カナダ)	1	1
1994	H6	38		2(イタリア、フランス)	1	0
1995	H7	39		0	1	0
1996	H8	40		3(ハンガリー、ドイツ、チェコ)	0	0
1997	H9	41		1(オーストラリア)	0	0
1998	H10	42		2(イタリア、イギリス)	0	0
1999	H11	43		2(スウェーデン、フィンランド)	1	0
2000	H12	44		0	2	0
2001	H13	45		2 (アメリカ、スイス)	2	0
2002	H14	46		2(ポーランド、チェコ)	2	1
2003	H15	47		2(イタリア、フランス)	2	0
2004	H16	48		2(オーストラリア、アメリカ)	1	1
2005	H17	49		2(オーストリア、アメリカ)	2	1
2006	H18	50	岩手大教授	0	1	0
2007	H19	51		1(イギリス)	1	0
2008	H20	52		1(アメリカ)	1	0
2009	H21	53		2(ドイツ、チェコ)	1	1
2010	H22	54		1(アメリカ)	1	0
2011	H23	55		2(オランダ、チェコ)	0	0
2012	H24	56		2(アメリカ、中国)	1	1
2013	H25	57		2(イタリア、チェコ)	1	1
2014	H26	58		2(アメリカ、カナダ)	1	1
2015	H27	59		3(イギリス、ベルギー、韓国)	0	1
2016	H28	60		1(アメリカ)	0	0
2017	H29	61		1(オランダ)	1	0
2018	H30	62		1(アメリカ)	1	0
2019	R1	63	理事・副学長	2 (チェコ、イギリス)	1	3
2020	R2	64		0	0	0
2021	R3	65		1(WEB)	0	1

43件 26件 13件

出席した国際会議の開催地

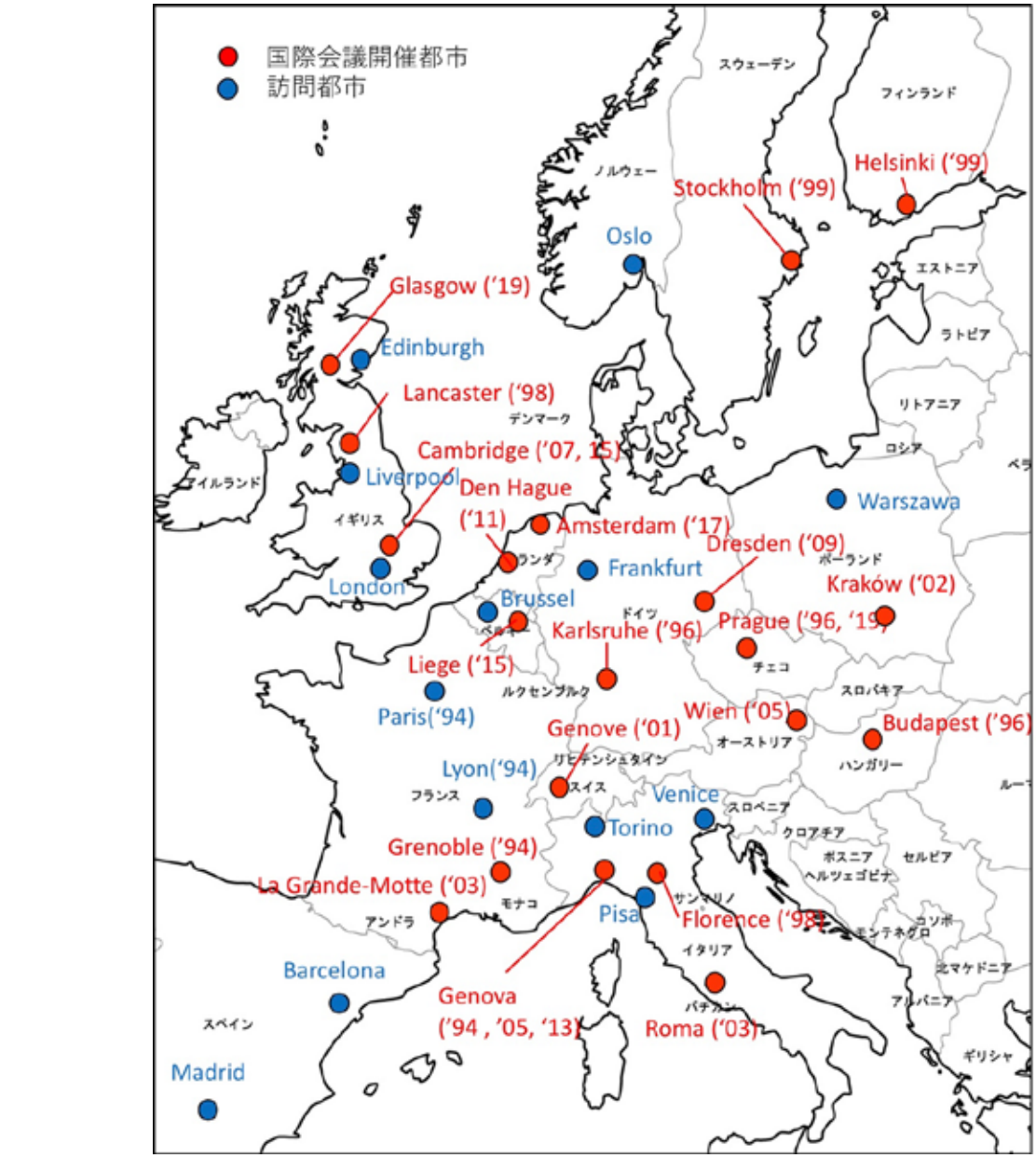

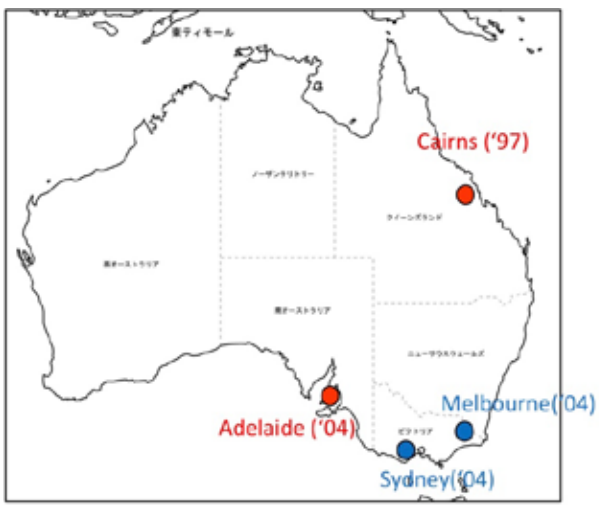

１１．外部資金獲得

『科学研究費補助金』（代表のみ）

(1) 基盤研究（C）:「ＣＭＲ効果を示す Co 系酸化物の磁気相転移とフォノン伝達」、(280 万円)、平成 14～15 年度
(2) 基盤研究（C）:「超強力な超伝導バルク磁石の実現と磁束ダイナミックスの解明」、(350 万円）平成 17～18 年度
(3) 基盤研究（C）:「新しいパルス着磁法による 7 テスラを越える超伝導バルク磁石の実現と磁束運動の解明」、(350 万円）平成 19～20 年度
(4) 基盤研究（C）:「スプリット型コイルによる超強力な超伝導バルク磁石の実現と磁気分離への応用」、(420 万円) 平成 23～25 年度
(5) 基盤研究（C）:「MgB_2 超電導バルク磁石の熱的安定化と強磁場捕捉を実現するパルス着磁技術の開発」、(380 万円) 平成 27～29 年度（藤代）
(6) 基盤研究（C）:「着磁磁場よりも大きな磁場を持続的に発生できる新規の超電導バルク磁石レンズ」、(330 万円) 令和元～令和 3 年度年度

『奨励金』（代表のみ）

(1) 池谷科学技術振興財団研究助成：「酸化物超伝導体を用いた低温領域における熱電冷却素子に関する研究」（150 万円)、平成 5 年度
(2) 池谷科学技術振興財団研究助成：「第１５回低温技術に関する国際会議 (ICEC-15) ジェノバ (Genova)、イタリア (Italy) 旅費」（35 万円）
(3) 平成 6 年度実吉奨学会研究奨励金：「Mn 系酸化物における金属・絶縁体転移近傍での電荷整列と熱伝導特性」（60 万円)、平成 9 年度
(4) 東京電力（株）研究振興財団海外渡航旅費：「9th International Conference on Modern Material & Technologies (CIMTEC '98)（第 9 回先端材料および技術に関する国際会議）イタリア・フロレンス」（30 万円)、平成 10 年度
(5) 日本原子力研究所先端基礎研究センター黎明研究：「ペロブスカイト鉄族系酸化物のフォノン伝導と格子異常」（200 万円)、平成 11 年度
(6) 岩手大学大学活性化経費（外部資金を導入するための経費・展開的な研究）:「Co 系酸化物熱電エネルギー変換材料の開発」（70 万円)、平成 14 年度
(7) 岩手大学学長裁量経費（萌芽的教育研究支援費）:「低環境負荷型エネルギー変換材料の探索とデバイス開発」（35 万円)、平成 17 年度
(8) 夢県土いわて戦略的研究推進事業：「バルク超伝導体の新しいパルス着磁法の開発と捕捉磁場向上に関する研究」（代表）（1050 万円)、平成 16～18 年度
(9) 岩手大学学長裁量経費「教員個人の研究業績に基づく研究費の配分」（100 万円)、平成 18～19 年度
(10) JST 地域イノベーション創出総合支援事業　重点地域研究開発プログラム　平成 20 年度「シーズ発掘試験」、「マイクロモーゼ効果を用いた有機半導体薄膜の微細結晶配向制御」（200 万円）
(11) 岩手大学学長裁量経費（萌芽的教育研究支援費）:「ソフトパスエンジニアリングに関する連続講演会の開催」（45 万円)、平成 20 年度
(12) JST 地域イノベーション創出総合支援事業　重点地域研究開発プログラム　平成 21 年度「シーズ発掘試験」、「マルチ超伝導バルク磁石を用いた高精度磁気分離技術の開発」（200 万円）
(13) 平成 23 年度 JST 研究成果展開事業 研究成果最適展開支援プログラムフィージビリティスタディ【ＦＳ】ステージ 探索タイプ「超電導バルク磁石を用いた放射能汚染土壌や水の除染用吸着剤の開発」(300 万円)
(14) 平成 24 年度 JST 復興促進プログラム(A-STEP)探索タイプ「モーゼ効果を用いた熱電変換用ポリマー薄膜の高性能化と特性向上」(300 万円)

(15) 日本学術振興会「二国間交流事業」、(英国との交流事業)「超電導モーター応用を目指した超電導バルク材の作製及び着磁・要素技術の開発」、平成 26 年～28 年 (442.5 万円)
(16) JST A-STEP 機能検証フェーズ、「着磁磁場より強い磁場を持続的に発生できるハイブリッド型超電導バルク磁石レンズの開発」(2018-2019) (300 万円)
(17) JST A-STEP トライアウト、「勾配磁場により微小重力環境を実現する新しい超電導バルク磁石装置の開発」(2020-2022) (300 万円)

推定分野

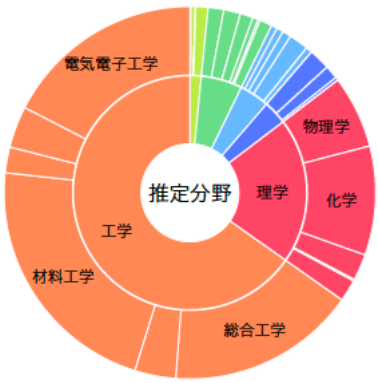

関連度TOP5

- 工学 / 材料工学
- 工学 / 電気電子工学
- 工学 / 総合工学
- 理学 / 化学
- 理学 / 物理学

推定関連キーワード

Superconducting / High-quality / 超電導バルク / パルス着磁技術 / デバイス実装 / 超伝導バルク磁石 / 超電導マグネット / 次世代半導体 / 臨界電流密度 / ピン止め中心

科研費、競争的外部資金の獲得状況

１２．研究室の卒業論文、修士論文、博士論文の題目

(平成 3 年度, 1991 年度：池部研究室)
卒業論文
B1.工藤優一「噴霧熱分解法による酸化物超伝導体超微粒子の作製」
B2.廻谷和志「Bi 系超伝導体における Pb 添加と超伝導特性の関係」
B3.諸井　睦「熱電対を用いた Bi 系超伝導体の熱伝導率測定」
B4.齊藤道明「$YBa_2Cu_3O_{7-\delta}$単結晶の作製」
B5.堀切祐仁「Y 系超伝導体の粒径と超伝導特性の関係」

(平成 4 年度,1992 年度：池部研究室)
卒業論文
B6.日下和彦「Bi 系酸化物超伝導体厚膜に関する研究」
B7.栗原　崇「低熱侵入型酸化物超伝導体/合金シーステープに関する研究」
B8.幸野泰史「酸化物超伝導体のゼーベック係数、熱伝導率に関する研究」
B9.内藤智之「酸化物超伝導体の熱拡散率に関する研究」
B10 佐竹隆志「ひずみゲージによる熱膨張測定に関する研究」
B11.菅尾克弘「差動変圧器を用いた熱膨張計の試作」
B12.中島正晶「低温で動作する熱電冷却素子に関する研究」

(平成 5 年度, 1993 年度：池部研究室)
修士学位論文
M1.工藤優一「酸化物超伝導体粒子の作製と線材化に関する研究」
卒業論文
B13.岩田邦男「酸化物超伝導体の熱起電力に関する研究」
B14.楠見武生「A/D コンバータを用いた熱拡散率測定システムの開発」
B15.生井正夫「酸化物超伝導体の熱電冷却への応用に関する研究」
B16.及川滋暁「Ag ドープ Bi2212 結晶の異方性輸送特性に関する研究」
B17.中川貴子「Y 系酸化物超伝導体の熱拡散率に関する研究」
B18.関　修章「Bi 系酸化物超伝導体の線材化に関する研究」
B19.八木真如「Bi(2201)系酸化物超伝導体試料の作製」

(平成 6 年度, 1994 年度：池部研究室)
修士学位論文
M2.内藤智之「酸化物超伝導体の熱拡散率、熱伝導率に関する研究」
M3.日下和彦「酸化物超伝導体を用いた低温で動作する熱電冷却素子に関する研究」
卒業論文
B20.久保澤　誠「Ag+$YBa_2Cu_3O_7$ 系のパーコレーション伝導に関する研究」
B21.岩　慎一「$Nd_{2-x}Ce_xCuO_4$ の Ce 濃度と熱伝導率」
B22.田鎖賢二「$Bi_2Sr_2CaCu_2O_x$ 酸化物超伝導体の超伝導特性に関する研究」
B23.中里規実生「酸化物超伝導体の熱拡散率と比熱に関する研究」
B24.野沢孝紀「$RBa_2Cu_3O_{7-\delta}$ (R:希土類元素）の超伝導特性に関する研究」
B25.橋山淳一「Y-Ni-B-C 及び Y-Pd-B-C の金属超伝導体に関する研究」
B26.福井達明「$YBa_2Cu_3O_{7-\delta}$の Zn 置換と超伝導特性に関する研究」
B27.吉田昌浩「酸化物超伝導体を用いた熱電冷却素子に関する研究」

(平成 7 年度, 1995 年度：池部研究室)

修士学位論文

M4.八木真如「$Nd_{2-x}Ce_xCuO_{4-\delta}$における熱輸送特性と超伝導」

卒業論文

B28.浜田和宏「GaAs 単結晶の熱伝導率と散乱機構」

B29.高橋重雄「$YBa_2Cu_3O_{7-\delta}$の Y サイト置換効果と熱伝導率」

B30.芝崎有三「$La_{2-x}Ba_xCuO_4$ 系超伝導体の熱的、電気的輸送特性」

B31.冨田　健「酸化物超伝導体の熱伝導率に関する理論解析」

B32.昆野吉幸「極低温(10 K 以下）における熱伝導率測定法の開発」

B33.湊　洋一「Ag+YBCO 系のパーコレーション伝導とモデル解析」

(平成 8 年度, 1996 年度：池部研究室)

修士学位論文

M5.中里規実生「酸化物超伝導体の熱伝導率及び熱拡散率に関する研究」

M6.小山道夫「MBE を用いた銅及び遷移金属酸化膜薄膜の作製」

卒業論文

B34.松枝　斉「酸化物超伝導体における接触電気抵抗と臨界電流に関する研究」

B35.杉村茂昭「室温以上の熱伝導率測定装置の開発と評価に関する研究」

B36.菅原至朗「V_2O_3 における金属・絶縁体転移と熱伝導率に関する研究」

B37.三上達也「３点法による熱拡散率測定と接触熱抵抗に関する研究」

B38.菊池　勉「MBE 法による銅およびマンガン酸化薄膜の作製及び評価に関する研究」

B39.松尾昌宏「T*構造を有する 214 系酸化物超伝導体の作製と熱伝導率に関する研究」

(平成 9 年度, 1997 年度：池部研究室)

修士学位論文

M7.芝崎有三「(214)系超伝導体における熱輸送特性」

M8.湊　洋一「室温以上の温度領域における熱拡散率、熱伝導率測定法の開発」

M9.昆野吉幸「$La_{1-x}Sr_xMnO_3$ の磁気相転移と熱輸送」

卒業論文

B40.王子田修一「FZ 法で作製した $La_{1-x}Sr_xMnO_3$ 結晶の熱伝導率と熱拡散率」

B41.岡本龍也「$Nd_{2-x}Ce_xCuO_{4-\delta}$超伝導体の Cu サイト置換効果」

B42.片桐洋一「Ag+YBCO 複合材料の熱起電力から見たパーコレーション」

B43.河西　孝「$La_{1-x}Ca_xMnO_3$ 結晶の磁気相転移と熱伝導率」

B44.根城智哲「FZ 法で作製した $Nd_{0.5}Sr_{0.5}MnO_3$ 結晶における電荷整列相転移と熱伝導」

B45.入江　剛「酸化物超伝導体ー銅ブロック間の接触熱抵抗」

(平成 10 年度, 1998 年度：池部研究室)

修士学位論文

M10.三上達也「$La_{1-x}Sr_xMnO_3$ ($0.48<x<0.82$)の電荷整列現象とフォノン散乱機構」

M11.菅原至朗「$R_{1-x}Sr_xMnO_3$ (R=Nd, Pr, Sm, Gd)の相転移と熱伝達特性」

M12.菊池　勉「$La_{1-x}Ca_xMnO_3$ の磁気相転移と熱輸送特性」

卒業論文

B46.小澤英行「Mn 酸化物 $R_{1-x}Sr_xMnO_3$ における R サイトのイオン半径と相転移」

B47.加納伸吾「$La_{1-x}Ca_xMnO_3$ の磁場中熱伝導率、熱拡散率測定」

B48.川村広貴「$Nd_{2-x}Ce_xCuO_{4-\delta}$超伝導体の Cu サイト置換効果」

B49.木沢健公「滴定法による Mn 酸化物中の Mn イオン価数の定量について」

B50.島　健悟「$Na(M_xCo_{1-x})_2O_4$ (M=Fe, Ni, Mn, Cu)の熱電効果」

B51.野　明彦「異方性物質に対する新しい異方的熱伝導率決定法の提案」

B52.藤原直将「$Pr_{1-x}Ca_xMnO_3$ (0＜x＜1)の作製と熱伝達特性」

(平成 11 年度, 1999 年度：池部研究室)

修士学位論文

M13.王子田修一「$RE_{1-x}AE_xMnO_3$ (x～0.9)のキャント磁性と輸送特性」

M14.岡本龍也「異方性物質に対する異方的熱伝導率の同時決定法」

卒業論文

B53.菅原昭洋「$(La_{1-z}Nd_z)_{1-x}Sr_xMnO_3$ の x=0.5 近傍における磁気・電荷秩序」

B54.高橋拓也「$RuSr_2GdCu_2O_8$ の超電導性と強磁性」

B55.滝口　勝「FZ 法で作製した $La_{1-x}Sr_xMnO_3$ (x～0.5)の磁化特性」

B56.照井明彦「$La_{1-x}Ba_xMnO_3$ の輸送特性と相図の決定」

B57.平松美穂「ヨウ素滴定法を用いた Mn 酸化物における酸素量の定量」

B58.山崎　哉「$Pr_{0.65}Ca_{0.35}MnO_3$ における Mn サイトの遷移金属置換効果」

(平成 12 年度, 2000 年度：池部研究室)

修士学位論文

M15.小澤英行「$R_{1-x}A_xMnO_3$ (R=La, Pr, Nd : A=Ca, Sr, Pb)における格子歪みと相転移」

M16.加納伸吾「$La_{1-x}Ba_xMnO_3$, $Pr_{1-x}Ca_xMnO_3$ の磁場中輸送特性」

M17.沼野　誠「$La_{1-x}Ca_xMnO_{3+\delta}$の相転移に及ぼす酸素含有量の影響」

卒業論文

B59.小林大悟「$La_{1-x}Pb_xMnO_{3+\delta}$の輸送特性と相図の決定」

B60.中家広顕「パイロクロア型酸化物 $R_2Mo_2O_7$ (R=Nd, Sm, Gd)の作製に関する研究」

B61.柏田陽平「$La_{0.65}Ca_{0.35}MnO_{3+\delta}$の低抵抗化に関する研究」

B62.大久保和紘「$RuSr_2GdCu_2O_8$ の超電導特性について」

B63.佐藤一晶「FZ 法による $La_{1-x}Ca_xMnO_{3+\delta}$単結晶の育成と評価」

B64.清水輝幸「$La_{1-x}Ca_xMnO_3$ の作製条件による電気抵抗率の変化について」

(平成 13 年度, 2001 年度：池部研究室)

修士学位論文

M18.高橋拓也「$RuSr_2GdCu_2O_8$ (Ru1212)の超電導特性向上に関する研究」

M19.滝口　勝「FZ 法による $La_{1-x}Ca_xMnO_3$ の単結晶成長と評価」

M20.山崎　哉「$Pr_{1-x}Ca_xMnO_3$ 系における Mn サイトへの遷移金属置換効果」

卒業論文

B65.伊藤健一「$CaMnO_{3+\delta}$の酸素含有量と諸物性について」

B66.小滝茂則「超電導体 MgB_2 の作製と評価」

B67.鈴木和義「$La_{0.8}Sr_{0.2}(Mn_{1-z}Co_z)O_3$ の磁性と伝導」

B68.西　利勝「CMR 効果を示す $La_{1-x}Sr_xCoO_3$ の作製と電気的、磁気的性質」

B69.村上　強「$La1_{-x}Ca_xMnO_3$ の単結晶育成に関する研究」

(平成 14 年度, 2002 年度：池部研究室)

修士学位論文

M21.柏田陽平「$La_{1-x}AE_xCoO_{3+\delta}$ (AE=Sr, Ba, Ca)の磁性と熱輸送特性」

卒業論文

B70.寺沢耕太郎「FZ 法による $La_{2-x}Sr_xNiO_{4+\delta}$単結晶の作製に関する研究」

B71.澤田健二「$La_{1-x}Sr_xCoO_3$ の作製と物性評価」

B72.三田泰久「$Ca_{1-x}Sr_xMn_{3-\delta}$の磁性と伝導に関する研究」

B73.内藤博史「FZ 法による $La_{1-x}Sr_xCoO_{3+\delta}$の単結晶作製に関する研究」

B74.伊藤俊彦「$RuSr_2GdCu_2O_{8-\delta}$の超電導特性向上に関する研究」

B75.佐々木　学「$La_{2-x}Sr_xNiO_{4+\delta}$焼結体作製と物性評価」

(平成 15 年度, 2003 年度：池部研究室)

修士学位論文

M22.熊谷達也「$Pr_{0.65}Ca_{0.35}MnO_3$ における Mn サイトの置換効果」

M23.鈴木和義「FZ 法における $La_{2-X}Sr_XNiO_4$ の結晶成長と物性評価」

卒業論文

B76.伊藤真治「$LaCoO_3$ 系酸化物における酸素量の決定」

B77.植田祐史「バルク超伝導体のパルス着磁における温度上昇」

B78.篠原　聡「$La_{2-x}Sr_xNiO_{4+\delta}$の FZ 成長と性能評価」

B79.鈴木　雄「$RE_{1-x}Ca_xMnO_3$ 系の熱電特性に及ぼすＡサイトのイオン半径の影響」

B80.藤原　篤「$Pr0_{.65}Ca_{0.35}MnO_3$ における Mn サイトへの置換効果」

(平成 16 年度, 2004 年度：池部研究室)

修士学位論文

M24.金山雅彦「バルク超伝導体のパルス着磁における捕捉磁場と発熱解析」

M25.内藤博史「$La_{1-X}Ca_XCoO_{3-\delta}$の酸素欠損量の低減と物性評価」

卒業論文

B81.赤間和也「DyBaCuO 系超伝導バルクの結晶成長と超伝導性」

B82.川口秀介「バルク超伝導体のパルス着磁における発熱現象と温度シミュレーション」

B83.久保田　徹「$SrPbO_3$ 系 n 型熱電変換材料の作製と性能評価」

B84.姿　拓幸「$RECoO_3$ (RE:希土類元素)の熱伝導率と熱膨張率」

B85.武田紘幸「$CaMnO_3$ の Mn サイト置換と熱伝導率」

B86.立岩達也「Gd 系バルク超伝導体を用いた 4 テスラを超える捕捉磁場の実現」

B87.長坂佑一「$Pr_{1-X}Ca_XMnO_3$ における Mn サイトの Ru 置換効果」

B88.箱石真弓「$(La_{1-Z}Y_Z)_{0.5}Ca_{0.5}CoO_3$ の熱電変換特性」

(平成 17 年度, 2005 年度)

修士学位論文

M26.藤原　篤「パルス着磁による新しい超電導バルク磁石の開発」

M27.鈴木　雄「$La_{1-X}AE_XCoO_3$ (AE=Ca, Sr, Ba)の熱電特性」

卒業論文

B89.菊池健太郎「n 型熱電材料 $RE_{1-X}Ce_XCoO_3$ 実現の可能性について」

B90.佐久山誉生「211 相を含まない DyBaCuO 系超伝導バルクの結晶成長」

B91.佐塚悠介「４角形超伝導バルクのパルス着磁特性」

B92.李沢未央「$RE_{1-X}Ca_XCoO_3$ のトレランス因子と物性評価」

B93.高橋則史「DyBaCuO 系超伝導バルクの結晶成長と超伝導性--2005」

B94.日山拓也「MMPSC 法による超伝導バルクのパルス着磁特性」

B95.八重樫晃一「FZ 法による $RECoO_3$ 系材料の作製と物性評価」

(平成 18 年度, 2006 年度)

修士学位論文

M28.立岩達也「MMPSC 法による超伝導バルクのパルス着磁現象と磁束運動」

卒業論文

B96.田澤淳一「DyBaCuO 系超伝導バルクの作製と評価 2006」

B97.岡村宏紀「磁気分離用５連型超伝導バルク磁石装置の作製と特性評価」

B98.欠端浩介「65mm 大型超伝導バルクのパルス着磁特性」 概要

B99.今野友貴「Co 系酸化物 $REBaCo_2O_{5-\delta}$の酸素量決定と物性評価」

B100.佐藤清知「含浸成長法による DyBaCuO 系超伝導バルクの作製と超伝導特性」
B101 野村幸靖「ErBaCuO 超伝導バルクの結晶成長と熱伝導率」
B102.松田寛之「$REBaCo_2O_{5-\delta}$の結晶構造と A サイトイオン半径との関係」

(平成 19 年度, 2007 年度)
博士学位論文
D1.藤根陽介「ペロブスカイト型 Co 系酸化物の熱電特性に関する研究」
修士学位論文
M29.石田未央「Pr イオンを含む $RE_{1-X}Ca_XCoO_3$ 系の金属絶縁対転移と格子異常」
M30.日山拓也「パルス磁場印加における超伝導バルク中の磁束の運動と捕捉特性」
卒業論文
B103.小林大地「バルク超伝導体のパルス着磁における発熱現象のシミュレーション」
B104.佐々木寛子「$Pr_{1-X}Ca_XCoO_3$ 系酸化物の金属絶縁体転移と格子異常」
B105.佐々木陽光「ZnO 系及び CuO 系熱電変換材料の創成と特性評価」
B106.三浦　崇「強いピン止め力を有する超伝導バルクに対するパルス着磁特性」
B107.三上真詩子「Ce 置換した $La_{2-X}Sr_XCuO_4$ の超伝導特性」
B108.山口大吾「Pr 置換した YBCO 系超伝導バルクの作製と超伝導特性」

(平成 20 年度, 2008 年度)
修士学位論文
M31.八重樫晃一「超伝導バルク磁石を用いた局所磁場変調に関する基礎的研究」
M32.今野友貴「$La_{2-x-y}Sr_xCe_yCuO_4$ 超伝導体の単結晶成長と Ce 置換効果」
M33.佐藤清知「YBaCuO バルク超伝導体における Y サイトの La, Pr 置換効果」
M34.欠端浩介「超伝導バルクのパルス着磁における磁束捕捉特性の向上に関する研究」
卒業論文
B109.上野康正「RE_2CuO_4 (RE:希土類元素)の作製と熱伝導率に関する研究」
B110.大畑量子「$La_{2-x}Sr_xCuO_4$ 超伝導体の La サイトの Ce 置換効果に関する研究」
B111.加藤元晴「$Pr_{1-X}Ca_XCoO_3$ 系酸化物の熱電変換特性に関する研究」
B112.菊池康晃「YBaCuO バルク超伝導体の結晶成長と Y211 粒子の微細化に関する研究」
B113.平井尚子「$La_{2-X}Sr_XCoO_4$ 系酸化物の作製と物性評価に関する研究」
B114.古澤　允「バルク超伝導体の着磁方法の違いによる捕捉磁場特性に関する研究」
B115.古田大樹「パルス着磁における超伝導バルク内部の温度測定に関する研究」

(平成 21 年度, 2009 年度)
修士学位論文
M35.佐々木寛子「$Pr_{1-x}Ca_xCoO_3$ 系の金属絶縁体転移とスピン状態転移の共存」
M36.三浦　崇「パルス磁場印加における超伝導バルク内部の磁束運動と捕捉磁場分布」
M37.山口大吾「RE_2CuO_4（RE：希土類金属）単結晶の育成と熱伝導特性」
M38.松田寛之「$LaCoO_3$ 系酸化物のスピン転移とフォノン散乱」
卒業論文
B116.荒屋敷貴大「スライスした超伝導バルクのパルス着磁特性と厚さ方向の捕捉磁場分布」
B117.小川　悟「$(Pr_{1-y}Y_y)_{1-x}Ca_xCoO_3$ 系の金属絶縁体・スピン状態転移」
B118.小山　允「2 段に重ねた超伝導バルクのパルス着磁特性」
B119.袖平智樹「$La_{2-x}AE_xCoO_4$ (AE=Ba, Ca)の作製と物性評価」
B120.高橋　良「La214 系超伝導体の La サイトの Ce, Tb 置換効果」
B121.半田拓也「マグネトスキャン法による臨界電流密度分布測定について」

(平成 22 年度, 2010 年度)

修士学位論文

M39.上野康正「$La_{2-x}Sr_xCuO_4$ 系超伝導体単結晶の育成と渦糸系相転移」

M40.加藤元晴「$A_{n+1}Co_nO_{3n+1}$ 系酸化物（n=1, 2, ∞）の次元性と熱電変換特性」

M41.菊池康晃「DyBaCuO 系超電導バルクの作製と Dy サイトの元素置換効果」

M42.古田大樹「超電導バルクのパルス着磁特性と臨界電流密度分布の相関」

卒業論文

B122.楳原久美子「$RE_{1-x}Ca_xCoO_3$ (x>0.5)の単相合成に関する研究」

B123.佐々木智久「大型 MgB_2 超電導体バルクの作製と捕捉磁場特性」

B124.関口哉太「$CaTiO_3$ 系熱電変換材料の作製と物性評価」

B125.玉田裕士「異なる J_c 分布を有する超電導バルクのパルス着磁特性」

B126.古森健太「Pr イオンを含まない $RE_{0.7}Ca_{0.3}CoO_3$ 系における金属絶縁体転移現象の探索」

B127.吉田直樹「熱電変換材料 $RE_{1-x}Sr_xCoO_3$ (X=0.5, 0.75)の作製と物性評価」

(平成 23 年度, 2011 年度)

修士学位論文

M43.荒屋敷貴大「超電導バルクの着磁における臨界電流密度の不均一が及ぼす磁束運動と捕捉磁場」

M44.小川　悟「Pr-Ca-Co-O 系酸化物の金属絶縁体転移における Pr イオンの価数シフト」

M45.高橋　良「$(Sm_{2-x}RE_x)CuO_4$ (RE=La, Nd)単結晶の熱伝導率におけるマグノンピーク」

卒業論文

B128.氏家　徹「酸化物超伝導体 Bi2201 単結晶の育成と超伝導特性」

B129.武田大輝「マグネトロンスパッタ法による Pr-Ca-Co-O 系薄膜の作製と物性評価」

B130.田村拓也「四角形状を有する超電導バルクの着磁特性」

B131.寺本惇一「有機半導体薄膜熱電材料の作製と熱電特性評価」

B132.松田英司「$In_{2-x}Ge_xO_3$ の熱電特性」

B133.渡辺卓真「$RE(Co_{1-y}M_y)O_3$ ((RE=Gd, Sm, M=Ni, Fe)の熱電特性」

(平成 24 年度, 2012 年度)

修士学位論文

M46.小山　允「超電導バルクのパルス着磁における磁束運動・温度変化シミュレーション」

M47.佐々木智久「大型 MgB_2 超電導バルクの実現と強磁場捕捉特性に関する研究」

M48.関口哉太「n 型 ZnO 系熱電変換材料の Zn サイト置換効果と熱電特性向上に関する研究」

M49.古森健太「n 型 In_2O_3 系及び $CaMnO_3$ 系熱電材料の高密度化と熱電特性向上に関する研究」

M50.吉田直樹「$Cu_{1-x}Li_xO$ 系熱電変換材料の高性能化に関する研究」

M51.半田拓也「Generic seed を用いた超電導バルクの結晶成長」

卒業論文

B134.阿部凛太郎「n 型 $RECoO_3$ 系熱電材料の探索に関する研究」

B135.佐藤史子「熱電モジュールの発電性能と耐久性に関する研究」

B136.細川潤基「FCM 法による GdBCO 系超電導バルクの捕捉磁場特性」

B137.吉田卓史「大型 MgB_2 バルクの作製と捕捉磁場特性に関する研究」　0

(平成 25 年度, 2013 年度)

修士学位論文

M52.氏家　徹「MgB_2 超電導バルクのパルス着磁特性に関する研究」

M53.武田大輝「(Pr,RE)-Ca-Co-O 系酸化物における(Pr,RE)イオンの価数シフトに関する研究」

M54.田村拓也「REBaCuO 系超電導バルクのパルス着磁シミュレーションに関する研究」

M55.渡辺卓真「不定比酸化物 TiO_x の作製と熱電特性に関する研究」

卒業論文

B138.大井絵里子「ストレインゲージ法を用いた超電導線材の熱収縮測定に関する研究」
B139.石戸谷　和「REBaCuO 系超電導バルクの磁場中冷却着磁に関する研究」
B140.貫洞翔太「FZ 法による Bi2223 系超伝導体の単結晶育成に関する研究」
B141.佐々木みなみ「MgB_2超電導バルクの捕捉磁場特性に対する不純物置換効果」
B142.高橋祥平「$CoSb_3$系スクッテルダイト化合物の作製と熱電特性に関する研究」
B143.野田裕介「Pr-Ca-Co-O 系酸化物の Pr サイト置換効果に関する研究」
B144.水野　州「A_xCoO_2系酸化物(A=Li, Na, K)の合成と熱電変換特性」
B145.望月豪彦「高性能 MgB_2超電導バルクのパルス着磁特性に関する研究」
B146.遠藤友理「SPS 法による MgB_2バルクの作製と捕捉磁場特性に関する研究」

(平成 26 年度, 2014 年度)

修士学位論文

M56.阿部凜太郎「In_2O_3-SnO_2系熱電変換材料の高性能化に関する研究」
M57.吉田卓史「Ti 添加 MgB_2超電導バルク磁石の高性能化」

卒業論文

B147.Amirah Binti Che Amat "Characteristics of MgB_2 superconducting bulks fabricated by spark plasma sintering"
B148.稲垣絵梨子「パルスレーザ蒸着法を用いた REBCO 系薄膜(RE=Nd, Sm)の作製と評価」
B149.荻野　新「Infiltration 法を用いた MgB_2超電導バルクの作製と超電導特性」
B150.佐々木一真「Nb-doped $SrTiO_3$の作製と熱電特性の評価」
B151.相馬史弥「円柱状超電導バルクにおけるパルス着磁と磁束侵入挙動に関する研究」
B152.原　貴充「ミスフィット型 $Ca_3Co_4O_9$系化合物の作製と熱電変換特性の向上」
B153.高杉　弥「TSMG 法による YBaCuO 超電導バルクの作製と評価」

(平成 27 年度, 2015 年度)

修士学位論文

M58.遠藤友理「スパークプラズマ焼結法で作製した MgB_2超電導バルクの捕捉磁場特性」
M59.野田裕介「パルスレーザ蒸着法より作製した$(Pr_{1-y}Y_y)_{1-x}Ca_xCoO_3$単結晶薄膜の作製と金属絶縁体転移」
M60.水野　州「BiCuSeO 系材料の熱電変換特性に及ぼすキャリアドープとボールミル効果」
M61.望月豪彦「MgB_2及び REBaCuO 超電導バルクのパルス着磁特性とシミュレーション解析」

卒業論文

B154.阿久澤慶太「MgB_2超電導体へのカーボンドープ効果」
B155.石澤　衛「Sr 置換した BiCuSeO 系材料の熱電変換特性とボールミル効果」
B156.高橋圭太「ソレノイド型とスプリット型コイルを用いた超電導バルクのパルス着磁とシミュレーション」
B157.高橋裕平「MgB_2超電導体の Mg サイトへのチタン族元素置換効果」
B158.高橋勇矢「GdBaCuO 超電導バルクの結晶成長と捕捉磁場特性」
B159.滝村　武「SnSe 系熱電変換材料における Sn サイトへの Cu 置換効果」
B160.照井　茜「MOD 法による $RENiO_3$系薄膜の作製と金属絶縁体転移」
B161.仲保雄平「MOD 法による $RECoO_3$系薄膜の作製と物性評価」

(平成 28 年度, 2016 年度)

修士学位論文

M62.稲垣絵梨子「バッファー層及び薄膜種結晶を用いた YBaCuO 超電導バルクの結晶成長」
M63.荻野　新「Infiltration Growth 法による MgB_2バルクの作製と浸透現象」
M64.佐々木一真「高温における熱電変換薄膜評価装置の構築と信頼性の評価」

M65.原　貴充「SnSe エピタキシャル薄膜作製の最適化と特性評価」

卒業論文

B162.赤石和典「(Y, Dy)BaCuO 超電導バルクの育成と捕捉磁場特性」
B163.叶　千学「$Pr_{1-x}Sr_xFeO_3$ の作製と熱電変換特性評価」
B164.熊谷　毬「MgB_2 バルクの捕捉磁場特性に対する Ge 添加効果」
B165.笹原隆太「SnSe の熱電特性に及ぼすボールミル効果」
B166.下屋敷郁陽「波形制御されたパルス磁場を印加した超電導バルクの捕捉磁場特性に関する研究」
B167.富樫遥太「非晶質ボロンを用いた浸透法による MgB_2 の作製と臨界電流特性」
B168.安里祐輝「BiCuSeO 化合物中の Se 欠損が熱電変換特性に及ぼす影響」

(平成 29 年度, 2017 年度)

修士学位論文

M66.阿久澤慶太「$(Pr,Ca)CoO_3$ 系試料の Co サイト置換や酸素欠損が金属絶縁体・スピン状態転移へ及ぼす影響」
M67.石澤　衛「PLD 法で作製した $Bi_{1-x}Sr_xCuSeO$ 系単結晶薄膜の結晶配向及び結晶性と熱電特性評価」
M68.高橋圭太「超電導バルクの着磁現象とその応用に関する研究」
M69.高橋裕平「高充填率 MgB_2 超電導バルクの作製と磁束ピン止め特性」
M70.高橋勇矢「複数の希土類元素を含む高温超電導バルク結晶の成長と超電導特性」

卒業論文

B169.佐々木駿一「BiCu(Te, Se)O の作製と熱電特性」
B170.澤田渓人「(Y, Gd)-Ba-Cu-O 超電導バルクの結晶成長と超電導特性」
B171.当摩悠希「SPS 法で作製した MgB_2 超電導バルクの捕捉磁場特性と粒間結合性の相関」
B172.永山正彦「$Bi_2Te_{3-x}Sb_x$ 熱電材料の SPS 法による作製の最適化と熱電特性」
B173.難波　空「超電導バルクの磁場中冷却着磁における電磁界・温度・応力の連成解析」
B174.平野達也「スプリットコイルを用いた超電導バルクのパルス着磁特性」

(平成 30 年度, 2018 年度)

修士学位論文

M71.叶　千学「$RE_{1-x}Sr_xFeO_3$ (RE:希土類元素)における金属-絶縁体転移」
M72.笹原隆太「p 型及び n 型 BiSb 系材料の熱電変換特性に関する研究」
M73.下屋敷郁陽「REBaCuO 系超電導ディスクバルクのパルス着磁における電磁界・温度・応力特性」

卒業論文

B175.青木亮汰「歪みゲージを用いた様々な材料の低温熱収縮測定」
B176.天瀬洸太「KFe_2Se_2 バルク体の作製と超伝導特性」
B177.伊藤直広「BiCuSeO の熱電特性に対する Ce 添加効果」
B178.鎌田大空「TSIG 法で作製した YBaCuO 系超伝導バルクのパルス着磁特性 」
B179.駒本康平「Nb_3Sn バルク体の作製と超伝導特性」
B180.近藤茜音「$PrBaFe_2O_5$ の固体燃料電池電極としての可能性評価」

(令和元年度, 2019 年度)

修士学位論文

M74.佐々木駿一「BiCuSeO の熱電特性に対する窒素置換効果」
M75.澤田渓人「FeSe 系超伝導バルク体の作製と超伝導特性」
M76.難波　空「ハイブリッド型超電導バルク磁石レンズ(HTFML)の実現と高性能化に関する研究」
M77.平野達也「超電導バルクのパルス着磁における磁束ダイナミックスに関する研究」

卒業論文

B181.千葉誠治「超伝導バルク磁石と励磁用超伝導電磁石との磁気カップリング現象」
B182.及川広希「Ti ドープした MgB_2 超伝導バルク体の浸透法による作製と捕捉磁場特性」
B183.大久保敬汰「シミュレーションを用いた形状の異なる超電導リングバルクのパルス着磁特性」
B184.小林大地「浸透法による Nb_3Sn 超伝導バルク体の作製と捕捉磁場特性 」
B185.新田基己「ハイブリッド型超電導バルク磁石レンズ(HTFML)のパルス着磁シミュレーション」
B186.菅原直人「Co 置換した $BaFe_2As_2$ 超伝導体の作製と超伝導特性」
B187.望月悠平「ペロブスカイト型 Fe 系酸化物の作製と輸送特性」
B188.本宮大輔「燃焼合成法による BiCuSeO の作製と熱電特性」

(令和 2 年度, 2020 年度)

博士学位論文

D2.高橋圭太「Realization of superconducting bulk magnets with higher magnetic field gradient to provide a quasi-zero gravity space on earth」

修士学位論文

M78.天瀬洸汰「Nb_3Sn および Nb_3Al 超伝導バルク体の作製と着磁特性の研究」
M79.鎌田大空「超電導バルクのパルス着磁におけるコイル形状とヨークの効果」

(令和 3 年度, 2021 年度)

博士学位論文

D3.高橋裕平「コンパクト NMR 装置の実現に向けた MgB_2 超伝導バルク磁石ユニットの開発」

修士学位論文

M80.新田基己「超電導リングバルクのパルス着磁における熱応力破壊の可能性に関する研究」

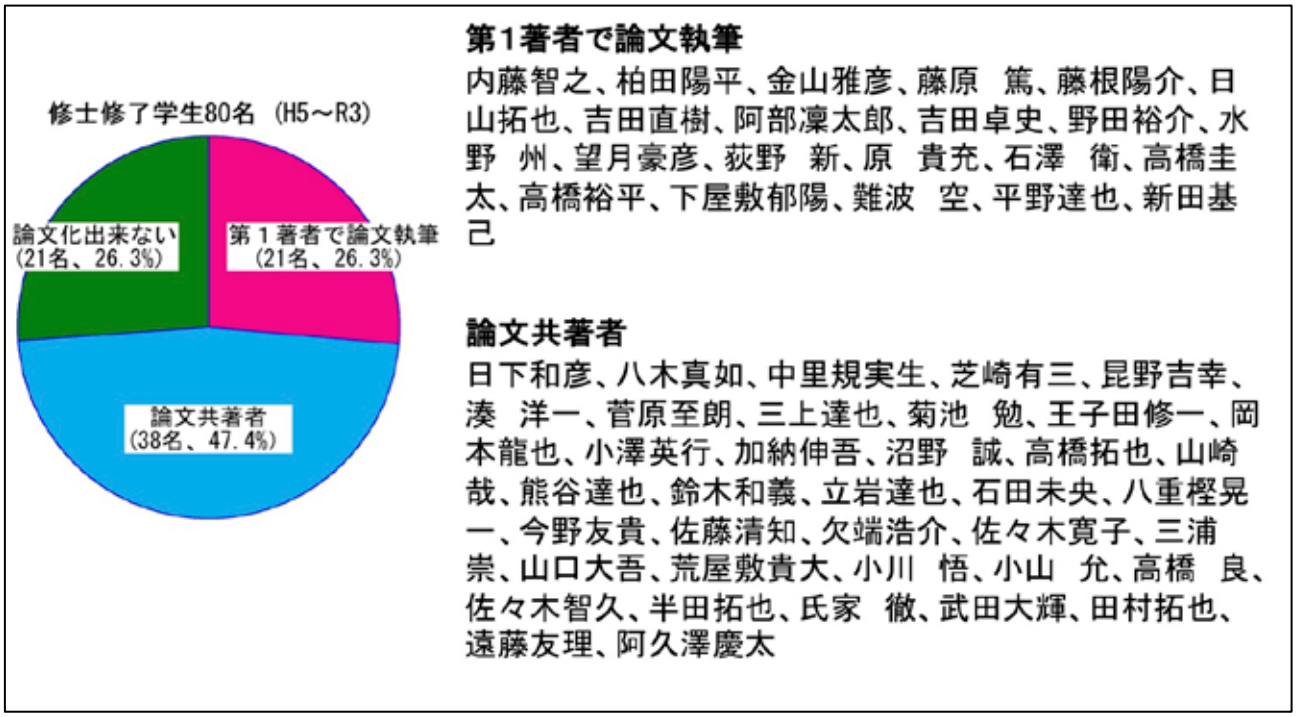

１３．担当した講義

学部

電子工学 (1994~1996)
物理学概論 (1994~1996)
電磁気学 (1996~2003)
電子工学概論 (1997)
電子材料学 II (1998~2000)
半導体材料学 (2001~2006)
電子デバイス工学 (2001~2019)
電磁気学 II (2004~2019)
微分方程式 (2006~2008)
科学技術英語 (2009~2010)
マテリアル工学概論 (2010~2015)
ソフトパス理工学概論 (2016~2019)

大学院

電子計測学特論 (1994~1996)
電子物性工学特論 (1998~2008)
半導体デバイス工学特論 (2009~2019)
機器分析学特論 (2011~2015)
電子機能材料工学特論 (2017~2019)
グローバルキャリアデザイン (2017~2021)

１４．略歴

昭和 32 年(1957 年) 3 月 8 日生まれ（岩手県東磐井郡千厩町（現:一関市千厩町））

昭和 50 年(1975 年) 3 月　岩手県立黒沢尻北高等学校　卒業
昭和 55 年(1980 年) 3 月　東北大学工学部電子工学科　卒業
昭和 55 年(1980 年) 4 月　東北大学大学院工学研究科博士前期課程電子工学専攻　入学
昭和 57 年(1982 年) 3 月　同上　修了
昭和 57 年(1982 年) 4 月　東北大学大学院工学研究科博士後期課程電子工学専攻　入学
昭和 60 年(1985 年) 3 月　同上　修了　工学博士
博士学位論文題目：「蒸気圧制御下における相図の研究」東北大学（工第 987 号）
昭和 60 年(1985 年) 4 月　(財)半導体研究振興会半導体研究所研究員
平成 元年(1989 年) 5 月　九州工業大学助手（情報工学部機械システム工学科）
平成　3 年(1991 年) 8 月　岩手大学助手（工学部電子工学科）
平成　4 年(1992 年) 4 月　岩手大学助手（工学部材料物性工学科）（学科改組による配置換え）
平成　5 年(1993 年)12 月　岩手大学助教授（工学部材料物性工学科）
平成 15 年(2003 年) 7 月　文部科学省短期在外研究員（チェコ科学アカデミー物理学研究所、平成 15 年 9 月まで）
平成 18 年(2006 年) 3 月　岩手大学教授（工学部材料物性工学科）
平成 19 年(2007 年) 4 月　岩手大学工学部材料物性工学科長（平成 20 年 5 月まで）
平成 20 年(2008 年) 6 月　岩手大学教育研究評議員（平成 24 年 3 月まで）
平成 23 年(2011 年) 4 月　岩手大学教授（工学部マテリアル工学科）（学科改組による配置換え）
平成 24 年(2012 年) 4 月　岩手大学地域連携推進センター長（平成 26 年 3 月まで）
平成 26 年(2014 年) 4 月　岩手大学教育研究評議員（平成 31 年 3 月まで）
平成 28 年(2016 年) 4 月　岩手大学教授（理工学部物理材料理工学科マテリアルコース）（学科改組による配置換え）
平成 31 年(2019 年) 3 月　岩手大学教授退職（理事就任のため）
平成 31 年(2019 年) 4 月　岩手大学理事（研究、復興、地域創生担当）・副学長（令和２年３月まで）
令和　2 年(2020 年) 4 月　岩手大学理事（総務、企画、評価、広報担当）・副学長（令和４年３月まで）
令和　4 年(2022 年) 4 月～　岩手大学理事（総務、戦略企画担当）・副学長

主要所属学会：低温工学会（1992~継続）、応用物理学会(1990~2020)、日本物理学会(1989~2020)
主要役職：低温工学協会 東北・北海道支部 支部長(2018~2021)

１５．研究生活の振り返りと謝辞

令和４年３月に 65 歳の定年となる年齢に達し、これまでの研究業績を整理し、自分自身の研究生活を振り返りたいと考え、この研究業績集を取り纏めた。あくまでも自分自身のための記録である。

私の研究人生は、1979 年の東北大学工学部電子工学科の卒論研究室配属で第３希望の西澤潤一教授の研究室に配属された時点がスタートである。当初は修士課程修了後に企業へ就職する予定であったが、次第に研究の面白さが分かってきて、博士課程への進学という他の同級生とは異なる未知の人生を歩むことを決断し、本格的な研究生活へ本格的に入った。博士論文のテーマは、前任者の博士論文内容の再現・検証と新たな展開であったが、再現性が得られなかった。様々な検討の結果、前任者の博士論文の主要な結果は装置誤差（エラー）を新規な信号と見誤っていたことが博士課程３年の春になって明らかになり絶望感に苛まれた。そのため博士論文の内容は、前任者が見誤った原因を明らかにし、非常に大きなエラーを取り除いた後の非常に小さな真の信号を見積もったことでまとめたが、外部投稿論文が１編も無いにも関わらず、博士学位論文として認めて頂いた。西澤教授には学位取得までの６年間と、その後４年間の(財)半導体研究所での研究員生活における化合物半導体デバイス開発の産学連携研究では、いろいろと迷惑をお掛けしたが、研究者の心構えや研究の本質、産学連携の重要性を学ばせて頂いたことに感謝している。

1989 年からの九州工業大学助手としての２年半は、これまで行って来た化合物半導体研究と決別し、酸化物超伝導材料研究に転向した。西澤研究室時代では当たり前だった上から研究テーマ・方針が与えられる環境から、一転して価値ある新しい研究テーマを自分で設定し成果を上げることの難しさを経験し、自立した研究者の在り方を苦しみながら模索する時間であった。

1991 年に 30 代前半で学術論文が４編しかなく、学科内で多くの反対意見があったにもかかわらず、池部　學先生に岩手大学助手として採用して頂き、これまでの経験を生かして腰を据えて教育研究に邁進しようと心に誓った。赴任当初の 30 代中盤から約 15 年間、研究室の全ての研究費を使わせて頂くと同時に、全ての学生のテーマ設定から研究指導までを主体的に行えたという非常に恵まれた経験が、現在まで続く何物にも代えがたい財産となった。さらに、競争的外部資金を獲得し研究業績を必ず学術論文や国際会議で発表するという大学研究者としての基本姿勢を学ぶことが出来た。改めて池部先生には感謝申し上げる。

2006 年に教授に昇進し研究室を主宰することになり、池部研究室の２期生である内藤智之君を助手に採用し、２人で教育・研究を推進してきた。研究室の方針は「自分で試料を作製し、自分で評価する」こととし、超電導体材料と熱電変換材料の研究を推進した。その中で、研究を通しての学生の成長と、「これは面白い」と思える研究にいくつか出会い、成果を発表することができた事は非常に幸せであった。50 歳位までは主に物理学会に参加し基礎知識や先端研究の状況を学び、自分では結晶成長や試料作製・評価と物性関係の「実験だけ」で研究を進めてきたが、物性物理の分野での研究推進に自分の知識・能力に関する行き詰まり感があった。2003 年頃から超電導バルクの着磁研究という応用物理学分野の実験を新たに始め、2010 年頃からは着磁シミュレーションを開始した。当初、着磁シミュレーションは実験結果の再現・確認が目的だったが、次第にシミュレーションによって実験を予測し、その後に実験で検証するという本来のシミュレーションの利点を発揮できるようになった。その結果として実現したハイブリッド型超電導バルク磁石の研究や超電導バルクの機械的補強の研究は、まさにシミュレーションと実験の融合で生まれた研究成果であり、自分の研究スタイルとして”Materials Science and Technology”は性に合っていたと感じる。2003 年のチェコ科学アカデミー物理学研究所への留学と、その後現在に至る Jiri Hejtmanek 博士との共同研究（共著論文 13 編）、更に 2013 年の Cambridge 大学の Mark Ainslie 博士との国際会議での偶然の出会いから始まった超電導バルクでの共同研究（共著論文 37 編）は、国際共同研究の重要性とグローバルスタンダードな研究スタイルを学び、実践する重要な経験となった。

1980 年代は実験装置が殆ど全て手作りで、全て手動計測・手動記録の時代で、仙台時代は連日研究室に泊まり込んでの実験が続いたが、その後 1990 年代に入りパソコンが導入され自動計測の時代になり、さらに図書館で文献をコピーしていた時代からインターネットで世界の研究論文が瞬時に入手できる環境になるなど研究環境も大きく変化した。また、1980 年代は産学官連携がまだ一般的では無い時代で、大学と企業の共同研究は「大学教員の魂を売るのか？」という反発が多く、産学官連携を行う教員

は肩身が狭かった時代だったと西澤教授からいつも聞かされていた。それから 40 年経過した現在、産学官連携を行わない大学教員は「社会の役に立っているか？」と肩身が狭くなるという 180 度の大転換を実感として経験してきた。大学における「研究の自由」は当然守らなければならないが、社会との連携の上に大学が存在するという今の常識は、そんなに昔から存在したのでは無いと自分の経験から感じる。しかし研究の本質は、研究者の知的興味、経験や勘による推進が第一で有り、現在でも、更に将来もその本質は変化しないと確信している。一方で、経験の積み重ねは重要だが、逆に経験の無さを長所に考え、詳細な文献調査や綿密な研究計画と自由な発想で研究を進めることも更に重要と考える。その意味で今後の若い研究者の斬新な発想と積極的な行動力に期待したい。

大学運営では、2008 年から教育研究評議員を、2019 年から理事・副学長を務め、運営に深く関わってきたが、大学組織全体としての教育・研究の質の向上の重要性を改めて感じてきた。特に大学における「研究の自由」の基本理念を尊重するとともに、国立大学教員としての恵まれた環境の中で、質の高い研究成果の継続的な発信と教育への還元という義務・責任を全教員が認識する必要性を強く感じている。引き続き 2024 年まで理事・副学長を務めるが、岩手大学の教職員、学生が同じ方向に向かって更に活躍できる環境の整備や組織・教育プログラムの改編に取り組みたい。

岩手大学に赴任した 1991 年から約 32 年間に、池部研究室の時代から数えて、卒論学生 188 名、修論学生 80 名、博士論文学生 3 名（藤根陽介君、高橋圭太君、高橋裕平君）を育て、学術論文を 291 編（その内、first author として 106 編、corresponding author として 51 編）を出版できたことは大きな誇りである。それぞれの学術論文には深い思い入れがあり、一緒に苦労して研究した学生達の顔が思い出される。各学術論文の出版は、「公共財」としてその時代のその研究分野での新規性を主張する内容が含まれ、それが査読で評価され公表された結果だったと確信している。学術論文掲載決定と競争的外部資金獲得決定の知らせが届いたときは、努力が評価されたという精神的な充実感や満足感を味わい、乾杯をし、それが次への活力に繋がったことは事実である。様々な企業等との共同研究、受託研究を実施したが、他では実現出来ない研究シーズ、例えば、熱伝導率測定や着磁シミュレーションなどがあったことが相手から信頼された結果として実施され成果が創出されたと考えている。2021 年に内藤君が教授に昇任し、今後も私と一緒に培った研究マインドを受け継いでくれると思う。今後の活躍を期待したい。

これまでの研究人生を振り返ると、20 代で学術論文が書けなかった悔しさからハングリー精神を持って誰よりも論文公表にこだわった事、30 代前半で仙台を離れてから新しい超電導研究の分野に飛び込んだ事、そして 30 代中盤に岩手大に赴任してからパーマネントの安定した職を得て、（今よりは）潤沢な講座費を自由に使って、思う存分自由な研究を出来たことが自分の研究生活にとって非常に重要な要素だったと感じている。また、これまで大学教員として教育研究に携わって来られたのは、様々な関係者、協力者があっての事である。今後は自分の研究経験を失敗談も含めて若い世代に伝え、励まし、支援する役目があると考えている。西澤研究室での卒論研究で始まった約 40 年の私の研究者人生は非常に充実していたと感じている。関係者、協力者の皆様に感謝申し上げる。

令和 4 年(2022 年)　3 月

藤代　博之

A: 最終講義予定スライド

教育と研究の醍醐味

藤代博之

1

経歴

1980年　東北大学工学部電子工学科卒　23歳
1985年　博士課程修了（GaAs半導体の物性研究）28歳

1985~1989年　財団法人の研究員（GaAS半導体デバイスの開発研究）　28歳

1989~1991年　九州工業大学助手（Si半導体、超電導材料の研究）　32歳

1991年　岩手大学工学部電子工学科助手　34歳
・超電導材料の作製と評価（主に物理的内容）

1993年　岩手大学工学部材料物性工学科助教授　37歳
・超電導材料の作製と評価（物理的＋応用物理的内容）
・熱電変換材料の作製と評価（応用物理的内容）

2006年　岩手大学工学部材料物性工学科（現在のマテリアルコース）教授 49歳
・超電導バルク材の強磁場捕捉に関する研究（実験とシミュレーション）
・新規熱電変換材料の創製
2013~2014年　地域連携推進センター長

2019年　理事（研究・復興・地域創生担当）・副学長　63歳
2020年　理事（総務・企画・評価・広報担当）・副学長　64歳

2

1980年　2000年　2022年　2050年
（約40年前）　（現在）　（約30年後）
電力消費は現在の半分
高度経済成長　バブル崩壊　低成長時代　デフレ　国際競争力低下
・超電導リニア新幹線2027
・新幹線（大宮ー盛岡）1982　・函館延伸2016
・東北自動車道（盛岡以南）1978
・カラーテレビ（ブラウン管）・・・・・・・・液晶、プラズマ・・・・・　有機EL-->
・ラジカセ・・・・・・・・・・CD/DVDプレーヤー・・・・ ブルーレイ・・・・・->
・ LPレコード　　CD/DVD　　Web配信 --->
・　パソコン普及1985(FD)・・・・・・・・HDD・・・・半導体メモリ(SD) -->
　　インターネットの普及 -->
・　ポケベル・・・・ケータイ1995・・・・・・・・スマートフォン --> 5G, 6G高速通信
・スパイクタイヤー＞スタッドレスタイヤ　　ハイブリッドカー　　電気自動車(EV)-->
？？？
・　青色LEDの実現1990 ー＞白色LED−＞2014ノーベル物理学賞
・1911低温超伝導体ーー＞1987高温超伝導体

3

1980年　学部卒（工学部電子工学科）23歳
1985年　博士課程修了（GaAs半導体の物性研究）28歳
1985~1989年　財団法人の研究員（GaAS半導体デバイスの開発研究）　28歳
学生（卒論、修論、博論6年間 1979-1985）＋半導体研究振興会研究員（4年間 1985-1989）

西澤潤一教授

・産学連携
当時の常識
大学教員が企業と連携することは稀
（魂を売るのか？）

向き不向き
・デバイス系（システム系）は向かない
・物性系が性に合っている

4

博士論文題目：「蒸気圧制御下における相図の研究」

ギブスの相律に間違いがある！

系の自由度(F)を規定する式　***F=C-P+2***　でCは成分の数、Pは相の数

Ga-Asの2元系
Ga溶液中に存在するAsが未飽和状態では、C=2、（GaとAs), P=2（気相と液相）であるから、F=2-2+2=2で温度の他にAs蒸気圧で溶解量が変化しても良い。
しかし、飽和溶解度以上にAsが存在すると固相が存在する。P=3(気相、液相、固相）でF=2-3+2=1となり、温度が決まれば溶解量はAs蒸気圧に無関係に決定される。

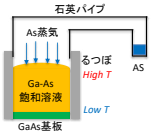

しかし、As蒸気圧制御したGaAS結晶成長の結果は、飽和領域でAs蒸気圧により成長した結晶の化学量論的組成が制御出来る。

飽和領域でも溶解量がAs蒸気圧で変化しているのでは無いかという実験結果が出されていた。

・たとえ固相(GaAs)が存在していても、印加As蒸気圧により液相中のAs濃度が変化していることを実験的に明らかにする（ギブスの相律に修正が必要）。

5

熱天秤法（温調器以外は自作）
・前任者（ドクター修了）の仕事を4年生の卒論で引き継ぐ

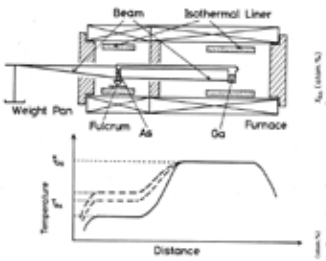

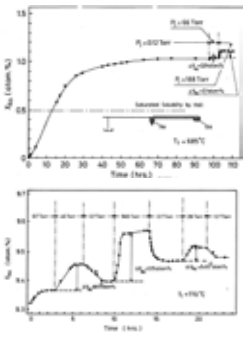

・あるときは前任者と同じようなデータ、あるときは再現されない
4年生から博士2年まで、「やり方が悪い」、「出来るはず」と言われ続ける。

6

何故出来ないのか？前任者の実験に間違いは無いのか？を博士2年から追試を始める
・博士3年の春に、信号ではなくエラー（主に、温度変化による石英の膨張・収縮とクリープ）を測っていたことを突き止める。
教授に前任者のデータはエラーを信号として発表していたと報告

・自分の青春の５年間は何だったのか？

・それから半年、エラーの中に僅かな信号が存在する可能性を明らかにし博士論文にまとめる。

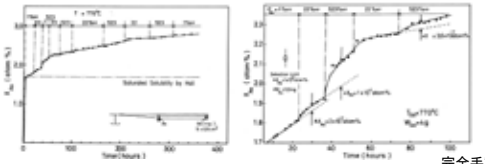

・学会発表ゼロ、学術論文ゼロで学位を頂く。

完全手動測定
（泊まり込み）

・学んだこと
・大学教員は辛抱強くなくてはならない（学生の教育に成果を過度に追い求めるな！）
・独創的な研究は成果が出にくいが、大学が行うべきこと。
・しかし、研究で生きて行くには、論文を書かなければ生き残れない。

7

1989~1991年　九州工業大学助手（Si半導体、超電導材料の研究）　32歳
・仙台時代の研究は行わないと決心。
・1987年に酸化物超電導体が発見・・・新たなテーマに挑戦

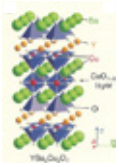

1991年　岩手大学工学部電子工学科助手　34歳
・採用時の論文数　4編・・・・公募なら不採用確実の論文数
　・超電導材料の作製と評価（主に物理的内容）・・・池部教授、能登教授
　・とにかく、論文を書く。
　・外部資金申請書を書く
　・国際会議で発表する

1993年　岩手大学工学部材料物性工学科助教授　37歳
（当時の論文数は約１５報）
・超電導材料の作製と評価（物理的＋応用物理的内容）
・熱伝導率
・熱拡散率

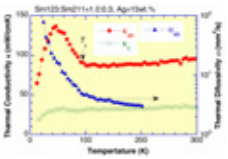

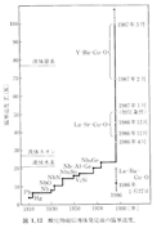

8

ペロブスカイト型Mn, Co酸化物の熱物性 (1998頃から)
・酸化物超電導体からMn酸化物、Co酸化物へ（多くの研究者のトレンド）

立方ペロブスカイト型酸化物: ABO_3
・Aサイト（希土類元素RE(La, Pr・・・・)、アルカリ土類金属AE(Ca, Sr, Ba・・・・)）
・Bサイト（遷移金属(Cu, Fe, Co, Ni, Mn・・・・）

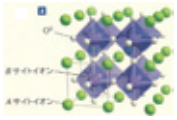

様々なイオンを広範囲に固溶することが出来る
ーーー＞様々な物性が出現

（例）$LaMnO_3$
3価のLaサイトの一部(x)を2価のアルカリ土類金属イオン(Ca^{2+}, Sr^{2+}, Ba^{2+})で置換する
$(La_{1-x}Ca_x)MnO_3$

3価のMnイオンのうち、xだけ4価のMnイオンになる・・・キャリアの導入

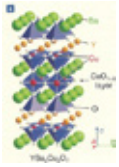

置換効果：Bイオンの価数変化、磁性の導入、イオン半径の変化、
結晶のひずみ
　・絶縁体->金属->（超伝導体）
　・反磁性体->常磁性体->強磁性体

銅酸化物超伝導体$YBa_2Cu_3O_7$もABO_3の類縁物質

9

2000 京都での国際会議・・・・・・・チェコの研究者J. Hejtmanek博士との出会い
チェコ科学アカデミー物理学研究所（プラハ）での留学生活(2003.7~9) 46歳

Dr. J. Hejtmanek, Dr. Z. Jirak

・これまで、2002年から通算7回訪問し、共同研究を継続
・文部科学省在外研究員でプラハに2ヶ月滞在
・研究所は殆どはチェコ人、他にドイツ、フランス、イタリアから多数の研究者が滞在
・共著で１５編の論文を執筆
・同じ問題意識を持った研究者を見つける。
・お互い母国語でない英語での議論やメールのやり取りは役に立つ。

10

10

岩手県地域結集型共同研究事業(1999~2004)　文部省補助事業
「生活・地域への磁気活用技術の開発」

多くの工学部教員が参画（能登、吉澤、片桐、森（邦）、小川、吉本、小林（宏）、大坊・・・）
・バルク超電導体の熱物性測定装置の開発、熱物性データベースの構築を担当

バルク超伝導体とは？
$REBa_2Cu_3O_x$（RE:Y, Sm, Gd など)+RE2BaCuO5の擬似単結晶
・約90K（−180℃）で超電導特性（電気抵抗0）を示す。
・冷却には液体窒素(77K)や冷凍機(～10K)を使用
・直径80mm程度の大型バルクの製作可能
・永久磁石の30～50倍強いバルク磁石(17T)が実現可能

浮上効果

電気抵抗ゼロ

磁場の捕捉（擬似永久磁石）

11

・バルク超電導体の熱物性測定装置の開発、データベースの構築

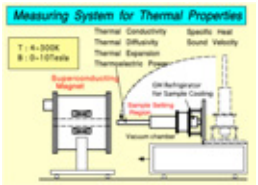

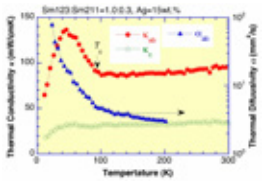

試料周辺の概略図

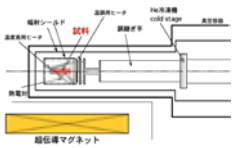

12

・パルス着磁法(PFM)との出会い(2003)

学会のポスター発表で見たシミュレーション結果がおかしいと感じ、実験で確認したいと考える。

発熱が数秒で回復する？なんて間違いだ！

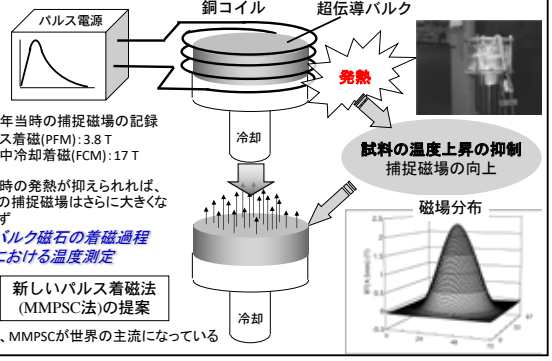

2003年当時の捕捉磁場の記録
パルス着磁(PFM)：3.8 T
磁場中冷却着磁(FCM)：17 T

着磁時の発熱が抑えられれば、PFMの捕捉磁場はさらに大きくなるはず

バルク磁石の着磁過程における温度測定

新しいパルス着磁法(MMPSC法)の提案

現在、MMPSCが世界の主流になっている

13

複数磁場パルスの印加・・・・温度上昇の低減と捕捉磁場の向上

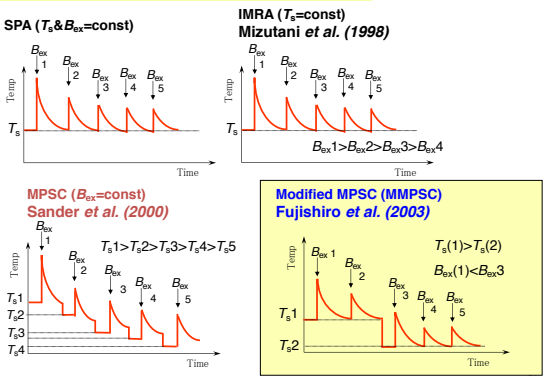

14

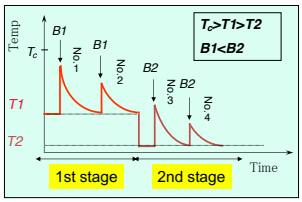

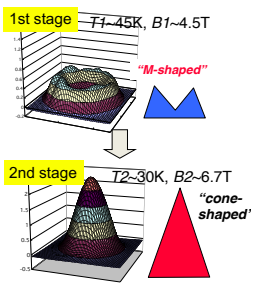

B_T=5.2 T by MMPSC (2004) M2立岩君
on GdBaCuO bulk (46mm)
PFM法による世界最高磁場の実現
（現在も破られていない）

これは面白い！

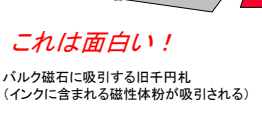

バルク磁石に吸引する旧千円札
（インクに含まれる磁性体粉が吸引される）

15

2005年8月28日
岩手日報朝刊1面掲載

パルス着磁で5 Tの捕捉を実現

16

モーゼ効果のデモ

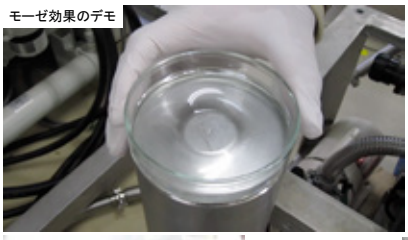

B_z=5.3T

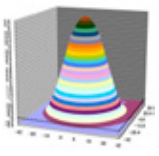

Si基板上の有機半導体溶液

レンツの法則

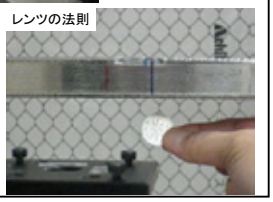

17

モーゼの海割れ

旧約聖書「出エジプト記」には、旧約聖書の中の一部で、エジプトで奴隷として虐げられていたユダヤ人を、モーセが率いて脱出する、という物語がある。

逃げ出した奴隷たちを連れ戻すべく王の軍が追いかけてくるが、奇跡が起こって海が割れ、モーセと一行は向こう岸へたどり着く。しかし、あとを追ってきた軍隊は、海が元に戻って呑み込まれてしまう。こうして、モーセたちは無事エジプトを出ることが出来た。

18

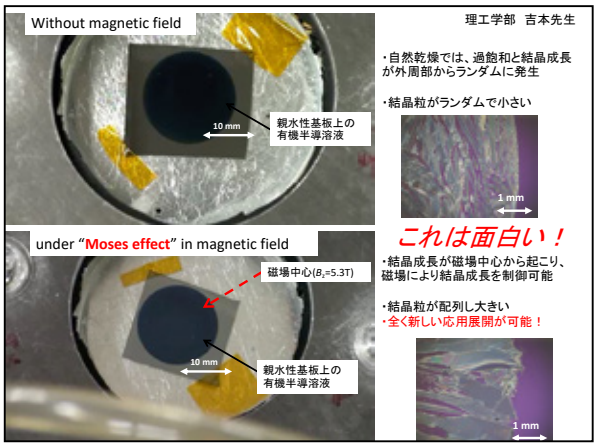

理工学部　吉本先生

・自然乾燥では、過飽和と結晶成長が外周部からランダムに発生

・結晶粒がランダムで小さい

これは面白い！

・結晶成長が磁場中心から起こり、磁場により結晶成長を制御可能

・結晶粒が配列し大きい
・全く新しい応用展開が可能！

19

Record-high trapped field using FCM and PFM

	Field cooled magnetization (FCM)	Pulsed field magnetization (PFM)
REBaCuO bulk	17.24 T (ISTEC) 17.6 T (Cambridge) 15.1 T (Iwate)	5.2 T (Iwate) on surface 5.3 T (Cambridge) in bulk pair
MgB_2 bulk	5.4 T (IFW Dresden) on surface 5.6 T (Iwate) in bulk pair	1.61 T (Iwate) on composite surface 1.1 T (Iwate) on surface

超伝導バルクのパルス着磁の分野では、岩手大が世界をリードしている。

今後（近い将来）、岩手大学が、FCMによりREBaCuOバルクで20 Tを越える捕捉磁場（世界最高捕捉磁場）を実現することを期待！
・機械的補強の設計が完了
・割れるか割れないか、あとは運

20

2006年　岩手大学工学部材料物性工学科（現在のマテリアルコース）教授 49歳

・様々な材料の熱伝導率測定（企業との共同研究）
・Co系酸化物の特異な転移現象
・超電導バルク材の強磁場捕捉に関する研究（実験とシミュレーション）
・新規熱電変換材料の創製

研究室の方針

・自分で試料を作製し、自分で測定する。

・1人1テーマ（自分で動かなければ、データが出ない）

・M1までは伴走、M2は自分で主体的な研究を奨励

・大学院生は第1著者で論文を書く（まずは英語らしい日本語で）

21

$(Pr_{1-y}RE_y)_{1-x}Ca_xCoO_3$の特異な転移現象とPrの価数

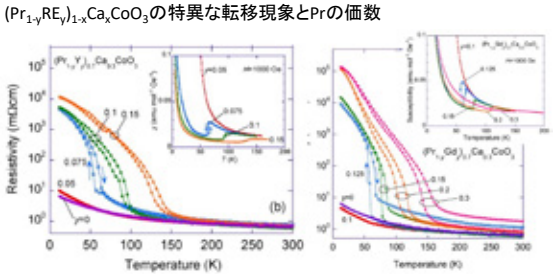

・非常に大きなシャープな金属・絶縁体転移（常磁性・反強磁性転移）・・・一次相転移
・Pr, Ca系だけで起こる
・組成x, yのある範囲内だけで起こる
・2010年当時、理由が不明
・興味を持っている研究者が少ない（チャンス！）

これは面白い！

・系統的にRE, x, yを変化させた試料を作製し、転移現象を追求！

22

チェコとの共同研究・・・・比熱測定、中性子回折等を依頼

比熱測定結果から推定したPrイオンの価数シフトとCoイオンの価数分配は

$(Pr^{3+}_{0.85}Y^{3+}_{0.15})_{0.7}Ca^{2+}_{0.3}Co^{3+}_{0.7}Co^{4+}_{0.3}O^{2-}_3$　　($T>>T_{MI}$)

$(Pr^{3+}_{0.59}Pr^{4+}_{0.26}Y^{3+}_{0.15})_{0.7}Ca^{2+}_{0.3}Co^{3+}_{0.88}Co^{4+}_{0.12}O^{2-}_3$　　($T<<T_{MI}$)

y=0.075　$Pr^{3.17+}$
y=0.15　$Pr^{3.29+}$

電荷中性が成り立つためには、
価数変化（価数揺動）が起こっているのでは無いか？

・X線吸収スペクトル(XAS)により、Prイオン価数のシフトを直接的に観測する。

・Prイオン価数のシフトと同時に起こることが予想されるCoイオン価数の変化を、XASにより実験的に測定する。

Spring-8での実験 (2011~2016)
・2010吉本先生に相談->Spring-8の研究者を紹介される->申請し採択される

2011.3.11東日本大震災

・2010にスペインの研究者がすでにXASの実験結果を発表していた（知らなかった）。

23

Valence Shift of Pr Ion from 3+ to 4+ in $(Pr_{1-y}Y_y)_{0.7}Ca_{0.3}CoO_3$
Estimated by X-Ray Absorption Spectroscopy

JPSJ 81 (2012) 064709

XANES (Pr *L*3 吸収端)　測定　at Spring-8

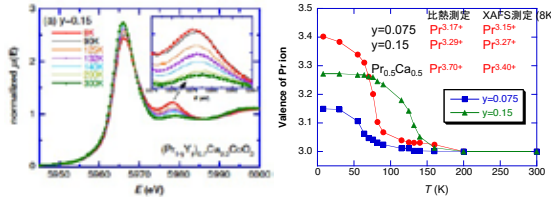

・温度低下と共に、$Pr^{4+}(4f^1)$ピークが増大し、$Pr^{3+}(4f^2)$ピークが減少する。（Prの価数シフトは起こっている）
・T_{MI}よりかなり高温から価数の変化が起こっている。

24

これまでのPYCCO研究は多結晶を用いた研究

物性研究・・・単結晶を用いた測定が必須

PYCCO単結晶育成に挑戦・・・・出来ない！！

薄膜単結晶におけるMISS転移現象

・Y. Noda, H. Fujishiro, T. Naito, A. Ito, T.Goto, J. Hejtmanek and Z. Jirak
AIP Advances **6** 025318 (2016)

・H. Fujishiro, Y. Noda, K. Akuzawa, T. Naito, A. Ito, T. Goto, M. Marysko, Z. Jirak, J. Hejtmanek and K. Nitta
J. Appl. Phys. **121** 115104 (2017)

・基板とのミスフィットによる圧力効果で転移温度は変化するか？
・多結晶と単結晶の中間的な結果を期待

これは面白い！

25

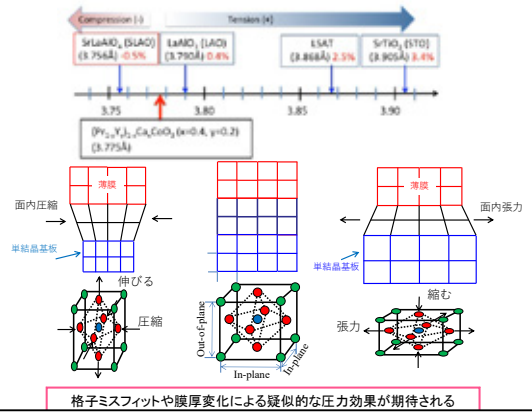

格子ミスフィットや膜厚変化による疑似的な圧力効果が期待される

26

基板依存性 $(Pr_{0.8}Y_{0.2})_{0.6}Ca_{0.4}CoO_3$

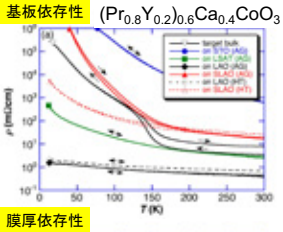

・大きなhysteresisを伴う異常なupturnが$SrLaAlO_4$ (SLAO)基板上（in-plane compressive stress）のみで確認される。

・アニールをすると異常が消失

・電気抵抗率の絶対値は、lattice mismatchの増加とともに増大する。

膜厚依存性

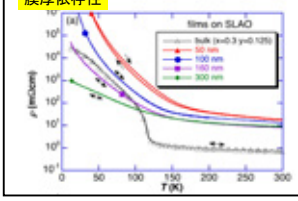

・電気抵抗率の異常は50 nm厚の薄膜のみで観測され、100 nm以上では認められない。

27

パルス着磁のシミュレーション（2010～）

・実験だけでは研究に限界を感じる・・・・実験で確認するには時間がかかる

・シミュレーションのメリット
　・実験結果の解釈
　・実験結果の予測（新たな提案）・・・・・HTFML、HG-TFMの提案に生かされる

2012 応用超電導に関する国際会議(ASC2012 in Portland, USA)
Dr. Mark Ainslieとの出会い
昼食で偶然に出会う。
同じ分野の研究者であることで様々なdiscussion

Dr. Mark Ainslie

2013 Markが初めて盛岡を訪問
2015 藤代がCambridgeを訪問

その後、交互に訪問（2014~2019: 助教1名、学生4名を2～4週間Cambridgeへ派遣）
・・・JST二国間交流事業に採択(2014~2016)

以降、36編の論文を発表

28

Cambridge大学との共同研究（2013~）56歳～

工学部超電導バルクグループ
2015~2016 学振二国間交流採択

D.A. Cardwell教授 (現Univ. Cambridge vice-chancellor)

・これまで5回訪問、講演
・研究室の助教1名(2015)、大学院生4名を2週間～4週間派遣(2015, 2016, 2018)
・Cambridgeの研究者・大学院生が毎年盛岡を訪問
・国際会議等で会う度に、共同研究・論文のdiscussion
・ほぼ毎週、定期的なメールの交換で研究の議論

29

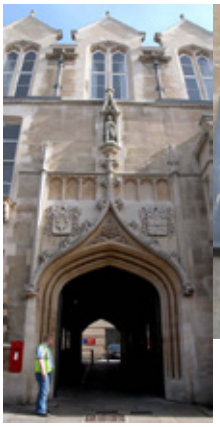

Cavendish Laboratory
・Maxwell（初代所長）
・J.J. Thomson, W. Bragg, E. Rutherford, A. Compton,
・Watson & Crick
・29人のノーベル賞受賞者を輩出している。

30

パブ　Eagle

・チャーチル
・ワトソン、クリックなど
研究の合間にくつろぐ

31

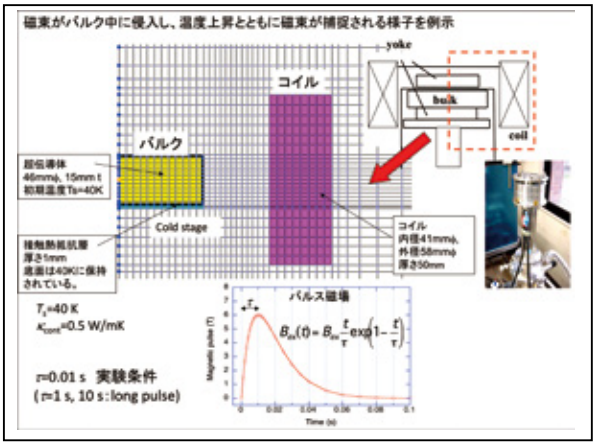

32

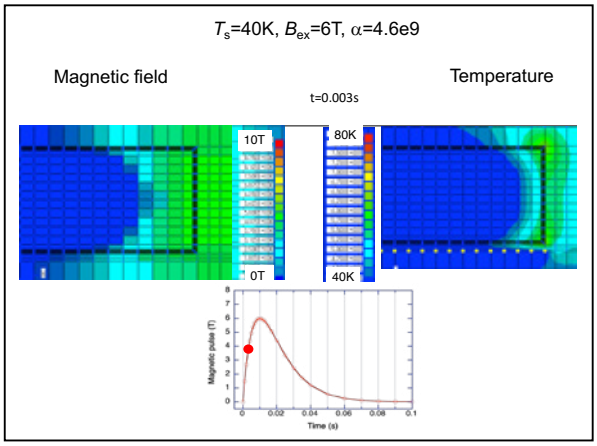

33

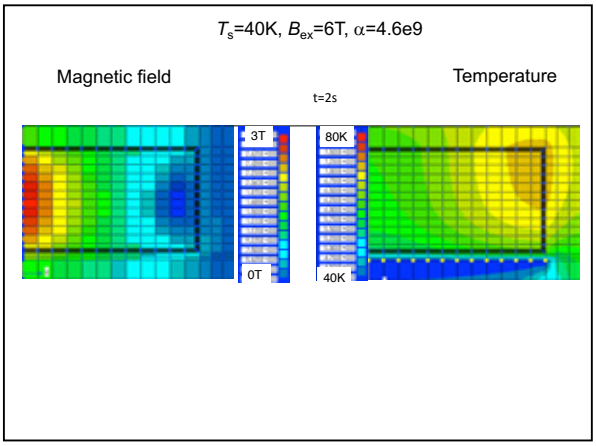

34

新しいバルク磁石（HTFMLとHG-TFM）の提案 (2017~2021)

当時はパルス着磁実験とシミュレーションでマンネリ化、停滞

2017.9 国際会議(MT23;アムステルダム))に学生と参加
その会議中に、高橋圭太君（現:学習院大学助教）が新しいバルク磁石構造を提案

2018: ハイブリッド型超伝導バルク磁石レンズ(HTFML)
　印加磁場よりも大きな磁場を持続的に捕捉する

2020: 高磁場勾配超伝導バルク磁石(HG-TFM)
　水滴の磁気浮上が可能な大きな磁場勾配が持続的に実現
　（地上での擬似微小重力環境の実現）

これは面白い！

　シミュレーションによる予測
　実証実験

特許出願と論文発表、国際会議での招待講演

35

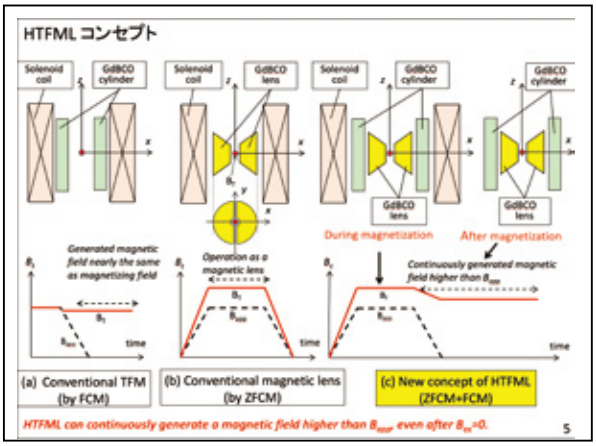

36

実証実験

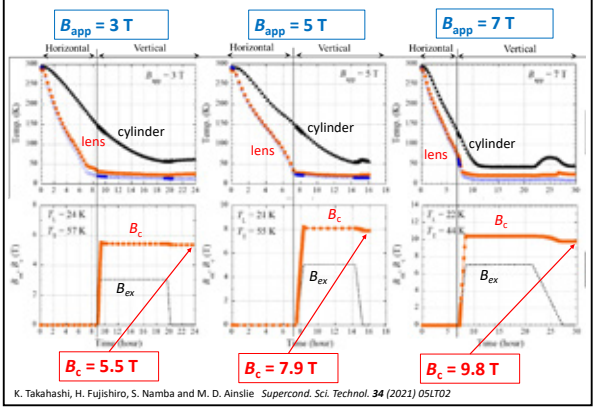

K. Takahashi, H. Fujishiro, S. Namba and M. D. Ainslie *Supercond. Sci. Technol.* **34** (2021) 05LT02

37

これまでの実験ノート（岩手大赴任後30年間で135冊）
・最近は実験ノートでは無く、会議（大学運営）ノートになっている。

38

これまでの発表論文の分析

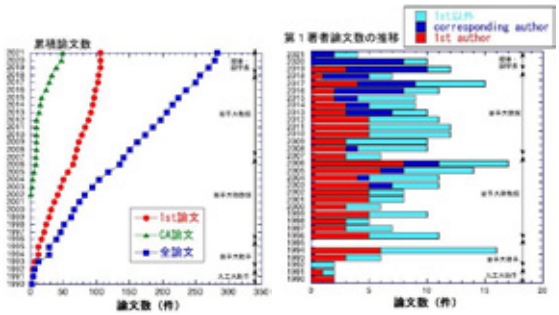

39

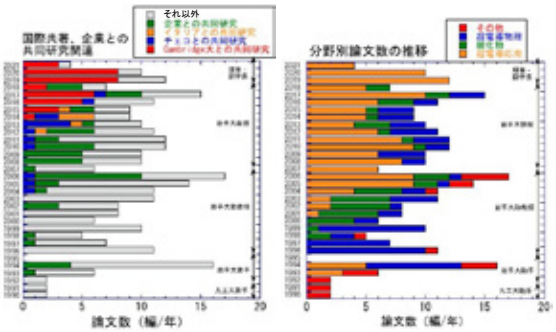

40

科研費の戦績、競争的外部資金の獲得状況

西暦	元号	年齢	所属・職位	科研費	科研費以外の競争的外部資金	企業等との共同研究、奨学寄付金
1990	H2	34	九州工大助手			
1991	H3	35	岩手大助手			
1992	H4	36				
1993	H5	37	岩手大助教授		池谷財団研究助成(150万円)	
1994	H6	38			池谷財団海外渡航経費(30万円)	
1995	H7	39		（C分担）		
1996	H8	40				
1997	H9	41			東吉奨学会研究奨励金(60万円)	
1998	H10	42		（B分担）	東京電力研究財団海外渡航経費(30万円)	
1999	H11	43			日本原子力研究所型明研究(200万円)	地域結集型事業
2000	H12	44				
2001	H13	45				
2002	H14	46		C	岩手大学活性化経費(70万円)	新日鐵
2003	H15	47		C		
2004	H16	48			夢県土いわて戦略的研究推進事業(1050万円)	
2005	H17	49		C	岩手大学学長裁量経費(35万円)	三菱重工
2006	H18	50	岩手大教授	C	学長裁量経費(100万円)	
2007	H19	51		C		
2008	H20	52		C	JST地域イノベーション研究開発プログラム(200万円)	東京エレクトロン
2009	H21	53			JST地域イノベーション研究開発プログラム(200万円)	九州電力
2010	H22	54				新日鐵住金
2011	H23	55		C	JST地域イノベーション研究開発プログラム(150万円)	住友電工
2012	H24	56		C	JST地域イノベーション研究開発プログラム(200万円)	
2013	H25	57		C		川崎重工業
2014	H26	58			AMED（理研の分担）	
2015	H27	59		C	JST二国間交流事業	イムラ材料開発研究所
2016	H28	60		C		JX金属
2017	H29	61		C		カネカ
2018	H30	62			JAT A-step 試験研究タイプ(300万円)	ミクニ
2019	R1	63	理事・副学長	C		鉄道総研
2020	R2	64		C	JAT A-step トライアウト(300万円)	
2021	R3	65		C		

41

国際会議での発表実績

西暦	元号	年齢	所属・職位	海外開催の国際会議発表	国内開催の国際会議発表	招待講演数
1990	H2	34	九州工大助手	0	0	0
1991	H3	35	岩手大助手	0	0	0
1992	H4	36		0	0	0
1993	H5	37	岩手大助教授	1（カナダ）	1	1
1994	H6	38		2（イタリア、フランス）	1	0
1995	H7	39		0	1	0
1996	H8	40		3（ハンガリー、ドイツ、チェコ）	0	0
1997	H9	41		1（オーストラリア）	0	0
1998	H10	42		2（イタリア、イギリス）	0	0
1999	H11	43		2（スウェーデン、フィンランド）	1	0
2000	H12	44		0	2	0
2001	H13	45		2（アメリカ、スイス）	2	0
2002	H14	46		2（ポーランド、チェコ）	2	1
2003	H15	47		2（イタリア、フランス）	2	0
2004	H16	48		2（オーストラリア、アメリカ）	1	1
2005	H17	49		2（オーストリア、アメリカ）	2	1
2006	H18	50	岩手大教授	0	1	0
2007	H19	51		1（イギリス）	1	0
2008	H20	52		1（アメリカ）	1	0
2009	H21	53		2（ドイツ、チェコ）	1	1
2010	H22	54		1（アメリカ）	1	0
2011	H23	55		2（オランダ、チェコ）	0	0
2012	H24	56		2（アメリカ、中国）	1	1
2013	H25	57		2（イタリア、チェコ）	1	1
2014	H26	58		2（アメリカ、カナダ）	1	1
2015	H27	59		3（イギリス、ベルギー、韓国）	0	1
2016	H28	60		1（アメリカ）	0	0
2017	H29	61		1（オランダ）	1	0
2018	H30	62		1（アメリカ）	1	0
2019	R1	63	理事・副学長	2（チェコ、イギリス）	1	3
2020	R2	64		0	0	0
2021	R3	65		1(WEB)	0	1

43件　26件　13件

42

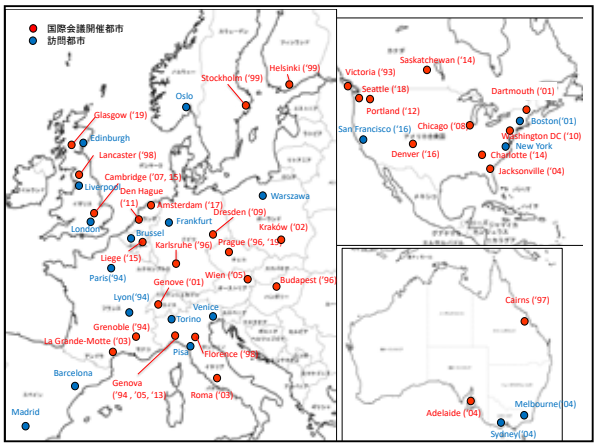

43

第1著者で論文執筆

内藤智之、柏田陽平、金山雅彦、藤原　篤、藤根陽介、日山拓也、吉田直樹、阿部凜太郎、吉田卓史、野田裕介、水野　州、望月豪彦、荻野　新、原　貴充、石澤　衛、高橋圭太、高橋裕平、下屋敷郁陽、難波　空、平野達也、新田基己

論文共著者

日下和彦、八木真如、中里規実生、芝崎有三、昆野吉幸、湊　洋一、菅原至朗、三上達也、菊池　勉、王子田修一、岡本龍也、小澤英行、加納伸吾、沼野　誠、高橋拓也、山崎哉、熊谷達也、鈴木和義、立岩達也、石田未央、八重樫晃一、今野友貴、佐藤清知、欠端浩介、佐々木寛子、三浦崇、山口大吾、荒屋敷貴大、小川　悟、小山　允、高橋　良、佐々木智久、半田拓也、氏家　徹、武田大輝、田村拓也、遠藤友理、阿久澤慶太

44

30年間、教育と研究の醍醐味を味わった。

・恩師や共同研究者との出会いが大きな財産
  ・西澤潤一教授
  ・池部　晃教授
  （赴任（34歳）以降、全ての研究テーマを決め、全ての研究費を使わせて貰う）

  ・深瀬哲郎教授、後藤　孝教授（東北大）、
  ・新日鐵、イムラ材料開発研究所、理化学研究所、東洋紡、SPring8の研究者

・わくわくする研究成果を何度か味わった。
  ・熱拡散率測定法の開発
  ・パルス着磁法への貢献（世界最高の捕捉磁場）
  ・Spring-8での研究
  ・PYCCO単結晶薄膜作製
  ・新しいバルク磁石の開発

・世界一流の研究者との共同研究を推進できた。
  ・チェコ科学アカデミーでの在外研究　（J. Hejtmanek博士）
  ・Cambridge大グループ　（Mark Ainslie博士）

・学生の成長を感じることができた。
  ・研究の面白さを感じた修士学生80名、博士学生3名が巣立つ。

45

研究者として成功するには、

・これまでの経験、スキルの蓄積
・研究者の興味、関心が強い
・自分が考えている事が現実にぴしっとはまる
・研究領域自体がその時期にちょうど盛り上がって結果を出すと評価が付いてくる
・研究業績は様々な出会い（人、テーマ、金）の集積・・・
・殆どの研究者は世界を驚かせる研究なんかできないで一生を終わる。

失敗と反省

・大学の組織に安住していなかったのか？
・もっと努力できたのでは無いか？
・自分の研究が、自己満足や狭い分野の研究の進展になっていなかったか？
・世の中の役に立つ研究レベルに達したか？（研究の価値を学術に留まらず、実用まで持って行けたか？）

・学生の心に火を付ける教育が本当に出来たか？
・社会が求める能力（答えの無い問題に答えを編み出すことが出来る能力が「想像する力」）を身に付けさせて、社会に送り出したか？

46

なぜ論文を書く必要があるのか？
・大学の研究者の義務（飯の種）・・・書かなければ昇任できない
・研究者は論文業績（数、質）が全て！
・研究成果を永久に世の中に残せる・・・芸術家における作品、小説家における小説と同じ

しかし、伝えたいこと（新事実、新発見）が無ければ、論文は書けない。

論文が書けるテーマをどのように見つけるか？

  ・自分で面白いと思うテーマを見つける努力（最初のアイディアをいかに出すか？）

  ・どんな（小さな）分野でも世界の先頭に立つテーマを見つける。

  ・2～3のテーマを同時に進める（花が咲く時期が異なる）。

  ・どんな研究テーマでも最後は論文にするという強い覚悟が必要！

  ・本当に素晴らしい成果は10年に1つ
  （ホームランはシングルヒット積み重ねの延長上にある）

  ・失敗した実験結果（特性が上がらなかった結果）の蓄積も、科学技術の発展には重要
  （新たな発想や方法の提案・実施こそが財産）

47

大学の組織運営について
（評議員9年、地連センター長2年、理事・副学長3年）

・大学は恵まれた職場・・・安住せず、常に努力（組織としてのポテンシャル向上）
・構成員は自分のためではなく、学科、コースのために働く
・学部長、評議員は自分の学部のためでは無く、全学のために働く

・大学は企業や軍隊では無い、行政組織でも無い。
・自由で十分な議論の後で、学長のリーダーシップによる決断が必要

大学　時間的自由と学問的自由を創造性の根源とする組織
  自由時間の確保のマネジメントが重要
  異質性の集合・・・異なる次元で高度に専門化された教員が研究を推進することで新たな知が創出される。

  これが大学の大学足ること

自由に研究を行う時間を作れ！　そして研究を行え！

48

イノベーションの創出例
・1989~1990: 青色発光ダイオードの開発を行う。
・用いた材料はZnSe・・・多くの研究者がZnSe研究に取り組む

2014年ノーベル物理学賞

中村　赤崎　天野

GaN（窒化ガリウム）

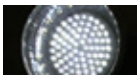

殆どの研究者は別の材料を研究

青色発光ダイオードの開発
・光の3原色が揃う（ディスプレー）
・白色発光ダイオード（照明）
・光通信の大容量化、高速化
・情報容量の大容量化

49

赤崎　勇先生
・京大理->1959名大工->1964松下電器->1980名大工->1992名城大
・窒化ガリウム(GaN)を用いた青色、白色LEDの開発

発明が実現した要因（談：濱口道成JST理事長）

1）極めて強固な意志（社会が求めているものを開発する）
2）研究計画に縛られずに目の前の課題に対応する資金（講座費）の重要性
3）企業（豊田合成）、JSTの継続的支援
4）天野先生の存在（講座制）
5）若い時期の研究
6）安定したポストの任用（長期に挑戦的に研究に専念）

・選択と集中か？全体的な底上げか？
・個人に依存するか？組織に依存するか？
・個人に投資するか？テーマに投資するか？研究環境に投資するか？

イノベーションを起こすには
・研究者の能力（センス、知識）を見極め、計画に縛られず、自由になる資金を長期に支援する。

50

学問の自由

時間と研究費の自由裁量

研究者の責任

51

最後に

52

盛岡高等工業学校

昭和21年頃

現在の理工学部第11駐車場

53

B: 代表的論文（10 編）

1. (D-1) 藤代博之、内藤智之、池部　学、能登宏七、「低温における熱拡散率と熱伝導率の同一セッティング測定」、
   低温工学 **28** (1993) pp. 533-539 (No. 10 paper)
2. (F-17) Hiroyuki Fujishiro, Tatsuya Tateiwa, Atsushi Fujiwara, Tetsuo Oka and Hidemi Hayashi, “Higher trapped field over 5 Tesla on HTSC bulk by modified pulse field magnetizing”,
   Physica C **445-448** (2006) pp. 334-338 (No. 134 paper)
3. (G-1) H. Fujishiro and T. Naito, “Simulation of temperature and magnetic field distribution in superconducting bulk during pulsed field magnetization”,
   Supercond. Sci. Technol. **23** (2010) 105021 (8 pages) (No. 174 paper)
4. (A-41) H. Fujishiro, T. Naito, S. Ogawa, K. Nitta, J. Hejtmanek, K. Knizek and Z. Jirak, “Valence shift of Pr ion from 3+ to 4+ in $(Pr_{1-y}Y_y)_{0.7}Ca_{0.3}CoO_3$ estimated by X-ray absorption spectroscopy”,
   J. Phys. Soc. Jpn. **81** (2012) 064709 (5 pages) (No. 189 paper)
5. (A-48) Y. Noda, H. Fujishiro, T. Naito, A. Ito, T. Goto, J. Hejtmanek and Z. Jirak, “Electrical resistivity anomaly in $(Pr_{1-y}M_y)_{1-x}Ca_xCoO_3$ epitaxial films (M = Y, Gd) fabricated by pulsed laser deposition”,
   AIP Advances **6** (2016) 025318 (9 pages) (No. 232 paper)
6. (H-1) K. Takahashi, H. Fujishiro and M. D. Ainslie, “A new concept of hybrid trapped field magnet lens (HTFML)”,
   Supercond. Sci. Technol. **31** (2018) 044005 (9 pages) (No. 257 paper)
7. (H-3) Sora Namba, Hiroyuki Fujishiro, Tomoyuki Naito, Mark D Ainslie, Keita Takahashi, “Experimental realization of a Hybrid Trapped Field Magnet Lens (HTFML) using a GdBaCuO magnetic lens and MgB_2 bulk cylinder”,
   Supercond. Sci. Technol. Letter **32** (2019) 12LT03 (7 pages) (No. 271 paper)
8. (I-25) Tatsuya Hirano, Yuhei Takahashi, Sora Namba, Tomoyuki Naito and Hiroyuki Fujishiro, “A record-high trapped field of 1.61 T in MgB_2 bulk comprised of copper plates and soft iron yoke cylinder using pulsed-field magnetization”,
   Supercond. Sci. Technol. **33** (2020) 085002 (10 pages) (No. 276 paper)
9. (H-8) K. Takahashi, H. Fujishiro and M. D. Ainslie, “A conceptual study of a high gradient trapped field magnet (HG-TFM) providing toward a quasi-zero gravity space on Earth”,
   Supercond. Sci. Technol. **34** (2021) 035001 (13 pages) (No. 283 paper)
10. (H-9) K. Takahashi, H. Fujishiro, S. Namba and M. D. Ainslie, “Experimental realization of an all-(RE)BaCuO hybrid trapped field magnet lens generating a 9.8 T concentrated magnetic field from a 7 T external field”,
    Supercond. Sci. Technol. **34** (2021) 05LT02 (9 pages) (No. 284 paper)

1. (D-1) 藤代博之、内藤智之、池部　学、能登宏七
「低温における熱拡散率と熱伝導率の同一セッティング測定」、
低温工学 **28** (1993) pp. 533-539 (No. 10 paper)

低温における熱拡散率と熱伝導率の同一セッティング測定

藤代　博之，内藤　智之，池部　學，能登　宏七

岩手大学工学部材料物性工学科　盛岡市上田 4-3-5

(1993年4月12日受理)

Low Temperature Thermal Diffusivity and Conductivity Measurements under an Identical Experimental Setup

Hiroyuki FUJISHIRO, Tomoyuki NAITO, Manabu IKEBE and Koshichi NOTO

Department of Materials Science and Technology, Faculty of Engineering, Iwate University, 4-3-5 Ueda, Morioka 020

(Received April 12, 1993)

Synopsis:

A thermal diffusivity measuring system employing a closed cycle helium refrigerator was developed, which also enabled the thermal conductivity measurement under an identical experimental setup. The diffusivity was measured by a discretional heating method and the conductivity was measured by a steady-state heat flow method. The errors and the accuracy in measurements were evaluated by measuring the diffusivities of an austenitic stainless steel standard sample (SRM 1460), a Pyrex glass (Corning #7740) and a high purity copper between 12 to 200 K. The diffusivity ranging from 10^{-3} to 2 cm^2/s could be determined with an uncertainty of 3 %. The results agreed with the reported values within 10 %.

1. はじめに

近年，酸化物超伝導体に代表される低温工学，低温物理学の発展に伴い，低温領域における諸材料の熱的物性値（熱伝導率κ，熱拡散率α，比熱Cなど）は，実用的見地からも重要な物理量である。例えば，超伝導機器やクライオスタットを設計する場合には，固体の熱容量が低温になるほど極端に小さくなるために，使用する材料を伝わる熱侵入が重要な問題となる。また，最近では新しい機能を持った各種複合材料，薄膜状材料の熱的測定も基礎，応用の両面から重要となり，測定技術の確立も必要となってきている[1]。これらの熱物性値は$\kappa=\rho\cdot C\cdot\alpha$（ただし，$\rho$は密度）という関係で結び付けられているので，$\rho$が既知の場合，$\kappa$と$\alpha$を独立に測定できれば比熱$C$を算出することが可能である。また，熱拡散率は$\alpha=v\ell/3$という関係で，熱キャリアの速度$v$と平均自由行程$\ell$に結び付けられるので，熱キャリアがフォノンのみでありフォノンの速度（音速）vが温度に依らず一定である場合には，αを測定することによってフォノンの平均自由行程ℓを直接測定することが可能になる。低温における固体の熱伝導率測定は一般に定常熱流法で行われ[2]，比熱の測定は断熱法[3]，熱緩和法[4]，交流法[5]などによって行われており，これまで多くの研究が報告されている。固体の熱拡散率測定は，ほとんどが非定常熱流法で行われ，レーザフラッシュ法に代表されるようなパルス状加熱による方法[6]，ステップ状加熱による方法[7,8]，周期加熱による方法[9]などが一般的である。これらの方法は，熱拡散方程式を解くための境界条件（例えば，理想的なパルス状，ステップ状の温度変化）を実験的にも実現する必要があり，また等方的で均一な試料を準備する必要がある。κとαの同時測定は，異なった試料や異なった実験から生じる誤差を少なくし，比熱Cの計算精度を上げることができる利点を持っており，低温における測定においてもPhotopyroelectric法[10]，温度の減衰曲線から解析する方法[11,12]など，いくつかの報告が行われている。

我々は，すでにヘリウム冷凍機を用いた熱伝導率の

完全自動測定システムを開発し，オーステナイト系ステンレス標準試料の熱伝導率を10～200 K の温度範囲で，2％の精度で測定できることを報告した[13]。また，種々の酸化物超伝導体の熱伝導率を測定し，熱的散乱機構の解析を行っている[14,15]。本研究では，この測定システムに改良を加え，熱伝導率の測定と同時に熱拡散率の測定を可能にした。低温における熱物性測定の場合に問題になる輻射損失を極力少なくするため，光学窓の必要なレーザ光などの熱源を用いずに，微小な金属皮膜チップ抵抗を熱源に用いた。熱伝導率 κ は定常熱流法により求め，熱拡散率 α は任意加熱法と呼ばれるパルス状加熱による非定常熱流法によって測定した。この方法は，任意の形状，大きさの熱パルスに対して熱拡散率 α を求めることができるという利点を持ち，測定精度を向上させることができる[16,17]。また，試料の形状が薄板状である場合，面内方向と厚さ方向の両方向の熱拡散率測定が可能であり，異方的な熱物性値を持つ酸化物超伝導体単結晶のような試料に対して，多くの情報を得ることができる。

2. 実験方法および解析

2.1 熱拡散率および熱伝導率の測定方法

熱伝導率に関する標準物質は，米国国立標準技術研究所 (National Institute of Standards and Technology : NIST) などにより，数種類の標準物質が確立され供給されている。しかし熱拡散率に関しては，公的な機関によって認定された標準物質は存在しない[18]。したがって，本研究では $\alpha=1$ cm^2/s 以上の大きな熱拡散率を持つ物質として高純度銅 (99.9999％：6 N：同和鉱業(株)製：サイズ 1 mmϕ，長さ 50 mm) を，$\alpha=0.01$～0.5 cm^2/s 程度の熱拡散率を持つ物質としてオーステナイト系ステンレス標準試料 (SRM 1460：NIST 製：サイズ 6.4 mmϕ，長さ 50 mm) を，それ以下の小さな熱拡散率を持つ物質としてパイレックスガラス (Corning #7740：Corning 社製：サイズ 5 mm×1 mm×15 mm) を測定し，測定システムの精度，信頼性を評価した。高純度銅は，精製した原料を線状に鋳造後，熱処理により鋳造欠陥を取り除き測定を行った。パイレックスガラスは，ダイヤモンドカッターで切り出した後，ミラー研磨し測定を行った。Fig. 1 に測定装置の試料周辺部分の概略図を示す。試料の一端をヘリウム冷凍機の cold head にインジウム半田または，GE 7031 ワニスを用いて熱的に接触させ，他端に熱伝導率測定の場合は温度差用ヒータ，熱拡散率

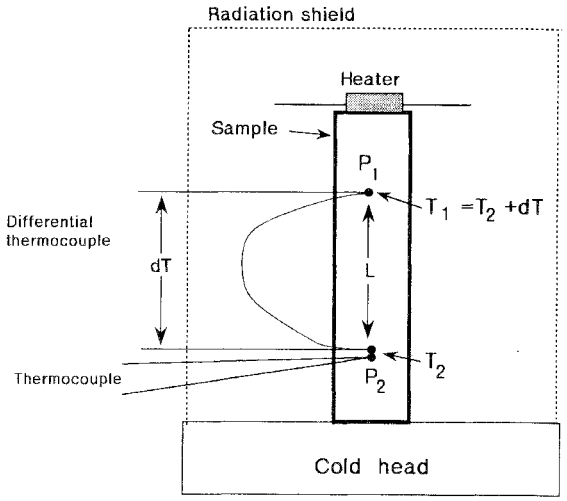

Fig. 1 Schematic diagram of the thermal diffusivity measurement system using a closed cycle helium refrigerator.

測定の場合は熱パルス用ヒータとなる金属皮膜チップ抵抗 10 kΩ (アルファ・エレクトロニクス(株)製：サイズ 3.2 mm×2.5 mm×1.2 mm) を GE 7031 ワニスを用いて接着した。cold head 側 (低温側) の P_2 点の温度 T_2 は，直径 73 μm の Au+0.07 at. ％ Fe-クロメル熱電対を用いて測定し，距離 L だけ離れたヒータ側 (高温側) の P_1 点の温度 T_1 は，differential thermocouple (Au+0.07 at. ％ Fe-クロメル-Au + 0.07 at. ％ Fe 差動熱電対) を用いて測定した P_1, P_2 の間の温度差 dT を用いて $T_1=T_2+dT$ より求めた。輻射による熱流入，熱損失を少なくするため，ニッケルメッキを施した銅製の輻射シールドを cold head に熱的に接触させた。雰囲気気体による対流と熱伝導を防ぐために，試料室全体を油拡散ポンプを用いて 10^{-6} Torr 程度まで真空に引き測定を行った。測定装置は closed cycle type のヘリウム冷凍機，デジタルボルトメータ (DVM)，定電流源，パソコン等を GPIB ケーブルで接続した自作の熱伝導率，熱拡散率自動測定システムを用い，12～200 K の温度範囲で測定を行った。熱拡散率の測定は，試料温度を安定させた後，ヒータに 5 秒から 10 秒の電流パルスを加え，その後の T_1, T_2 の時間変化を毎秒 3.1 回，100 (または 200) 秒間記録するという非定常熱流法により行った。用いた直径の熱電対の応答時間は 1 ms 程度という報告があり[19]，十分正確に試料の温度変化を測定していると考えられる。この結果を，2.2 節で述べる熱拡散方程式の数値解析の結果と比較することにより熱拡散率 α

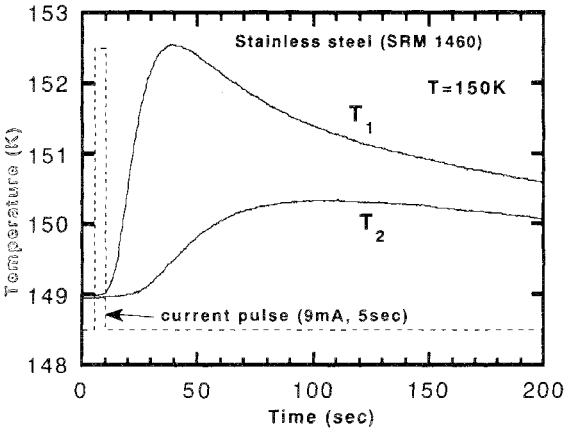

(a)

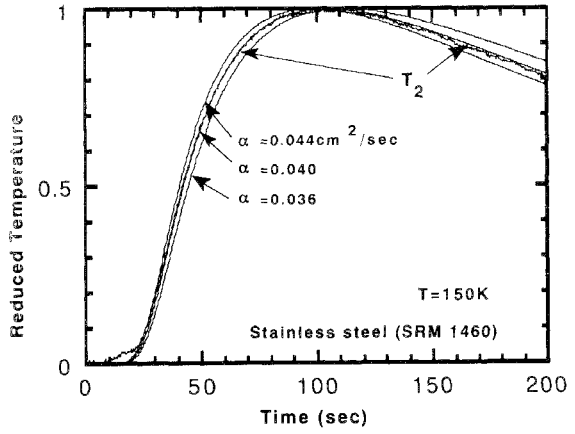

(b)

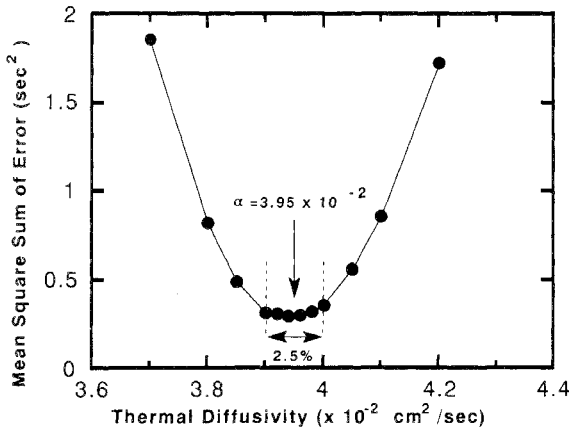

(c)

Fig. 2 The principle of determination of the thermal diffusivity α. (a) the temperature changes ($T_1(t)$, $T_2(t)$) at the two measuring points (P_1, P_2)for the stainless steel specimen (SRM 1460) at 150 K, after applying the current pulse (9 mA, 5 s). (b) the comparison of the measured temperature change $T_2(t)$ with the calculated curves, $T_2'(t)$, for various thermal diffusivity α: the measured change $T_1(t)$ was used as the boundary condition. (c) the mean square sum of the time differences, $<(t'-t'')>^2$ to fulfill the equivalent condition for the two curves, $T_2(t')=T_2'(t'')$, against the parameter α. Eighty points between the reduced temperatures 0.1 to 0.9 were used to evaluate the time difference, $<\Delta t>^2$.

を求めた。熱伝導率の測定は，各測定温度で熱拡散率を測定した後，ヒータに P_1, P_2 間の温度差 dT が約 1 K となるように一定の電流を流し，$\kappa=Q/L(dT\cdot S)$（ただし，Qは熱量，Sは試料の断面積）を用いて定常熱流法によって求めた。

2.2 熱拡散率の決定方法

試料にヒータから熱パルスを加えた場合，輻射による損失がなく熱が cold head 側に一方向に流れると仮定すると，次の 1 次元の熱拡散方程式が成立する。

$$dT/dt=\alpha(d^2T/dx^2) \qquad (1)$$

ここで，Tは温度，tは時間，xは距離，αは熱拡散率である。ここで，時間軸を時間刻み幅 Δt（刻み数 i），距離軸を距離刻み幅 Δx（刻み数 j）で分割し格子点（$u[i, j]$）を作る。この微分方程式を（2）式のようにクランク・ニコルソン法[20]を用いて陰的な差分をとり近似差分方程式を作る。

$$(1+C)u[i,j+1]-(C/2)(u[i-1,j+1]+u[i+1,j+1])=(1-C)u[i,j]+(C/2)(u[i-1,j]+u[i+1,j]) \qquad (2)$$

これに境界条件を代入すると，（1）の微分方程式は n 元の線形代数方程式に書き換えることができる。この連立方程式をガウスの消去法を用いて解くことで任意の時間 t，任意の距離 x における温度 $T(t, x)$ を種種の熱拡散率 α に対して計算することができる。本研究では，時間刻み幅 Δt を 0.32 秒，距離刻み幅 Δx を 0.5 mm で分割し，一連の計算を FORTRAN 言語でプログラムし，パソコンで計算を行った。実験においては，ヒータに電流をパルス状に流しているが，ヒータ部分の温度はヒータが有限の熱容量を持っているために理想的なパルス状の温度変化をせずに，時間遅れを生じて変化する。そのため，境界条件として理想的なパルス状の温度変化（例えば，$0\leqq t\leqq 5$ で $T=T_0$（一定））を代入することはできない。そこで，実験で求められた P_1 点の温度変化 $T_1(t)$ を熱拡散方程式の境界条件として代入し，距離 L だけ離れた P_2 点

の温度変化 $T_2'(t)$ を任意の α に対して数値計算して，実験値 $T_2(t)$ と一致する α の値を最小自乗法により決定した。この方法を用いれば，熱パルスの幅，大きさが任意であっても試料中の距離 L だけ離れた2点の過渡的な温度変化から熱拡散率を決定することが可能となる。

Fig. 2 (a) に 150 K でステンレス標準試料に5秒間，9 mA の電流パルスを印加した場合に測定された温度変化，$T_1(t)$，$T_2(t)$ を示す。また，Fig. 2 (b) に $T_1(t)$ を境界条件として（2）式に代入し，種々の α の値に対して計算した温度変化 $T_2'(t)$ と，実際に測定された温度変化 $T_2(t)$ とのフィッティングの様子を最大温度変化を1に規格化して示す。フィッティングを系統的に行うため，立ち上がりの10％から90％の間の80点の温度について計算値 $T_2'(t)$ と測定値 $T_2(t)$ の時間のずれ Δt の平均自乗和を計算し，この和が最小になるように α を決定した。Δt の平均自乗和と α の関係を Fig. 2 (c) に示す。この図から 150 K における α の最確値は $(3.95\pm0.05)\times10^{-2}\mathrm{cm^2/s}$ と ±1.25％ の精度で決定することができた。

3. 結果および考察

3.1 任意加熱法の検証実験

本研究で用いている任意加熱法は，文字どおり任意形状の熱パルスに対して熱拡散率が求められるという利点を持っている[16]。本研究で用いた測定システムでこのことを確認するために，入力電流パルスのパルス幅や大きさと，求められる熱拡散率の関係について検討した。Fig. 3 にステンレス標準試料についてヒータ電流値を一定とし電流パルス幅を変化させた場合の 150 K, 45 K, 12 K での熱拡散率の値を示す。電流パルス幅が極端に短い場合（2秒以下）には温度変化が DVM の測定限界に近づくため測定精度が悪くなるが，4秒から12秒まで電流パルス幅を変化させても，熱拡散率はばらつき2％以内でほぼ一定の値となることがわかった。Fig. 4 に同じ試料について電流パルス幅を10秒（一定）とし，電流パルスの大きさを変化させた場合の 150 K, 45 K, 12 K における熱拡散率の値を示す。電流パルスの大きさを変化させても，熱拡散率はばらつき3％以内でほぼ一定の値となることがわかった。同様の確認実験は，熱拡散率の絶対値が異なる高純度銅とパイレックスガラスに対しても行い，同程度のばらつきで熱拡散率が決定できることを確認した。以上のことより，この熱拡散率測定法は任意形状の熱パルスに対してばらつき3％以内で熱拡散率を決定できることが明らかになった。DVM の分解能や輻射損失の影響を考慮して，入力電流パルスの幅と大きさは，$T_1(t)$ の変化が 3～5 K となるように各測定温度で設定した。

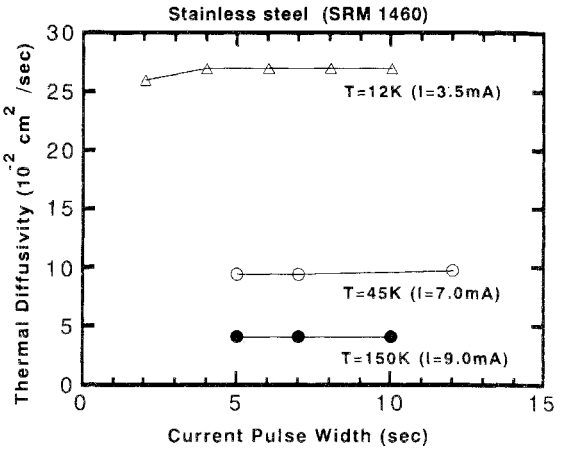

Fig. 3 Dependence of the determined thermal diffusivity on the current pulse width applied to the heater.

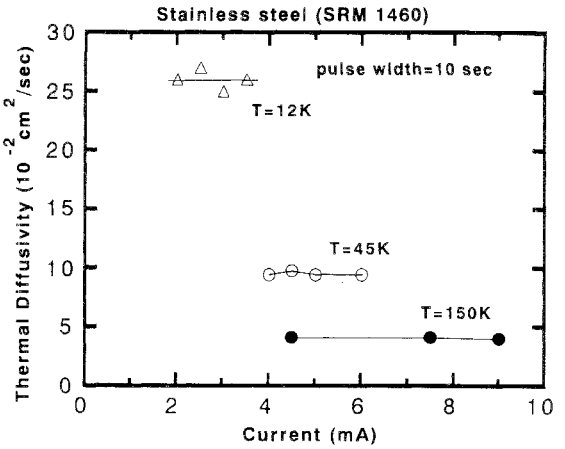

Fig. 4 Dependence of the determined thermal diffusivity on the current pulse height applied to the heater when the current pulse windth is fixed at 10 s.

3.2 ステンレス標準試料（SRM 1460）の測定結果

Fig. 5 (a) にステンレス標準試料の熱伝導率 κ を，Fig. 5 (b) に熱拡散率 α の温度依存性の測定結果を示す。Fig. 5 (a) 中には，熱伝導率の NIST による較正データ[21]を実線で示した。測定された熱伝導率は NIST の較正データと比較して 150 K 以下で約2％，150 K 以上で約4％以内で精度よく測定された。Fig. 5 (b) には，NIST により計算されたステンレス標準試料の熱

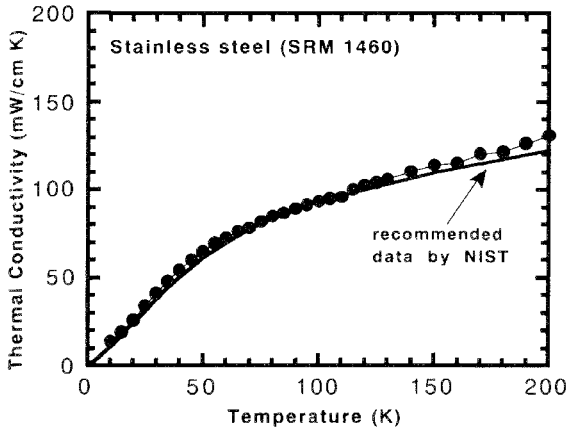

(a)

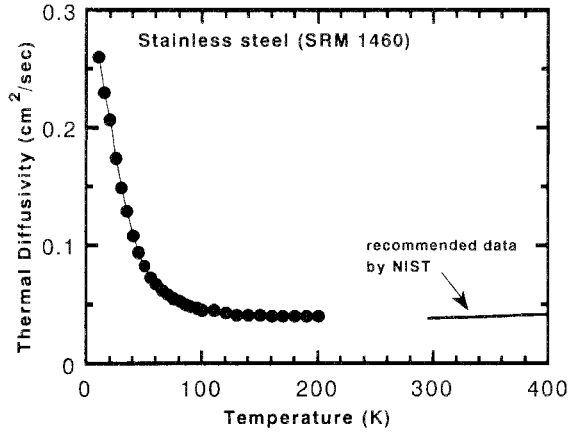

(b)

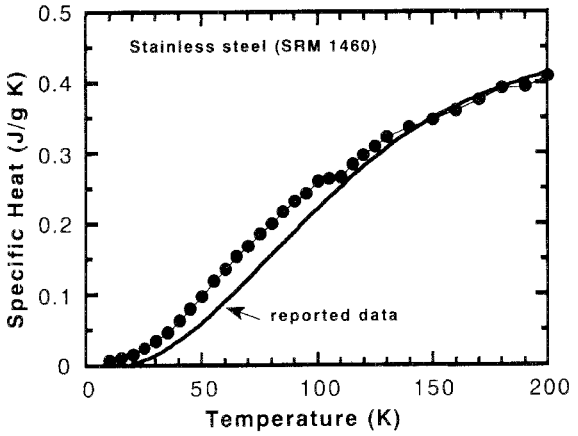

(c)

Fig. 5 The results of simultaneous measurement of (a) the thermal conductivity κ and (b) the thermal diffusivity α for the austenitic stainless steel standard sample (SRM 1460), respectively. (c) shows the calculated specific heat using κ, α and ρ.

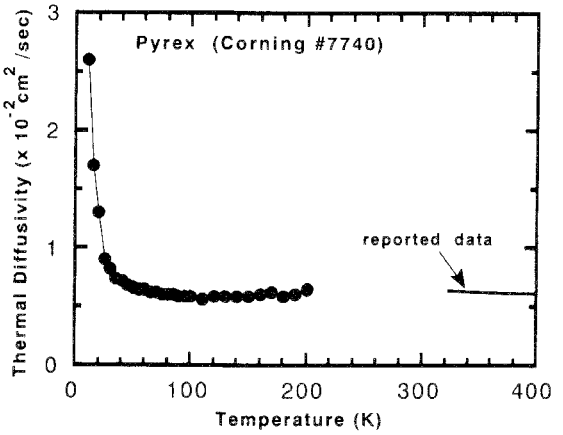

Fig. 6 Temperature dependence of the thermal diffusivity of the Pyrex glass (Corning #7740). The thick line in the figure represents the data reported by Hulstrom, et al.[24]

拡散率[22]を実線で示した。NIST のデータを低温側に外装した結果，実験値と 200 K で約 10 %の違いで一致した。測定された 200 K 以下でのステンレス標準試料の熱拡散率は 100 K 付近まではほぼ一定であるが，その後急激に増大して 12 K では α=0.26 cm²/s であった。Fig. 5(c) に，κ, α, ρ(=8.00 g/cm³) から計算されたステンレス標準試料の比熱の温度依存性を示す。文献[23]のステンレス鋼が今回測定したステンレス標準試料 (SRM 1460) と同一であるかどうかは不明であるが，文献値と比較して 120 K 以上で 3 %，120 K 以下で約 15 % 以内で一致した。

3.3 パイレックスガラスの測定結果

Fig. 6 にパイレックスガラスの熱拡散率 α の温度依存性を示す。図中には，レーザフラッシュ法で Hulstrom らにより測定された室温以上の熱拡散率の値[24]を実線で示した。200 K 以下のパイレックスガラスの熱拡散率の報告例は現在のところ見つからず直接的な比較はできないが，Hulstrom らのデータを低温側に外挿した結果，測定値は 200 K で約 2 % 以内の誤差で一致した。測定された 200 K 以下での熱拡散率は，50 K 付近まではほぼ一定であるが，その後急激に増大して 12 K では α=0.026 cm²/s であった。

3.4 高純度銅の測定結果

高純度銅の熱拡散率は，ステンレス鋼やパイレックスガラスに比べ 2 ～ 3 桁大きく，かつ 100 K 以下の低温では指数関数的に大きくなると報告されている[25]。そのため，高純度銅の測定では大きな熱拡散率の測定も可能になるように，温度計距離 L を長くして (38

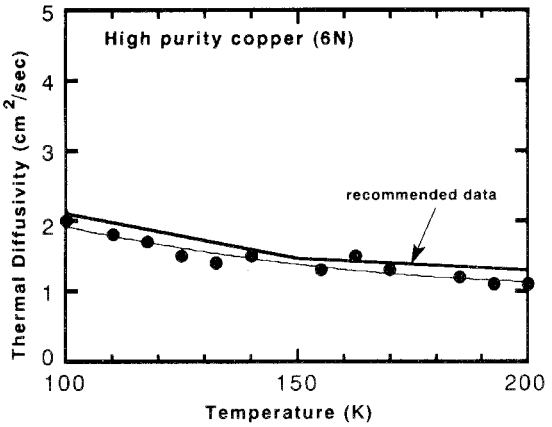

Fig. 7 The temperature dependence of the thermal diffusivity of the high purity copper (6 N). The thick line represents the recommended data by Touloukian, et al.[25]

mm) 測定を行ったが，測定器のサンプリング速度やGPIBによるデータ転送速度で決定される毎秒 3.1 回のサンプリング速度では 100 K 以下の大きな熱拡散率は決定できなかった。Fig. 7 に高純度銅の熱拡散率 α の 100～200 K の温度依存性を示す。図中には，高純度銅に対して推奨されている熱拡散率の文献値[25]を太い実線で示す。測定された熱拡散率は文献値と比較して，この温度範囲で最大誤差 7 %以内で一致した。高速 AD 変換などの手法を用いれば，さらに大きな熱拡散率の測定も精度よく行うことが可能になると思われる。

4. まとめ

ヘリウム冷凍機を用いて，固体の熱拡散率 α を熱伝導率 κ と同一セッティングで測定するシステムを開発し，オーステナイト系ステンレス標準試料 (SRM 1460)，パイレックスガラス(Corning #7740)，高純度銅 (99.9999 %：6 N) を 12～200 K の温度範囲で測定した。10^{-3}～2 cm^2/s の範囲にある試料の熱拡散率 α をばらつきが 3 %以内で，また他の報告例と比較した誤差が 10 % 以内で測定できることがわかった。熱電対の接点は有限の大きさを持ち，その接点をワニスを用いて試料に接着しているので，L の測定精度が熱伝導率，熱拡散率の絶対精度に影響を及ぼすと考えられる。本研究の場合の L の測定には，ステンレス標準試料，高純度銅の場合は最大約 3 %，パイレックスガラスの場合は約 8 %の誤差を含むと考えられる。L の測定精度の向上とデータサンプリングの高速化によりさらに大きな α の測定や，さらに絶対精度がよい α，κ の測定が可能になり，酸化物超伝導体の散乱機構の解明や各種低温材料の熱物性値の評価に役立つものと考えられる。

本研究を進めるにあたり有益なご助言をいただきました，岩手大学工学部，松川倫明助教授に感謝いたします。また，熱拡散率の報告例を提供してくださった計量研究所，計測システム部，計測情報研究室，新井照男氏に感謝いたします。

参考文献

1) H. Shibata, H. Ohta and Y. Waseda : Materials Transactions, JIM **32** (1991) 837
2) R. Berman : Proc. Roy. Soc. **A 208** (1951) 90
3) H. Suga and S. Seki : Bull. Chem. Soc. Jpn. **38** (1965) 1000
4) R. Bachmann, F. J. Di Salvo, T. H. Geballe, R. Green, R. E. Howard, C.N.King, H.C.Kirsch, K. N. Lee, R. E. Schwall, H. U. Thomas and R. B. Zubeck : Rev. Sci. Instrum. **43** (1972) 205
5) P. F. Sullivan and G. Seidel : Phys. Rev. **173** (1968) 679
6) W. T. Parker, et al. : J. Appl. Phys. **32**(1961) 1679
7) 小林清志，熊田俊明：日本原子力学会誌 **9** (1967) 58
8) 熊田俊明，小林清志：日本原子力学会誌 **11** (1969) 462
9) 山田利之ら：第 6 回熱物性シンポジウム論文集 (1985) 229
10) S. B. Peralta, Z. H. Chen and A. Mandelis : Appl. Phys. **A 52** (1991) 289
11) R. S. Knok, et al. : Rev. Sci. Instrum. **61** (1990) 809
12) A. Khalil : Cryogenics **22** (1982) 310
13) 保原夏朗，松川倫明，松浦伸悌，藤代博之，能登宏七：低温工学（印刷中）
14) K. Noto, M. Matsukawa, K. Mori, Y. Ogiso and K. Sato : Cryogenics **30** (1990) 868
15) M.Matsukawa, K.Noto, M.Ikebe and K.Mori: Proc. 7th US-Workshop on High Field Superconducting Materials, Wire and Conductors and Standardizing Procedures for HTSC Wires Testing (1991) 159
16) 飯田嘉宏，重田治彦：日本機械学会論文誌 **47** (1981) 470
17) 斎藤彬夫ら：日本機械学会論文誌 **52** (1986) 144

18) 日本熱物性学会編：熱物性ハンドブック，養賢堂，584
19) C. D. Henning and R. Perker : J. Heat Transfer Trans. ASME **39** (1967) 146
20) J. Crank : *The Mathematics of Diffusion*, 2nd Edition, Clarendon Press, London (1975) 144
21) J. G. Hust and A. B. Lankford : *NBS Special Publication* (1984) 260
22) H. Groot : *Proceedings of the 20th International Conference on Thermal Conductivity*, Plenum Press, New York (1989) 357
23) 低温工学協会編：低温工学ハンドブック，内田老鶴圃新社，192
24) L. C. Hulstrom, R. P. Tye and S. E. Smith : *Proceedings of the 19th International Conference on Thermal Conductivity*, Plenum Press, New York (1988) 199
25) Y. S. Touloukian, et al. : *Thermal Properties of Matter*, Vol. 1, 4, 7, IFI/Plenum Press, New York (1970)

2. (F-17) Hiroyuki Fujishiro, Tatsuya Tateiwa, Atsushi Fujiwara, Tetsuo Oka and Hidemi Hayashi,
"Higher trapped field over 5 Tesla on HTSC bulk by modified pulse field magnetizing",
Physica C **445-448** (2006) pp. 334-338 (No. 134 paper)

Available online at www.sciencedirect.com
ScienceDirect
Physica C 445–448 (2006) 334–338
PHYSICA C
www.elsevier.com/locate/physc

Higher trapped field over 5 T on HTSC bulk by modified pulse field magnetizing

Hiroyuki Fujishiro [a,*], Tatsuya Tateiwa [a], Atsushi Fujiwara [a], Tetsuo Oka [b], Hidemi Hayashi [c]

[a] Iwate University, 3-4-5 Ueda, Morioka 020-8551, Japan
[b] IMRA Material R&D Co., Ltd., 5-50 Hachiken-cho, Kariya 448-0021, Japan
[c] Kyushu Electric Power Co., Inc., 2-1-47 Shiobaru, Fukuoka 815-8520, Japan

Received 21 March 2006
Available online 23 June 2006

Abstract

The trapped field $B_T^P = 5.20$ T has been realized on the GdBaCuO bulk superconductor by a modified multi pulse technique combined with a stepwise cooling (MMPSC), which surpassed the previous highest record of $B_T^P = 4.47$ T. At the first stage, a small amount of the magnetic field ~1 T was trapped at the bulk center with a concave field distribution at a high starting temperature $T_s \sim 45$ K by the low pulse field application $B_{ex} \sim 4.5$ T. Following the first stage, the higher field of $B_{ex} \sim 6.7$ T was applied at a lower $T_s \sim 30$ K at the second stage. The concave trapped field profile over the bulk at the first stage and the optimization of the higher applied pulse field at the second stage are key points to enhance B_T above 5 T.

PACS: 74.25.Bt; 74.80.Bj; 74.60.Ge

Keywords: Pulse field magnetizing; Temperature rise; Bulk superconductor; Trapped field

1. Introduction

The pulse field magnetizing (PFM) on high-T_c bulks has been recently intensively investigated instead of the field cooled magnetizing (FCM) because of the relatively compact, inexpensive and mobile setup [1]. However, the trapped field B_T^P by PFM had been pretty smaller than that attainable by FCM at low temperatures possibly due to the large temperature rise ΔT by the dynamical motion of the magnetic flux. The highest B_T^P value ever reported had been 3.80 T on the SmBaCuO bulk at 30 K by an improved iterative pulse field magnetization method with reduced amplitude (IMRA) [2]. We have systematically measured the time evolution of the temperature rise $\Delta T(t)$ on the surface of the cryo-cooled REBaCuO bulks during the PFM and investigated the relation between ΔT and B_T^P [3–5]. The heat generation results from both the pinning loss Q_p related to the flux trapping and the viscous loss Q_v related to the flux movement. The successive pulses with the same strength make the ΔT value decrease and the B_T^P value increase with increasing number of the pulse application. The lowering of the bulk starting temperature T_s is expected to result in a higher B_T^P due to the enhanced pinning force F_p but it also brings about a larger ΔT due to an increase of Q_p and a decrease of the specific heat $C(T)$. As a result, B_T^P at $T_s = 10$ K was not enhanced contrary to our expectation [6]. Recently, we proposed a new PFM technique named as a modified multi-pulse technique combined with a stepwise cooling (MMPSC) [7]. This technique consists of two stages; firstly, a small amount of magnetic field ($B_T^P \sim 1$ T) is trapped in the bulk center by applying a lower field $B_{ex}(1) \sim 4.5$ T at a higher temperature $T_s(1) \sim 45$ K, realizing a concave trapped field distribution over the bulk

* Corresponding author. Tel./fax: +81 19 621 6363.
E-mail address: fujishiro@iwate-u.ac.jp (H. Fujishiro).

0921-4534/$ - see front matter © 2006 Elsevier B.V. All rights reserved.
doi:10.1016/j.physc.2006.04.077

sample. Secondly, the bulk is cooled down to $T_s(2) \sim 30$ K and the higher pulse fields of $B_{ex}(2) \sim 6.7$ T are applied twice. As a result, we obtained $B_T^P = 4.47$ T on the surface of the GdBaCuO bulk, which was the highest record using PFM technique at that time [8]. The reduction of ΔT due to the already trapped flux at the first stage and the application of the higher $B_{ex}(2)$ at the second stage are key points to enhance B_T^P.

In this paper, we inquire into this technique and report the renewed highest B_T^P value of 5.20 T by the MMPSC technique. We elucidate the importance of the optimization of $B_{ex}(2)$ at the second stage and investigate the effect of the stainless steel ring set onto the bulk disk on the B_T^P value.

2. Experimental

A highly *c*-axis oriented GdBaCuO bulk disk (45 mm in diameter and 15 mm in thickness, Nippon Steel Co., Ltd.) was used. The experimental setup around the bulk is shown in the inset of Fig. 1(a). The stainless steel ring with 4 mm in thickness and 15 mm in height was tightly set onto the bulk disk using Apiezon-N grease in order to reduce ΔT during PFM [8]. The bulk with the ring was stacked on the soft-iron disk on the cold stage of the GM cycle helium refrigerator and was magnetized using a solenoid-type pulse coil dipped in liquid N_2 with a soft-iron cylinder [7]. Three Hall sensors (F.W. Bell, model BHA 921) were

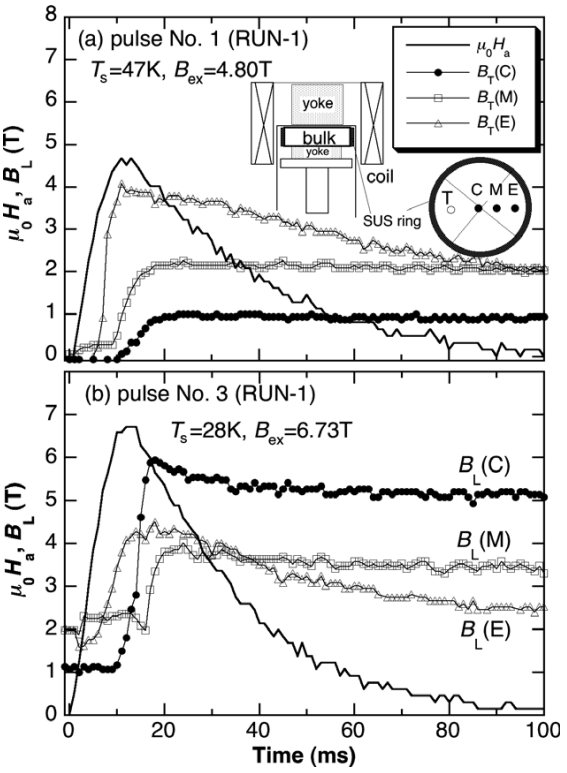

Fig. 1. The applied field $[\mu_0 H_a(t)]$ and the local fields $[B_L(C)(t), B_L(C)(t), B_L(E)(t)]$ for RUN-1 after applying the (a) pulse No. 1 and (b) pulse No. 3.

adhered to the position C (bulk center), M (8 mm distant from the bulk center) and E (16 mm distant from the bulk center) and the time evolutions of the local fields $[B_L(C)(t), B_L(C)(t)$ and $B_L(E)(t)]$ were monitored on a digital oscilloscope. The applied field $\mu_0 H_a(t)$, of which the maximum strength was defined as B_{ex}, was monitored by the current $I(t)$ flowing through the shunt resistor. The rising time of the pulse field was 13 ms and the duration was ~80 ms. The bulk temperature $T(t)$ was measured at the position T using a fine thermocouple.

3. Results and discussion

We have performed three MMPSC runs (RUN-1–RUN-3). Table 1 summarizes the initial conditions [T_s and B_{ex}] and the results [T_{max}, ΔT_{max} and $B_T(C)$] for each run, where B_T^P means B_L ($t \to \infty$). For RUN-1, at the first stage, the pulse field of $B_{ex}(1) = 4.8$ T was applied twice (pulse No. 1 and No. 2) at $T_s(1) = 47$ K. Then the bulk was cooled down to $T_s(2) \sim 28$ K and the higher $B_{ex}(2) \sim 6.7$ T was applied twice at the second stage (pulse No. 3 and No. 4). The highest $B_T^P = B_T(C) = 5.20$ T was attained for the pulse No. 4. The first stage procedure of RUN-2 and RUN-3 was performed under the similar conditions to that of RUN-1 and, for the second stage, the higher $B_{ex}(2)$ (=7.01 T for RUN-2) and lower $B_{ex}(2)$ (=6.04 T for RUN-3) were applied in order to clarify the importance of the strength of $B_{ex}(2)$. In Table 1, the initial conditions and the results using the same bulk without the stainless steel ring are also shown as RUN-0, in which $B_T^P = 4.47$ T was obtained [7].

Figs. 1(a) and (b) show the time dependences of the applied field $\mu_0 H_a(t)$ and the local fields $[B_L(C)(t), B_L(M)(t), B_L(E)(t)]$ for RUN-1 after applying the pulse No. 1 and No. 3, respectively. $B_L(E)(t)$, $B_L(M)(t)$, and $B_L(C)(t)$ rise up in this order, take a maximum and then slowly decrease to a final stable value. The maximum value of $B_L(E)(t)$ is 4.0 T but that of $B_L(C)(t)$ reaches only about 0.9 T. The maximum temperature rise ΔT_{max} (=18 K) takes place, which may mainly come from the heat generation due to the flux trapping. For the pulse No. 2, the maximum of $B_L(E)(t)$ decreases to 2.9 T and ΔT_{max} also decreases to 5 K due to the already trapped fluxes which obstruct the intrusion of the magnetic flux. $B_T(C)$ shows a slight increase to 1.10 T but the $B_T(M)$ and $B_T(E)$ are nearly unchanged, both of which are higher than $B_T(C)$. For the pulse No. 3 as shown in Fig. 1(b), the maximum of $B_L(E)(t)$ remains at 4.2 T, while that of $B_L(C)(t)$ increases to 6.0 T and $B_T^P = B_T(C)$ survives at 5.12 T. These results come from the ΔT reduction due to the trapped fluxes during the first stage and the small ΔT_{max} (=29 K) and low T_{max} (=57 K) prevent the escape of the magnetic fluxes from the bulk. For the pulse No. 4, $B_T^P = B_T(C)$ slightly increases to 5.20 T.

Figs. 2(a) and (b) present the time evolution of the local field $B_L(t)$ as a function of the distance along the radius direction on the bulk for the pulse No. 1 of RUN-1 for

Table 1
The initial conditions [T_s, B_{ex}] and the results [T_{max}, ΔT_{max}, final B_T^P] of three MMPSC runs; the RUN-0 shows the previous results in which $B_T^P = 4.47$ T was attained [7]

Run		First stage		Second stage		Final B_T^P
		Pulse No.1	Pulse No. 2	Pulse No. 3	Pulse No. 4	
RUN-1	$T_s(B_{ex})$	47 K (4.80 T)	47 K (4.80 T)	28 K (6.73 T)	28 K (6.56 T)	
	$T_{max}(\Delta T_{max})$	65 K (18 K)	52 K (5 K)	**57 K (29 K)**	50 K (22 K)	**5.20 T**
RUN-2	$T_s(B_{ex})$	47 K (4.80 T)	48 K (4.94 T)	27 K (7.01 T)	29 K (6.72 T)	
	$T_{max}(\Delta T_{max})$	65 K (18 K)	52 K (4 K)	**59 K (32 K)**	53 K (24 K)	**3.02 T**
RUN-3	$T_s(B_{ex})$	46 K (4.52 T)	46 K (4.52 T)	29 K (6.04 T)	30 K (6.87 T)	
	$T_{max}(\Delta T_{max})$	64 K (18 K)	50 K (4 K)	**49 K (20 K)**	52 K (22 K)	**4.10 T**
RUN-0	$T_s(B_{ex})$	45 K (4.54 T)	48 K (4.60 T)	29 K (6.72 T)	29 K (6.59 T)	
	$T_{max}(\Delta T_{max})$	62 K (18 K)	53 K (5 K)	**58 K (29 K)**	53 K (24 K)	**4.47 T**

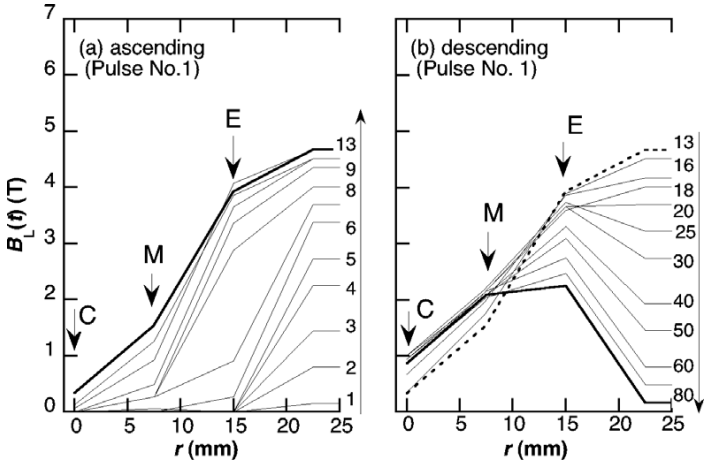

Fig. 2. The time evolution of the local field $B_L(t)$ as a function of the distance along the radius direction for the pulse No. 1 of RUN-1 for the (a) ascending and the (b) descending processes.

the ascending and descending processes, respectively, both of which are reconstructed on the basis of Fig. 1(a). For the ascending process, the flux intrusion starts to increase from the periphery and the small amount of the fluxes arrives at the bulk center. After the $\mu_0 H_a(t)$ value takes a maximum at $t = 13$ ms, the intruded fluxes gradually escape in the region outer than $r = 10$ mm but the local fields at positions C and E continue to increase slightly. If the B_T profile is assumed to be symmetrical along the circumferential direction, it should be noted that the B_T profile for the first stage shows the concave and "*M-shaped*" one. This B_T distribution must be a key point to bring about the trapped field higher than 5 T at the second stage.

Figs. 3(a) and (b) show the similar $B_L(t)$ profile for the pulse No. 3 ($B_{ex} = 6.73$ T) of RUN-1 for the ascending and descending processes, respectively. $B_L(E)(t)$ increases but $B_L(C)(t)$ and $B_L(M)(t)$ hardly change for the ascending process. For the descending process, however, $B_L(C)(t)$ sharply increases just after $\mu_0 H_a(t)$ takes a maximum and $B_L(M)(t)$ also slightly increases and the conical trapped field distribution with $B_L(C) > B_L(M) > B_L(E)$ is obtained. These behaviors suggest that the already trapped fluxes in the first stage are pushed into the bulk center and that the additional fluxes are supplied from the peripheral region. The "*M-shaped*" profile in the first stage changes to the "*cone-shaped*" one at $T_s \sim 30$ K for the pulse No. 3 with $B_{ex} = 6.73$ T. It was pointed out in the previous paper [9] that the height of the cone ($=B_T(C)$) at the second stage depends on the height of the edge in the "*M-shaped*" profile; $B_T(E)$ should be higher and $B_T(C)$ should be lower at the first stage.

Figs. 4(a) and (b) present the time dependences of the applied field and the local fields for RUN-2 and RUN-3 on applying the pulse No. 3, respectively. In RUN-2, where $B_{ex} = 7.01$ T of the pulse No. 3 is higher than that in RUN-1, all the maximum values of local fields, especially $B_L(M)(t)$, increase. Then $B_L(C)(t)$ cannot maintain the higher value and drastically decreases for $t > 60$ ms by a spontaneous flux jump. As a result, the trapped fields at the positions C, M and E decrease to ~2 T and the large heat generation should be the origin for the depression. For RUN-3 shown in Fig. 4(b), where lower pulse field

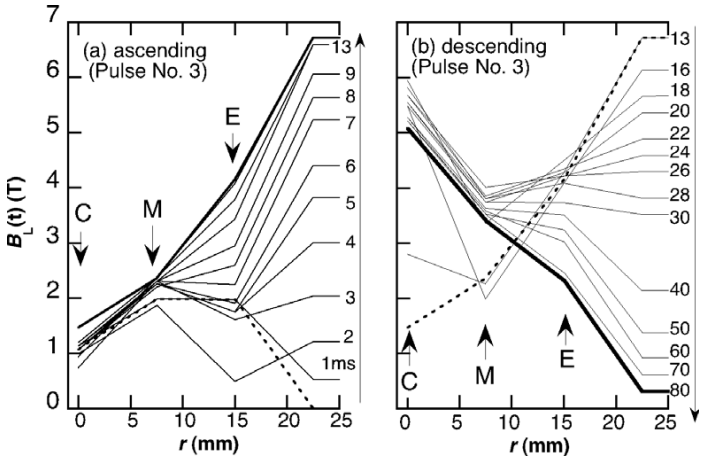

Fig. 3. $B_L(t)$ as a function of the distance along the radius direction on the bulk for the pulse No. 3 of RUN-1 for the (a) ascending and the (b) descending processes.

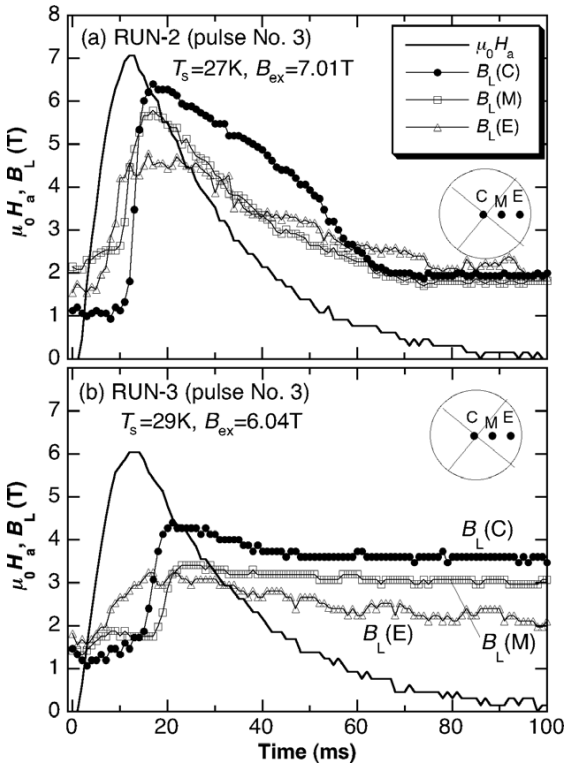

Fig. 4. The time dependences of the applied field and the local fields for (a) RUN-2 and (b) RUN-3 after applying the pulse No. 3.

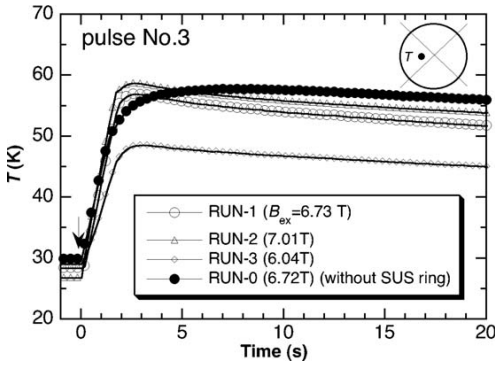

Fig. 5. The time dependences of temperature $T(t)$ at position T after the pulse No. 3 application of each run.

of $B_{ex} = 6.04$ T was applied, the increase of the $B_L(t)$ at each position is small and the B_T(C) value attains only 3.6 T with a round shaped B_T distribution.

Finally we comment on the effect of the stainless steel ring. Fig. 5 shows the time dependences of temperature $T(t)$ after the pulse No. 3 application of each run. For RUN-1 to RUN-3, $T(t)$ rises up, takes a maximum at $t = 2$ s and then slowly decreases. The local heat generation and the large temperature rise must mainly occur in the inner part of the bulk within the pulse duration $t \sim 0.1$ s, but the temperature change is observable with a long time delay determined by the thermal diffusivity. The maximum temperature rise ΔT_{max} increases with increasing B_{ex} of the pulse No. 3. $T(t)$ of RUN-0 without stainless steel ring is also shown in Fig. 5 for comparison. It is to be noticed that $T(t)$ for RUN-0 is much different; $T(t)$ slowly increases and takes a maximum at $t \sim 7$ s in spite of the identical ΔT_{max} and T_{max} values to those in RUN-1. These results suggest that the heat propagation changes owing to the metal ring setting and, as a result, the B_T^P is enhanced from 4.47 T to 5.20 T.

In summary, we performed the MMPSC method on the GdBaCuO bulk under several conditions and clarified what are the important factors to enhance B_T^P over 5 T. At the first stage in the MMPSC process, the "*M-shaped*" trapped field profile should be realized on the bulk; B_T(C) at the bulk center should be as low as ~1 T and the barrier height B_T(E) at the periphery region must be enhanced to 2.5–3 T.

At the second stage at lower T_s, the optimum higher field B_{ex}, which is 6.7 T for this bulk, should be applied. The B_T^P value increased from 4.47 T to 5.20 T as a result of the stainless steel ring setting onto the bulk disk. The microscopic change in the heat propagation should take place by the ring setting onto the bulk. The detailed study is in progress.

References

[1] U. Mizutani, H. Hazama, T. Matsuda, Y. Yanagi, Y. Itoh, K. Sakurai, A. Imai, Supercond. Sci. Technol. 16 (2003) 1207.
[2] Y. Yanagi, Y. Itoh, M. Yoshikawa, T. Oka, T. Hosokawa, H. Ishihara, H. Ikuta, U. Mizutani, in: T. Yamashita, K. Tanabe (Eds.), Advances in Superconductivity XII, Springer-Verlag, Tokyo, 2000, p 47.
[3] H. Fujishiro, K. Yokoyama, T. Oka, K. Noto, Supercond. Sci. Technol. 17 (2004) 51.
[4] H. Fujishiro, M. Kaneyama, K. Yokoyama, T. Oka, K. Noto, Jpn. J. Appl. Phys. 44 (2005) 4919.
[5] H. Fujishiro, K. Yokoyama, M. Kaneyama, M. Ikebe, T. Oka, K. Noto, Physica C 426–431 (2005) 594.
[6] K. Yokoyama, M. Kaneyama, H. Fujishiro, T. Oka, K. Noto, Physica C 426–431 (2005) 671.
[7] H. Fujishiro, M. Kaneyama, T. Tateiwa, T. Oka, Jpn. J. Appl. Phys. 44 (2005) L1221.
[8] H. Fujishiro, K. Yokoyama, M. Kaneyama, T. Oka, K. Noto, IEEE Trans. Appl. Supercond. 15 (2005) 3762.
[9] H. Fujishiro, M. Kaneyama, T. Tateiwa, T. Oka, to be published in J. Phys. Conf. Series (2006).

3. (G-1) H. Fujishiro and T. Naito,
"Simulation of temperature and magnetic field distribution in superconducting bulk during pulsed field magnetization",
Supercond. Sci. Technol. **23** (2010) 105021 (8 pages) (No. 174 paper)

Supercond. Sci. Technol. **23** (2010) 105021 (8pp) doi:10.1088/0953-2048/23/10/105021

Simulation of temperature and magnetic field distribution in superconducting bulk during pulsed field magnetization

Hiroyuki Fujishiro and Tomoyuki Naito

Faculty of Engineering, Iwate University, 4-3-5 Ueda, Morioka 020-8551, Japan

E-mail: fujishiro@iwate-u.ac.jp

Received 4 July 2010, in final form 3 September 2010
Published 17 September 2010
Online at stacks.iop.org/SUST/23/105021

Abstract
A theoretical simulation of electromagnetic and thermal fields was performed for a cryocooled superconducting bulk disc after applying a magnetic pulse. The results of the simulation qualitatively reproduced the experimental ones for the time and applied field dependences of the trapped field B_z and the temperature T on the bulk surface. For magnetic pulse application with a rise time of $\tau = 0.01$ s, the magnetic flux propagation was about two orders of magnitude faster than the heat propagation because of the low thermal conductivity of the bulk. The results show that the intruding magnetic flux escaped because of the delayed temperature rise. For a longer magnetic pulse application with $\tau = 1$ or 10 s, the flux propagation speed becomes slow and approaches the heat propagation speed. In this case, the magnetic flux escape attributable to the flux creep becomes small and a higher trapped field can be achieved. The method of exploring the enhancement of the trapped field using pulsed field magnetization is discussed.

1. Introduction

Recently, pulsed field magnetization (PFM) for REBaCuO bulk (RE: rare earth element or Y) has been investigated intensively for practical applications as a substitute for field-cooled magnetization (FCM) because PFM is an inexpensive and mobile experimental set-up with no need for a superconducting magnet. The trapped field B_z achievable by PFM is nonetheless lower than that achievable by FCM because of the large temperature rise caused by the dynamical motion of the magnetic flux. Several approaches have been performed and have succeeded in enhancing B_z including an iteratively magnetizing pulsed field method with reducing amplitude (IMRA) [1] and a multi-pulse technique with step-wise cooling (MPSC) [2]. We have experimentally examined the time and spatial dependences of the temperature $T(t, x)$, local field $B_z(t, x)$, and the trapped field B_z on the surface of cryocooled REBaCuO bulks during PFM for various starting temperatures T_s and applied fields B_{ex} [3–5]. To enhance B_z, it is believed that the reduction in temperature rise ΔT and the lowering of T_s are effective because of the enhancement of the critical current density J_c, similar to the case for FCM. Considering the obtained experimental results, we proposed a new PFM technique named modified MPSC (MMPSC) [6] and successfully realized a highest field trap of $B_z = 5.20$ T on a $\varnothing$45 mm GdBaCuO bulk at 30 K [7], which is a record-high value by PFM to date. However, experimental research has been limited. Results have shown little progress to explore the enhancement of the trapped field using PFM. It is necessary to use a theoretical simulation to elucidate the multi-physics in the bulk during PFM.

Several studies of theoretical simulations for PFM have been reported. Many of the studies were performed under conditions in which the bulk was immersed in liquid nitrogen. Simulations have been performed also for cryocooled bulks; Kajikawa *et al* reported theoretical results of the MMPSC method, in which the experimental results were reproduced qualitatively through the simulation [8]. Komi *et al* reported magnetic and thermal fields during PFM in a cryocooled bulk with inhomogeneous superconducting properties [9]. We investigated heat propagation in drilled holes in the bulk both experimentally [10] and theoretically [11]. The results suggest that the heat generation took place adiabatically because of its greater heat generation than the cooling power of the refrigerator.

As described in this paper, we constructed the framework of the theoretical simulation in the superconducting bulk with

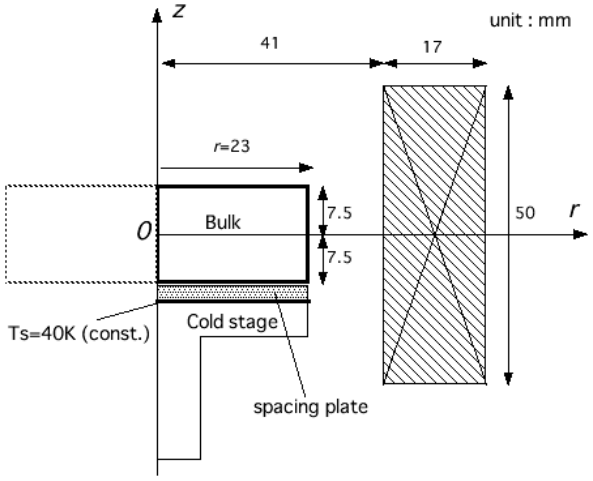

Figure 1. Structure and dimensions around the bulk and solenoid copper coil for pulsed field magnetization (PFM). The 1 mm thick spacing plate with thermal conductivity of $\kappa_{\rm cont}$ was placed between the bulk and the cold stage of the refrigerator, which imaginarily represents the cooling power of the refrigerator and the thermal contact of the bulk on the cold stage.

homogeneous superconducting properties after a magnetic pulse application using the finite element method (FEM). We reproduced the experimental results using the simulation. We also investigated the effect of a magnetic pulse application with a longer rise time of $\tau = 1$ or 10 s on the $B_z(t)$ and $T(t)$ values than those using a magnetic pulse with $\tau = 0.01$ s, which was used experimentally because the long pulse application enhanced the trapped field experimentally [12]. The direction to explore the enhancement of the trapped field by PFM is discussed herein.

2. Modelling and theoretical simulation

Based on our experimental set-up around the bulk [5], the framework of the theoretical simulation was constructed. A schematic view is presented in figure 1. A superconducting bulk disc of 46 mm diameter and 15 mm thickness was stacked on the cold stage of a refrigerator in a vacuum chamber and cooled to the starting temperature $T_{\rm s} = 40$ K. We set the spacing plate with thermal conductivity $\kappa_{\rm cont}$ between the bulk and the cold stage to 1 mm thickness, which imaginarily represents both the cooling power of the refrigerator and the thermal contact. Then $\kappa_{\rm cont}$ was set as 0.5 W mK^{-1} based on the experimental results of $T(t)$ on the bulk surface [6]. In the simulation, the bulk was magnetized using a solenoid-type copper coil (82 mm I.D., 116 mm O.D., and 50 mm height). Physical phenomena during PFM are described using electromagnetic and thermal fields. The equations and parameters were taken from [9]. Commercial software, Photo-Eddy, combined with Photo-Thermo (Photon Ltd, Japan), was used for analyses of the magnetic field and temperature distribution in superconducting bulk during PFM.

Their fundamental equations on the axisymmetric coordinate are as follows.

$$\frac{\partial}{\partial r}\left[\frac{\nu}{r}\frac{\partial}{\partial r}(r\boldsymbol{A})\right] + \frac{\partial}{\partial z}\left(\nu\frac{\partial \boldsymbol{A}}{\partial z}\right) = J_0 + J \tag{1}$$

$$\rho C\frac{\partial T}{\partial t} = \frac{1}{r}\frac{\partial}{\partial r}\left(r\kappa_{ab}\frac{\partial T}{\partial r}\right) + \frac{\partial}{\partial z}\left(\kappa_c\frac{\partial T}{\partial z}\right) + Q. \tag{2}$$

Therein, $\boldsymbol{A}$ represents the magnetic vector potential, J_0 is the forced current density or coil current density, J denotes the superconducting current density or induced current density, and Q signifies the heat generation. In equation (2), T denotes the temperature, C is the specific heat, and κ_{ab} and κ_c respectively denote the thermal conductivity in the ab-plane and along the c-axis.

The J value is given as

$$J = \sigma E = -\sigma\frac{\partial \boldsymbol{A}}{\partial t}, \tag{3}$$

where E is the electric field and σ is the electrical conductivity. Then FEM analysis of the coupled problem with electromagnetic field and heat diffusion was performed.

The power-n model was used to describe the nonlinear E–J characteristic in superconducting bulk, as

$$E = E_{\rm c}\left(\frac{J}{J_{\rm c}}\right)^n, \tag{4}$$

where $J_{\rm c}$ is the critical current density and $E_{\rm c}$ is the reference electric field. The magnetic field dependence of the $J_{\rm c0}$ was described using the Kim model [13] as

$$J_{\rm c} = J_{\rm c0}\frac{B_0}{|B| + B_0}, \tag{5}$$

where $J_{\rm c0}$ is $J_{\rm c}$ for $B = 0$ and B_0 is constant. The temperature dependence of $J_{\rm c0}$ is described by the following equation,

$$J_{\rm c0} = \alpha\left\{1 - \left(\frac{T}{T_{\rm c}}\right)^2\right\}^{\frac{3}{2}}, \tag{6}$$

where $T_{\rm c}$ is the critical temperature (=92 K) at $B = 0$ and α is constant. Heat generation Q in the conductor is given as $Q = JE$. Iterative calculations were performed to obtain the convergence of σ in the superconductor at each time step.

The applied pulsed field $B_{\rm ex}(t)$ with the rise time of $\tau = 0.01$ s was approximated in the following equation:

$$B_{\rm ex}(t) = B_{\rm ex}\frac{t}{\tau}\exp\left(1 - \frac{t}{\tau}\right). \tag{7}$$

The numerical values for the parameters used in the simulation are presented in table 1. The κ_{ab}, κ_c and C values were presumed to be temperature-independent for simplicity.

3. Example of experimental results

Let us show an example of the experimental results of the trapped field on the bulk magnetized by PFM. Figure 2(a)

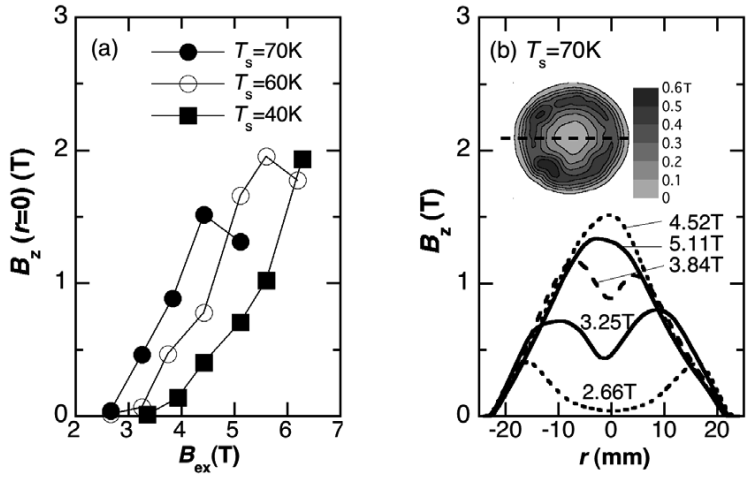

Figure 2. Example of experimental results for the trapped field on the GdBaCuO bulk magnetized by PFM [4]. (a) Trapped field $B_z(r = 0)$ at the centre of the bulk at various starting temperatures T_s after applying a pulsed field B_{ex} with a rise time of $\tau = 0.01$ s. (b) Cross-section of the B_z profiles for various applied pulsed fields B_{ex} at $T_s = 70$ K. In the inset, an example of the two-dimensional B_z profile is shown for $B_{ex} = 2.66$ T.

Table 1. Numerical values for parameters used in the simulation.

Symbol	Parameter	Value
T_c	Transition temperature in equation (6)	92 K
ρ	Mass density of bulk in equation (2)	5.9×10^3 kg m^{-3}
C	Specific heat of bulk in equation (2)	1.32×10^2 J kg^{-1} K^{-1}
κ_{ab}	Thermal conductivity of bulk along the *ab*-plane in equation (2)	20 W mK^{-1}
κ_c	Thermal conductivity of bulk along the *c*-axis in equation (2)	4 W mK^{-1}
n	n-value in equation (4)	8
E_c	Constant in equation (4)	1×10^{-6} V m^{-1}
B_0	Constant in equation (5)	1.3 T
α	Constant in equation (6)	0.23–1.83×10^9 A m^{-2}
σ	Electrical conductivity ($T > T_c$) in equation (3)	1×10^3 S cm^{-1}
τ	Rise time of the pulse in equation (7)	0.01, 1, 10 s
κ_{cont}	Thermal conductivity of spacing plate	0.5 W mK^{-1}

shows the trapped field $B_z(r = 0)$ at the centre of the GdBaCuO bulk (45 mm in diameter and 18 mm in thickness) after applying a pulsed field B_{ex} at various starting temperatures T_s [4]. The rise time τ of the pulsed field was 0.01 s. $B_z(r = 0)$ at $T_s = 70$ K starts to increase for $B_{ex} \geqslant 2.7$ T, takes a maximum at $B_{ex} = 4.4$ T and then decreases with increasing B_{ex}. For lower T_s, the applied field, at which the magnetic flux starts to be trapped at the bulk centre, and the peak of the $B_z(r = 0)$ value increase with decreasing T_s because of the enhancement of the critical current density J_c.

Figure 2(b) presents a vertical cross-section of the $B_z(r)$ profiles after applying a pulsed field at $T_s = 70$ K [4]. In the inset, an example of the two-dimensional B_z profile is shown for $B_{ex} = 2.66$ T. The trapped field profile changes from a concave shape for $B_{ex} \leqslant 3.84$ T to a convex shape for $B_{ex} \geqslant 4.52$ T. For lower $T_s = 40$ K, similar changes of the B_z profile were observed as a function of B_{ex} (not shown). However, $B_z(r = 0)$ at the bulk centre was small, even if a pulsed field with identical strength was applied as that at 70 K. The maximum $B_z(r = 0)$ increases to 1.8 T for $B_{ex} = 6.29$ T, but the convex profile cannot be realized because of the strong pinning force at low temperatures.

4. Results of simulation and discussion

4.1. Applied field dependence of trapped field

Figure 3(a) depicts the results of the simulation of the trapped field $B_z(r = 0)$ at the centre of the bulk surface as a function of the applied field B_{ex} for various α values in equation (6). The J_{c0} values at 40 K for $\alpha = 1.83 \times 10^9$, 9.2×10^8, 4.6×10^8 and 2.3×10^8 are, respectively, $J_{c0} = 1.33 \times 10^9$, 6.6×10^8, 3.3×10^8 and 1.6×10^8 A m^{-2}. The J_{c0} values for a typical superconducting bulk are, respectively, 2–3×10^9 A m^{-2} at 40 K and 1–2×10^8 A m^{-2} at 77 K [14]. Therefore, $\alpha = 1.83 \times 10^9$ is a typical value of the bulk at 40 K. In all cases, the $B_z(r = 0)$ starts to increase concomitantly with increasing applied pulsed field B_{ex}, becomes maximum and then decreases with a further increase in B_{ex}. The critical applied field B_{ex}^C, at which the magnetic flux starts to trap at the bulk centre, increases concomitantly with increasing α. The results presented in figure 3(a) can also be interpreted as the T_s dependence of $B_z(r = 0)$ for various B_{ex} for the bulk with constant α, which is consistent with the experimental results shown in figure 2(a). Although the trapped field B_z^{FC} achieved by FCM increases concomitantly with increasing J_c, the trapped field B_z achieved by PFM is not necessarily enhanced for higher J_c because of the large temperature rise, as described in section 4.2.

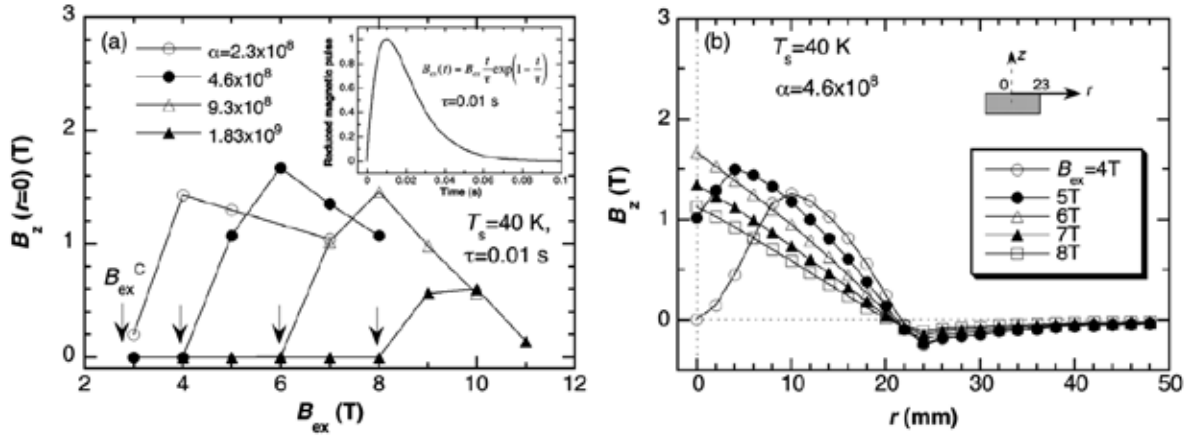

Figure 3. (a) Results of simulation of applied field dependence of the trapped field B_z at the bulk centre ($r = 0$) for various α values ($T_s = 40$ K). The inset shows the time dependence of the normalized magnetic pulse. Arrows indicate the critical applied field B_{ex}^{C} for each α value (see the text). (b) Cross-section of the trapped field profiles for $\alpha = 4.6 \times 10^8$ at $T_s = 40$ K as a function of B_{ex} (simulation).

In the simulation, the maximum temperature $T_{max}(r = 0)$ at the centre of the bulk surface increased concomitantly with increasing B_{ex}, which was independent of the α value. These results suggest that the generated heat was determined by the strength of B_{ex} and that the temperature rises adiabatically because of the smaller heat transfer to the cold stage. The result reproduces the experimental results, in which T_{max} for the YBaCuO bulk with a lower pinning force is nearly the same as that for the GdBaCuO bulk with a higher pinning force [5].

Figure 3(b) presents a cross-section of the trapped field $B_z(r)$ profile for $\alpha = 4.6 \times 10^8$ for various applied fields B_{ex}. The positions of $r = 0$ and 23 mm are, respectively, the centre and edge on the bulk surface. The $B_z(r)$ profile changes from concave for lower B_{ex} to convex for higher B_{ex} and then the $B_z(r = 0)$ value decreases with further increases in B_{ex}. These behaviours are apparent for each α value and are consistent with the experimental ones as shown in figure 2(b). In this way, the results of the numerical simulation reproduced the experimental ones qualitatively.

4.2. Time dependence of local field and temperature

Figures 4(a) and (b) respectively show the time evolution and spatial distribution of the local magnetic field $B_z(t, r)$ and the temperature $T(t, r)$ on the bulk surface after applying a pulsed field of $B_{ex} = 6$ T for $\alpha = 4.6 \times 10^8$ ($J_{c0} = 3.3 \times 10^8$ A m^{-2}). The left and right parts of each figure respectively show ascending ($t \leqslant 0.01$ s) and descending ($t \geqslant 0.01$ s) stages. For the ascending stage, the magnetic flux intrudes gradually into the bulk from the bulk periphery and the magnetic gradient increases with approach to the bulk centre at $t = 0.01$ s. It should be noted that the magnetic flux concentration took place outside the bulk because of the diamagnetism of superconducting bulk, and that a magnetic field of 6.8 T was applied along the z-axis at $r = 23$ mm. For the descending stage ($t \geqslant 0.01$ s), the magnetic field decreased gradually at the outer region with increasing time. On the other hand, the local field near the bulk centre increases to 3 T at $t = 0.1$ s and then decreases gradually to $B_z = 1.7$ T at the steady state.

In figure 4(b), the temperature $T(t)$ at the bulk periphery increases gradually with time at the ascending stage, e.g. $T = 78$ K at $t = 0.01$ s. However, the temperature for $r = 0$ remains as 40 K. At the descending stage, the generated heat diffuses to the bulk centre gradually. In line with the isothermal temperature profile along the r-direction at $t = 5$ s, the temperature decreases concomitantly with increasing time. In this case, a temperature gradient exists along the z-direction because the bottom of the spacing plate was fixed at 40 K.

Figures 5(a) and (b) show the time dependence of local fields $B(r, t)$ and the temperatures $T(r, t)$ at $r = 0$, 10 and 20 mm on the bulk surface, respectively, which were re-plotted from figure 4. The time dependence of the magnetic pulse $B_{ex}(t)$ is also shown. In figure 5(a), the local field $B_z(t)$ near the bulk periphery starts to increase rapidly; it then decreases. On the other hand, $B_z(t)$ at the inner position rises with a time lag, decreases gradually, and approaches the final value for $t > 10$ s.

In figure 5(b), the temperature $T(t)$ near the bulk periphery starts to rise rapidly. It then decreases. The time at which the temperature starts to rise becomes delayed at the inner measuring position. At the bulk centre ($r = 0$), $T(t)$ takes a maximum at $t = 7$ s and is independent of the measuring position. It is noteworthy that the time at which $B_z(t)$ becomes maximum is about two orders of magnitude faster than the time at which $T(t)$ reaches its maximum value. These results are attributable to the lower thermal conductivity of the bulk and smaller heat transfer to the cold stage. After $B_z(t)$ reaches its maximum value, $T(t)$ becomes maximum. As a result, the local field decreases because of the flux creep. For $t > 7$ s, $B_z(t)$ becomes constant because the temperature decreases.

Figures 6(a) and (b) respectively show a simulation of the time dependence of the local field $B_z(t)$ and temperature $T(t)$ at the centre of the bulk surface ($\alpha = 4.6 \times 10^8$) after applying pulsed fields of $B_{ex} = 5$, 6 and 8 T. The peak height of $B_z(t)$

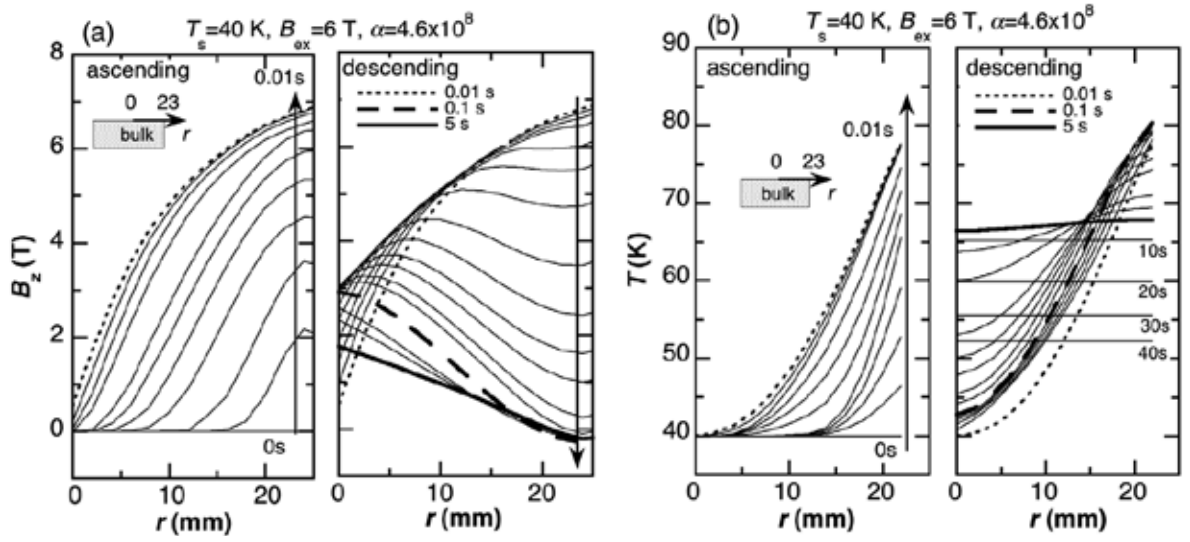

Figure 4. Time and distance dependence of (a) the local magnetic field $B(t, r)$ and (b) the temperature $T(t, r)$ on the bulk surface after applying a pulsed field of $B_{ex} = 6$ T at $T_s = 40$ K for $\alpha = 4.6 \times 10^8$. The left and right parts of each figure respectively show the ascending ($t \leqslant 0.01$ s) and descending ($t \geqslant 0.01$ s) stages.

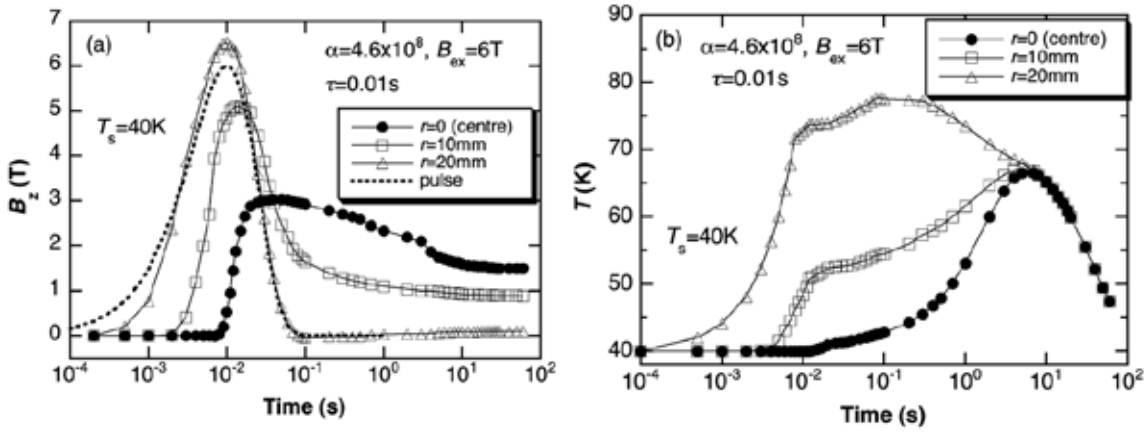

Figure 5. Time dependence of (a) the local field $B_z(t)$ and (b) the temperature $T(t)$ for $r = 0$, 10 and 20 mm on the bulk surface after applying a pulsed field of $B_{ex} = 6$ T ($\alpha = 4.6 \times 10^8$).

increases concomitantly with increasing B_{ex}. However, the time at which $B_z(t)$ takes a maximum value is about 0.05 s; it is independent of B_{ex}. In fact, $B_z(t)$ approaches the final value for $t > 10$ s. The temperature $T(t)$ increases and reaches its peak at about 7 s, which is independent of B_{ex}. The peak height of $T(t)$ increases with increasing B_{ex}.

The results of the simulation shown in figures 5 and 6 well reproduce the experimental results reported in previous papers [4, 5]. It is noteworthy that the simulation model used for this study can qualitatively demonstrate $B_z(t)$ and $T(t)$ in the bulk. However, some differences from the experimental results do exist. In the experiments at $T_s = 40$ K, the magnetic flux started to intrude and trap from 3 T at the centre of the bulk with 45 mm diameter and 15 mm thickness, which was as high-performance as $\alpha = 1.83 \times 10^9$ [4]. In existing bulks, an inhomogeneous J_c distribution exists, which arises from the crystal growth mechanism. The magnetic flux intrudes through the lower J_c paths and traps them inhomogeneously. The numerical simulation must be performed for the bulk with an inhomogeneous J_c distribution.

4.3. Application of long magnetic pulse

An extremely useful PFM technique is zero-field cooling (ZFC), of which the ascending and descending periods are of the order of 100–1000 s. Considering the Bean model, a magnetic field resembling that by FCM can be trapped by ZFC after a magnetic field twice as high as that for FCM is applied. We have reported that a trapped field B_z can be enhanced using a longer ascending magnetic pulse [12]. In

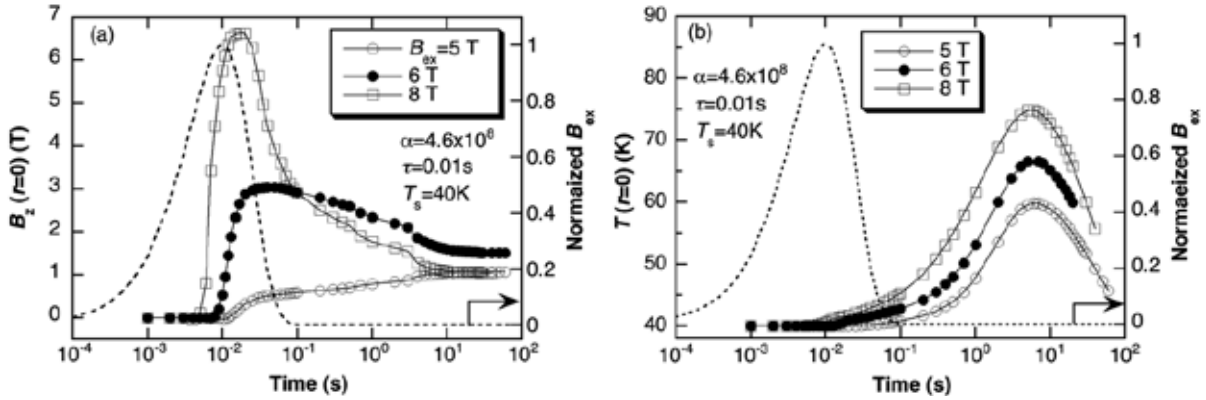

Figure 6. Time dependence of (a) the local field $B_z(t)$ and (b) the temperature $T(t)$ at the centre of the bulk surface after applying a pulsed field of $B_{ex} = 5$, 6 and 8 T ($\alpha = 4.6 \times 10^8$).

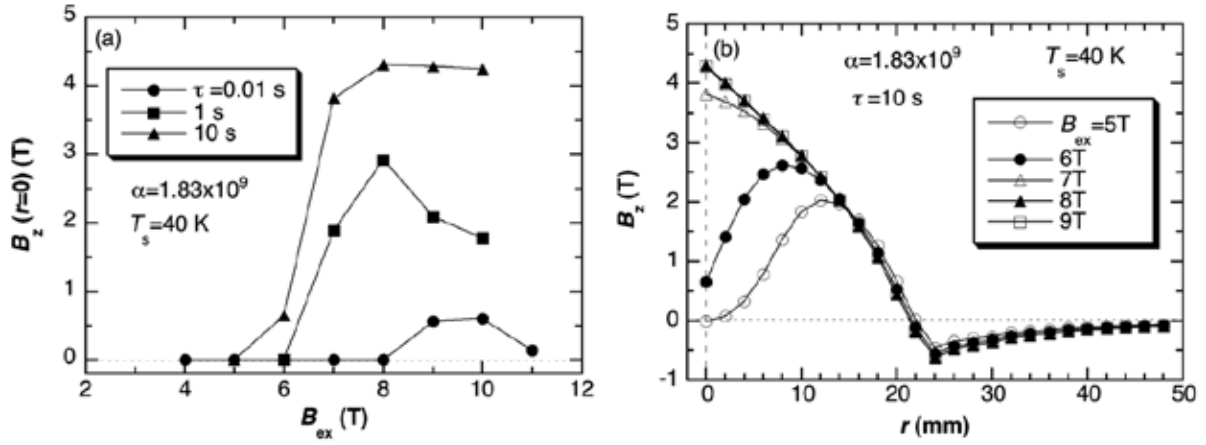

Figure 7. (a) Applied field dependence of the trapped field $B_z(r = 0)$ at the bulk centre for $\tau = 0.01$, 1 and 10 s. (b) Cross-section of the trapped field profiles for $\tau = 10$ s as a function of applied pulsed field B_{ex} ($\alpha = 1.83 \times 10^9$).

section 4.2, we presented a simulation for the bulk with lower J_c ($\alpha = 4.6 \times 10^8$; $J_{c0} = 3.3 \times 10^8$ A m^{-2} at 40 K) using a pulsed field with a rise time of $\tau = 0.01$ s. In this subsection, we present a simulation of B_z on the bulk with higher J_c ($\alpha = 1.83 \times 10^9$; $J_{c0} = 1.33 \times 10^9$ A m^{-2} at 40 K) using a longer magnetic pulse field. We discuss the origin of the B_z enhancement using a longer pulsed field and discuss the direction for the B_z enhancement using PFM.

Figure 7(a) presents the calculated trapped field $B_z(r = 0)$ on the bulk surface ($\alpha = 1.83 \times 10^9$) as a function of an applied field B_{ex} with a rise time of $\tau = 1$ and 10 s. The results for $\tau = 0.01$ s are also shown. With increasing rise time τ, the maximum trapped field $B_z(r = 0)$ increases concomitantly with increasing τ. In addition, the applied field B_{ex}^C, at which the magnetic flux starts to be trapped at the bulk centre, decreases. For example, for $\tau = 10$ s, $B_z(r = 0)$ reaches 4.3 T and B_{ex}^C decreases to 5 T. Figure 7(b) shows a typical cross-section of the trapped field profiles for $\tau = 10$ s. The $B_z(r)$ profile changes from concave to convex with increasing B_{ex} and maintains a higher B_z value. It is noteworthy that the $B_z(r = 0)$ value is enhanced for the longer τ values.

Figures 8(a) and (b) show the time evolution of local field $B_z(t)$ and temperature $T(t)$ at the centre of the bulk surface ($\alpha = 1.83 \times 10^9$) after applying a pulsed field of $B_{ex} = 8$ T with $\tau = 1$ and 10 s, respectively. In both figures, the time t_T^P at which $T(t)(r = 0)$ peaks is about 10 s, which is independent of the τ value because the thermal conductivity (κ_{ab}, κ_c) of the bulk and that of the spacing plate (κ_{cont}) are fixed. On the other hand, the time t_B^P, at which $B_z(t)(r = 0)$ peaks, increases concomitantly with increasing τ. In fact, t_B^P were, respectively 4 s and 15 s for $\tau = 1$ and 10 s. For a longer pulse application, t_B^P increases and approaches $t_T^P = 10$ s. For $\tau = 1$ s presented in figure 8(a), $B_z(t)$ decreases and saturates for $t > 10$ s, at which $T(t)$ decreases concomitantly with increasing time. The results show that the flux creep was suppressed and that a large amount of the magnetic flux remained near the bulk centre. For $\tau = 10$ s presented in figure 8(b), t_B^P is nearly equal to t_T^P; their similar behaviour is visible. This scenario is the main reason why the higher field was trapped for the long magnetic pulse application. In this regard, the long pulse application is effective for trapping a higher magnetic field. To realize a longer magnetic pulse experimentally, it is

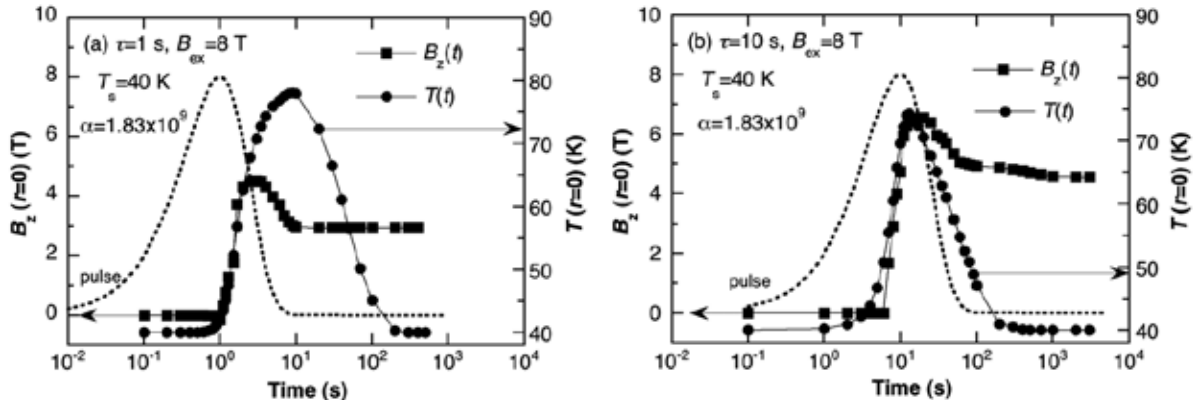

Figure 8. Time dependence of the local field $B_z(t)(r = 0)$ and temperature $T(t)(r = 0)$ for a pulsed magnetic field of $B_{ex} = 8$ T with (a) $\tau = 1$ s and (b) $\tau = 10$ s at $T_s = 40$ K. Time dependences of the applied magnetic pulse $B_{ex}(t)$ are also shown as a dotted line.

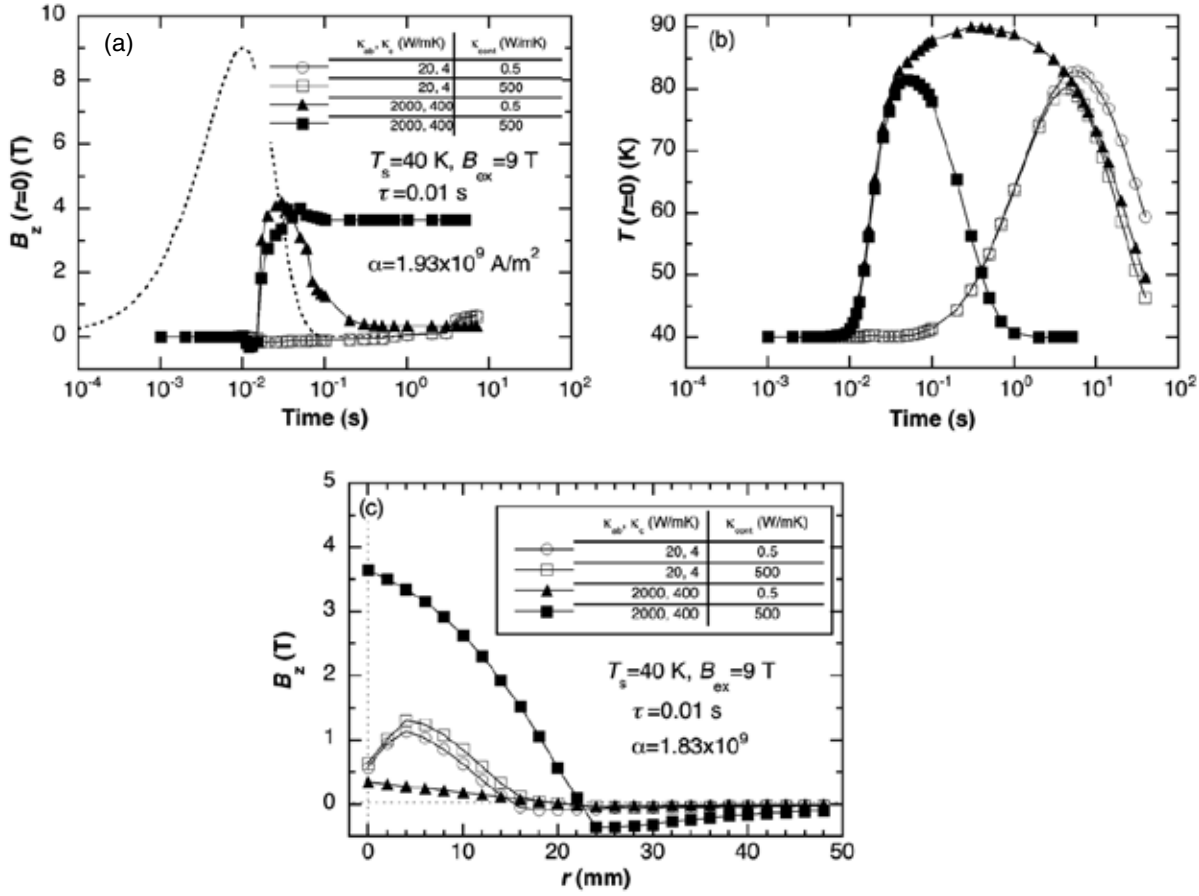

Figure 9. Time dependence of (a) the local field $B_z(t)(r = 0)$ and (b) the temperature $T(t)(r = 0)$ for a pulsed magnetic field of $B_{ex} = 9$ T with $\tau = 0.01$ s for various thermal conductivities (κ_{ab}, κ_c, κ_{cont}) ($\alpha = 1.83 \times 10^9$). (c) Trapped field profiles for respective conditions.

necessary to use a condenser bank to store a large amount of electrical energy. However, using such a device is unrealistic for practical applications at present because such condenser banks are prohibitively expensive.

4.4. Effect of thermal conductivity enhancement on the trapped field

As explained in section 4.3, a long pulsed field application is a possible solution to realize a large B_z value. However,

it is difficult to prepare a large condenser bank for a longer magnetic pulse. Using a simulation in which we can investigate an unrealistic case, exploration was performed to enhance B_z using a conventional condenser bank with $\tau = 0.01$ s. To enhance the B_z value, the time difference between t_B^P and t_T^P should be minimized. In this subsection, the effects of the thermal conductivity enhancement of the bulk and the spacing plate on the trapped field B_z are discussed.

Figures 9(a) and (b) respectively show the time evolution of a local field $B_z(t)$ and temperature $T(t)$ for the bulk with various thermal conductivities of the bulk (κ_{ab}, κ_c) and the spacing plate (κ_{cont}) after applying a pulsed field of $B_{ex} = 9$ T at 40 K. Figure 9(c) presents the trapped field profiles for each condition. For a real condition with $\kappa_{ab} = 20$, $\kappa_c = 4$ and $\kappa_{cont} = 0.5$ W mK^{-1}, the trapped field profile is shown as concave. When κ_{cont} increases to 1000 times ($\kappa_{cont} = 500$ W mK^{-1}), the trapped field does not change, although the temperature increase was reduced for $t > 10$ s. When the thermal conductivity increases to 100 times ($\kappa_{ab} = 2000$, $\kappa_c = 400$ W mK^{-1}), the generated heat diffuses over the bulk. However, the trapped field is convex but remains small because of the smaller heat transfer to the cold stage. When the thermal conductivities of both the bulk and the spacing plate increase, trapped field enhancement is predicted because the time delay between $B_z(t)$ and $T(t)$ becomes small. These results suggest that similar phenomena took place for applying a pulsed field with $\tau = 0.01$ s to those for the long pulse application ($\tau = 10$ s). However, the enhancement of the thermal conductivity for the Ag-doped bulk is as low as 10–20% [15] and enhancement of the contact thermal conductivity, i.e. enhancement of κ_{cont} cannot be realized in actual experimental set-ups.

5. Summary

A theoretical simulation of electromagnetic and thermal fields has been performed for a cryocooled superconducting bulk disc with homogeneous superconducting properties after applying a magnetic pulse. Important simulation results and conclusions obtained from this study are summarized as follows.

(1) Simulation results for bulks with various critical current densities J_{c0} qualitatively reproduced experimental results such as time and applied field dependences of the trapped field $B_z(t, r)$ and the temperature rise $T(t, r)$ on the bulk surface.

(2) For a rise time $\tau = 0.01$ s of the magnetic pulse, which is an ordinary experimental condition, the magnetic flux propagation is about two orders of magnitude faster than the heat propagation at the bulk centre because of the low thermal conductivity in the bulk. Consequently, the intruding magnetic flux escapes by the flux creep because of the delayed temperature rise.

(3) A magnetic pulse application as long as $\tau = 1$ or 10 s, which enhanced the trapped field experimentally, reduces the speed of the magnetic flux propagation. Then the difference in the propagation speed between magnetic flux and temperature becomes small. The results show that the influence on the flux creep becomes slight and the trapped field maintains a higher value. A long magnetic pulse application during PFM is a possible solution to enhance the trapped field.

(4) Based on analyses of long pulse application, we can enhance the trapped field for short pulse application through enhancement of bulk thermal conductivity and cooling power, which are two or three orders of magnitude higher than those of the real system. However, that simulation is unrealistic. Using numerical simulation, we must explore another direction to enhance the trapped field such as a multi-pulse technique for a bulk with an inhomogeneous J_c distribution.

References

[1] Yanagi Y, Itoh Y, Yoshikawa M, Oka T, Hosokawa T, Ishihara H, Ikuta H and Mizutani U 2000 *Advances in Superconductivity* vol 12 (Tokyo: Springer) p 470

[2] Sander M, Sutter U, Koch R and Klaser M 2000 *Supercond. Sci. Technol.* **13** 841

[3] Fujishiro H, Oka T, Yokoyama K, Kaneyama M and Noto K 2004 *IEEE Trans. Appl. Supercond.* **14** 1054

[4] Fujishiro H, Hiyama T, Miura T, Naito T, Nariki S, Sakai N and Hirabayashi I 2009 *IEEE Trans. Appl. Supercond.* **19** 3545

[5] Fujishiro H, Hiyama T, Tateiwa T, Yanagi Y and Oka T 2007 *Physica* C **463–465** 394

[6] Fujishiro H, Kaneyama M, Tateiwa T and Oka T 2003 *Japan. J. Appl. Phys.* **44** L1221

[7] Fujishiro H, Tateiwa T, Fujiwara A, Oka T and Hayashi H 2006 *Physica* C **445–448** 334

[8] Kajikawa K, Yokoo R, Tomachi K, Enpuku K, Funaki K, Hayashi H and Fujishiro H 2008 *Physica* C **468** 1494

[9] Komi Y, Sekino M and Ohsaki H 2009 *Physica* C **469** 1262

[10] Fujishiro H, Naito T, Furuta D and Kakehata K 2010 *Physica* C **470** 1181

[11] Fujishiro H, Kawaguchi S, Kaneyama M, Fujiwara A, Tateiwa T and Oka T 2006 *Supercond. Sci. Technol.* **19** S540

[12] Fujishiro H, Kaneyama M, Yokoyama K, Oka T and Noto K 2005 *Japan. J. Appl. Phys.* **44** 4919

[13] Kim Y B, Hempstead C F and Stand A R 1965 *Phys. Rev.* **139** A1163

[14] Ishii Y, Shimoyama J, Ogino H and Kishio K 2009 *J. Cryog. Soc. Japan* **44** 573

[15] Fujishiro H and Kohayashi S 2002 *IEEE Trans. Appl. Supercond.* **12** 1124

4. (A-41) H. Fujishiro, T. Naito, S. Ogawa, K. Nitta, J. Hejtmanek, K. Knizek and Z. Jirak,
"Valence shift of Pr ion from 3+ to 4+ in $(Pr_{1-y}Y_y)_{0.7}Ca_{0.3}CoO_3$ estimated by X-ray absorption spectroscopy",
J. Phys. Soc. Jpn. **81** (2012) 064709 (5 pages) (No. 189 paper)

Journal of the Physical Society of Japan **81** (2012) 064709 **FULL PAPERS**
DOI: 10.1143/JPSJ.81.064709

Valence Shift of Pr Ion from 3+ to 4+ in $(Pr_{1-y}Y_y)_{0.7}Ca_{0.3}CoO_3$ Estimated by X-Ray Absorption Spectroscopy

Hiroyuki FUJISHIRO*, Tomoyuki NAITO, Satoru OGAWA, Naoki YOSHIDA, Kiyofumi NITTA[1], Jiri HEJTMÁNEK[2], Karel KNÍŽEK[2], and Zdenek JIRÁK[2]

Faculty of Engineering, Iwate University, Morioka 020-8551, Japan
[1]*Japan Synchrotron Radiation Research Institute, Sayo, Hyogo 679-5198, Japan*
[2]*Institute of Physics, ASCR, Cukrovarnická 10, 162 00 Prague 6, Czech Republic*

(Received January 12, 2012; accepted April 2, 2012; published online May 17, 2012)

The temperature dependence of the X-ray absorption near-edge structure (XANES) spectra at the Pr L_3 edge was measured for the $(Pr_{1-y}Y_y)_{0.7}Ca_{0.3}CoO_3$ samples ($y = 0.075$ and 0.15), in which a peculiar metal–insulator (MI) transition and a spin-state (SS) transition took place simultaneously at a critical temperature T_{MI}. The valence states of praseodymium ion were determined using the analyses of XANES spectra. The results suggest that the average valence of the praseodymium ion increases below room temperature from the common value 3.0+, undergoes a steepest change at T_{MI}, and reaches finally 3.15+ and 3.27+ at 8 K for the $y = 0.075$ and 0.15 samples, respectively. The final valences are consistent with those estimated by the entropy change using the Schottky peak due to the Pr^{4+} Kramers doublet in the low-temperature specific heat shown in our previous paper [Phys. Rev. B **82** (2010) 165107].

KEYWORDS: Pr–Ca–Co–O, XANES, Pr valence shift, metal–insulator transition

1. Introduction

The undoped perovskite cobaltites $RECoO_3$ (RE: rare-earth element and Y) show a temperature-induced spin-state (SS) transition of Co^{3+} ions from a low spin state (LS; $t_{2g}^6e_g^0$) to a high spin state (HS; $t_{2g}^4e_g^2$), followed by the formation of the metallic state of the intermediate spin state (IS; $t_{2g}^5\sigma^*$) at higher temperatures.[1)] The transition indicates a small difference in the electronic energy δE between the crystal-field splitting and Hund's coupling energy.[2,3)] The doped systems with a mixed Co^{3+}/Co^{4+} valence generally show a stable metallic state, but a first-order metal–insulator (MI) transition was observed on cooling some Pr-based cobaltites, reported for the first time in $Pr_{0.5}Ca_{0.5}CoO_3$ at $T_{MI} = 90$ K under ambient pressure by Tsubouchi and coworkers.[4,5)] The electronic structure of this system was investigated by photoemission spectroscopy soon after the first report, revealing that the electronic structure changes at T_{MI}.[6)] The mechanism of the transition was tentatively ascribed to a spin-state crossover from itinerant cobalt states $t_{2g}^5\sigma^*$ to an ordered mixture of localized LS Co^{3+} ($t_{2g}^6e_g^0$, $S = 0$) and LS Co^{4+} ($t_{2g}^5e_g^0$, $S = 1/2$) states. Shortly thereafter, the existence of Co^{3+}/Co^{4+} ordering was questioned since the same transition was evidenced in the less doped samples $Pr_{1-x}Ca_xCoO_3$ ($x = 0.3$) under high pressures,[7)] or in $(Pr_{1-y}RE_y)_{1-x}Ca_xCoO_3$ ($0.2 \leq x \leq 0.5$) with a partial substitution of Pr by smaller RE cations or Y under ambient pressure.[8,9)] It has been found that MI transition accompanied by SS transition is conditioned not only by the presence of praseodymium ions, but also by a suitable structural distortion that depends on the average ionic radius and size mismatch of perovskite *A*-site ions.[9)] Furthermore, the critical temperature T_{MI} changes depending on the applied magnetic field, so that T_{MI} decreases with increasing magnetic field and the metallic state is finally stabilized.[10,11)] The applied field effect is thus opposite to the pressure dependence of T_{MI}, where T_{MI} increases with increasing applied pressure.[7)]

An alternative explanation has been proposed by Knížek *et al.* on the basis of electronic-structure calculations and some experimental data for $Pr_{0.5}Ca_{0.5}CoO_3$ such as the significant lattice contraction and decrease in Pr–O bond lengths that accompany MI transition.[12)] It is suggested, in their paper, that the formal cobalt valence changes below T_{MI} from mixed-valence $Co^{3.5+}$ toward pure Co^{3+} with strong preference for the LS state, and that the praseodymium valence increases simultaneously from Pr^{3+} toward Pr^{4+}. The SS transition and formation of an insulating state are thus an analogy of the compositional transition from the ferromagnetic metal $La_{0.5}Sr_{0.5}CoO_3$ to the diamagnetic insulator $LaCoO_3$.[13,14)]

The idea of praseodymium valence shift was experimentally confirmed in a study of the transport, magnetic, and thermal properties of $(Pr_{1-y}Y_y)_{0.7}Ca_{0.3}CoO_3$ ($y = 0$–0.15) by Hejtmánek *et al.*[15)] The crucial finding is the occurrence of a Schottky peak at a low-temperature specific heat, which results from a significant population of Kramers Pr^{4+} ions. Very recently, the valence transition of Pr has been probed in $Pr_{0.5}Ca_{0.5}CoO_3$ using Pr L_3 and $M_{4,5}$ edge X-ray absorption spectroscopy (XAS) by García-Munoz *et al.*[16)] They estimated that the valence of Pr ion shifted from 3.0+ to 3.15+ at 10 K. This seems to be a rather modest change in view of the above-mentioned theoretical predictions and specific-heat measurements in related $(Pr_{1-y}Y_y)_{0.7}Ca_{0.3}CoO_3$.

In this work, we applied a similar XAS spectroscopy to the analysis of $(Pr_{1-y}Y_y)_{0.7}Ca_{0.3}CoO_3$ ($y = 0.075$ and 0.15), the same samples as those used previously in the study of a low-temperature specific heat.[15)] A detailed temperature dependence of the XANES spectra around the Pr L_3 edge was measured using the bulk sensitive transmission method, and population of the Pr^{4+} state was derived from the spectra. In the calculation of average Pr valences, the detected Pr^{4+} ions are taken as formally tetravalent, although their electronic state is in fact a combination of the ionic $4f^1$ and oxygen-hole $4f^2\underline{L}$ configurations, making the number of $4f$ electrons a non-integer. The Pr^{3+} ions are essentially in an ionic $4f^2$ electron configuration.

*E-mail: fujishiro@iwate-u.ac.jp

2. Experimental Procedure

Polycrystalline $(Pr_{1-y}Y_y)_{0.7}Ca_{0.3}CoO_3$ ($y = 0$, 0.075, and 0.15) samples were prepared by a solid-state reaction. The detailed sample preparation procedures were described elsewhere.[15] For the XANES measurements, some of the samples were pulverized, mixed with 3N boron nitride (BN) powder with proper molar ratios in order to optimize absorption, and pelletized to be 6 mm in diameter and 0.5 mm in thickness.

The Pr L_3-edge XANES spectra of the samples were measured at BL01B1 of SPring-8 in Japan. The beam was monochromatized using a Si(111) double-crystal monochromator. The spectra were recorded in the transmission mode with the detectors of the ionization chambers and obtained at various temperatures from 8 to 300 K using a cryocooler. The valence of all the Pr ions was supposed to be 3.0+ for the samples at 300 K. This is a justified assumption for $T \gg T_{MI}$, also supported by the oxygen stoichiometry of the present samples fabricated under the ambient pressure, in contrast to common problem of oxygen deficiency in the prototypical $Pr_{0.5}Ca_{0.5}CoO_3$ system.[8] To determine the mixed Pr^{3+}/Pr^{4+} content at low temperatures, a comparative measurement of Pr_6O_{11} was carried out.

The recorded XANES spectra were modeled by the sum of three Lorentzian functions and one arctangent function representing the step like edge of continuum excitations. One Lorentzian function (peak A: 5966 eV) shows an excitation from $2p_{3/2}$ to $4f^2 5d^*$, which represents Pr^{3+} ions. The other Lorentzian functions (peak B2: 5969 eV and peak B1: 5979 eV) show the excitations from $2p_{3/2}$ to $4f^2\underline{L}5d^*$ and $4f^1 5d^*$, $\underline{L}$ being a ligand hole in the O $2p$ orbital, both of which represent Pr^{4+} ions.[17,18] The energy differences between peaks A, B2, and B1 were fixed according to results of Hu *et al.*[19] The curve fittings were performed in the energy range from 5944 to 5985 eV using Athena software.[20]

3. Results and Discussion

3.1 Physical properties

The electrical resistivities and specific heats of the $(Pr_{1-y}Y_y)_{0.7}Ca_{0.3}CoO_3$ samples for $y = 0.075$ and 0.15 are presented in Figs. 1 and 2. (More detailed physical properties of the samples are reported in ref. 15.) The $y = 0$ sample, which is metallic over the entire temperature range, is also shown for comparison. For the Y-substituted samples, the resistivity exhibits a sharp jump below the transition temperatures of $T_{MI} = 64$ and 132 K for $y = 0.075$ and 0.15, respectively, and increases further with decreasing temperature, pointing to a localized character of the low-temperature phase. Note that magnetic susceptibility drops markedly at the same temperature, which is a strong sign that cobalt ions transform to LS states below T_{MI}.[15] MI transition was further manifested by a pronounced peak in the specific heat, as shown in Fig. 2(a). The transitions in the resistivity and specific heat of the $y = 0.075$ sample are very sharp, suggesting a first-order character, while those for the $y = 0.15$ sample are much broader.

The low-temperature specific heat of the samples is shown in the C_p/T vs T plot in Fig. 2(b), in which the lattice and linear electronic terms of C_p as well as the nuclear heat anomaly at low temperatures were subtracted. The anomalous peak observed for the $y = 0.075$ and 0.15 samples is understood as a Schottky peak associated with the ground doublet of Kramers ion Pr^{4+}, split by the internal magnetic field existing in the samples. On the other hand, for the $y = 0$ sample, there is no Schottky peak in the range of 1–2 K,

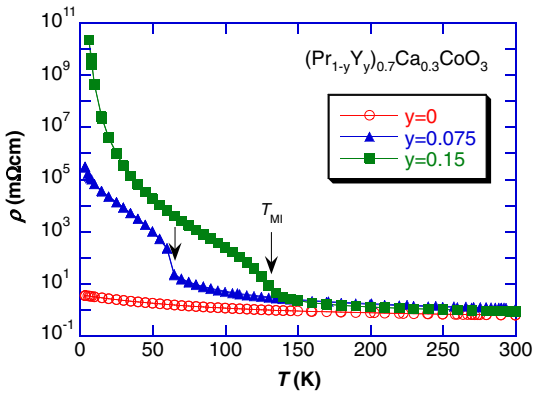

Fig. 1. (Color online) Temperature dependence of the electrical resistivity of $(Pr_{1-y}Y_y)_{0.7}Ca_{0.3}CoO_3$ ($y = 0$, 0.075 and 0.15).[15]

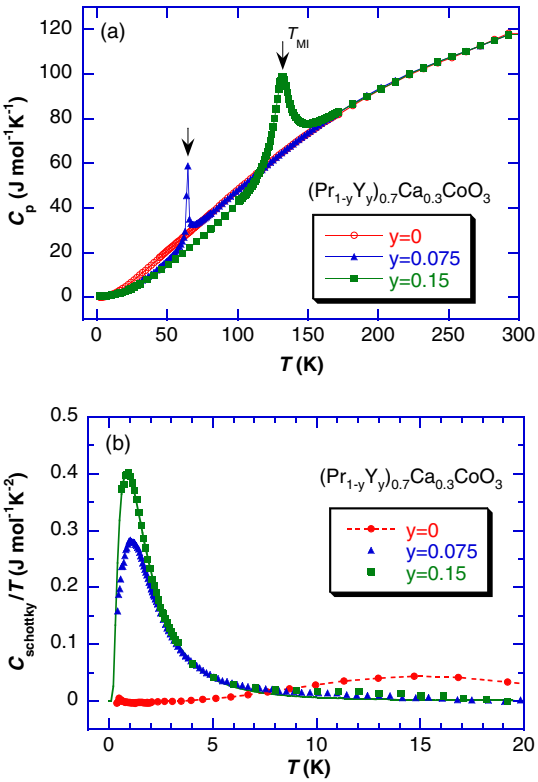

Fig. 2. (Color online) (a) Temperature dependence of the specific heat of $(Pr_{1-y}Y_y)_{0.7}Ca_{0.3}CoO_3$ ($y = 0$, 0.075 and 0.15).[15] (b) Low-temperature specific heat shown in the $C_{Schottky}/T$ vs T plot. The lattice and linear electronic terms for C_p, as well as the nuclear heat anomaly at low temperatures, were subtracted. (The full line shows the fit of the Schottky peak for $y = 0.15$.)

because all praseodymium ions remained in the Pr^{3+} valence with a nonmagnetic singlet ground state.[21] Instead, one may notice a broad maximum in Fig. 2(b) with a center at about 17 K, which is a sign of a closely-lying exited singlet state at an energy of about 4 meV. The total entropy change, which was obtained by the integration of C_{Schottky}/T over T, was determined to be 0.61 and 0.98 $\mathrm{J\,K^{-1}\,mol^{-1}}$ for the $y = 0.075$ and 0.15 samples, respectively. Considering the theoretical $R\ln 2 = 5.77\,\mathrm{J\,K^{-1}\,mol^{-1}}$, the number of Kramers ions amounts to 0.12 and 0.17 Pr^{4+} per f.u., which corresponds to average valences of praseodymium, i.e., 3.17+ and 3.29+ for the $y = 0.075$ and 0.15 samples, respectively.

It should be noted that the original interpretation of the low-temperature Schottky peak in the $(Pr_{1-y}Y_y)_{0.7}Ca_{0.3}CoO_3$ samples presumed a purely ionic state of Pr^{4+}, particularly the free-ion multiplet $^2F_{5/2}$ split by a crystal field to Kramers doublets. The character of these states may change significantly in the covalent case, but the number of Pr^{4+} species determined in ref. 15 remains valid, since both the ionic $4f^1$ and oxygen-hole $4f^2\underline{L}$ states involve odd number of electrons and display Kramers degeneracy.

3.2 *XAS measurements*

Figure 3(a) shows the temperature dependence of the XANES spectra at the Pr L_3-edge for the $y = 0.15$ sample. The two main peaks situated at 5966 and 5979 eV (named peaks A and B1) originate from the Pr $2p \rightarrow 5d$ transitions. At 300 K, $Pr^{3+}(4f^2)$ sites essentially contribute to the peak A, with a little component at peak B1 caused presumably by multiple scattering, which is commonly introduced in the theoretical calculation of XANES.[16] When the temperature crosses the transition temperature $T_{\mathrm{MI}} =$ 132 K, the shape of the XANES spectra changes markedly. The intensity of peak B1 increases and, at the same time, the intensity of peak A decreases and a new component (peak B2 at 5969 eV) can be resolved on its high-energy slope. The B1 and B2 peaks are manifestations of Pr^{4+} states, namely, of the configurations $4f^1$ and $4f^2\underline{L}$, respectively.[17–19] Similar behaviors are also observed for the $y = 0.075$ sample below $T_{\mathrm{MI}} = 64$ K, as shown in Fig. 3(b). These results suggest that the valence of the Pr ions increases from 3+ toward 4+ below T_{MI}, consistently with what was reported for the $Pr_{0.5}Ca_{0.5}CoO_3$ sample by García-Munoz *et al.*[16] The temperature dependence of the XANES spectra at the Pr L_3-edge was also measured for the $Pr_{0.7}Ca_{0.3}CoO_3$ sample (not shown), which was metallic over the entire temperature range. There was no spectral change down to 8 K, which suggested that the valence of the Pr ion remained at 3.0+, as shown in the results of the metallic $Pr_{0.55}Ca_{0.45}CoO_3$ sample.[16]

In order to determine the valence shift quantitatively, the XANES spectra were fitted to a sum of three Lorentzian functions (peak A for Pr^{3+} and peaks B1 and B2 for Pr^{4+}) and one arctangent function representing the continuum excitations, as indicated in §2. The Pr_6O_{11} spectrum shown in Fig. 3(c), in which no relevant spectroscopic changes were detected at low temperatures, was regarded as a standard for $Pr^{3.667+}$. The spectra at 300 K for each of the $(Pr_{1-y}Y_y)_{0.7}Ca_{0.3}CoO_3$ samples served as standards of $Pr^{3.0+}$. In the fitting of the temperature-dependent spectra,

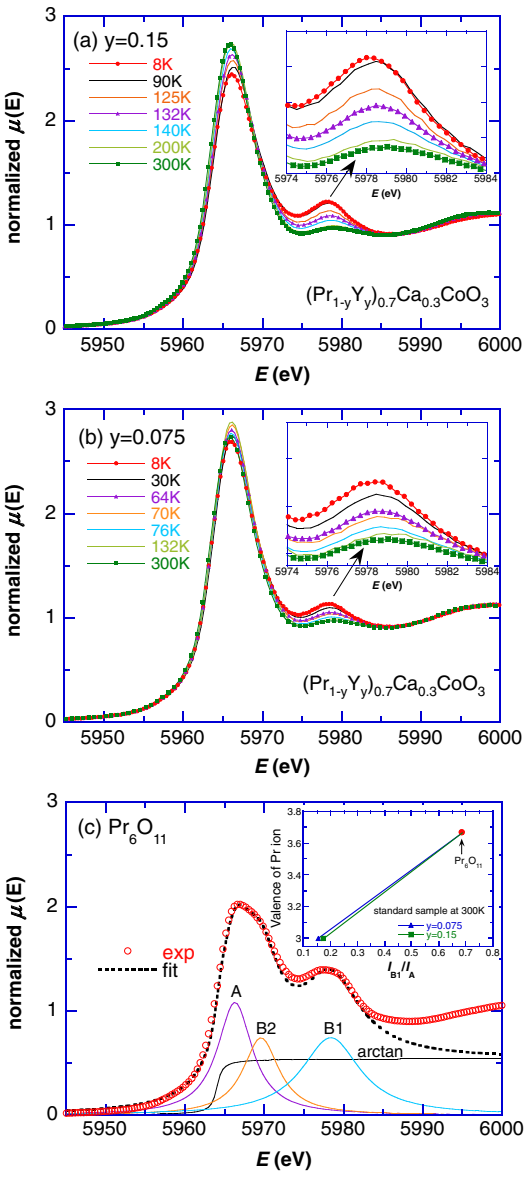

Fig. 3. (Color online) Temperature dependence of the XANES spectra at the Pr L_3-edge for the (a) $y = 0.15$ and (b) 0.075 samples. The inset of each figure shows the magnification of the spectra related to Pr^{4+} ions. (c) XANES spectra for Pr_6O_{11} at 300 K, for which the fitting were performed (see text). The inset shows the calibration line for the determination of the valence of the Pr ion used in the study.

the intensity ratio of B1 to B2 was fixed to be unity. The valence of Pr ions for the samples in the course of temperature was simply deduced from the intensity ratio $I_{\mathrm{B1}}/I_{\mathrm{A}}$ of the B1 spectral peak to the A spectral peak[22] using the calibration line in the inset of Fig. 3(c). The validity of this procedure is based on the fact that the Pr^{3+} and Pr^{4+} valence states in Pr_6O_{11} are manifested in XANES spectra by single and double peaks, respectively (see also ref. 23), which points to the same ionic $4f^2$ and covalent $4f^1/4f^2\underline{L}$ configurations as those of the praseodymium ions in the present cobaltites.

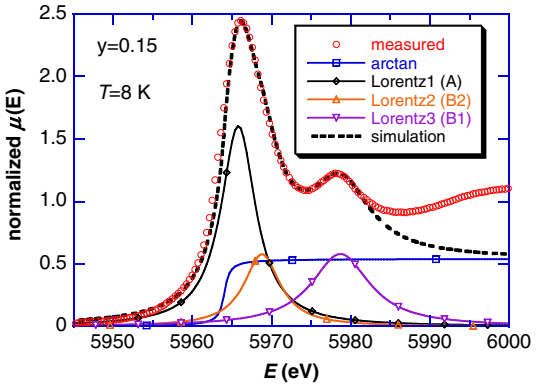

Fig. 4. (Color online) Example of the fitting of the XANES spectrum for the $y = 0.15$ sample at 8 K. For the fitting, one arctangent function and three Lorentzian functions are used (see text).

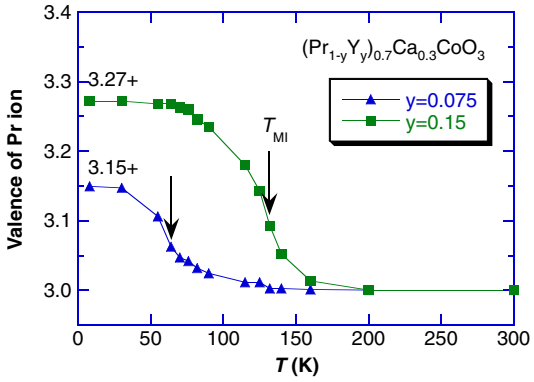

Fig. 5. (Color online) Temperature dependence of the valence of Pr ions in the samples estimated using the XANES spectra and curve fitting.

Figure 4 shows an example of the fitting curve of the XANES spectrum for the $y = 0.15$ sample at 8 K, where the valence change achieves a maximum. It is seen that the XANES spectrum can be well fitted within the energy range including the related peaks of Pr^{3+} and Pr^{4+}. The B2 component is also resolved and appears notable so that the resemblance with the Pr^{3+}/Pr^{4+} mixture in Pr_6O_{11} is obvious. The temperature course is shown in Fig. 5. The average valence changes gradually on cooling from 300 K, with the steepest increase at T_{MI}, and reaches final values of 3.15+ and 3.27+ at 8 K for the $y = 0.075$ and 0.15 samples, respectively. The ambiguity of the estimated valence values is ± 0.03, which results from the arbitrariness of the parameters in the arctangent and Lorentzian functions used. We also deduced the average valence of Pr ions from the intensity ratio $(I_{B1} + I_{B2})/(I_A + I_{B1} + I_{B2})$ of the B1, B2, and A spectral peaks using another calibration line, in which all the contributions of $4f^1$, $4f^2$, and $4f^2\underline{L}$ were considered to be the same as those adopted by Yamaoka *et al.*[17] Under this condition, the average valences of Pr ions were 3.15+ and 3.31+ for the $y = 0.075$ and 0.15 samples, which are nearly the same as that decided from the intensity ratio I_{B1}/I_A. Note that the estimated valences of the Pr ions are in very good agreement with that determined from the low-temperature specific-heat experiments, i.e., 3.17+ and 3.29+ for the $y = 0.075$ and 0.15 samples, respectively.[15] The gradual increase in the average valence of the Pr ions at $T > T_{MI}$ on cooling from 300 K also suggests that the valence of the Co ion must evolve from 3.3+ to a lower value in order to maintain the charge neutrality. This means that, with decreasing temperature, part of the LS-Co^{4+} changes to IS-Co^{3+} still within the metallic phase, and then the IS-Co^{3+} states transform to LS-Co^{3+} below T_{MI}. The gradual charge transfer between the praseodymium and cobalt subsystem is in striking contrast to the abrupt (first-order) character of the physical properties such as resistivity and susceptibility, especially at $y = 0.075$.

The valences of the Pr ions of 3.15+ and 3.27+ for the $y = 0.075$ and 0.15 samples, respectively, estimated from the intensity ratio I_{B1}/I_A in XANES spectra, correspond to 0.097 and 0.161 Pr^{4+} per f.u. and is indicative of a significant change in doping level in the cobalt subsystem (Co^{4+} content) in the low-temperature insulating state. For $y = 0.075$, the common valence distribution in the metallic state ($T \gg T_{MI}$), i.e., $(Pr_{0.925}{}^{3+}Y_{0.075}{}^{3+})_{0.7}Ca_{0.3}{}^{2+}Co_{0.7}{}^{3+}$-$Co_{0.3}{}^{4+}O_3{}^{2-}$, changes to $(Pr_{0.786}{}^{3+}Pr_{0.139}{}^{4+}Y_{0.075}{}^{3+})_{0.7}$-$Ca_{0.3}{}^{2+}Co_{0.797}{}^{3+}Co_{0.203}{}^{4+}O_3{}^{2-}$ ($T \ll T_{MI}$). For $y = 0.15$, the $(Pr_{0.85}{}^{3+}Y_{0.15}{}^{3+})_{0.7}Ca_{0.3}{}^{2+}Co_{0.7}{}^{3+}Co_{0.3}{}^{4+}O_3{}^{2-}$ in the metallic state changes to $(Pr_{0.620}{}^{3+}Pr_{0.230}{}^{4+}Y_{0.15}{}^{3+})_{0.7}$-$Ca_{0.3}{}^{2+}Co_{0.861}{}^{3+}Co_{0.139}{}^{4+}O_3{}^{2-}$ in the low-temperature insulating state. The electron transfer between the praseodymium and cobalt subsystems thus acts as the driving force for the stabilization of the LS-Co^{3+} states in the low-temperature insulating state. Discussions of the relation between the valence shift and the transition temperature T_{MI}, and of the effect of the Ca ions on the transition are in progress.

4. Conclusion

The temperature dependence of the X-ray absorption near edge spectra (XANES) at the Pr L_3-edge was measured for two $(Pr_{1-y}Y_y)_{0.7}Ca_{0.3}CoO_3$ samples ($y = 0.075$ and 0.15), in which a peculiar metal–insulator (MI) transition and a spin-state (SS) transition took place simultaneously at critical temperatures $T_{MI} = 64$ and 132 K, respectively. The existence of two distinct praseodymium species was evidenced: the Pr^{3+} valence state of the ionic $4f^2$ configuration and the formal Pr^{4+} valence state of highly covalent character with admixed $4f^1$ and oxygen-hole $4f^2\underline{L}$ configurations. The average valences of the praseodymium ion were estimated by analyzing the XANES spectra. The important experimental results and conclusions are summarized as follows.

(1) The room-temperature XANES experiment spectra show a dominant single-peaked feature A (5966 eV), characteristic of the presence of the pure Pr^{3+} valence state. On cooling across the transition temperature T_{MI}, an increasing population of Pr^{4+} states becomes evident from the fast increase in the intensity of peak B1 (5979 eV) in the spectrum. At the same time, the intensity of peak A due to Pr^{3+} decreases.

(2) The results obtained are indicative of a rather gradual charge transfer between the praseodymium and cobalt sites in the perovskite structure, which precedes the spin-state

transition of cobalt ions that occurs abruptly at a well-defined T_{MI}.

(3) Below T_{MI}, the population of Pr^{4+} ions continues to increase, reaching saturation at low temperatures. Using the quantitative analysis of the XANES spectra, the average valence of Pr ions at 8 K is determined to be 3.15+ and 3.27+ for the $y = 0.075$ and 0.15 samples, respectively. These valences are in good agreement with those obtained from the entropy change using the Schottky peak due to the Pr^{4+} Kramers doublet in the low-temperature specific heat, i.e., 3.17+ and 3.29+.

Acknowledgments

The synchrotron radiation experiments were performed at the BL01B1 of SPring-8 with approval of Japan Synchrotron Radiation Research Institute (JASRI) (Proposal No. 2011A1060). Part of the work was performed under the financial support of the Grant Agency of the Czech Republic within the Project No. 204/11/0713.

1) Z. Jirák, J. Hejtmánek, K. Knížek, and M. Veverka: Phys. Rev. B **78** (2008) 014432.
2) M. A. Korotin, S. Yu. Ezhov, I. V. Solovyev, V. I. Anisimov, D. I. Khomskii, and G. A. Sawatzky: Phys. Rev. B **54** (1996) 5309.
3) J.-Q. Yan, J.-S. Zhou, and J. B. Goodenough: Phys. Rev. B **69** (2004) 134409.
4) S. Tsubouchi, T. Kyomen, M. Itoh, P. Ganguly, M. Oguni, Y. Shimojo, Y. Morii, and Y. Ishii: Phys. Rev. B **66** (2002) 052418.
5) S. Tsubouchi, T. Kyomen, M. Itoh, and M. Oguni: Phys. Rev. B **69** (2004) 144406.
6) T. Saitoh, Y. Yamashita, N. Todoroki, T. Kyomen, M. Itoh, M. Higashiguchi, M. Nakatake, and K. Shimada: J. Electron Spectrosc. Relat. Phenom. **144–147** (2005) 893.
7) T. Fujita, T. Miyashita, Y. Yasui, Y. Kobayashi, M. Sato, E. Nishibori, M. Sakata, Y. Shimojo, N. Igawa, Y. Ishii, K. Kakurai, T. Adachi, Y. Ohishi, and M. Takata: J. Phys. Soc. Jpn. **73** (2004) 1987.
8) T. Fujita, S. Kawabata, M. Sato, N. Kurita, M. Hedo, and Y. Uwatoko: J. Phys. Soc. Jpn. **74** (2005) 2294.
9) T. Naito, H. Sasaki, and H. Fujishiro: J. Phys. Soc. Jpn. **79** (2010) 034710.
10) M. Maryško, Z. Jirák, K. Knížek, P. Novák, J. Hejtmánek, T. Naito, H. Sasaki, and H. Fujishiro: J. Appl. Phys. **109** (2011) 07E127.
11) T. Naito: private communication.
12) K. Knížek, J. Hejtmánek, P. Novák, and Z. Jirák: Phys. Rev. B **81** (2010) 155113.
13) J. Wu and C. Leighton: Phys. Rev. B **67** (2003) 174408.
14) K. Knížek, Z. Jirák, J. Hejtmánek, and P. Novák: J. Magn. Magn. Mater. **322** (2010) 1221.
15) J. Hejtmánek, E. Šantavá, K. Knížek, M. Maryško, Z. Jirák, T. Naito, H. Sasaki, and H. Fujishiro: Phys. Rev. B **82** (2010) 165107.
16) J. L. García-Munoz, C. Frontera, A. J. Barón-González, S. Valencia, J. Blasco, R. Feyerherm, E. Dudzik, R. Abrudan, and F. Radu: Phys. Rev. B **84** (2011) 045104; J. Herrero-Martín, J. L. García-Munoz, S. Valencia, C. Frontera, J. Blanco, A. J. Barón-González, G. Subías, R. Abrudan, F. Radu, E. Dudzik, and R. Feyerherm: Phys. Rev. B **77** (2011) 115131.
17) H. Yamaoka, H. Oohashi, I. Jarrige, T. Terashima, Y. Zou, H. Mizota, S. Sakakura, T. Tochio, Y. Ito, E. Ya. Sherman, and A. Kotani: Phys. Rev. B **77** (2008) 045135.
18) A. Bianconi, A. Kotani, K. Okada, R. Giorgi, A. Gargano, A. Marcelli, and T. Miyahara: Phys. Rev. B **35** (1987) 806.
19) Z. Hu, S. Bertram, and G. Kaindl: Phys. Rev. B **49** (1994) 39.
20) B. Ravel and M. Newville: J. Synchrotron Radiat. **12** (2005) 537.
21) A. Podlesnyak, S. Rosenkranz, F. Fauth, W. Marti, H. J. Scheel, and A. Furrer: J. Phys.: Condens. Matter **6** (1994) 4099.
22) J. Richter, A. Braun, A. S. Harvey, P. Holtappels, T. Graule, and L. J. Gauckler: Physica B **403** (2008) 87.
23) F. W. Lytle, G. van der Laan, R. B. Greegor, E. M. Larson, C. E. Violet, and J. Wong: Phys. Rev. B **41** (1990) 8955.

5. (A-48) Y. Noda, H. Fujishiro, T. Naito, A. Ito, T. Goto, J. Hejtmanek and Z. Jirak, "Electrical resistivity anomaly in $(Pr_{1-y}M_y)_{1-x}Ca_xCoO_3$ epitaxial films (M = Y, Gd) fabricated by pulsed laser deposition",
   AIP Advances **6** (2016) 025318 (9 pages) (No. 232 paper)

Electrical resistivity anomaly in $(Pr_{1-y}M_y)_{1-x}Ca_xCoO_3$ epitaxial films (M=Y, Gd) fabricated by pulsed laser deposition

Y. Noda,[1] H. Fujishiro,[1,a] T. Naito,[1] A. Ito,[2] T. Goto,[2] J. Hejtmanek,[3] and Z. Jirak[3]

[1]*Faculty of Engineering, Iwate University, 4-3-5 Ueda, Morioka 020-8551, Japan*
[2]*Institute for Materials Research, Tohoku University, 2-1-1 Katahira, Sendai 980-8577, Japan*
[3]*Institute of Physics, ASCR, Cukrovarnicka 10, 162 00 Prague 6, Czech Republic*

(Received 27 November 2015; accepted 9 February 2016; published online 18 February 2016)

$(Pr_{1-y}M_y)_{1-x}Ca_xCoO_3$ epitaxial films (M=Y, Gd) have been successfully fabricated by pulsed laser deposition on the single crystal substrates with different lattice constant. The polycrystalline bulk of this material shows a first-order metal-insulator (MI) transition below the critical temperature. Although $\rho(T)$ of all the as-grown films shows a semiconducting behavior at entire temperature range, an anomalous $\rho(T)$ upturn with wide hysteresis can be clearly seen for the film grown on the $SrLaAlO_4$ (SLAO) substrate, which applied the in-plane compressive stress to the film. Such anomaly in $\rho(T)$ is interpreted as a sign of the first-order phase transition related with the spin-state (SS) transition, which was observed in the polycrystalline bulk. [http://dx.doi.org/10.1063/1.4942558]

I. INTRODUCTION

The perovskite cobaltites $RECoO_3$ (RE=rare-earth element and Y) show a spin-state (SS) transition of Co^{3+} ions from a low spin state (LS; $t_{2g}^6e_g^0$, S=0) to a high spin state (HS; $t_{2g}^4e_g^2$, S=2) with increasing temperature, followed by the formation of the metallic state of the intermediate spin state (IS; $t_{2g}^5\sigma^*$, S=1) at higher temperatures.[1] The temperature induced SS transition indicates a small energy difference δE between the crystal-field splitting and Hund coupling energy.[2,3] The hole-doped systems such as $La_{1-x}Sr_xCoO_3$ generally show a temperature stable phase with itinerant cobalt states, which result presumably from the mixed IS Co^{3+}/LS Co^{4+} or HS Co^{3+} /IS Co^{4+} configurations, and undergo a ferromagnetic ordering at low temperatures. Most interestingly, some Pr-based cobaltites exhibit a pronounced first-order transition to a low-temperature phase of weakly paramagnetic character and reduced conduction. This effect was revealed for the first time on $Pr_{0.5}Ca_{0.5}CoO_3$ at ~ 90 K by the step-like resistivity jump and concomitant anomalies in the magnetic susceptibility, heat capacity, lattice dilatation and photoemission spectroscopy.[4–6] The mechanism of the transition was tentatively ascribed to a spin state crossover from the itinerant cobalt states to an ordered mixture of localized LS Co^{3+} and LS Co^{4+} ($t_{2g}^5e_g^0$, S=1/2) states. Similar metal-insulator (MI) transition was evidenced also in the less doped $Pr_{1-x}Ca_xCoO_3$ (x=0.3) under higher hydrostatic pressures and in the $(Pr_{1-x}RE_y)_{1-x}Ca_xCoO_3$ system ($0.2<x<0.5$) with a partial substitution of Pr by smaller RE cations such as Sm, Eu, and Y under ambient pressure.[7–9] This peculiar transition appeared to be conditioned not only by the presence of both Pr and Ca ions, but also by a larger structural distortion of the CoO_6 network, depending on the average ionic radius and size mismatch of perovskite A-site ions.[9] Furthermore, the critical temperature T_{MI} was found

[a]corresponding author fujishiro@iwate-u.ac.jp

to decrease in a quadratic dependence of applied magnetic field, so that the transition could be completely suppressed in very high fields.[10]

An alternative scenario explaining the nature of such specific transition was proposed on the basis of electronic structure calculations exploiting the temperature dependence of the structural experimental data for $Pr_{0.5}Ca_{0.5}CoO_3$,[11] in which the formal cobalt valence should change below T_{MI} from mixed-valence $Co^{3.5+}$ towards pure $Co^{3.0+}$ with strong preference for the LS state and, concomitantly, the praseodymium valence should increase simultaneously from Pr^{3+} towards Pr^{4+}. The theoretical hypothesis about the crucial role of variable praseodymium valence was experimentally supported by the observations of a Schottky peak in the low temperature specific heat of $(Pr_{1-y}Y_y)_{0.7}Ca_{0.3}CoO_3$ (y=0.075 and 0.15),[12] and by the x-ray absorption near-edge structure (XANES) spectra at the Pr L_3 edge directly.[13–16]

It is widely desirable to use a single crystal or an epitaxial film for the physical investigation. In the $La_{1-x}Sr_xCoO_3$ system, single crystals and thin films have been fabricated and investigated.[17–19] In the epitaxial thin film, the electrical conduction and the spin state change depending on the film thickness and fabrication condition.[19] However, for the $(Pr_{1-y}M_y)_{1-x}Ca_xCoO_3$ system with the simultaneous MI and SS transition, only polycrystalline bulk materials have been investigated experimentally in the previous studies and there is no investigations using a single crystal or an epitaxial film because of the difficulty of the fabrication.

When the material is prepared in the thin film form, the physical properties are sensitive to crystal structure, metallic composition, oxygen content *etc*, mainly depending on the lattice mismatch between the substrate and the material. Thin films experience a stress due to mismatch of the lattice and the thermal expansion to the substrate, in addition to the intrinsic internal stress. In particular, the interface between the film and the substrate can play an important role, giving rise to boundary regions with different structures and affecting the transport and magnetic properties due to the induced strain especially in very thin films. The strain in the epitaxial thin films can be easily manipulated by the film thickness and the lattice parameter of the substrate material. For example, in the $RNiO_3$ thin film, which shows the bandwidth controlled MI transition, the transition temperature, T_{MI}, was increased (decreased) by tensile (compressive) in-plane strain.[20] The strain effect is attributed to an increase (decrease) of the Ni-O-Ni bond angle, which affects to films in the same way as the bulk under higher pressure.[21] Thin films of these materials have potential for various applications such as the use in resistive switches and phase-change memory.

In the present work, we fabricated the $(Pr_{1-y}M_y)_{1-x}Ca_xCoO_3$ epitaxial films (M=Y, Gd) by pulsed laser deposition (PLD) on the single crystal substrates with different lattice constant. We investigated the electrical resistivity anomaly, which seemed to be related with the spin-state transition shown in the bulk materials.

II. EXPERIMENTAL PROCEDURE

$(Pr_{1-y}Y_y)_{1-x}Ca_xCoO_3$ (PYCCO) and $(Pr_{1-y}Gd_y)_{1-x}Ca_xCoO_3$ (PGCCO) thin films were prepared by the PLD method using a fifth harmonic wave of YAG laser with λ=213 nm and a repetition rate of 10 Hz. The pulse duration is 5 ns and the power is 18 mJ. $(Pr_{0.8}Y_{0.2})_{0.6}Ca_{0.4}CoO_3$ and $(Pr_{0.7}Gd_{0.3})_{0.6}Ca_{0.4}CoO_3$ polycrystalline targets with nominal composition were prepared by a standard solid-state reaction. Pr_6O_{11}, Y_2O_3, Gd_2O_3, $CaCO_3$, Co_3O_4 raw powders with purity higher than 99.9% were used as starting materials. The powders were mixed, calcined at 1000°C for 12 h, pressed into pellets with a diameter of 20 mm and a thickness of 5 mm and then sintered at 1200°C for 48 h in flowing oxygen gas. Powder X-ray diffraction analysis revealed that the sintered targets were a single phase. The target and the substrate were mounted in the vacuum chamber and were rotated at the speed of 7 rpm and 3 rpm, respectively, to reduce non-uniform erosion and to deposit uniformly. The deposition was carried out for 1 - 4 hours in a pure oxygen atmosphere of 0.1 to 1.0 Torr and at a substrate temperature of 600°C and the film thickness was measured to be about 50~100 nm. The films were grown on (001) oriented $SrTiO_3$ (STO: a=0.3905 nm), $(LaAlO_3)_{0.3}(Sr_2AlTaO_6)_{0.7}$ (LSAT: a=0.3868 nm), $LaAlO_3$ (LAO: a=0.3790 nm) and $SrLaAlO_4$ (SLAO: a=0.3756 nm, c=1.2636 nm) single crystal substrates. The pseudo cubic lattice parameter of the $(Pr_{1-y}Y_y)_{1-x}Ca_xCoO_3$ bulk (x=0.4, y=0.2) is a=0.3775 nm and the lattice mismatch using

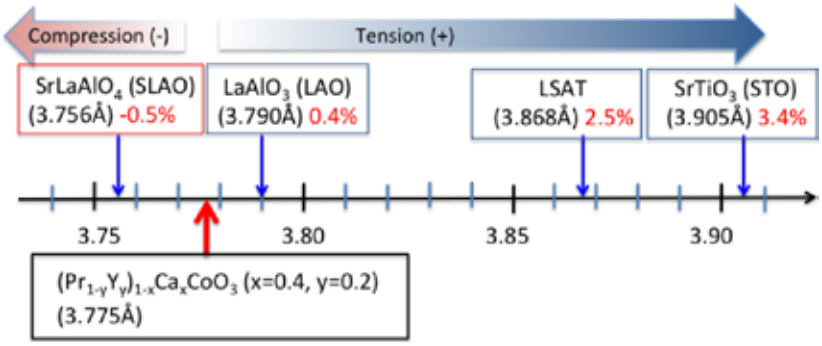

FIG. 1. The relation between the lattice parameters of the $(Pr_{0.8}Y_{0.2})_{0.6}Ca_{0.4}CoO_3$ and those of the used single crystal substrates.

the relation of $\varepsilon=(a_{PYCCO}-a_{sub})/a_{sub}$ is +3.4% for STO, +2.5% for LSAT, +0.4% for LAO and -0.5% for SLAO. The relation of the lattice parameters between the material and the substrates is shown in Fig. 1, in which the in-plane tensile stress is applied to the film grown on the STO, LSAT and LAO substrates and the in-plane compressive stress is applied in the film grown on the SLAO substrate. The chemical composition of the grown films was measured by electron probe microanalysis (EPMA), in which the measured composition of (x, y) of the film was decreased to (0.3, 0.13) from the nominal composition of (0.4, 0.2) for the PYCCO sample. To clarify the crystalline quality of the grown films, X-ray diffraction analyses of θ-2θ and ϕ-2θ scans were performed, both of which identified the out-of-plane and in-plane alignments, respectively. The electrical resistivity $\rho(T)$ was measured on cooling and heating runs in the 10 - 300 K range by a standard four-probe method for the as-grown films and heat-treated films under high-pressure oxygen gas (2.0 MPa) at 600°C for 3 h.

III. RESULTS AND DISCUSSION

Figure 2 shows the out-of-plane XRD patterns (θ-2θ scan) of the PYCCO films fabricated on the STO and SLAO substrates. The PYCCO films display clear (00l) reflections of the pseudo cubic structure with no indications of impurities or miss-orientation together with the strong (00l) reflections from the substrates. These results demonstrate the out-of-plane orientation of PYCCO thin films on the substrates.

Figure 3 presents the ϕ-2θ azimuth scan for the PYCCO film, fabricated on the SLAO substrate. Four sharp peaks of the (002) reflections were observed every 90 deg. and the in-plane alignment can be confirmed, which were also confirmed for the films grown on the other substrates. These results suggest that the PYCCO films are epitaxial films grown on the substrates.

Figure 4 shows the (002) intensity of the out-of-plane XRD patterns of the PYCCO films on the STO substrate, as a function of the film thickness, d. The diffraction peak angle of the films decreases with increasing film thickness, d, and shifts toward the peak position for the bulk crystal. These results suggest that the out-of-plane lattice constant of the epitaxial films on the STO substrate is smaller than that of the bulk crystal and approaches the lattice constant of the bulk material. This is because the tensile stress was induced in the film surface due to the positive lattice mismatch ε (= +3.4%), and then was relaxed with increasing film thickness. On the other hand, for the films grown on the SLAO substrate, the (002) peak was found at 2θ=47.70° for the d=100 nm film (not shown), which was the lower angle than that of the bulk crystal (2θ=47.21°). In this case, the in-plane compressive stress is induced in the film surface because of negative lattice mismatch ε (= -0.5%).

Figure 5(a) shows the temperature dependence of the electrical resistivity, $\rho(T)$, of the as-grown PYCCO films grown on the each substrate. The thickness of each film was about 50 nm. $\rho(T)$ of the target bulk is also shown in the figure, in which $\rho(T)$ shows a jump with about two orders of magnitude at T_{MI}=140 K on the cooling run, and shows a sharp drop at T_{MI}=150 K with a hysteresis. The absolute value of $\rho(T)$ on the heating run was larger than that on the cooling

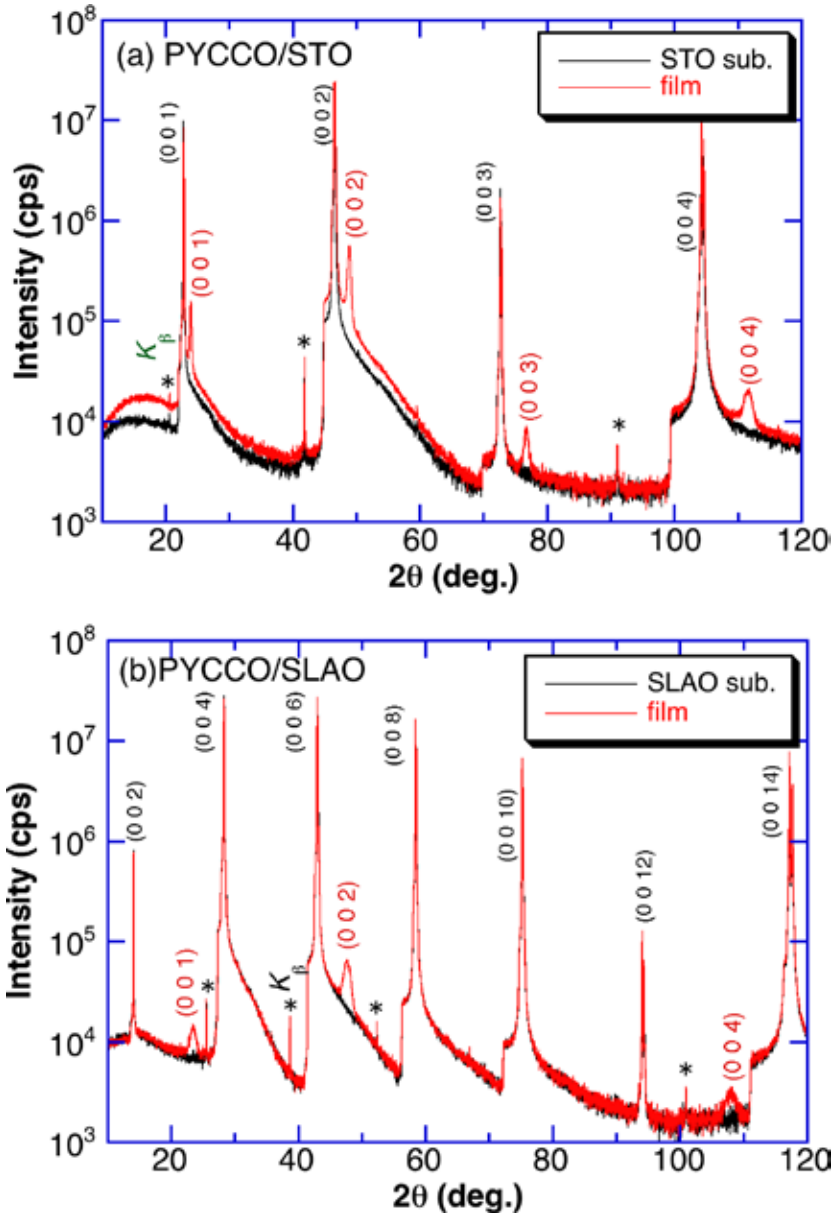

FIG. 2. The out-of-plane XRD patterns (θ-2θ scan) of the PYCCO films grown on the (a) STO and (b) SLAO substrates in the case of the target composition of (x=0.4, y=0.2).

run above T_{MI}. The irreversibility in $\rho(T)$ might come from the occurrence of micro cracks created by the large volume contraction and expansion passing through the transition temperature.[4] On the other hand, the $\rho(T)$ curves for all the as-grown films show a semiconducting behavior without pronounced anomaly, the absolute $\rho(T)$ values change depending on the substrate used, and no irreversibility is detectable after the cooling and heating runs for the films grown on the STO, LSAT and LAO substrates. Nonetheless, one may notice a distinct behavior of the film grown on the SLAO substrate, namely the anomalous inflection point at 170 K and a wide hysteresis in $\rho(T)$ below this temperature that are seen in more detail Figure 5(b), where an alternative plot of $\log\rho vs.T^{-1/4}$, commonly used for variable range hopping (VRH), is displayed. To understand this observation, we refer to the fact that MI transition can be induced in polycrystalline $Pr_{1-x}Ca_xCoO_3$ (x=0.3) under high hydrostatic pressures and the critical temperature T_{MI} increases with increasing pressure.[7] The compression stress in the present PYCCO film on SLAO substrate seems to have analogical effect to

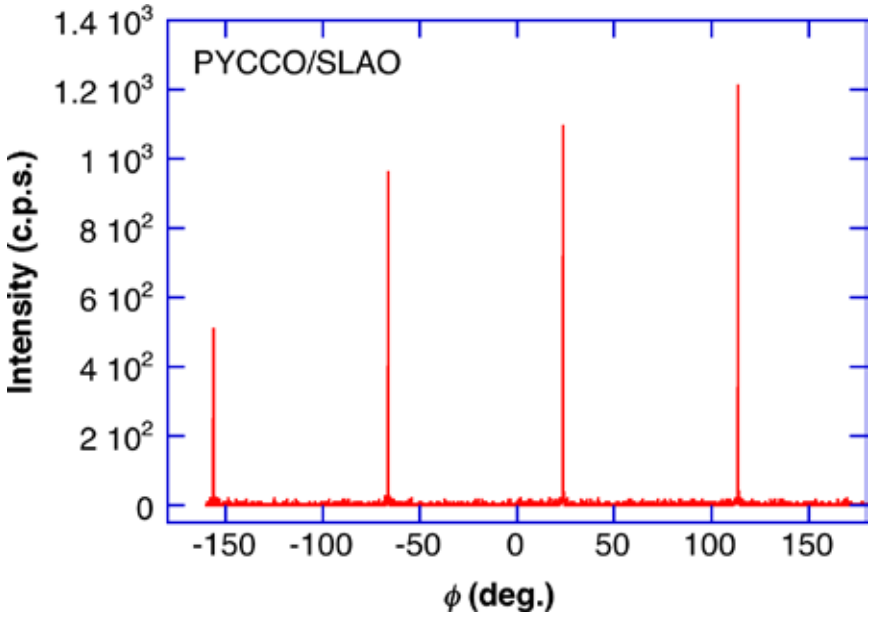

FIG. 3. The in-plane XRD patterns (ϕ-2θ scan) of the PYCCO film fabricated on the SLAO substrate in the case of the target composition of (x=0.4, y=0.2).

the hydrostatic pressure. In this sense, the anomalous $\rho(T)$ upturn followed by a hysteresis region is likely a sign of a similar first-order phase transition.

A question arises why the MI transition in the film grown on the SLAO substrate is less pronounced compared to the bulk material. This is unexpected, especially in view of the fact that actual mismatch conditions seem to be much in favor of the transition. Firstly, the out-of-plane lattice constant of the film, 0.3820 nm, at room temperature (see Figure 6 below) combined with the in-plane a=0.3756 nm imposed by SLAO substrate illustrates some deformation of the PYCCO structure, but the unit cell volume remains exactly same as for bulk material. This is a signature that

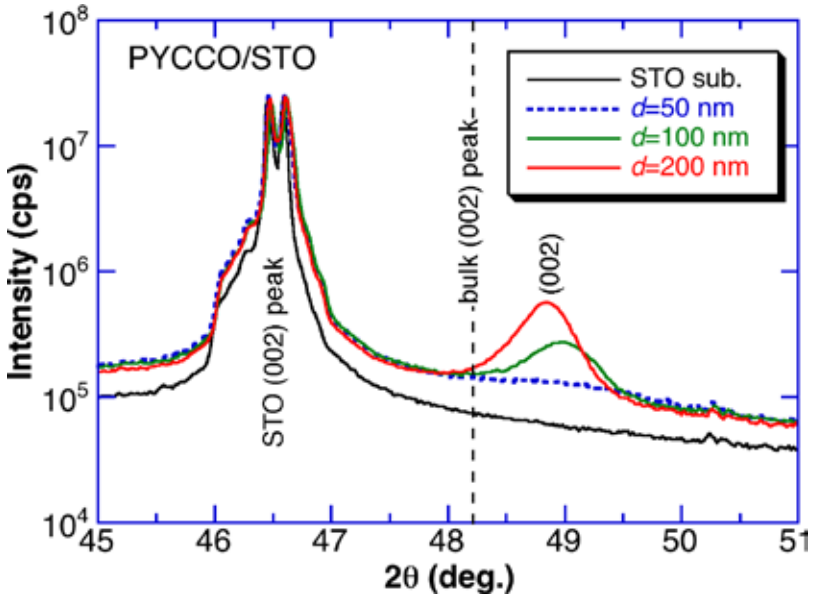

FIG. 4. The (002) intensity in the out-of-plane XRD patterns of the PYCCO films, as a function of the thickness of the film in the case of the target composition of (x=0.4, y=0.2).

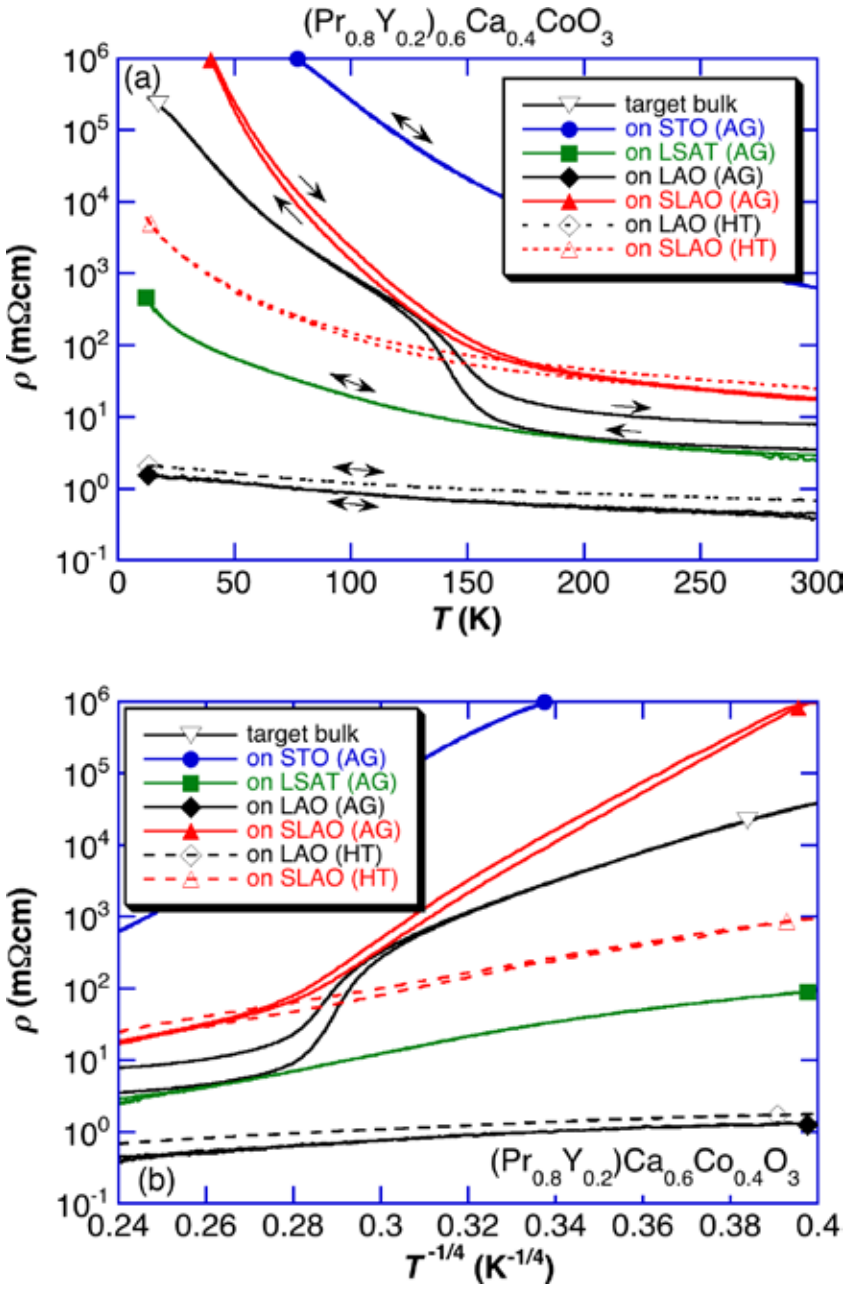

FIG. 5. Temperature dependence of the electrical resistivity, $\rho(T)$, at the cooling and heating runs: (a) The log$\rho vs.T$ plot for the as-grown (AG) PYCCO films on different substrates; (b) An alternative log$\rho vs.T^{-1/4}$ plot with linear low-temperature trend demonstrating the viability of the VRH scenario. The data shown by dashed lines refer to PYCCO films grown on LAO and SLAO substrates, after a heat-treatment (HT) in high-pressure oxygen gas at 600°C for 3 h.

film is likely well developed on the substrate without cracks. Secondly, it can be anticipated that the unit cell of PYCCO is shrank at the MI transition to the same extent as it is in the bulk material, 1.0% in volume or 0.3% in linear dimensions.[22] Therefore, the deformation energy comprised in the film at room temperature will be removed below the transition to the low-temperature phase. There should be evidently another reason for the less pronounced anomaly at T_{MI}. It is worth mentioning that early experiments on prototypical compound $Pr_{0.5}Ca_{0.5}CoO_3$ revealed a critical sensitivity of the MI transition to any oxygen deficiency. To check such hypothesis, the PYCCO films grown on the each substrate were post-annealed under high-pressure oxygen gas (2.0 MPa) at 600°C for

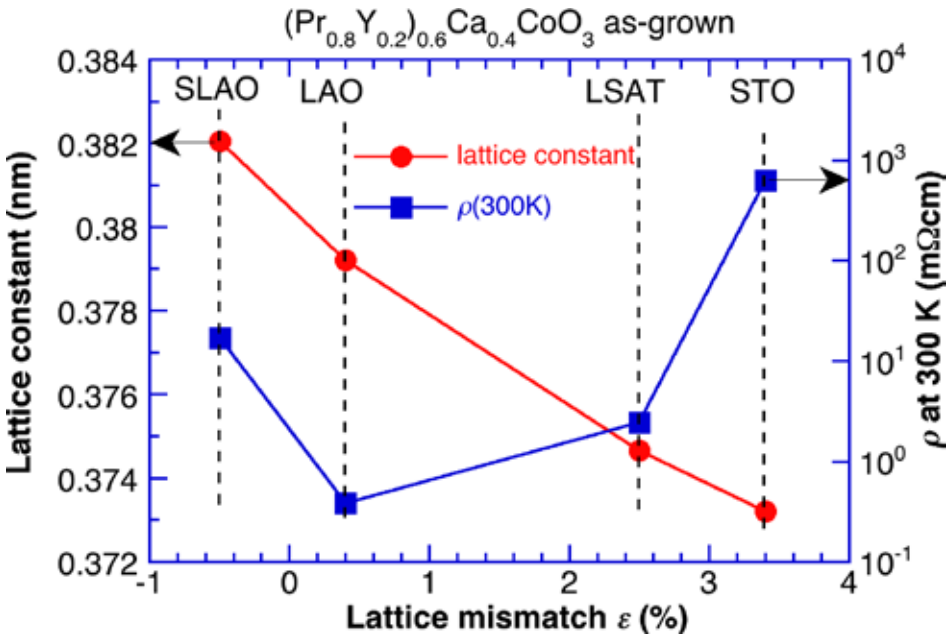

FIG. 6. The out-of-plane lattice constant a and the electrical resistivity for the PYCCO films at 300 K, ρ(300 K), of the as-grown films on each substrate, as a function of lattice mismatch ε.

3 h. The resistivity data on two samples with minimum film/substrate mismatch were added to the results on as-grown samples in Figures 5(a) and 5(b). For the film grown on the SLAO substrate, the anomalous $\rho(T)$ upturn disappeared in the oxygenized sample and some irreversibility in the cooling and heating runs arose. These changes suggest that, contrary to our expectation, the first-order phase transition vanished by the heat treatment. For the film grown on the LAO substrate, the absolute $\rho(T)$ value was only slightly increased by the post annealing.

Figure 6 presents the lattice constant a determined by out-of-plane measurements and the electrical resistivity at 300 K, ρ(300 K), of the as-grown films on each substrate, as a function of lattice mismatch ε. The thickness of each film was about 50 nm. The out-of-plane lattice constant a monotonically decreases with increasing lattice mismatch ε, which suggests that the film was extended in plane due to the tensile stress for the positive ε value. The ρ(300 K) value takes a minimum around ε=0, which is a reasonable trend. Namely, the deformation of CoO_6 octahedra due to the lattice mismatch affects the electron transport in the film.

Figures 7(a) and 7(b), respectively, show the temperature dependence of the electrical resistivity, $\rho(T)$; the logρ*vs*.T plot and the alternative logρ*vs*.$T^{-1/4}$ plot at the cooling and heating runs of the as-grown $(Pr_{1-y}Gd_y)_{1-x}Ca_xCoO_3$ (PGCCO) films on the each substrate. $\rho(T)$ of the heat-treated PGCCO films grown on the LAO and SLAO substrates are also shown. All the films, of which the thickness was about 100 nm, were confirmed to be epitaxial films by XRD analysis. $\rho(T)$ of the target bulk is also shown in the figures, in which T_{MI} was 70 K and 80 K on the cooling and heating runs, respectively. $\rho(T)$ of all the as-grown films shows a semiconducting behavior at entire temperature range. Similarly to the PYCCO film, an anomalous $\rho(T)$ upturn with a wide hysteresis can be clearly observed only for the as-grown film on the SLAO substrate, which is interpreted as a sign of the first-order phase transition. However, the $\rho(T)$ upturn seems to remain after the heat treatment as can be seen in Fig. 7(b). For the thinner PYCCO film on SLAO substrate about 50 nm in thickness shown in Fig. 5, the transition was clearly suppressed by the heat treatment under the high-pressure oxygen gas, where the heat treatment removed the stress. On the other hand, in the present thicker PGCCO film on SLAO substrate with 100 nm in thickness, the heat treatment made only much smaller change. The appearance of the anomalous $\rho(T)$ upturn and the relaxation after the heat treatment change depending on the film thickness.

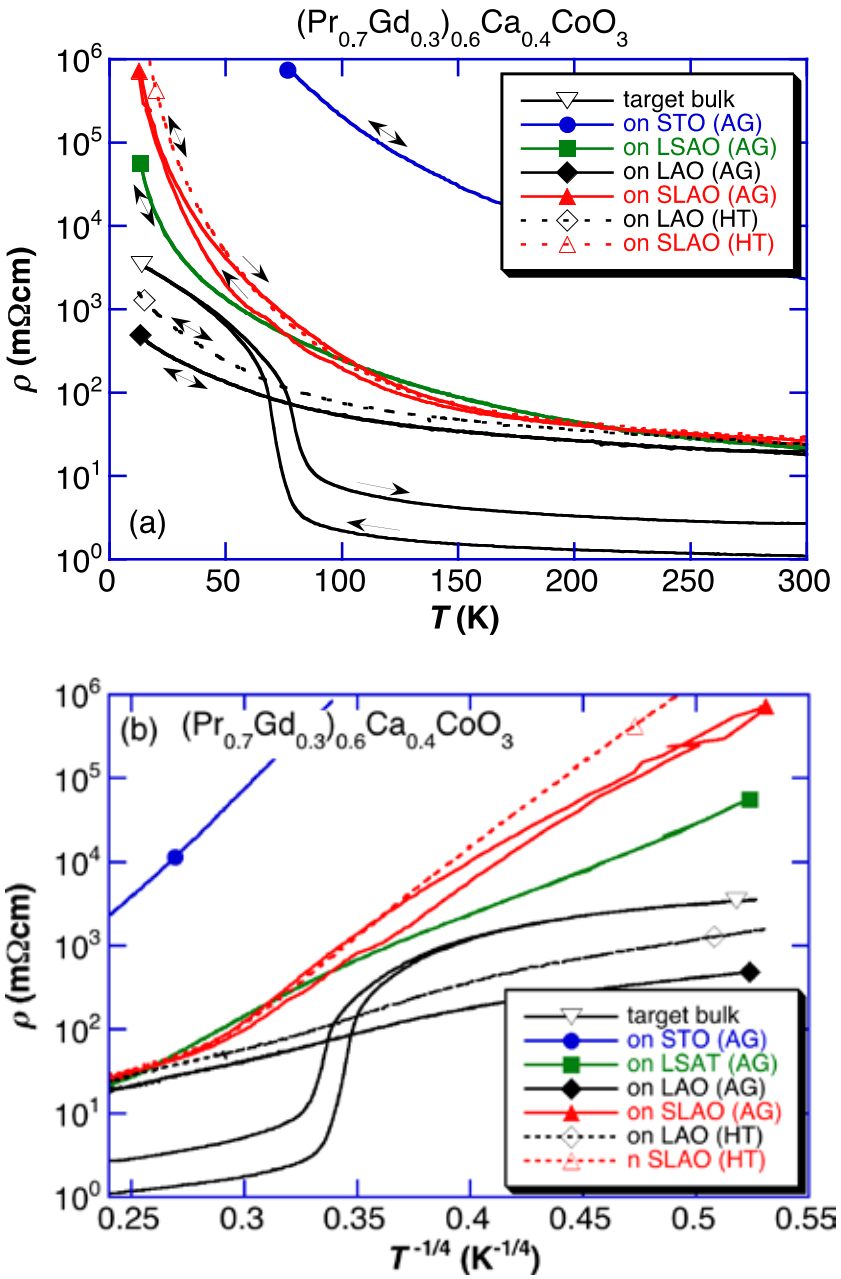

FIG. 7. Temperature dependence of the electrical resistivity, $\rho(T)$, at the cooling and heating runs: (a) the log$\rho vs.T$ plot and (b) the alternative log$\rho vs.T^{-1/4}$ plot for the as-grown (AG) PGCCO films on different substrates. The data shown by dashed lines refer to the heat-treatment (HT) PGCCO films grown on LAO and SLAO substrates after the heat treatment in high-pressure oxygen gas at 600°C for 3 h.

IV. SUMMARY

The $(Pr_{1-y}Y_y)_{1-x}Ca_xCoO_3$ (PYCCO) and $(Pr_{1-y}Gd_y)_{1-x}Ca_xCoO_3$ (PGCCO) films have been fabricated by pulsed laser deposition (PLD) method on the single crystal substrates with different lattice constants, and their crystallographic and electrical properties have been investigated. The important experimental results and conclusions are summarized as follows.

(1) The obtained films have been confirmed to be epitaxial films grown on the single crystal substrates with different lattice constants by XRD measurements.

(2) The electrical resistivity, $\rho(T)$, of all the as-grown films shows a semiconducting behavior at entire temperature range. However, the anomalous $\rho(T)$ upturn with a wide hysteresis can be clearly observed only for the films grown on the SLAO substrate, which applied the in-plane compressive stress. The $\rho(T)$ anomaly of the thin PYCCO film 50 nm in thickness on SLAO vanished after the heat treatment in high-pressure oxygen gas. On the other hand, the $\rho(T)$ upturn of the thick PGCCO film 100 nm in thickness on SLAO seems to remain after the heat treatment.

(3) The anomaly in $\rho(T)$ is interpreted as a sign of the first-order phase transition accompanied by the spin-state transition, which was observed in the polycrystalline bulk.

ACKNOWLEDGEMENTS

The authors thank Prof. N. Yoshimoto of Iwate University for his assistance in the in-plane X-ray diffraction measurement. This work was partly supported by JSPS KAKENHI Grant No. 24540355 and was performed under the Inter-university Cooperative Research Program of the Institute for Materials Research, Tohoku University.

[1] Z. Jirak, J. Hejtmanek, K. Knızek, and M. Veverka, Phys. Rev. **B 78**, 014432 (2008).
[2] M. A. Korotin, S. Yu. Ezhov, I. V. Solovyev, V. I. Anisimov, D. I. Khomskii, and G. A. Sawatzky, Phys. Rev. **B 54**, 5309 (1996).
[3] J.-Q. Yan, J.-S. Zhou, and J. B. Goodenough, Phys. Rev. **B 69**, 134409 (2004).
[4] S. Tsubouchi, T. Kyômen, M. Itoh, P. Ganguly, M. Oguni, Y. Shimojo, Y. Morii, and Y. Ishii, Phys. Rev. **B 66**, 052418 (2002).
[5] S. Tsubouchi, T. Kyômen, M. Itoh, and M. Oguni, Phys. Rev. **B 69**, 144406 (2004).
[6] T. Saitoh, Y. Yamashita, N. Todoroki, T. Kyomen, M. Itoh, M. Higashiguchi, M. Nakatake, and K. Shimada, J. Electron Spectrosc. Relat. Phenom. **144–147**, 893 (2005).
[7] T. Fujita, T. Miyashita, Y. Yasui, Y. Kobayashi, M. Sato, E. Nishibori, M. Sakata, Y. Shimojo, N. Igawa, Y. Ishii, K. Kakurai, T. Adachi, Y. Ohishi, and M. Takata, J. Phys. Soc. Jpn. **73**, 1987 (2004).
[8] T. Fujita, S. Kawabata, M. Sato, N. Kurita, M. Hedo, and Y. Uwatoko, J. Phys. Soc. Jpn. **74**, 2294 (2005).
[9] T. Naito, H. Sasaki, and H. Fujishiro, J. Phys. Soc. Jpn. **79**, 034710 (2010).
[10] T. Naito, H. Fujishiro, T. Nishizaki, N. Kobayashi, J. Hejtmanek, K. Knızek, and Z. Jirak, J. Appl. Phys. **115**, 233914 (2014).
[11] K. Knızek, J. Hejtmanek, P. Novak, and Z. Jirak, Phys. Rev. **B 81**, 155113 (2010).
[12] J. Hejtmanek, E. Santava, K. Knizek, M. Marysko, Z. Jirak, T. Naito, H. Sasaki, and H. Fujishiro, Phys. Rev. **B 82**, 165107 (2010).
[13] H. Fujishiro, T. Naito, S. Ogawa, N. Yoshida, K. Nitta, J. Hejtmanek, K. Knizek, and Z. Jirak, J. Phys. Soc. Jpn. **81**, 064079 (2012).
[14] J. L. Garcia-Munoz, C. Frontera, A. J. Baron-Gonzalez, S. Valencia, J. Blasco, R. Feyerherm, E. Dudzik, R. Abrudan, and F. Radu, Phys. Rev. **B 84**, 045104 (2011).
[15] J. Herrero-Martın, J. L. Garcıa-Munoz, S. Valencia, C. Frontera, J. Blasco, A. J. Barón-González, G. Subías, R. Abrudan, F. Radu, E. Dudzik, and R. Feyerherm, Phys. Rev. **B 84**, 115131 (2011).
[16] J. Herrero-Martín, J. L. García-Muñoz, K. Kvashnina, E. Gallo, G. Subías, J. A. Alonso, and A. J. Barón-González, Phys. Rev. **B 86**, 125106 (2012).
[17] M. Kriener, C. Zobel, A. Reichl, J. Baier, M. Cwik, K. Berggold, H. Kierspel, O. Zabara, A. Freimuth, and T. Lorenz, Phys. Rev. **B 69**, 094417 (2004).
[18] K. Daoudia, T. Tsuchiya, T. Nakajima, A. Fouzri, and M. Oueslati, J. Alloys Comp. **506**, 483 (2010).
[19] D. Fuchs, O. Morán, P. Adelmann, and R. Schneider, Phys. **B 349**, 337 (2004).
[20] A. S. Disa, D. P. Kumah, J. H. Ngai, E. D. Specht, D. A. Arena, F. J. Walker, and C. H. Ahn, APL Mat. **1**, 032110 (2013).
[21] A. Ikeda, T. Manabe, and M. Naito, Physica C **505**, 24 (2014).
[22] K. Knizek, J. Hejtmanek, M. Marisko, P. Novak, E. Santava, Z. Jirak, T. Naito, H. Fujishiro, and Clarina de la Cruz, Phys. Rev. **B 88**, 224412 (2013).

6. (H-1) K. Takahashi, H. Fujishiro and M. D. Ainslie,
"A new concept of hybrid trapped field magnet lens (HTFML)",
Supercond. Sci. Technol. **31** (2018) 044005 (9 pages) (No. 257 paper)

OPEN ACCESS
IOP Publishing
Superconductor Science and Technology
Supercond. Sci. Technol. 31 (2018) 044005 (9pp)
https://doi.org/10.1088/1361-6668/aaae94

A new concept of a hybrid trapped field magnet lens

Keita Takahashi[1,3], **Hiroyuki Fujishiro**[1] and **Mark D Ainslie**[2]

[1] Department of Physical Science and Materials Engineering, Faculty of Science and Engineering, Iwate University, Morioka 020-8551, Japan
[2] Bulk Superconductivity Group, Department of Engineering, University of Cambridge, Cambridge CB2 1PZ, United Kingdom

E-mail: t2216017@iwate-u.ac.jp and fujishiro@iwate-u.ac.jp

Received 22 December 2017, revised 7 February 2018
Accepted for publication 12 February 2018
Published 7 March 2018

Abstract

In this paper, a new concept of a hybrid trapped field magnet lens (HTFML) is proposed. The HTMFL exploits the 'vortex pinning effect' of an outer superconducting bulk cylinder, which is magnetized as a trapped field magnet (TFM) using field-cooled magnetization (FCM), and the 'diamagnetic shielding effect' of an inner bulk magnetic lens to generate a concentrated magnetic field higher than the trapped field from the TFM in the bore of the magnetic lens. This requires that, during the zero-field-cooled magnetization process, the outer cylinder is in the normal state ($T >$ superconducting transition temperature, T_c) and the inner lens is in the superconducting state ($T < T_c$) when the external magnetizing field is applied, followed by cooling to an appropriate operating temperature, then removing the external field. This is explored for two potential cases: (1) exploiting the difference in T_c of two different bulk materials ('case-1'), e.g. MgB_2 ($T_c = 39$ K) and GdBaCuO ($T_c = 92$ K) or (2) using the same material for the whole HTFML, e.g., GdBaCuO, but utilizing individually controlled cryostats, the same cryostat with different cooling loops or coolants, or heaters that keep the outer bulk cylinder at a temperature above T_c to achieve the same desired effect. The HTFML is verified using numerical simulations for 'case-1' using an MgB_2 cylinder and GdBaCuO lens pair and for 'case-2' using a GdBaCuO cylinder and GdBaCuO lens pair. As a result, the HTFML could reliably generate a concentrated magnetic field $B_c = 4.73$ T with the external magnetizing field $B_{app} = 3$ T in the 'case-1', and a higher $B_c = 13.49$ T with higher $B_{app} = 10$ T in the 'case-2', respectively. This could, for example, be used to enhance the magnetic field in the bore of a bulk superconducting NMR/MRI system to improve its resolution.

Keywords: hybrid trapped field magnet lens, bulk superconductors, trapped field magnets, magnetic lens, vortex pinning effect, diamagnetic shielding effect, finite element method

(Some figures may appear in colour only in the online journal)

1. Introduction

The superconducting characteristics of REBaCuO bulks (RE: rare earth element or Y) continue to be enhanced due to the introduction of strong pinning centers and the improvement of crystal growth techniques, which have resulted in increased critical current density, J_c [1, 2]. As a result, such bulks exhibit higher trapped field capabilities using field-cooled magnetization (FCM) and have significant potential for practical applications as high-strength trapped field magnets (TFMs) capable of generating magnetic field of several Tesla. Figure 1(a) shows the time sequence of conventional FCM of superconducting bulks to utilize them as TFMs (the case shown is for a cylindrical ring bulk superconductor). Although the trapped field, B_T, of REBaCuO bulks, which can be estimated from the $J_c(B, T)$

[3] Author to whom any correspondence should be addressed.

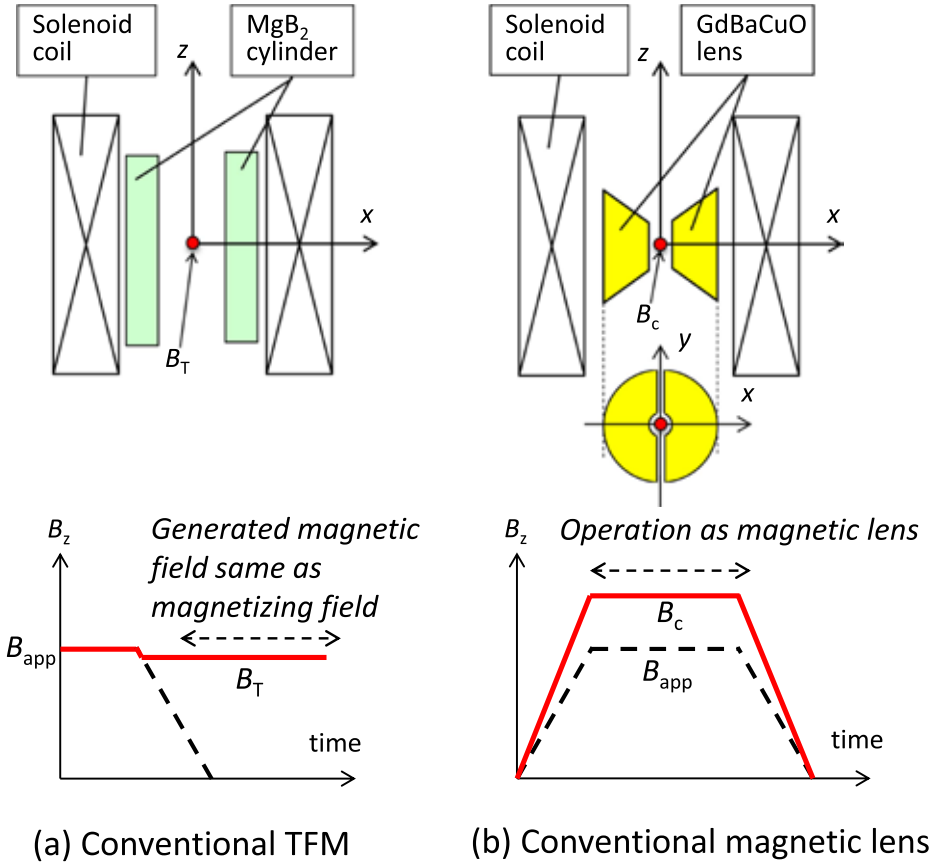

Figure 1. Time sequence of (a) conventional magnetizing process of field-cooled magnetization (FCM) of superconducting bulks to utilize them as TFMs and (b) magnetizing process of zero-field-cooled magnetization (ZFCM) for a conventional superconducting bulk magnetic lens.

characteristics, could be over 20 T at 20 K in a bulk pair [3], the mechanical strength of the brittle ceramic material restricts the practical maximum trapped field of such TFMs experimentally. To date, REBaCuO disk bulks have been shown to trap magnetic field over 17 T by mechanical reinforcement using glass fiber reinforced epoxy resin or shrink-fit stainless steel to reduce the electromagnetic hoop stress [3, 4]. Such TFMs, in which the field is trapped using the strong 'vortex pinning effect' of the material, require a high, stationary magnetic field to magnetize them and they can trap fields nearly the same or slightly lower than the applied field, B_{app}, using FCM, but such high fields are only available from specialized magnets at a limited number of facilities worldwide. In this sense, such high-strength TFMs are not practical for applications and much research has been carried out on the pulsed field magnetization (PFM) technique as a fast, compact and relatively inexpensive magnetization technique. However, due to the large temperature rise associated with the rapid dynamic movement of the magnetic flux within the bulk, the trapped field capability is severely limited and only fields up to around 5 T have been achieved using PFM [5].

On the other hand, a 'magnetic lens' using cone-shaped superconducting bulks has been investigated, in which the magnetic flux is concentrated in the bore of the magnetic lens using the 'diamagnetic shielding effect' of superconducting materials and the available magnetic field in the lens is larger than the applied field generated by the external magnetizing coil [6–9]. Figure 1(b) shows the time sequence of magnetizing process for a conventional bulk superconducting magnetic lens, for which zero-field-cooled magnetization (ZFCM) is used. The existence of slits in the superconducting hollow cone is essential to suppress the current along the circumferential direction and to concentrate the magnetic flux. A concentrated field of $B_c = 12.42$ T has been achieved at 20 K for a background field of $B_{app} = 8$ T using a bulk GdBaCuO magnetic lens [10] and $B_c = 30.4$ T has been achieved at the center of the lens in higher background field of $B_{app} = 28.3$ T elsewhere [11]. Using a bulk MgB_2 magnetic lens, a concentrated field of $B_c = 2.18$ T at 4.2 K has also been achieved for a background field of $B_{app} = 1$ T [12]. Mechanical reinforcement of the magnetic lens and the avoidance of the flux jump are necessary to achieve the magnetic lens effect stably [13]. Since the magnetic lens effect vanishes after the applied field decreased to zero, the external magnet must be operated continuously, which consumes a large amount of energy.

In this paper, we propose a new concept of a hybrid trapped field magnet lens (HTFML), consisting of a cylindrical bulk TFM using the vortex pinning effect, combined with a bulk magnetic lens using the diamagnetic shielding effect. The HTFML can reliably generate a magnetic field at the center of the magnetic lens higher than the trapped field in the single cylindrical bulk TFM and the external magnetizing field, even after the

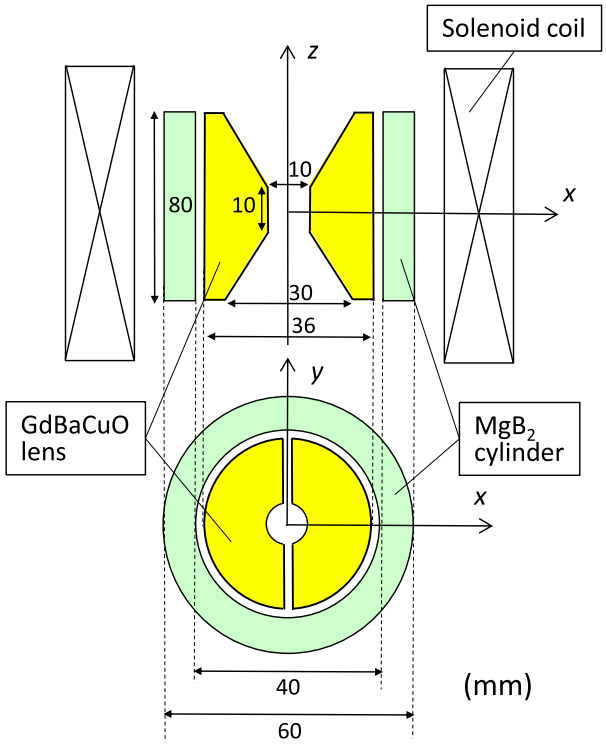

Figure 2. Numerical model and dimensions of the MgB_2 cylinder, GdBaCuO magnetic lens and solenoid magnetizing coil for 'case-1'. The MgB_2 cylinder is replaced by a GdBaCuO cylinder in 'case-2'.

externally applied field decreases to zero. This concept requires that, during the ZFCM process, the outer cylinder is in the normal state ($T >$ superconducting transition temperature, T_c) and the inner lens is in the superconducting state ($T < T_c$) when the external magnetizing field is applied, followed by cooling to an appropriate operating temperature, then removing the external field. This is explored for two potential cases: (1) exploiting the difference in T_c of two different bulk materials ('case-1'), e.g. MgB_2 ($T_c = 39$ K) and GdBaCuO ($T_c = 92$ K) or (2) using the same material for the whole HTFML, e.g., GdBaCuO, but utilizing individually controlled cryostats, the same cryostat with different cooling loops or coolants, or heaters that keep the outer bulk cylinder at a temperature above T_c to achieve the same desired effect. The effectiveness and superiority of the HTFML is verified using numerical simulations for two cases: 'case-1' using an MgB_2 cylinder and REBaCuO lens pair, and 'case-2' using a REBaCuO cylinder and REBaCuO lens pair. The concentrated magnetic field in the HTFML changes depending on the superconducting characteristics of the bulks [14, 15], their shape and size [12], as well as the magnetizing conditions.

2. Numerical simulation framework

The following numerical simulation framework for the magnetizing process of the HTFML has been developed. A schematic view of the three-dimensional numerical model and the relevant dimensions are shown in figure 2, in which the superconducting cylinder is made from bulk MgB_2 and the superconducting magnetic lens is made from bulk GdBaCuO. This model is abbreviated as 'case-1'. The bulk MgB_2 cylinder is 60 mm in outer diameter (O.D.), 40 mm in inner diameter (I.D.) and 80 mm in height (H). The shape of the magnetic lens is referred from [13] so that the present numerical framework explains the concept of the HTFML based on such a typical lens geometry (as shown in figure 2), but importantly two slits exist that are 10° wide. The MgB_2 cylinder and GdBaCuO lens are magnetized by a solenoid coil of 170 mm in O.D., 120 mm in I.D. and 200 mm in H. Another example is also provided, in which both the superconducting cylinder and magnetic lens are made from bulk GdBaCuO, which is abbreviated as 'case-2'. The numerical simulation results for 'case-1' and 'case-2' are presented in sections 4.1 and 4.2, respectively.

Table 1. Numerical parameters for the $J_c(B)$ characteristics of the bulk GdBaCuO material at 20 and 40 K using equation (2).

T (K)	J_{c1} (A m^{-2})	B_L (T)	J_{c2} (A m^{-2})	B_{max} (T)	α
40	3.5×10^9	0.9	2.7×10^9	6.0	0.8
20	9.0×10^9	1.5	5.4×10^9	8.0	0.5

Electromagnetic phenomena during the magnetization process are described by the fundamental equations shown elsewhere in detail [16–18]. The E–J power law is assumed to describe the nonlinear electrical properties of the superconducting bulk:

$$E = E_c\left(\frac{J}{J_c}\right)^n, \tag{1}$$

where E_c ($=10^{-4}$ V m^{-1}) is the characteristic electric field. $n = 20$ for the GdBaCuO bulk and $n = 100$ for the MgB_2 bulk are used [19]. The numerical simulation results depend strongly on the $J_c(B, T)$ characteristics of the superconductor [20–22]. For this study, the $J_c(B)$ characteristics for the GdBaCuO bulk are based on the equation presented by Jirsa *et al* to represent the so-called 'fish-tail' or 'peak' effect found in such superconducting materials [18, 23],

$$J_c(B) = J_{c1}\exp\left(-\frac{B}{B_L}\right) + J_{c2}\frac{B}{B_{max}}\exp\left[\frac{1}{\alpha}\left(1-\left(\frac{B}{B_{max}}\right)^{\alpha}\right)\right]. \tag{2}$$

The values for the parameters J_{c1}, B_L, J_{c2}, B_{max} and α at 20 and 40 K used in the model are shown in table 1, respectively.

The $J_c(B)$ of the MgB_2 bulk is described by the following equation [24],

$$J_c(B) = J_{c0}\exp\left[-\left(\frac{B}{B_0}\right)^{\beta}\right], \tag{3}$$

where J_{c0}, B_0 and β are fitting parameters, which are summarized in table 2. Isothermal conditions are assumed while ramping down the field because the magnetization process is slow; hence, no thermal model is included.

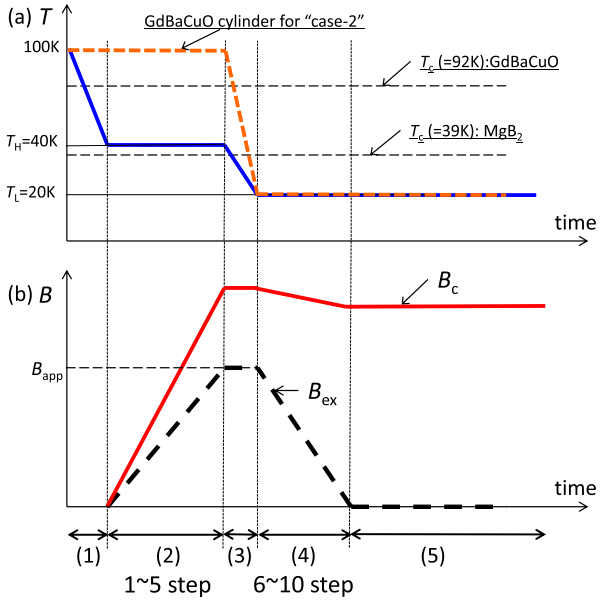

Figure 3. Time step sequence of (a) the temperature, T and (b) the external field, B_{ex}, and concentrated magnetic field, B_c, at the center of magnetic lens for 'case-1', in which an MgB_2 cylinder and GdBaCuO magnetic lens are used. In 'case-2', the temperature of the GdBaCuO lens follows the blue line and the GdBaCuO cylinder follows the dotted orange line in the upper panel (see text).

3. Magnetizing procedure

First, the magnetizing process is described for the following time step sequence, from (1) to (5), for the HTFML for 'case-1', in which the bulk MgB_2 cylinder and the bulk GdBaCuO magnetic lens are used. Figure 3 shows the time sequence of (a) the temperature, T and (b) the external field, B_{ex}, and concentrated magnetic field, B_c, at the center of the magnetic lens. The magnetizing applied field, B_{app}, corresponds to the maximum value of B_{ex}.

(1) The bulk MgB_2 cylinder and the bulk GdBaCuO lens are cooled from 100 K to $T_H = 40$ K, which is higher than the superconducting transition temperature of MgB_2, $T_c = 39$ K, but lower than that of GdBaCuO ($T_c = 92$ K). In this stage, the MgB_2 cylinder is in the normal state and the GdBaCuO lens is in the superconducting state (step 0).
(2) The external magnetic field, B_{ex}, is ramped up linearly at 0.222 T min^{-1} over five steps (steps 1–5) up to B_{app}, which corresponds to ZFCM of the GdBaCuO lens. The magnetic field, essentially higher than B_{app} because of the shielding effect by the magnetic lens, completely penetrates the MgB_2 cylinder and the magnetic field is concentrated at the center of the lens.
(3) The temperatures of both MgB_2 cylinder and GdBaCuO lens are then decreased to $T_L = 20$ K, which is lower than the T_c of MgB_2.
(4) B_{ex} is decreased linearly at 0.222 T min^{-1} over five steps (steps 6–10) down to zero. During this process, the MgB_2 cylinder is magnetized by FCM and magnetic flux is trapped in the cylinder. The magnetic field concentration effect slightly decreases due to the decrease of external field. However, a magnetic field at the center of the magnetic lens still remains due to the existence of the trapped field in the MgB_2 cylinder.
(5) As a result, HTFML can reliably generate a magnetic field higher than B_T of the single cylindrical TFM and B_{app}, even after $B_{ex} = 0$.

Table 2. Numerical parameters for the $J_c(B)$ characteristics of the bulk MgB_2 material at 20 K using equation (3).

T (K)	J_{c0} (A m^{-2})	B_0 (T)	α
20	4.3×10^9	1.1	1.5

There are some examples of a practical cooling system using the difference in T_c of two superconducting components for an aircraft motor design [25] and a magnetic levitation application [26].

In 'case-2', in which both the superconducting cylinder and magnetic lens are made from bulk GdBaCuO, (1) and (2) above are changed as follows, labeled at (1') and (2'):

(1') The bulk GdBaCuO cylinder is maintained at 100 K (dotted orange line in figure 3) and the bulk GdBaCuO magnetic lens is cooled to $T_H = 40$ K (blue line in figure 3). Hence, the bulk GdBaCuO cylinder is in the normal state and the bulk GdBaCuO lens is in the superconducting state (step 0).
(2') The external magnetic field, B_{ex}, is increased linearly over five steps (steps 1–5) up to B_{app}, and the magnetic field, essentially equal to B_{app}, completely penetrates the GdBaCuO cylinder, but the GdBaCuO lens is magnetized by ZFCM.

In the next section, the results of the numerical simulation for 'case-1' and 'case-2' are presented to prove the effectiveness of the HTFML.

4. Simulation results and discussion

4.1. 'Case-1': MgB_2 cylinder–GdBaCuO lens

Figure 4 shows the time step dependence of the magnetic field profile along the x-direction across the center of the lens during (a) the ascending stage and (b) the descending stage of ZFCM of the GdBaCuO lens under an applied field, $B_{app} = 3$ T in 'case-1', which incorporates FCM of the MgB_2 cylinder. In figure 4(a), during the ascending stage from steps 0–5, the concentrated magnetic field, B_c, at the center of the GdBaCuO lens was enhanced with increasing B_{ex} owing to the diamagnetic shielding effect of the GdBaCuO lens. It can be found that there is little or no flux penetration in the GdBaCuO lens region ($r = \pm 5 \sim 18$ mm) in this case applying a relatively low magnetic field of 3 T by a magnetizing coil. The magnetic flux intrudes into the lens from inner

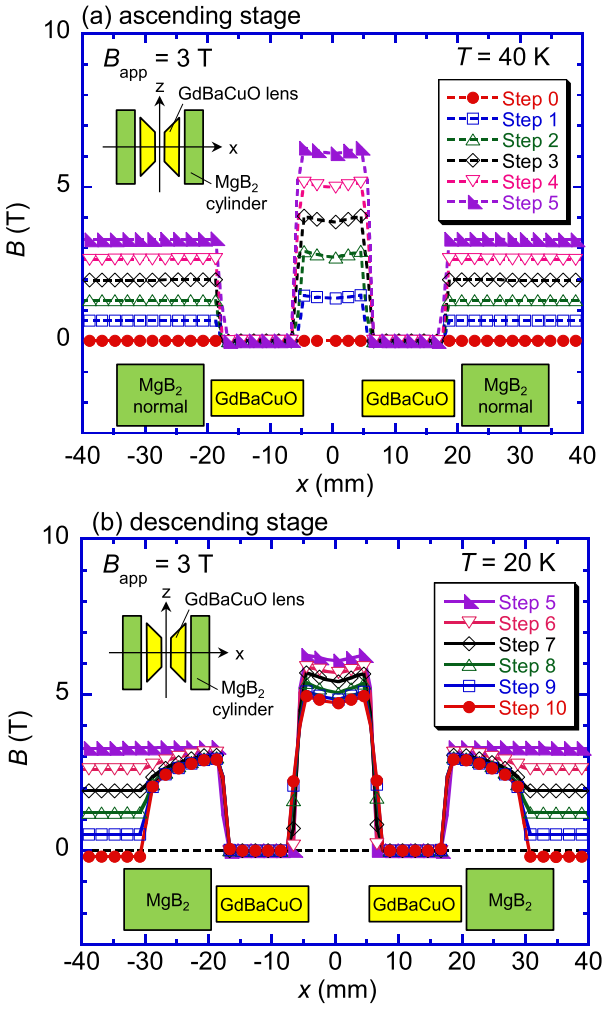

Figure 4. Time step dependence of the magnetic field profile along the *x*-direction across the center of the lens during (a) the ascending stage and (b) the descending stage of ZFCM of the GdBaCuO lens under an applied field, $B_{app} = 3$ T in 'case-1', which incorporates FCM of the MgB_2 cylinder.

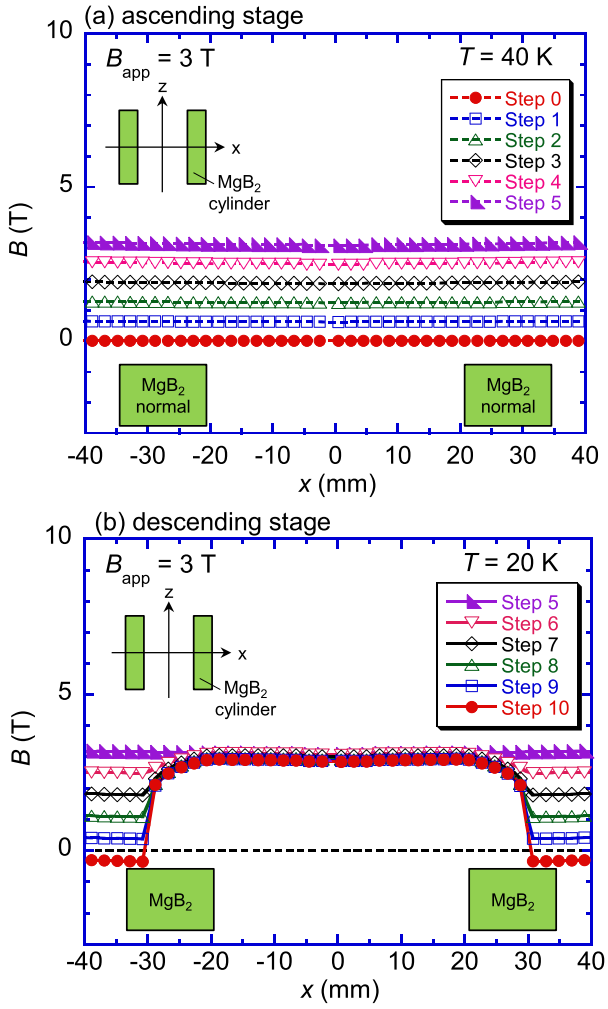

Figure 5. Time step dependence of the magnetic field profile along the *x*-direction across the center of the lens during (a) the ascending stage and (b) the descending stage of FCM of the MgB_2 cylinder without the GdBaCuO lens for an applied field, $B_{app} = 3$ T at 20 K.

periphery rather than outer edge because of the magnetic flux concentration, which will be discussed later for higher B_{app} in 'case-2'. In this ascending stage, the GdBaCuO lens is under ZFCM conditions at 40 K; however, the MgB_2 cylinder is in the normal state and is not yet utilized as a TFM. In figure 4(b), during the descending stage of B_{ex} from steps 5–10, which incorporates FCM of the MgB_2 cylinder during ZFCM of the GdBaCuO lens, B_c decreased with decreasing B_{ex}, but becomes stable after the external field decreases to zero and a magnetic field is trapped in the MgB_2 cylinder. As a result, B_c at the center of the GdBaCuO lens settled to $B_c = 4.73$ T at the final step (step 10), which can be realized quasi-permanently by the novel combination of the 'vortex pinning effect' and 'diamagnetic shielding effect' of superconducting bulk materials.

Figures 5(a) and (b), respectively, show the time step dependence of the magnetic field profiles along the *x*-direction across the center of the lens during the ascending and descending stages of FCM for an applied field, $B_{app} = 3$ T for only the MgB_2 cylinder, without the GdBaCuO lens, in 'case-1'. In figure 5(a), when only the MgB_2 cylinder is considered, the B_T value is nearly the same as B_{ex} in the ascending stage (steps 0–5), and attains a maximum value $B_{ex} = 3$ T at step 5 with a uniform magnetic field profile along *x*-direction, which corresponds to the applied field profile generated by the externally magnetizing coil. During this ascending stage, the MgB_2 cylinder is in the normal state. In figure 5(b), in the descending stage (steps 6–10), the trapped field, B_T, of the MgB_2 cylinder by FCM decreases slightly with decreasing B_{ex}, and settles to a final value of $B_T = 2.85$ T at the final step (step 10) in the bore of MgB_2 cylinder, now acting as a TFM that can continue to provide the trapped field quasi-permanently. One of the particular characteristics of the HTFML device is to utilize the trapped field from this TFM, instead of requiring a continuously applied field from an external magnetizing coil. Thus, it is useful to be able to reproduce a magnetic field profile similar to that which might be produced

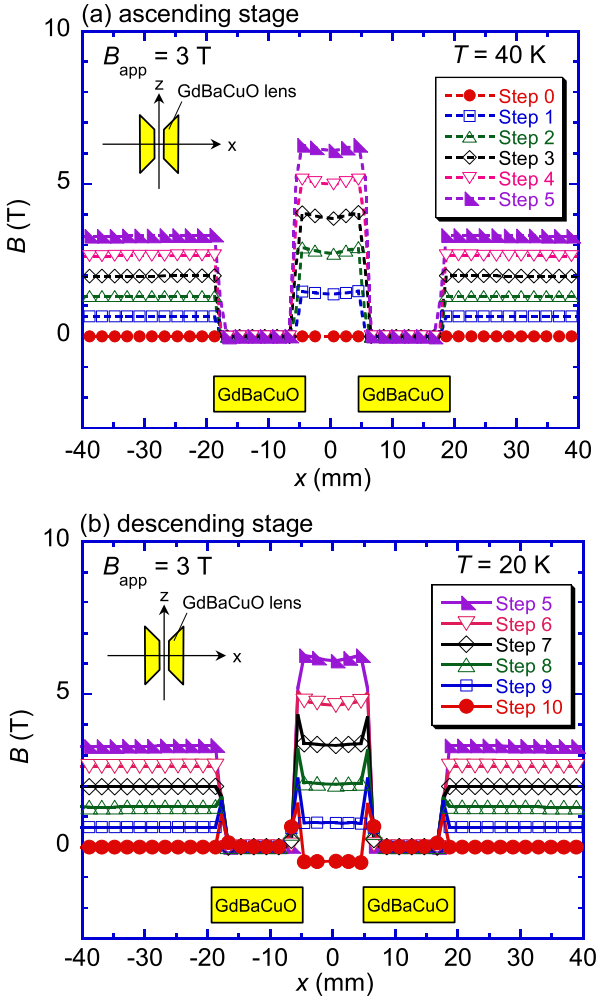

Figure 6. Time step dependence of the magnetic field profile along the x-direction across the center of the lens during (a) the ascending stage and (b) the descending stage of ZFCM of the GdBaCuO lens without the MgB_2 cylinder for an applied field, $B_{app} = 3$ T at 20 K.

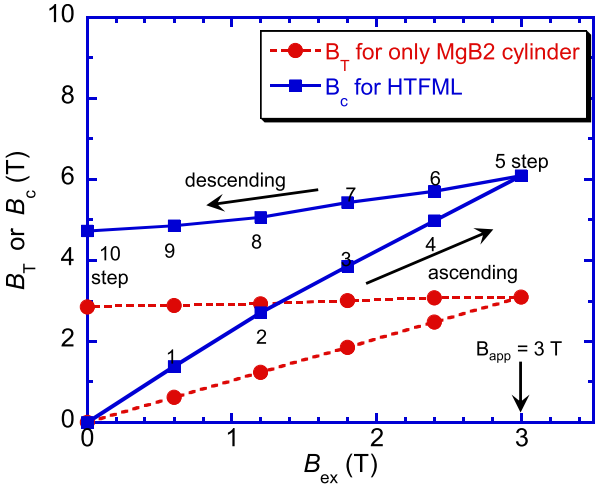

Figure 7. Concentrated magnetic field, B_c, at the center of the magnetic lens as a function of the external field, B_{ex}, for $B_{app} = 3$ T. The trapped field, B_T, at the center of the MgB_2 cylinder for the case without the GdBaCuO lens extracted from figure 5 is also shown.

by a magnetizing solenoid coil when we use the TFM as a source of magnetic field for the HTFML, for further concentration of the magnetic flux in the HTFML. This could, for example, allow the realization of higher resolution in a compact and cryogen-free NMR/MRI system using annular REBaCuO superconducting bulks [27, 28].

To achieve the highest concentrated field in the lens, the GdBaCuO magnetic lens must, in the ideal case, completely shield the magnetic field from its interior. However, since it is a type II superconductor, some magnetic flux will penetrate the material, depending on its $J_c(B, T)$ characteristics (and hence operating temperature), as well as its geometry, during the HTFML magnetizing procedure. Figures 6(a) and (b), respectively, show the time step dependence of the magnetic field profiles along the x-direction across the center of the lens during the ascending and descending stages of ZFCM for an applied field, $B_{app} = 3$ T for the only GdBaCuO lens without the MgB_2 cylinder in 'case-1'. Figure 6(a) is exactly the same as figure 4(a), in which B_c at the center of the GdBaCuO lens was enhanced gradually with increasing B_{ex} in the ascending stage from steps 0–5. In figure 6(b), in the descending stage from steps 6–10, it can be seen that there is some flux penetration into the inner edge of GdBaCuO lens at around $r = \pm 5 \sim 7$ mm from step 7 even for a relatively low applied field of 3 T during ZFCM. The magnetic field reached eventually becomes −0.46 T at the center of the GdBaCuO lens at the final step (step 10) after ZFCM, resulting in a reduction from the ideal of the GdBaCuO lens shielding effect in those regions where the magnetic flux penetrates during ZFCM. Thus, to maximize the lens's shielding, and hence its ability to concentrate the magnetic field, the flux penetration should be minimized.

Figure 7 shows the concentrated magnetic field, B_c, at the center of magnetic lens as a function of external field, B_{ex}, for $B_{app} = 3$ T, which was extracted from figure 4. The trapped field, B_T, at the center of the MgB_2 cylinder was also extracted from figure 5 for the case without the GdBaCuO lens, which clarifies the effectiveness of the HTFML. For only MgB_2 cylinder, the B_T value is nearly the same as B_{ex} in the ascending stage from step 0 and attains a maximum value $B_{ex} = 3$ T at step 5. The B_T value is then 2.85 T at the final step (step 10) once $B_{ex} = 0$, showing that 3 T is a reasonable value to fully magnetize the MgB_2 cylinder by FCM at 20 K. In the case of the HTFML using both the MgB_2 cylinder and GdBaCuO lens, B_c at the center of the GdBaCuO lens was enhanced up to 6.10 T at step 5 due to the shielding effect of lens and settled to $B_c = 4.73$ T at the final step (step 10), which is higher than both B_{app} from the magnetizing coil and B_T from the MgB_2 TFM. These results indicate the superiority of the proposed HTFML device, which can reliably generate the concentrated magnetic field higher than the applied field by the external magnetizing coil and the trapped field of the TFM, even after removal of the external field.

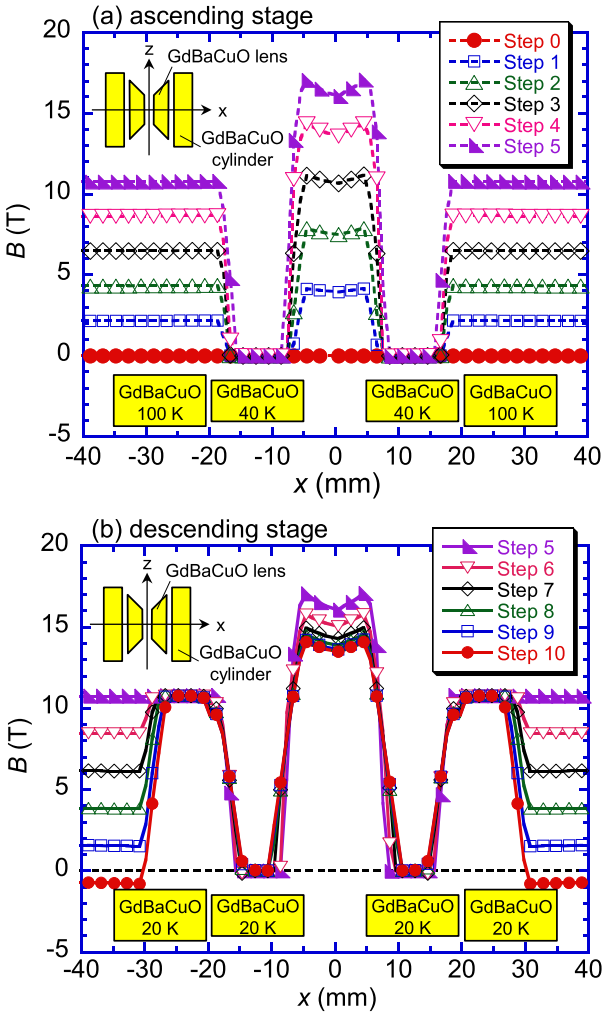

Figure 8. Time step dependence of magnetic field profile along the *x*-direction across the center of the lens during (a) the ascending stage and (b) the descending stage for $B_{app} = 10$ T in 'case-2'.

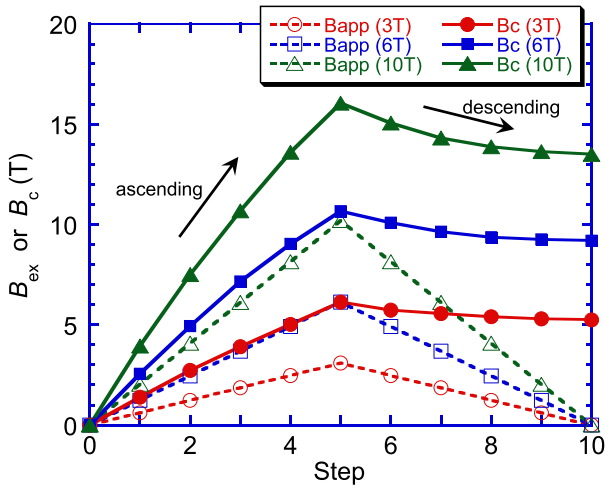

Figure 9. Time step dependence of the concentrated magnetic field, B_c, at the center of the GdBaCuO lens in the HTFML for $B_{app} = 3$, 6 and 10 T for 'case-2'. The external field, B_{ex}, generated by the solenoid magnetizing coil is also shown for each B_{app}.

4.2. 'Case-2': GdBaCuO cylinder–GdBaCuO lens

In the previous section, the superiority of the HTFML device in 'case-1' using a MgB_2 cylinder and REBaCuO lens pair was verified, for which the concentrated magnetic field was enhanced up to $B_c = 4.73$ T at the center of the GdBaCuO lens, which is higher than the trapped field of $B_T = 2.8$ T generated by the MgB_2 cylinder and the applied field, $B_{app} = 3.0$ T, generated by the external magnetizing coil. In this section, the other example of 'case-2' using a REBaCuO cylinder and REBaCuO lens pair for further concentration of the trapped magnetic flux is explored.

Figure 8 shows the time step dependence of the magnetic field profile along the *x*-direction across the center of the lens during (a) the ascending stage and (b) the descending stage for $B_{app} = 10$ T in 'case-2'. In this case, it should be noted that the temperature of the GdBaCuO cylinder and lens must be controlled individually. Similar results were shown previously for 'case-1' in figure 4(a), where the magnetic field profile was shown during the ascending stage of ZFCM for $B_{app} = 3$ T for the GdBaCuO lens from steps 0–5 (noting that the MgB_2 cylinder is in the normal state). In figure 8(a), the B_c value was enhanced up to $B_c = 16$ T at the center of the lens at step 5 when applying $B_{app} = 10$ T. The GdBaCuO lens could retain its shielding effect even in a higher external magnetic field of 10 T, although the magnetic shielding effect weakens with increasing applied field due to further penetration of magnetic flux [11]. In figure 8(b), during the descending stage (steps 5–10), the GdBaCuO cylinder maintains a trapped field similar to B_{app} at the final step (step 10) as it is magnetized by FCM, but below its full capability based on its high J_c–B characteristics at 20 K. The B_c value gradually decreased during the descending stage and settled to a final value of $B_c = 13.5$ T at the center of the lens.

Figure 9 shows the time step dependence of the concentrated magnetic field, B_c, and external field, B_{ex}, at the center of the GdBaCuO lens for $B_{app} = 3$, 6 and 10 T for 'case-2'. Table 3 summarizes the concentrated magnetic field, B_c, trapped field from the TFM, B_T, when only considering the TFM cylinder (i.e., the lens is not present), at the central position at the final step (step 10), and the concentration ratio, B_c/B_{app}, in 'case-2' extracted from figure 9 for each actual B_{app}. An accurate value of B_{app} is shown as $B^*_{app} = 3.09$ T, 6.13 T and 10.18 T in this table, which was named roughly as $B_{app} = 3$, 6, 10 T so far. Similar results for 'case-1' from figure 4 are also shown for comparison. For the lower $B_{app} = 3$ T, a magnetic field concentration ratio of $B_c/B_{app} = 1.70$ is achieved at the final step (step 10) in 'case-2', which is higher than 1.53 when using the MgB_2 cylinder in 'case-1'. This results from the higher B_T value of 3.09 T in 'case-2', where the outside GdBaCuO cylinder was magnetized below its full capability. Furthermore, in 'case-2', the concentration ratio decreased with increasing B_{app} from 1.70 for $B_{app} = 3$ T to 1.33 for $B_{app} = 10$ T. In figure 9, the higher B_{app} resulted in a larger flux creep during the descending stage of FCM of the TFM cylinder and further penetration of magnetic flux in the ZFCM of the GdBaCuO lens. There is a possibility to achieve further

Table 3. Concentrated magnetic field, B_c, trapped field by TFM, B_T, at the center of the GdBaCuO lens at the final step (step 10), and magnetic field concentration ratio, B_c/B_{app}, in 'case-2' extracted from figure 9 for each actual applied field, B^*_{app}. Similar results for 'case-1' from figure 4 are also shown for comparison.

	B_{app} (T)	B^*_{app} (T)	B_T (T)	B_c (T)	B_c/B_{app}
'case-1' (MgB2 cylinder)	3	3.09	2.85	4.73	1.53
'case-2' (GdBaCuO cylinder)	3	3.09	3.09	5.25	1.70
	6	6.13	6.13	9.19	1.50
	10	10.18	10.18	13.49	1.33

enhancement of B_c and B_c/B_{app} by optimization of the magnetic design, including the geometry of the cylinder and lens, and the magnetization conditions, including temperature and applied field. The shielding property of the magnetic lens should be also exploited for further concentration of the trapped field, such as for hollow bulk cylinders [14]. These results show that the effectiveness of the HTFML would be enhanced in terms of the characteristics of the superconducting material(s) used, including the possibility of utilizing new and improved materials, such as $BaFe_2As_2$ ($T_c = 38$ K) [29, 30].

5. Conclusion

A new concept of an HTFML, consisting of a superconducting bulk cylinder TFM using the vortex pinning effect, combined with a bulk magnetic lens using the diamagnetic shielding effect, is proposed, which can reliably generate a magnetic field at the center of the magnetic lens higher than the trapped field by TFM and the maximum external magnetizing field, even after the externally applied field decreases to zero. The effectiveness and superiority of the HTFML was verified using numerical simulations for two examples: (1) an MgB_2 cylinder and GdBaCuO lens pair ('case-1') and (2) a GdBaCuO cylinder and GdBaCuO lens pair ('case-2'). In 'case-1', using the outer MgB_2 cylinder and inner GdBaCuO lens pair, the MgB_2 cylinder was magnetized by FCM with an applied field, $B_{app} = 3$ T, during the descending stage, also corresponding to ZFCM of the GdBaCuO lens. The trapped field, $B_T = 2.85$ T, in the MgB_2 TFM cylinder was concentrated by the introduction of GdBaCuO lens, and a concentrated magnetic field, $B_c = 4.73$ T, was reliably achieved at the center of the lens. In 'case-2', using the outer GdBaCuO TFM cylinder and inner GdBaCuO lens pair, in which the GdBaCuO cylinder is held above T_c and the GdBaCuO lens is cooled below T_c for the ascending stage of magnetization, followed by both bulks being cooled below T_c for the descending stage, a higher $B_c = 13.49$ T, was reliably achieved at the center of the magnetic lens for $B_{app} = 10$ T.

The advantages and disadvantages of each HTFML, comparing use of the MgB_2 cylinder and the GdBaCuO cylinder are summarized as follows:

'case-1': The MgB_2 HTFML only needs one cooling process for the whole device by exploiting the difference in T_c of the two superconducting materials. Its weight would also be lower due to the use of the lighter bulk MgB_2 cylinder. However, the trapped field capability is limited in comparison to the GdBaCuO cylinder ('case-2') because of the comparatively inferior $J_c(B)$ characteristics of MgB_2 and it must operate at a temperature lower than the superconducting transition temperature of MgB_2, $T_c = 39$ K.

'case-2': The all-GdBaCuO HTFML offers higher concentrated fields at temperatures much higher than 39 K, but does require separate cooling of the cylinder and lens parts to obtain the necessary effect and it would weigh more.

This HTFML device could become a standard method for trapped field enhancement in several practical applications using a superconducting bulk and there is a scope for optimization of the magnetic design, including geometry around two bulks, and magnetization conditions, including temperature and applied field. The effectiveness of the HTFML would be enhanced with improvements in the characteristics of the superconducting material(s) used, including the possibility of utilizing new and improved materials such as $BaFe_2As_2$ ($T_c = 38$ K). The device could, for example, be used to enhance the magnetic field in the bore of a bulk superconducting NMR/MRI system to improve its resolution.

Acknowledgments

This research is partially supported from JSPS KAKENHI Grant No. 15K04646. Mark Ainslie would like to acknowledge financial support from an Engineering and Physical Sciences Research Council (EPSRC) Early Career Fellowship EP/P020313/1. All data are provided in full in the results section of this paper.

ORCID iDs

Keita Takahashi https://orcid.org/0000-0002-8278-2688
Hiroyuki Fujishiro https://orcid.org/0000-0003-1483-835X
Mark D Ainslie https://orcid.org/0000-0003-0466-3680

References

[1] Shi Y-H, Namburi D K, Zhao W, Durrell J H, Dennis A R and Cardwell D A 2016 *Supercond. Sci. Technol.* **29** 015010
[2] Muralidhar M, Sakai N, Chikumoto N, Jirsa M, Machi T, Nishiyama M, Wu Y and Murakami M 2002 *Phys. Rev. Lett.* **89** 237001
[3] Tomita M and Murakami M 2003 *Nature* **421** 517–20

[4] Durrell J H *et al* 2014 *Supercond. Sci. Technol.* **27** 082001
[5] Fujishiro H, Tateiwa T, Fujiwara A, Oka T and Hayashi H 2006 *Physica* C **334–338** 445–8
[6] Matsumoto S, Kiyoshi T, Asano T, Ozaki O, Koyanagi K, Fujihira J and Wada H 2003 *IEEE Trans. Appl. Supercond.* **13** 1652–5
[7] Matsumoto S, Asano T, Kiyoshi T and Wada H 2004 *IEEE Trans. Appl. Supercond.* **14** 1666–9
[8] Asano T, Itoh K, Matsumoto S, Kiyoshi T, Wada H and Kido G 2005 *IEEE Trans. Appl. Supercond.* **15** 3157–60
[9] Kiyoshi T, Choi S, Matsumoto S, Asano T and Uglietti D 2009 *IEEE Trans. Appl. Supercond.* **19** 2174–7
[10] Zhang Z Y, Matsumoto S, Teranishi R and Kiyoshi T 2012 *Supercond. Sci. Technol.* **25** 115012
[11] Choi S, Yoon J-H, Lee B-S, Won M-S, Ok J-W, Zhang Z-Y, Kiyoshi T, Matsumoto S and Lee S-H 2012 *J. Appl. Phys.* **111** 07E728
[12] Zhang Z Y, Choi S, Matsumoto S, Teranishi R, Giunchi G, Albisetti A F and Kiyoshi T 2012 *Supercond. Sci. Technol.* **25** 025009
[13] Zhang Z Y, Matsumoto S, Teranishi R and Kiyoshi T 2013 *Supercond. Sci. Technol.* **26** 045001
[14] Lousberg G P, Fagnard J F, Ausloos M, Vanderbemden P and Vanderheyden B 2010 *IEEE Trans. Appl. Supercond.* **20** 33–41
[15] Rabbers J J, Oomen M P, Bassani E, Ripamonti G and Giunchi G 2010 *Supercond. Sci. Technol.* **23** 125003
[16] Fujishiro H and Naito T 2011 *Supercond. Sci. Technol.* **23** 105021
[17] Fujishiro H, Ainslie M D, Takahashi K, Naito T, Yanagi Y, Itoh Y and Nakamura T 2017 *Supercond. Sci. Technol.* **30** 085008
[18] Takahashi K, Fujishiro H, Naito T, Yanagi Y, Itoh Y and Nakamura T 2017 *Supercond. Sci. Technol.* **30** 115006
[19] Fujishiro H, Naito T and Yoshida T 2014 *Supercond. Sci. Technol.* **27** 065019
[20] Ainslie M D, Zou J, Mochizuki H, Fujishiro H, Shi Y-H, Dennis A R and Cardwell D A 2015 *Supercond. Sci. Technol.* **28** 125002
[21] Ainslie M D and Fujishiro H 2015 *Supercond. Sci. Technol.* **28** 053002
[22] Ainslie M D, Zhou D, Fujishiro H, Takahashi K, Shi Y-H and Durrell J H 2016 *Supercond. Sci. Technol.* **29** 124004
[23] Jirsa M, Půst L, Dlouhý D and Koblischka M R 1997 *Phys. Rev.* B **55** 3276–84
[24] Xiang F X, Wang X L, Xun X, Silva K S B D, Wang Y X and Dou S X 2013 *Appl. Phys. Lett.* **102** 152601
[25] Masson P J, Breschi M, Tixador P and Luongo C A 2007 *IEEE Trans. Appl. Supercond.* **17** 1533–6
[26] Patel A, Giunchi G, Albisetti A F, Shi Y, Hopkins S C, Palka R, Cardwell D A and Glowacki B A 2012 *Phys. Proc.* **36** 937–42
[27] Nakamura T, Tamada D, Yanagi Y, Itoh Y, Nemoto T, Utsumi H and Kose K 2015 *J. Magn. Reson.* **259** 68–75
[28] Ogawa K, Nakamura T, Terada Y, Kose K and Haishi T 2011 *Appl. Phys. Lett.* **98** 234101
[29] Weiss J D, Yamamoto A, Polyanskii A A, Richardson R B, Larbalestier D C and Hellstrom E E 2015 *Supercond. Sci. Technol.* **28** 112001
[30] Ainslie M D, Yamamoto A, Fujishiro H, Weiss J D and Hellstrom E E 2017 *Supercond. Sci. Technol.* **30** 105009

7. (H-3) Sora Namba, Hiroyuki Fujishiro, Tomoyuki Naito, Mark D Ainslie and Keita Takahashi,
   “Experimental realization of a Hybrid Trapped Field Magnet Lens (HTFML) using a GdBaCuO magnetic lens and MgB_2 bulk cylinder”,
   Supercond. Sci. Technol. Letter **32** (2019) 12LT03 (7 pages) (No. 271 paper)

OPEN ACCESS
IOP Publishing
Letters
Superconductor Science and Technology
Supercond. Sci. Technol. 32 (2019) 12LT03 (7pp)
https://doi.org/10.1088/1361-6668/ab5048

Letter

Experimental realization of a hybrid trapped field magnet lens using a GdBaCuO magnetic lens and MgB_2 bulk cylinder

Sora Namba[1,3], Hiroyuki Fujishiro[1], Tomoyuki Naito[1], Mark D Ainslie[2] and Keita Takahashi[1]

[1] Department of Physical Science and Materials Engineering, Faculty of Science and Engineering, Iwate University, 4-3-5 Ueda, Morioka 020-8551, Japan
[2] Department of Engineering, University of Cambridge, Trumpington Street, Cambridge CB2 1PZ, United Kingdom

E-mail: g0318128@iwate-u.ac.jp

Received 13 August 2019, revised 13 October 2019
Accepted for publication 18 October 2019
Published 5 November 2019

Abstract

A hybrid trapped field magnet lens (HTFML) is a promising device that is able to concentrate a magnetic field higher than the applied field continuously, even after removing an external field, which was conceptually proposed by the authors in 2018. This paper presents, for the first time, the experimental realization of the HTFML using a GdBaCuO magnetic lens and MgB_2 trapped field magnet cylinder. A maximum concentrated magnetic field of $B_c = 3.55$ T was achieved at the central bore of the HTFML after removing an applied field of $B_{app} = 2.0$ T at $T = 20$ K. For higher B_{app}, the B_c value was not enhanced because of a weakened lens effect due to magnetic flux penetration into the bulk GdBaCuO material comprising the lens. The enhancement of the trapped field using such an HTFML for the present experimental setup is discussed in detail.

Keywords: hybrid trapped magnet field lens, bulk superconductors, trapped field magnets, magnetic lens, vortex pinning effect, magnetic shielding effect

(Some figures may appear in colour only in the online journal)

1. Introduction

Trapped field magnets (TFMs) using superconducting bulks such as REBaCuO (RE: a rare earth element or Y) and MgB_2 have been vigorously investigated for various practical applications; for example, rotating machines, magnetic separation, flywheel energy storage systems and so on [1–3]. Superconducting bulk TFMs, in which magnetic flux is trapped by the strong 'vortex pinning effect', are usually magnetized by field-cooled magnetization (FCM) using a high, stationary magnetic field, for which a magnetic field nearly the same or slightly lower than the applied field can be trapped. The trapped field capability of such bulks, as estimated from state-of-the-art $J_c(B, T)$ characteristics could exceed 20 T at 20 K in a disk bulk pair [4]. However, the trapped field is limited experimentally by the poor mechanical strength of the brittle ceramic material [5]. A large Lorentz force is developed in the bulk during the magnetization process, which sometimes results in crack formation and propagation, leading to eventual mechanical failure [6, 7]. To date, REBaCuO disk bulks have trapped magnetic fields over 17 T by mechanical reinforcement using glass fiber reinforced epoxy resin or shrink-fit stainless steel to reduce the

[3] Author to whom any correspondence should be addressed

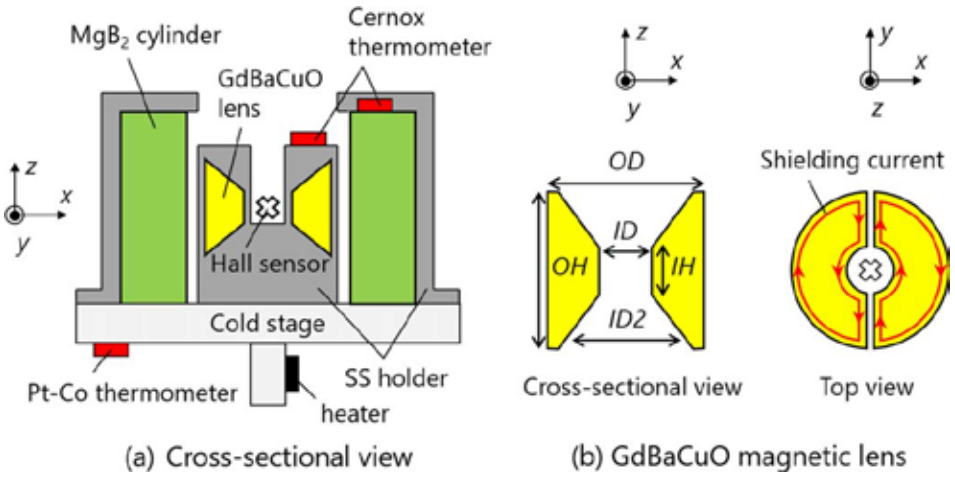

Figure 1. (a) Cross-sectional view of the schematic illustration of the experimental setup for the HTFML on the cold stage of a refrigerator. (b) Cross-sectional and top views of the GdBaCuO magnetic lens with slits. When a magnetic field is applied along the $+z$-axis direction to the GdBaCuO magnetic lens, the magnetic field penetrates from the slits and the shielding current flows as shown by the red arrows. As a result, the magnetic field increases along the $+z$-direction due to the shielding current.

electromagnetic hoop stress [4, 8]. A ring-shaped bulk superconductor that can produce uniform, high magnetic fields within the central bore is a strong candidate for compact cryogen-free nuclear magnetic resonance (NMR) and magnetic resonance imaging (MRI) systems [9–11]. The ^{1}H spectra of toluene with a full width at half maximum of 0.4 ppm (80 Hz) was achieved in the 10 mm room temperature bore in the bulk NMR [10]. The first MRIs using annular EuBaCuO bulks were also reported with a magnetic homogeneity of 37 ppm (peak-to-peak) achieved in a Φ 6.2 mm $\times$ 9.1 mm cylindrical space with first order shimming [11]. Using this system, a clear 3D image of a chemically-fixed mouse fetus was acquired.

On the other hand, a 'magnetic lens' using cone-shaped superconducting bulks has been investigated, in which a magnetic field is concentrated in the bore of the lens using the 'diamagnetic shielding effect' of superconducting materials and the available magnetic field in the lens is higher than the applied field generated by an external magnetizing coil [12–18]. For example, a concentrated field of $B_c = 12.42$ T has been achieved at 20 K for a background field of $B_{app} = 8$ T using a bulk GdBaCuO magnetic lens [12]. Since the magnetic lens effect vanishes after the applied field decreased to zero, the external magnet must be operated continuously, which consumes energy and is not environmentally friendly.

We recently proposed a new concept of a hybrid trapped field magnet lens (HTFML) [19], consisting of a cylindrical bulk TFM exploiting the 'vortex pinning effect', combined with a bulk magnetic lens exploiting the 'diamagnetic shielding effect'. Using numerical simulations, the HTFML was shown to be able to reliably generate a magnetic field in the central bore of the magnetic lens that is higher than both the trapped field in the single cylindrical bulk TFM and the external magnetizing field, even after the externally applied field decreases to zero. For a REBaCuO magnetic lens and MgB_2 TFM cylinder, the HTFML could reliably generate a concentrated magnetic field of $B_c = 4.73$ T with an external magnetizing field $B_{app} = 3$ T. For an HTFML comprised of REBaCuO bulks for both magnetic lens and TFM cylinder, a concentrated magnetic field of $B_c = 13.49$ T could be generated with an external magnetizing field $B_{app} = 10$ T, where the temperature of both parts is controlled independently [19]. In addition, the shape of the magnetic lens in the HTFML has been optimized, and the mechanical stress in the cylinder and lens parts has also been estimated during the magnetizing process [20].

In this paper, we present, for the first time, the experimental realization of the HTFML using a GdBaCuO magnetic lens and MgB_2 TFM cylinder, based on the same magnetizing procedure proposed in [19]. The experimental results are compared with the simulated ones and enhancement of the B_c value in HTFML is discussed in detail.

2. Experimental procedure

2.1. Experimental setup

Figure 1(a) shows the schematic cross-section of the experimental setup of the HTFML on the cold stage of a refrigerator. The MgB_2 cylindrical bulk (60 mm in outer diameter (OD), 40 mm in inner diameter (ID), and 60 mm in height (H)) was fabricated using the infiltration method by Experiments Projects Constructions S. R. I., Italy [21, 22]. Figure 1(b) shows the cross-section and top view of the GdBaCuO magnetic lens. The GdBaCuO magnetic lens was prepared by the following process: stacked GdBaCuO cylindrical bulks (OD = 36 mm, ID = 10 mm, H = 30 mm), fabricated using the QMG™ method by Nippon Steel Corporation, Japan [23, 24], were machined into a cone-shape of OD = 30 mm, ID = 10 mm, ID2 = 26 mm, outer height (OH) = 30 mm and inner height (IH) = 8.0 mm, as shown in figure 1(b). The dimensions of the bulk magnetic lens were

optimized using numerical simulations [20]. Thin slits of width 200 μm was made to disrupt the circumferential flow of the shielding current during the zero-field-cooling (ZFC) process, which plays an important role in magnetic flux concentration for the magnetic lens [19]. When an external magnetic field is applied along the $+z$-axis direction to the GdBaCuO magnetic lens, the same magnetic field penetrates into the central bore from the slits. The shielding current flows as shown by the red arrows in figure 1(b) and an additional magnetic field exists along the $+z$-axis direction, mainly due to the counterclockwise shielding current nearest to the central bore. As a result, the magnetic field is enhanced along the $+z$-axis direction, which is then higher than the applied field.

The GdBaCuO magnetic lens was encapsulated in a stainless steel (SS) holder to prevent fracture of the bulk due to the large Lorentz force during the magnetization process, and was connected thermally to the cold stage of the refrigerator. The MgB_2 cylindrical bulk was reinforced by a SS cylinder (ID = 60 mm, OD = 66 mm and H = 60 mm) and the top SS plate (ID = 36 mm, OD = 66 mm and H = 3 mm), which were effective in preventing mechanical fracture [25, 26]. These SS holders apply a compressive stress to the bulk cylinder and bulk lens during the cooling process from room temperature to the operating temperature (e.g. 20 K) due to the difference in the coefficient of thermal expansion between SS and the bulk superconducting materials. Two CERNOX™ thermometers were attached for monitoring the temperature of the HTFML; one was mounted directly on the top surface of the MgB_2 cylinder, and the other was placed on the top surface of the SS holder of the GdBaCuO lens. Thin indium sheets were inserted between the bulks and the cold stage of the refrigerator (or SS holder) to obtain good thermal contact. The temperature of the cold stage was controlled using a Pt-Co thermometer and a resistive heater, attached to bottom surface of the cold stage. The concentrated field, B_c, was measured in the central bore of the HTFML by an axial-type Hall sensor (F W Bell, BHA-921). The HTFML device was placed in a vacuum chamber and then evacuated by a vacuum pump system.

2.2. Magnetization procedure

Figure 2 shows the time sequence of the external field (left vertical axis), B_{ex}, at the center of the HTFML and the operating temperature (right vertical axis), T, during the magnetizing process of the HTFML. The magnetizing external field, B_{app}, corresponds to the maximum value of B_{ex}. The HTFML device set in the vacuum chamber was inserted into a cryocooled 10 T superconducting solenoid magnet (JASTEC JMTD-10T100). First, the MgB_2 bulk cylinder and GdBaCuO bulk lens were cooled to T = 40 K. In this stage, the MgB_2 cylinder is in the normal state and the GdBaCuO lens is in the superconducting state, where the time step (TS) is defined as TS = 0. The proof-of-concept experiments of the HTFML were performed according to the following magnetizing process.

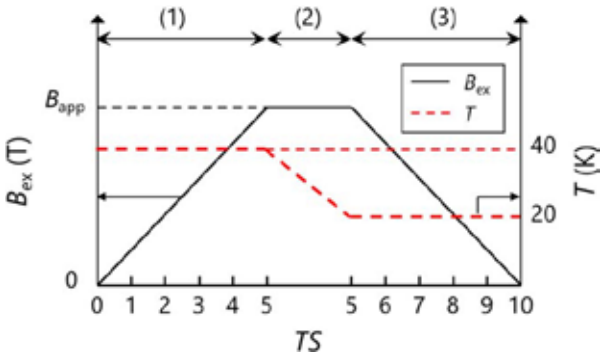

Figure 2. Time step (TS) sequence of the external field (black: left vertical axis), B_{ex}, at the center of the HTFML and the operating temperature (red: right vertical axis), T, during the magnetizing process to realize the HTFML. The magnetizing applied field, B_{app}, corresponds to the maximum value of B_{ex}.

(1) The external magnetic field, B_{ex}, was ramped up linearly at $+0.222\ \mathrm{T\ min^{-1}}$ to $B_{app} = 1-3$ T over five steps, where TS of the ascending stage is defined as TS = 1–5. This process corresponds to ZFC magnetization of the GdBaCuO lens, in which the magnetic field at the center is essentially higher than B_{app} because of the shielding effect by the magnetic lens.
(2) The temperatures of both the MgB_2 cylinder and GdBaCuO lens were decreased to T = 20 K under the applied field B_{app}, with both materials now in the superconducting state.
(3) B_{ex} was decreased linearly at $-0.011\ \mathrm{T\ min^{-1}}$ over five steps (TS = 6–10) down to zero. During this process, the MgB_2 cylinder was magnetized by FCM and magnetic flux was trapped in the cylinder. A magnetic field at the center of the magnetic lens still remains due to the existence of the trapped field in the MgB_2 cylinder. As a result, the HTFML can reliably generate a magnetic field higher than the trapped field in the single MgB_2 TFM cylinder and B_{app}, even after $B_{ex} = 0$.

Prior to the HTFML experiments, the trapped field properties of the MgB_2 cylinder and the magnetic concentration capability of the GdBaCuO lens were investigated independently using the same time sequence as shown in figure 2 under the external magnetic field of $B_{app} = 1-3$ T, in which either the MgB_2 cylinder or GdBaCuO lens was set on the cold stage.

3. Results and discussion

3.1. Trapped field capability of the single MgB_2 cylinder

To confirm the trapped field capability of MgB_2 cylinder, the trapped field properties of the single MgB_2 cylinder was measured. Figure 3(a) shows the time evolution of the external field, B_{ex}, and trapped field, B_c, at the center of the single MgB_2 cylinder during the same time sequence shown

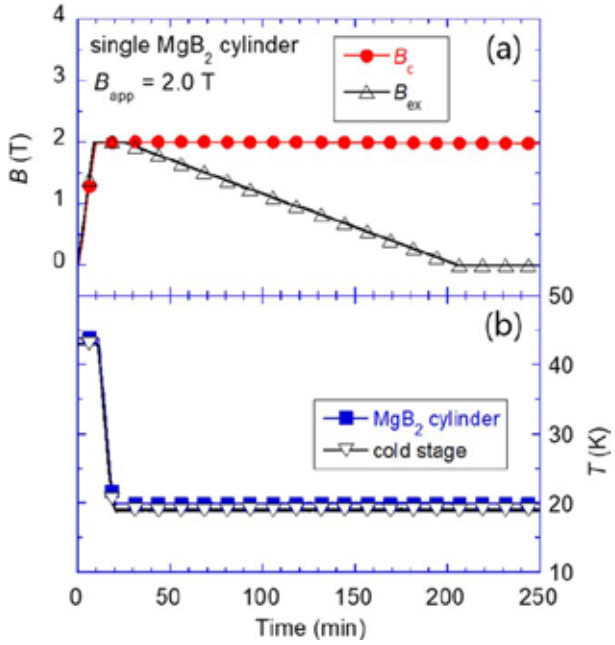

Figure 3. Time evolution of (a) the measured magnetic field, B_c, at the center of the single MgB_2 cylinder and external field, B_{ex}, and (b) the temperatures of MgB_2 cylinder and cold stage during the magnetization process for an applied field of $B_{app} = 2.0$ T.

in figure 2 under an external magnetic field of $B_{app} = 2.0$ T. Figure 3(b) shows the time evolution of the temperatures of the cold stage and the MgB_2 cylinder for the same process. In the ascending stage, the magnetic field, B_c, increased linearly with increasing B_{ex} and the magnitude of B_c was the same as the external field ($B_c = B_{ex} = 2.0$ T) because the MgB_2 cylinder was in normal state ($T = 40$ K). In the descending stage, after cooling to 20 K, the B_{ex} was slowly decreased at a constant rate of -0.011 T min^{-1} and the FCM process was performed for the MgB_2 cylinder. As a result, a trapped field remained of $B_c = 2.0$ T after B_{ex} was decreased to zero due to the conventional vortex pinning effect. In figure 3(b), the temperature of the MgB_2 cylinder was nearly the same as that of the cold stage because of the good thermal contact.

Figure 4 shows the TS dependence of the trapped field, B_c, at the center of the single MgB_2 cylinder under external magnetic fields of $B_{app} = 1-3$ T. In the ascending stage from TS = 0 to 5, the magnetic field increases linearly with increasing *TS* and the magnitude is the same as the external field because the MgB_2 cylinder is in normal state. In the descending stage of the FCM process, for the applied fields of $B_{app} = 1.0$ and 2.0 T, trapped fields of 1.00 T and 1.98 T, respectively, were achieved at TS = 10 without flux creep. On the other hand, for higher applied fields of 2.5 and 3.0 T, the TS dependence of B_c after TS = 5 gradually decreased and the final trapped field was 2.18 T, which suggests the maximum trapped field capability of the MgB_2 cylinder at $T = 20$ K. The trapped field cannot increase over 2.18 T, even if applied field is higher than 3.0 T. In the conceptual paper [19], $B_c = 2.85$ T was predicted at the final step at $T = 20$ K in the bore of MgB_2 cylinder for $B_{app} = 3.09$ T. The lower B_c

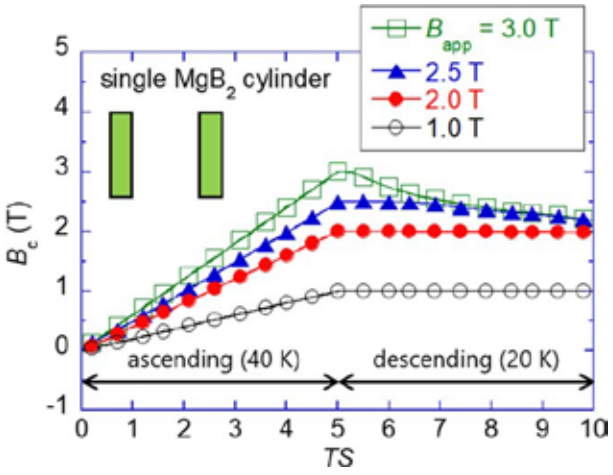

Figure 4. Time step (TS) dependence of the measured magnetic field, B_c, at the center of the single MgB_2 cylinder during the magnetization process for applied fields $B_{app} = 1.0$–3.0 T.

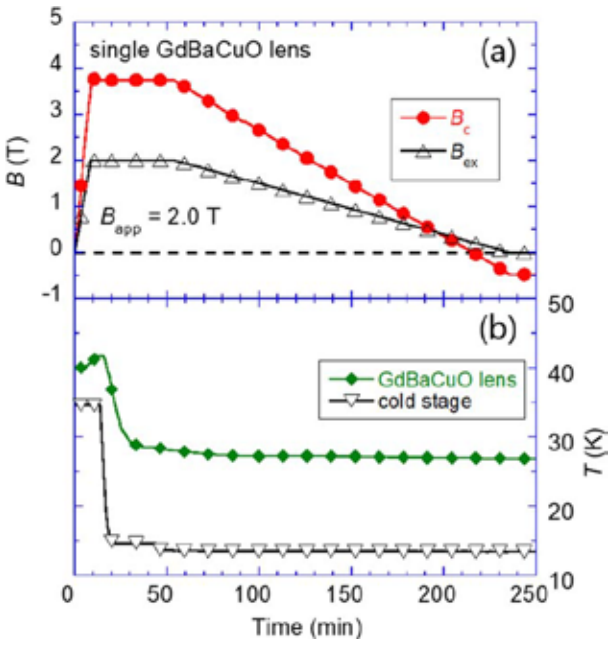

Figure 5. Time evolution of (a) the measured magnetic field, B_c, at the center of the single GdBaCuO bulk lens and external field, B_{ex}, and (b) the temperatures of GdBaCuO bulk lens and cold stage during the magnetization process for an applied field of $B_{app} = 2.0$ T.

value in the present experiment results from the lower $J_c(B, T)$ of the present MgB_2 cylinder, compared with that used in the simulations in [19].

3.2. Magnetic shielding capability of the single GdBaCuO bulk lens

The magnetic shielding capability of the GdBaCuO bulk lens was measured using the single GdBaCuO bulk lens during the ZFC process. Figure 5(a) shows the time evolution of the magnetic field, B_c, at the center of the single GdBaCuO bulk

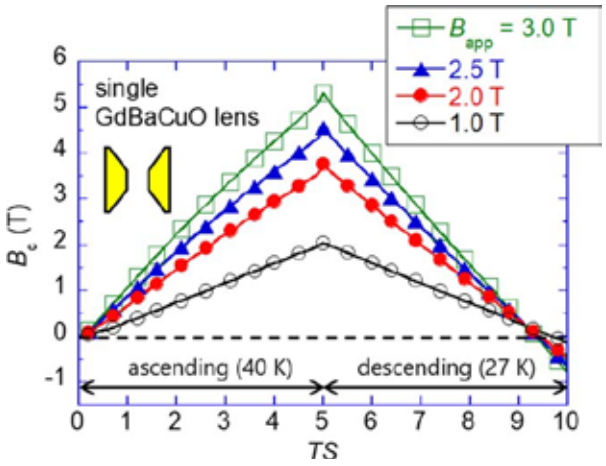

Figure 6. TS dependence of the measured magnetic field, B_c, at the center of the single GdBaCuO magnetic lens during the magnetization process under applied fields, B_{app} = 1.0–3.0 T. For TS = 10, the B_c value increased negatively with increasing B_{app}.

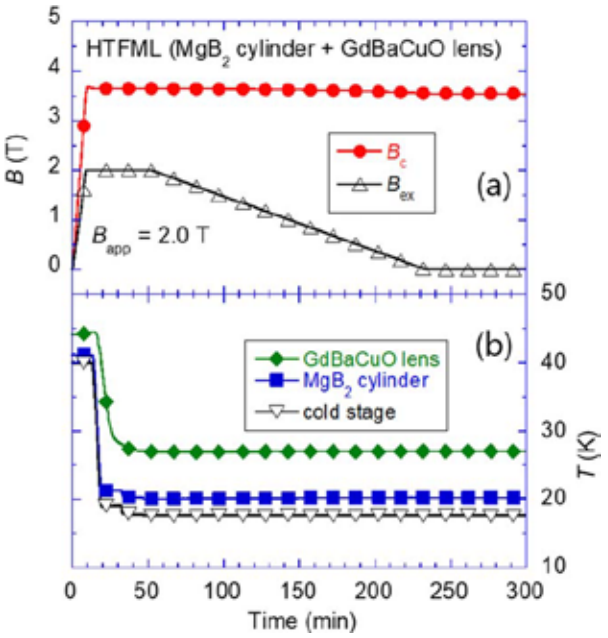

Figure 7. Time evolution of (a) the measured magnetic field, B_c, at the center of the HTFML and external field, B_{ex}, and (b) the temperatures for each measurement point during the magnetizing process for B_{app} = 2.0 T.

lens and the external field, B_{ex}, during the same time sequence shown in figure 2, under an external magnetic field of B_{app} = 2.0 T. Figure 5(b) shows the time evolution of the temperatures of GdBaCuO bulk lens and the cold stage under the same process. In the ascending stage, a clear magnetic field concentration was observed; B_c = 3.76 T was achieved, which resulted in a magnetic field concentration ratio of B_c/B_{app} = 1.88. A temperature rise of about 2.1 K took place during ascending stage from 0 to 10 min, originating from magnetic flux penetration into the magnetic lens. When the temperature of the cold stage was set to 20 K, the minimum temperature of the GdBaCuO bulk lens encapsulated by the SS holder was only 26.5 K, which may come from an imperfect thermal contact between the bulk lens and the SS holder. It should be noted that the final B_c value was not zero, but a negative one of −0.48 T. This result suggests that some magnetic flux penetrated into the surface of the bulk lens and a residual magnetic field along the –z-direction existed due to the vortex pinning effect.

Figure 6 shows the TS dependence of the magnetic field, B_c, at the center of the single GdBaCuO bulk lens during the ZFC process under applied magnetic fields of B_{app} = 1.0−3.0 T. In the ascending stage from TS = 0 to 5, the magnetic field was concentrated by the shielding current. For lower B_{app} = 1 and 2 T, B_c = 2.04 and 3.76 were achieved at TS = 5, which correspond to magnetic field concentration ratios, B_c/B_{app}, of 2.04 and 1.88, respectively. The B_c values increased for higher B_{app}, which were 4.55 T and 5.19 T for B_{app} = 2.5 and 3.0 T at TS = 5, respectively. However, the magnetic field concentration ratio, B_c/B_{app}, gradually decreased due to increased magnetic flux penetration into the bulk lens. For the final stage (TS = 10), at which the external field was zero, the B_c value increased negatively with increasing B_{app} for the same reason. For all the cases, the minimum temperature of the GdBaCuO bulk lens encapsulated by the SS holder was only 26.5 K. To improve the performance of the magnetic lens, lowering its temperature is necessary.

3.3. Realization of the HTFML

Finally, we present the experimental realization of the HTFML using GdBaCuO magnetic lens, combined with the MgB_2 bulk cylinder. Figure 7(a) shows the time evolution of the magnetic field, B_c, at the center of the HTFML during the magnetizing process shown in figure 2 under an external magnetic field of B_{app} = 2.0 T. Figure 7(b) shows the time evolution of the temperatures measured at each position. In the ascending stage, the B_c value reached 3.65 T and then slightly decreased to 3.55 T at the end of the descending stage due to flux flow. The magnetic field concentration ratio, B_c/B_{app}, was 1.76 at the end of the ramp. The temperatures of the MgB_2 cylinder and the GdBaCuO bulk lens on the SS holder were 20.0 and 26.5 K, respectively. These results demonstrate the HTFML effect experimentally for the first time.

Figure 8 shows the TS dependence of the magnetic field, B_c, at the center of the HTFML during the magnetizing process under applied fields of B_{app} = 1.0–3.0 T. At the end of the ascending stage (TS = 5), the B_c value for each B_{app} was nearly the same as that for the single GdBaCuO magnetic lens case, as shown in figure 6. In the descending stage, for B_{app} = 1.0 and 2.0 T, the B_c value was nearly the same as that at TS = 5. On the other hand, for B_{app} = 2.5 and 3.0 T, the B_c value gradually decreases with increasing TS. As a result, the final B_c value for B_{app} = 2.5 and 3.0 T was smaller than that for B_{app} = 2.0 T. The concentrated magnetic field, B_c, at

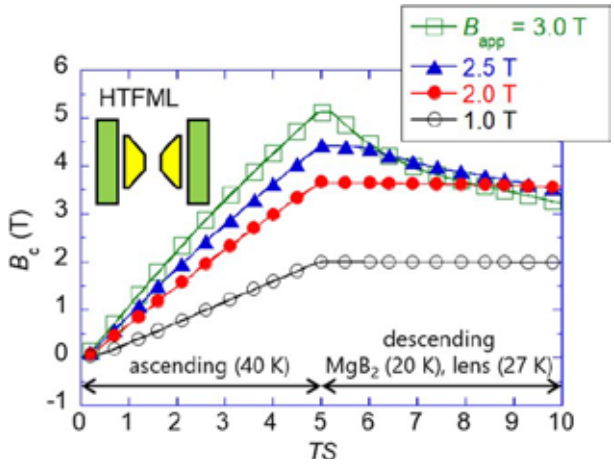

Figure 8. TS dependence of the measured magnetic field, B_c, at the center of the HTFML device during the magnetization process under various applied fields, B_{app} = 1.0–3.0 T.

Table 1. Concentrated magnetic field, B_c, at TS = 5 and 10 at the center of the HTFML, and calculated magnetic field concentration ratio, B_c/B_{app} for various applied magnetic fields, B_{app}.

B_{app} (T)	B_c (T) at TS = 5	B_c (T) at TS = 10	B_c/B_{app} at TS = 10
1.0	2.00	1.99	1.99
2.0	3.65	3.55	1.76
2.5	4.45	3.46	1.38
3.0	5.19	3.22	1.07

TS = 5 and 10 at the center of the HTFML, and calculated magnetic field concentration ratio, B_c/B_{app}, for the various applied magnetic fields, B_{app}, are summarized in table 1. A maximum B_c value of 3.55 T was achieved for B_{app} = 2.0 T.

In the concept paper, in which the HTFML was proposed to be constructed using a REBaCuO magnetic lens and MgB_2 TFM cylinder, a concentrated magnetic field B_c = 4.73 T was predicted for an external magnetizing field B_{app} = 3 T using numerical simulations [19]. However, the maximum B_c value was as low as 3.55 T experimentally under the same magnetizing process for B_{app} = 2.0 T. This difference occurs for the following reasons. Firstly, the assumed J_c (B, T) characteristics of the MgB_2 and GdBaCuO bulks used in the simulations were higher than those of the actual bulks used in the experiments. Secondly, the minimum temperature of the GdBaCuO bulk lens was only 26.5 K, when the temperature of the cold stage was set to 20.0 K. To enhance the HTFML effect for the present MgB_2 cylinder and GdBaCuO bulk lens, the thermal contact between the GdBaCuO bulk lens and the SS holder must be improved. Nevertheless, we have realized the HTFML effect experimentally for the first time. Our final goal is to build and test an HTFML using a GdBaCuO cylinder and GdBaCuO lens, for which a B_c value in excess of 10 T (e.g. B_c = 13.5 T [19]) is predicted for a magnetizing process with B_{app} = 10 T. A cryocooled 10 T superconducting solenoid magnet with a large room temperature bore (e.g. 100 mm in ID) has become more readily available in the science and engineering research communities outside of the field of superconductivity. Thus, building on these findings, we aim to provide easily a concentrated magnetic field higher than 10 T in an open space using this HTFML system.

4. Conclusion

We have presented, for the first time, the experimental realization of a HTFML, based on the device design and magnetizing procedure recently proposed in [19, 20]. The important results and conclusions in this study are summarized as follows.

(1) The HTFML effect was demonstrated experimentally using GdBaCuO magnetic lens and MgB_2 TFM cylinder for the first time, such that a magnetic field can be generated in the central bore of the magnetic lens that is higher than both the trapped field in the single cylindrical bulk TFM and the external magnetizing field, even after the externally applied field decreases to zero.
(2) A maximum concentrated magnetic field of B_c = 3.55 T was achieved in the central bore of the HTFML device after removing an applied field of B_{app} = 2.0 T at T = 20 K. The maximum B_c value was smaller than the one estimated by numerical simulations, which results from the lower J_c (B, T) and higher operating temperature, compared with those of the numerical predictions.
(3) For higher B_{app}, the B_c value was not enhanced because of a weakened lens effect due to magnetic flux penetration into the bulk GdBaCuO material comprising the lens. To enhance the HTFML effect, improving the thermal contact between the HTFML and the cold stage and lowering temperature of the GdBaCuO lens and MgB_2 TFM cylinder is necessary for the present setup.

Acknowledgments

The authors thank Mr Y Yanagi of IMRA Material R&D Co., Ltd, Japan, and Dr G Giunchi of Materials Science Consultant, Italy, for their valuable experimental supports. This research is supported by Adaptable and Seamless Technology transfer Program through Target-driven R&D (A-STEP) from Japan Science and Technology Agency (JST), Grant No. VP30218088419 and by JSPS KAKENHI Grant No. 19K05240. M D Ainslie would like to acknowledge financial support from an Engineering and Physical Sciences Research Council (EPSRC) Early Career Fellowship, EP/P020313/1. All data are provided in full in the results section of this paper.

ORCID iDs

Sora Namba https://orcid.org/0000-0001-7268-5326
Hiroyuki Fujishiro https://orcid.org/0000-0003-1483-835X
Tomoyuki Naito https://orcid.org/0000-0001-7594-3466
Mark D Ainslie https://orcid.org/0000-0003-0466-3680
Keita Takahashi https://orcid.org/0000-0002-8278-2688

References

[1] Zhou D, Izumi M, Miki M, Felder B, Ida T and Kitano M 2012 *Supercond. Sci. Technol.* **25** 103001
[2] Hayashi H, Tsutsumi K, Saho N, Nishijima N and Asano K 2003 *Physica* C **392–396** 745–8
[3] Werfel F N, Floegel-Delor U, Rothfeld R, Riedel T, Goebel B, Wippich D and Schirrmeister P 2012 *Supercond. Sci. Technol.* **25** 014007
[4] Tomita M and Murakami M 2003 *Nature* **421** 517–20.
[5] Sakai N, Seo S-J, Inoue K, Miyamoto T and Murakami M 2000 *Physica* C **335** 107–11
[6] Ren Y, Weinstein R, Liu J, Sawh R P and Foster C 1995 *Physica* C **251** 15–26
[7] Fuchs G, Schätzle P, Krabbes G, Gruß S, Verges P, Müller K-H, Fink J and Schultz L 2000 *Appl. Phys. Lett.* **76** 2107–9
[8] Durrell J H *et al* 2014 *Supercond. Sci. Technol.* **27** 082001
[9] Nakamura T, Itoh Y, Yoshikawa M, Oka T and Uzawa J 2007 *Concepts Magn. Reson.* B **31B** 65–70
[10] Nakamura T, Tamada D, Yanagi Y, Itoh Y, Nemoto T, Utumi H and Kose K 2015 *J. Magn. Reson.* **259** 68–75
[11] Ogawa K, Nakamura T, Terada Y, Kose K and Haishi T 2011 *Appl. Phys. Lett.* **98** 234101
[12] Zhang Z Y, Matsumoto S, Teranishi R and Kiyoshi T 2012 *Supercond. Sci. Technol.* **25** 115012
[13] Choi S, Yoon J-H, Lee B-S, Won M-S, Ok J-W, Zhang Z-Y, Kiyoshi T, Matsumoto S and Lee S-H 2012 *J. Appl. Phys.* **111** 07E728
[14] Kiyoshi T, Choi S, Matsumoto S, Asano T and Uglietti D 2009 *IEEE Trans. Appl. Supercond.* **19** 2174–7
[15] Zhang Z Y, Matsumoto S, Teranishi R and Kiyoshi T 2013 *Supercond. Sci. Technol.* **26** 045001
[16] Asano T, Itoh K, Matsumoto S, Kiyoshi T, Wada H and Kido G 2005 *IEEE Trans. Appl. Supercond.* **15** 3157–60
[17] Choi S, Kiyoshi T and Matsumoto S 2009 *J. Appl. Phys.* **105** 07E705
[18] Miyazoe A, Nakagawa R, Hori C, Tanaka H and Imamura Y 2018 *IEEE Trans. Appl. Supercond.* **28** 4700205
[19] Takahashi K, Fujishiro H and Ainslie M D 2018 *Supercond. Sci. Technol.* **31** 044005
[20] Namba S *et al* 2019 *IEEE Trans. Appl. Supercond.* **29** 6801605
[21] Giunchi G, Raineri S, Wesche R and Bruzzone P L 2004 *Physica* C **401** 310–5
[22] Giunchi G, Ripamonti G, Cavallin T and Bassani E 2016 *Cryogenics* **46** 237–42
[23] Morita M, Sawamura M, Takebayashi S, Kimura K, Teshima H, Tanaka M, Miyamoto K and Hashimoto M 1994 *Physica* C **235–240** 209–12
[24] Nariki S, Teshima H and Morita M 2016 *Supercond. Sci. Technol.* **29** 034002
[25] Fujishiro H, Takahashi K, Naito T, Yanagi Y, Itoh Y and Nakamura T 2018 *Physica* C **550** 52–6
[26] Fujishiro H, Naito T, Yanagi Y, Itoh Y and Nakamura T 2019 *Supercond. Sci. Technol.* **32** 065001

8. (I-25) Tatsuya Hirano, Yuhei Takahashi, Sora Namba, Tomoyuki Naito and Hiroyuki Fujishiro,
"A record-high trapped field of 1.61 T in MgB_2 bulk comprised of copper plates and soft iron yoke cylinder using pulsed-field magnetization",
Supercond. Sci. Technol. **33** (2020) 085002 (10 pages) (No. 276 paper)

IOP Publishing Superconductor Science and Technology
Supercond. Sci. Technol. **33** (2020) 085002 (10pp) https://doi.org/10.1088/1361-6668/ab9542

A record-high trapped field of 1.61 T in MgB_2 bulk comprised of copper plates and soft iron yoke cylinder using pulsed-field magnetization

Tatsuya Hirano, Yuhei Takahashi, Sora Namba, Tomoyuki Naito and Hiroyuki Fujishiro

Department of Physical Science and Materials Engineering, Faculty of Science and Engineering, Iwate University, Morioka 020-8551, Japan

E-mail: fujishiro@iwate-u.ac.jp and thirano1995@gmail.com

Received 10 March 2020, revised 3 May 2020
Accepted for publication 21 May 2020
Published 18 June 2020

Abstract

A trapped field of $B_T = 1.61$ T was experimentally achieved at the central surface of an MgB_2 bulk composite (60 mm in diameter and 20 mm in height) at 20 K by double pulsed-field magnetization (PFM) using a split-type coil. The composite bulks consisted of two MgB_2 ring bulks sandwiched by thin copper ring plates, which were then stacked, and a soft iron yoke cylinder was inserted in the central bore of the rings. The copper ring plates delayed the rise time and duration of the magnetic pulse due to eddy currents. The inserted soft iron yoke attracted the magnetic flux and enhanced the trapped field strength mainly due to its large permeability. As a result, the trapped field was enhanced from $B_T = 0.34$ T for the single MgB_2 ring bulk without the copper plates and soft iron yoke to $B_T = 1.00$ T for the composite with both copper plates and the soft iron yoke. The inserted soft iron yoke can be exploited to enhance the trapped field because the intrinsic B_T of the single MgB_2 ring bulk was smaller than the saturation field of the yoke (~2 T). Using an optimized second pulse application after suitable flux trapping from the first pulse application, the trapped field was enhanced considerably to $B_T(2nd) = 1.61$ T, which is a record-high trapped field for an MgB_2 bulk by PFM to date. The combination of the longer magnetic pulse application by the copper plates, the enhancement of the effective applied field by the inserted soft iron yoke, and the double pulse application using split-type coil is an effective technique to enhance the trapped field in the MgB_2 bulk using PFM.

Keywords: MgB_2, pulsed field magnetization, trapped field, soft iron yoke cylinder, double pulse application, copper plate stack, rise time elongation

(Some figures may appear in colour only in the online journal)

1. Introduction

Large, single-grain RE-Ba-Cu-O (REBaCuO, RE: a rare earth element or Y) bulk superconductors can trap higher magnetic field by strong vortex pinning effect and are a promising material for use as a compact, high-strength trapped field magnet (TFM) [1] for various practical applications, such as rotating machines, magnetic separation, flywheel energy storage systems and compact cryogen-free nuclear magnetic resonance (NMR) and magnetic resonance imaging (MRI) systems [2–6]. A record high trapped field of $B_T(FCM) = 17.6$ T at 26 K has been achieved in the GdBaCuO disk bulk pair activated by field-cooled magnetization (FCM) [7, 8]. During FCM, the bulk is cooled below the transition temperature, $T_c = 92$ K, under the applied field, B_{ex}, using superconducting magnet (SM) and then the magnetic field decreases to zero.

On the other hand, MgB_2 bulk superconductors have also promising potential as TFMs, such as being rare-earth-free, lightweight and presenting a homogeneous trapped field distribution [9], which are in clear contrast with REBaCuO bulks. The better and larger MgB_2 polycrystalline TFMs can be realized because of their long coherence length, ξ, below $T_c = 39$ K [10]. MgB_2 bulks with high critical current density, J_c, have been fabricated by various methods and usually activated by FCM [11–15]. A record-high trapped field of B_T(FCM) = 5.4 T has been achieved at 12 K on a surface of a MgB_2 disk bulk 20 mm in diameter [16]. In this way, FCM can achieve the maximum trapped field of the bulk. However, since the SM is expensive and heavy, FCM is generally ill-suited for wide practical applications.

Pulsed-field magnetization (PFM) is another magnetizing method to magnetize bulk superconductors [17–21], which is mobile, inexpensive experimental setup with no use of SM. During PFM, the bulk is cooled below T_c, and the magnetic pulsed field with the rise time of milliseconds is applied using a copper coil and condenser bank. However, the trapped field by PFM, B_T(PFM), is generally lower than that by FCM because of a large temperature rise caused by the dynamics of the magnetic flux during the magnetic pulse application [22].

Multi-pulse techniques are effective to enhance the B_T value for REBaCuO bulks due to the reduction of the temperature rise [23–26]. We have achieved the trapped field of B_T(PFM) = 5.20 T on a GdBaCuO bulk 45 mm in diameter at 29 K using a modified multi-pulse technique with stepwise cooling (MMPSC) [17], which is a record-high B_T(PFM) for REBaCuO bulk by PFM to date. The PFM technique has also been applied to MgB_2 bulks [27–32]. B_T(PFM) = 0.81 T was achieved at 14 K for a high-J_c MgB_2 bulk fabricated by the hot isostatic pressing (HIP) method magnetized using a copper solenoid coil, in which B_T(FCM) = 2.23 T was trapped at 16 K by FCM [29]. However, flux jumps took place frequently during PFM in the high-J_c MgB_2 bulks and consequently the final B_T(PFM) value decreased for larger pulsed fields. The multi-pulse application would be to enhance the trapped field for the MgB_2 bulk.

The effectiveness of the split-type coil (or vortex-type coil) during PFM has been clarified for REBaCuO bulks experimentally [33, 34] and numerically [19, 35]. The magnetic flux starts to intrude not from the periphery, but mainly from the both surfaces of the disk bulk, and is trapped in the center of the bulk, even for lower pulsed fields. It was shown that the maximum B_T could be enhanced in comparison to that obtained using the solenoid-type coil. In this case, the temperature rise during PFM for the split-type coil was smaller than that for the solenoid-type coil. We have achieved a trapped field of B_T(PFM) = 1.1 T on a high-J_c MgB_2 bulk at 13 K without flux jumps by PFM using a split-type coil, in which a pair of soft iron yokes were inserted in the bore of the split-type coil. B_T(PFM) = 1.1 T has been the record high trapped field by PFM for MgB_2 bulk since 2016 [36]. We have performed many PFM experiments and numerical simulations for REBaCuO and MgB_2 bulks, in which the following effectiveness has been suggested to enhance the trapped field; the use of split-type coil [19, 33–35], the multi-pulse application for the REBaCuO bulk [17, 23, 24], the use of soft iron yoke in the pulse coil [19] and the long pulse application [37].

In this study, we have investigated the trapped field properties of MgB_2 ring bulk composites inserted by soft iron yoke at 20 K by single and double pulsed field applications using a split-type coil. Furthermore, the effect of thin copper plates, which sandwiched the MgB_2 ring bulks, was investigated to expect the longer magnetic pulse application. As a result, a new record-high trapped field of $B_T = 1.61$ T was experimentally achieved at 20 K for an MgB_2 ring bulk comprised of both copper plates and a soft iron yoke using double pulsed-field application by split-type coil.

2. Experimental details

We performed the PFM experiments using three types of bulk modules. An MgB_2 ring bulk (20 mm in inner diameter (I.D.), 60 mm in outer diameter (O.D.) and 19 mm in height (H)) was fabricated by an *in-situ* infiltration method [38], in which B_T(FCM) = 1.57 T was trapped by FCM at 20 K. We abbreviate this as 'single bulk', as shown in figure 1(a). The single bulk was sliced in half (H = 9 mm), and each ring bulk was sandwiched by oxygen-free copper plates 0.5 mm in thickness using Apiezon-N^{TM} grease, and then stacked, as shown in figure 1(b). We abbreviate this as 'composite (w/o yoke)'. A soft iron yoke cylinder (20 mm in diameter and 20 mm in H) was inserted in the composite (w/o yoke), as shown in figure 1(c). We abbreviate this as 'composite (w/yoke)'.

Figure 2 shows the experimental setup for PFM using the split-type coil. Each MgB_2 bulk module was fastened in a brass holder using a stainless steel (SS) bolt and nut with thin indium foil and connected to the cold stage of a Gifford–McMahon (GM) cycle helium refrigerator in a vacuum chamber. In the previous study, a copper holder was used to fasten the disk bulk for the split-type coil [19], in which non-negligible temperature rise was observed due to the eddy current flowing in the holder during PFM. To eliminate the temperature rise in the holder, a brass holder was used in this study, which has lower electrical conductivity. A Hall sensor (HG-106 C; ASAHI KASEI) was placed to the center of the bulk surface, and a thermometer (Cernox^{TM}) was connected to the brass holder. The split-type coil (72 mm in I.D., 124 mm in O.D., 35 mm in H), which was submerged in liquid nitrogen, was placed outside the vacuum chamber, in which a pair of Ni-plated soft iron yokes (60 mm in diameter and 65 mm in height) was inserted in the central bores of the coil.

The strength of the magnetic pulse was estimated using the following methods. Figure 3 shows the experimental method to estimate the magnitude of pulsed field, B_{ex}(shunt) and B_{ex}(Hall). The time evolution of magnetic field, B_{ex}(shunt)(t), was estimated by observing the current, $I(t)$, flowing through the shunt resistor from the pulse current source (condenser bank) using a digital oscilloscope (YOKOGAWA Electric, DL1640). For example, to achieve $B_{ex}(\text{shunt})^{max} = 1.5$ T at the center of the split coil at $T_s = 40$ K ($>T_c$ of the MgB_2 bulk), $I_{peak} = 440$ A. The time evolution of the magnetic field, B_{ex}(Hall)(t), was also simultaneously monitored at the central

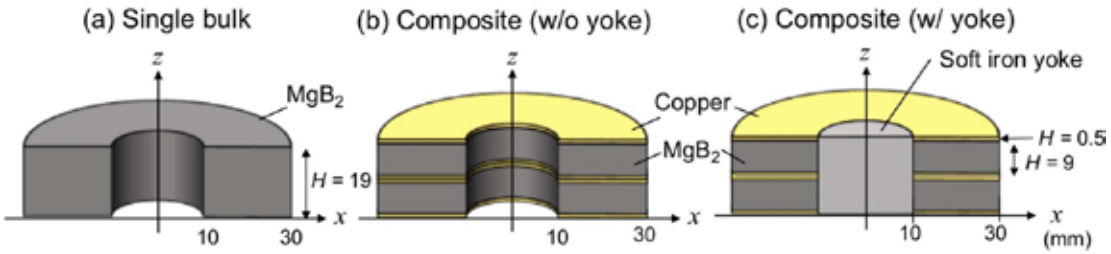

Figure 1. Three types of MgB_2 bulk modules used for the PFM experiments: (a) 'single bulk', (b) 'composite (w/o yoke)', where two sliced ring bulks were sandwiched by oxygen-free copper plates and are stacked, and (c) 'composite (w/yoke)', where a soft iron yoke cylinder is inserted in (b).

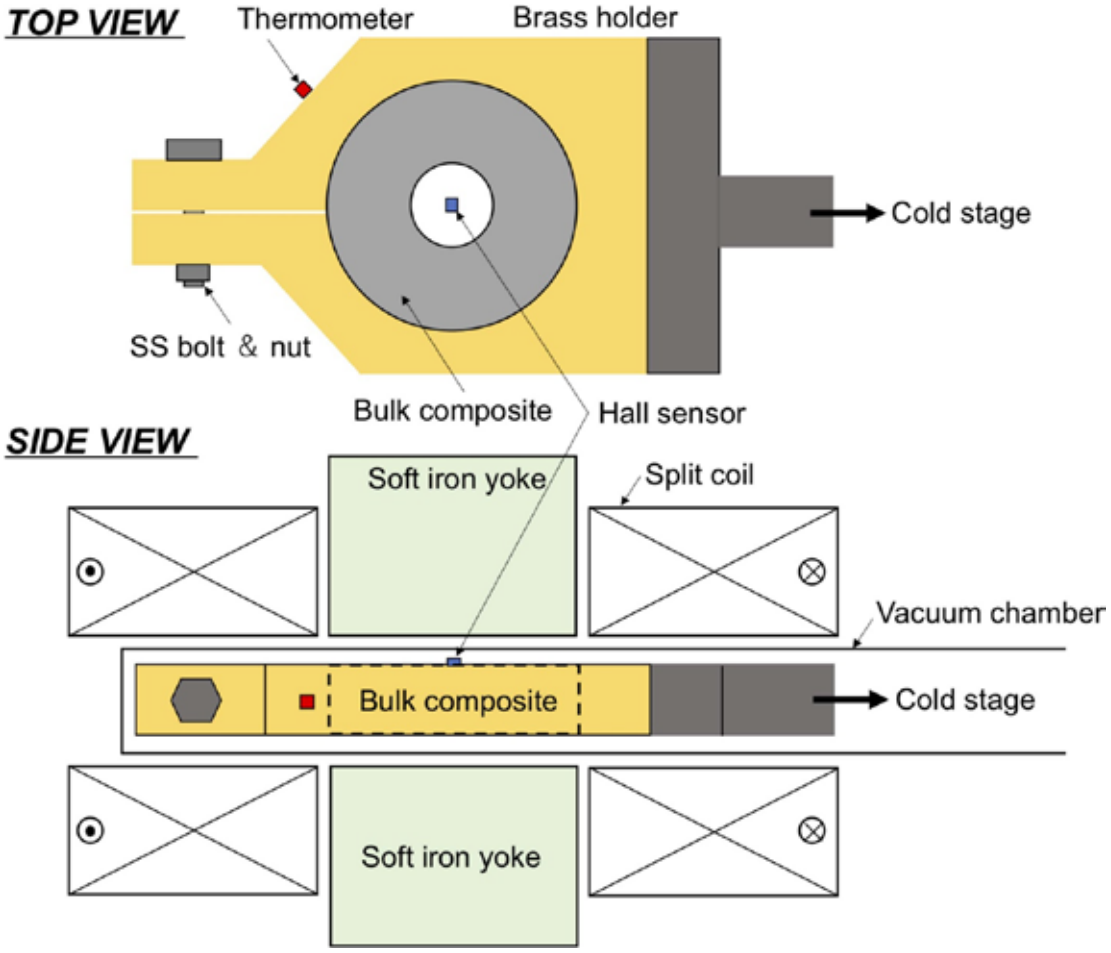

Figure 2. Experimental setup of the PFM for the three types of bulk modules using split-type coil with soft iron yoke.

surface of the single MgB_2 ring bulk and the composite (w/o yoke) by measuring the Hall voltage of the Hall sensor using the digital oscilloscope. For the composite (w/yoke), the time evolution of magnetic field, $B_{ex}(\mathrm{Hall})(t)$, which is defined as $B_{ex}(\mathrm{yoke})(t)$ hereafter, was monitored by measuring the Hall voltage at the central surface of the soft iron yoke.

The initial temperature, T_s, of the bulk was set to 20 K, and a single magnetic pulse, $B_{ex}(\mathrm{Hall})(t)$, with a peak up to 2.0 T was applied via a pulsed current flowing in the coil, as shown in figure 4(a). The PFM experiments were also performed using double pulse application, as shown in figure 4(b). The first pulse of $B_{ex1}(\mathrm{Hall})^{max} = 1.20$ or 1.32 T was applied at 20 K. Next, once the temperature of the bulk returned to 20 K, the second pulse, $B_{ex2}(\mathrm{Hall})^{max}$, ranging from 1.1 to 1.6 T, was applied to the bulk.

During PFM, the time evolution of the temperature, $T(t)$, and the trapped field, B_T, which was defined as the final value of $B_T(t)$ at 500 ms, were measured. After the removal of the

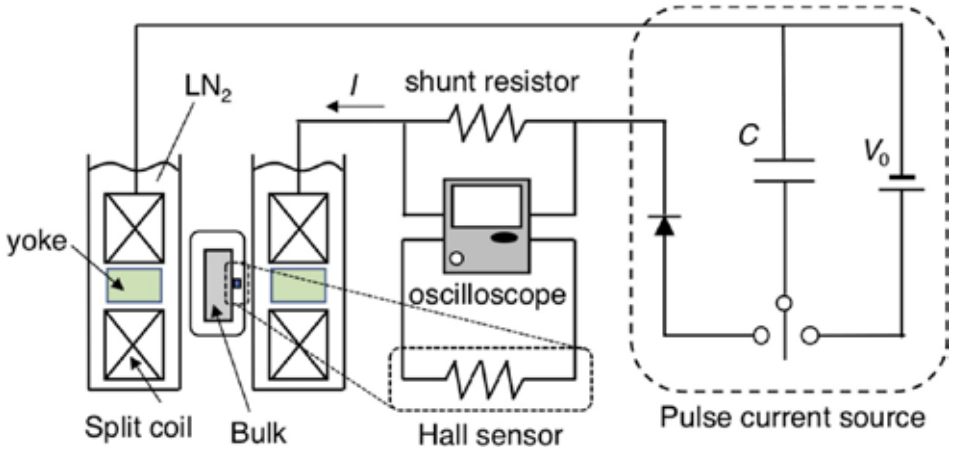

Figure 3. The experimental method to estimate the magnitude of pulsed field, B_{ex}(shunt) and B_{ex}(Hall).

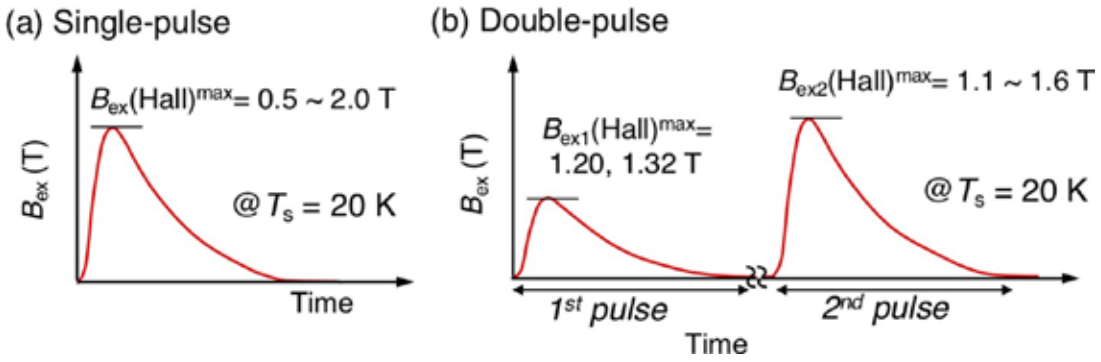

Figure 4. Schematic illustration of (a) single-pulse and (b) double-pulse application during PFM at $T_s = 20$ K.

split-type coil (15 min after the each pulse application), two-dimensional trapped field profiles were mapped at 5 mm above the bulk surface (on the outer surface of the vacuum chamber) by scanning a Hall sensor (BHA 921; F W Bell) using an x–y stage controller.

3. Results and discussion

3.1. Effect of the copper plates and soft iron yoke

First, we clarify the effects of the copper plate stack and soft iron yoke insertion on the magnetic pulse, $B_{ex}(t)$. Figure 5(a) shows the time dependence of B_{ex}(shunt)(t) for an applied magnetic field of 1.03 T, which was measured for the 'single bulk' case at $T_s = 40$ K. The rise time, t_{rise}, was about 20 ms, and the pulse duration was about 400 ms, which were determined by the coil inductance and the existence of the ferromagnetic soft iron yoke inserted in the bore of the split-type coil. In the figure, the B_{ex}(Hall)(t) profiles for the single bulk, composite (w/o yoke) and composite (w/yoke) cases are also shown, which were measured by the adhered Hall sensors. B_{ex}(Hall)(t) for the single bulk was slightly delayed, compared with B_{ex}(shunt)(t). However, the magnitude, rise time and duration of B_{ex}(Hall)(t) for the composites (w/o yoke) and (w/yoke) cases are quite different with those for the single bulk case.

Figure 5(b) shows the relationship between the maximum values (B_{ex}(Hall)^{max} and B_{ex}(shunt)^{max}) of the curves B_{ex}(Hall)(t) and B_{ex}(shunt)(t) for each case at $T_s = 40$ K. The maximum value of the B_{ex}(Hall)(t) curve, named as B_{ex}(Hall)^{max} for the composite (w/o yoke) was about 20% smaller than that of the B_{ex}(shunt)(t), named as B_{ex}(shunt)^{max}, because of eddy currents flowing in the high-conductive copper plates along the direction to avoid the magnetic flux intrusion. On the other hand, the B_{ex}(Hall)^{max} value for the composite (w/yoke) was much larger than B_{ex}(shunt)^{max}, and its rate increases with increasing B_{ex}(shunt)^{max}. The B_{ex}(Hall)^{max} enhancement for the composite (w/yoke) mainly results from flux concentration in the ferromagnetic yoke cylinder, although the induced current flowing in the yoke acts to reduce the flux intrusion.

Figure 5(c) shows the rise time, t_{rise}(Hall), measured by the Hall sensor and t_{rise}(shunt), as a function of B_{ex}(shunt)^{max} at $T_s = 40$ K. The magnitude of t_{rise}(Hall) for the composite (w/o yoke) increased due to the copper plates, and that for the composite (w/yoke) increased more due to the existence of the yoke, compared with that for the single bulk. The detailed study using the copper plates is planned in the next paper.

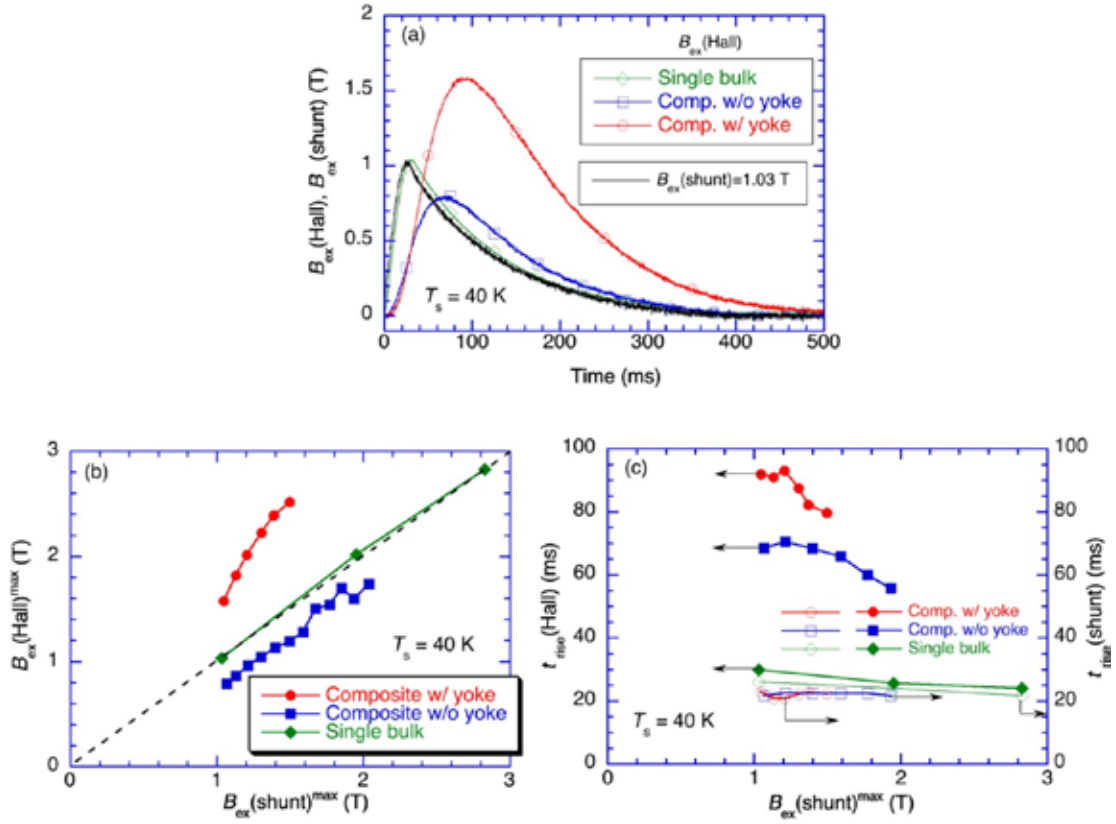

Figure 5. (a) The time dependence of B_{ex}(shunt)(t) for an applied magnetic field of 1.03 T, measured for the single MgB_2 bulk case, and B_{ex}(Hall)(t) for the single bulk, composite (w/o yoke) and composite (w/yoke) cases at $T_s = 40$ K. (b) The relationship between the maximum values (B_{ex}(Hall)^{max} and B_{ex}(shunt)^{max}) of the curves B_{ex}(shunt)(t) and B_{ex}(Hall)(t) for each case at $T_s = 40$ K. (c) The rise time, t_{rise}(Hall) and t_{rise}(shunt), as a function of B_{ex}(shunt)^{max} at $T_s = 40$ K.

3.2. Results for single pulse application

The PFM experiments were performed for the three types of MgB_2 modules at $T_s = 20$ K ($<T_c$ of the MgB_2 bulk). Figure 6 shows the trapped field, B_T, which is defined as the steady value of the curves $B_T(t)$ at $t = 500$ ms, at the central surface of each MgB_2 module, as a function of B_{ex}(Hall)^{max} at 20 K. The trapped field profiles for each case, when the maximum B_T value was achieved, are also shown. For the single MgB_2 bulk case, the magnetic flux started to penetrate into the center at B_{ex}(Hall)$^{max} = 0.85$ T, and a maximum of $B_T = 0.34$ T was trapped at the central surface. For larger B_{ex}(Hall)^{max}, the B_T value decreased due to a larger temperature rise. The trapped field profile is shown, for which a trapezoidal profile was measured 5 mm above the bulk surface. For the composite (w/o yoke), the magnetic flux started to penetrate into the center at B_{ex}(Hall)$^{max} = 1.23$ T, and then decreased with increasing B_{ex}(Hall)^{max}. A maximum $B_T = 0.44$ T was trapped at the central surface. The B_{ex}(Hall)^{max} value for the composite (w/o yoke), at which the B_T value took a maximum, was larger than that for the single MgB_2 bulk. Here, a larger magnetic pulse is necessary to trap the magnetic flux at the center due to the existence of the copper plates, as shown in figure 5(b). The maximum B_T value for the composite (w/o yoke) was slightly larger than that for the single bulk case. For the composite (w/yoke), the magnetic flux started to penetrate into the center around B_{ex}(Hall)$^{max} = 1.03$ T, took a maximum of $B_T = 1.00$ T at B_{ex}(Hall)$^{max} = 1.20$ T, and then decreased with increasing B_{ex}(Hall)^{max}. It should be noted that for the composite (w/yoke), the B_T value was enhanced, but the B_{ex}(Hall)^{max} value at which B_T value took a maximum was nearly the same as that for the composite (w/o yoke). These results suggest that the enhancement of the B_T value resulted mainly from the yoke cylinder and that the B_{ex}(Hall)^{max} value at which B_T value takes a maximum was mainly determined by the copper plates, although we did not perform PFM experiments for the MgB_2 bulk with only the yoke without the copper plates.

Figure 7(a) shows the maximum temperature rise, T_{max}, during PFM for each composite, as a function of B_{ex}(Hall)^{max} at 20 K. For the single bulk, T_{max} abruptly increases at B_{ex}(Hall)$^{max} = 0.85$ T due to the pinning loss of the flux trap [39], at which the magnetic flux reached the center of the bulk, and $B_T = 0.34$ T was trapped. T_{max} increased with increasing B_{ex}(Hall)^{max} due to the viscous loss of the flux movement [39]. For the composites (w/yoke) and (w/o yoke) cases, T_{max} linearly increased with increasing B_{ex}(Hall)^{max}, even though the magnetic flux was not trapped the center of the bulk for

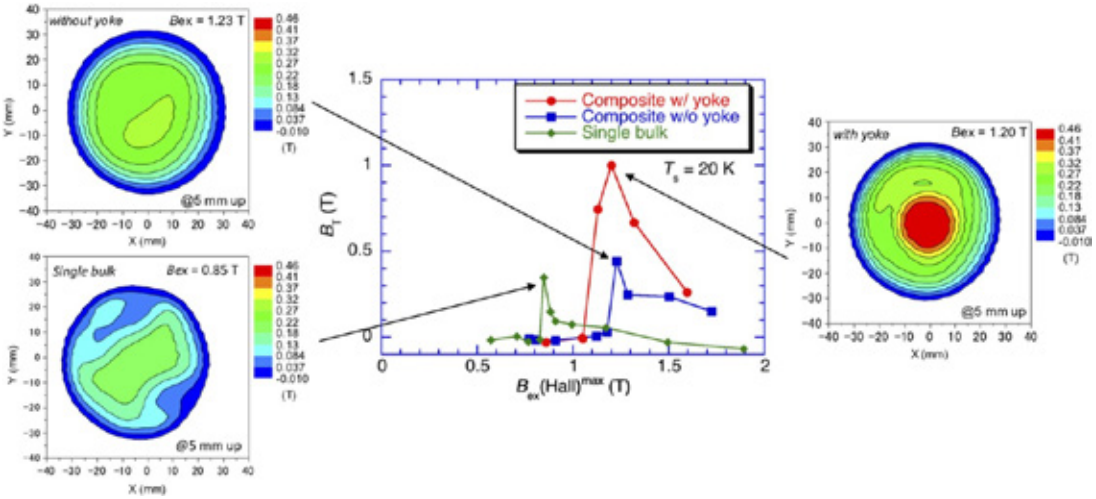

Figure 6. The trapped field, B_T, at the central surface of each module, as a function of $B_{ex}(\text{Hall})^{max}$ at 20 K. The trapped field profiles for each case, when the maximum B_T value was achieved, are also shown.

$B_{ex}(\text{Hall})^{max} < 1.2$ T. These results indicate that the heat generation took place mainly in the copper plates due to the eddy currents in addition to the heat generation due to the flux trap. For $B_{ex}(\text{Hall})^{max} > 1.2$ T, for which the magnetic flux was trapped, the temperature rise due to the flux trap was superimposed and T_{max} was larger than that of the single bulk. Because of the additional heat generation from the eddy current in the inserted yoke, the temperature rise of the composite (w/yoke) was larger than that of the composite (w/o yoke) for higher $B_{ex}(\text{Hall})^{max}$.

Figure 7(b) shows an example of the time dependence of the temperature, $T(t)$, in the composite (w/o yoke) for $B_{ex}(\text{Hall})^{max} = 0.91$, 1.23 and 1.29 T, which was measured on the surface of the brass holder. $T(t)$ took a maximum at $t = 2 \sim 3$ s and then linearly decreased with increasing time. The maximum temperature increased with increasing $B_{ex}(\text{Hall})^{max}$. Similar trends were also observed for other cases. The results in figure 7 reflect indirectly the trapped field properties during PFM, even though the thermometer was not adhered directly on the bulk surface.

Figure 8 shows the time dependence of the applied field, $B_{ex}(t)$, and the trapped field, $B_T(t)$, for each case and for each single pulse application of $B_{ex}(\text{Hall})^{max}$. Figures 8(a) to (c) show the results for the single MgB_2 ring bulk, where $B_{ex}(\text{shunt})(t)$ and $B_{ex}(\text{Hall})(t)$ are also shown. The magnetic flux cannot penetrate well to the center of the bulk due to its magnetic shielding for $B_{ex}(\text{Hall})^{max} = 0.83$ T (figure 8(a)). With increasing $B_{ex}(\text{Hall})^{max}$, the magnetic flux was able to penetrate into the center, and the $B_T(t = 500$ ms) value took a maximum at $B_{ex}(\text{Hall})^{max} = 0.85$ T (figure 8(b)). For $B_{ex}(\text{Hall})^{max} = 0.88$ T, the $B_T(t = 500$ ms) value decreased due to a large flux flow out of the bulk (figure 8(c)). Figures 8(d) to (f) show the results for the composite (w/o yoke). Here, similar trends to the single bulk were observed. The B_T value took a maximum of $B_T = 0.42$ T at $B_{ex}(\text{Hall})^{max} = 1.23$ T (figure 8(e)), and then decreased at $B_{ex}(\text{Hall})^{max} = 1.30$ T. For higher $B_{ex}(\text{Hall})^{max}$, as shown in figure 8(f), a long gradual decay in $B_T(t)$ can be seen at 100 ms $< t <$ 250 ms. This is a characteristic decay in MgB_2 bulk during PFM [30], which was also reported by other researcher [32], but has not been clarified the reason. Figures 8(g) to (i) show the results for the composite (w/yoke), where $B_{ex}(\text{yoke})(t)$ is also shown, in addition to $B_{ex}(\text{shunt})(t)$ and $B_{ex}(\text{Hall})(t)$. The B_T value took a maximum of 1.00 T at $B_{ex}(\text{Hall})^{max} = 1.21$ T (figure 8(h)) and then decreased at $B_{ex}(\text{Hall})^{max} = 1.32$ T. The trapped field of the composite (w/yoke) was higher than that of the composite (w/o yoke), because the iron yoke has a large permeability. The period of the characteristic $B_T(t)$ decay for the composite (w/yoke) becomes longer at 150 ms $< t <$ 400 ms. These results indicate that the composite bulk is considered to be pseudo-long pulsed field magnetization technique.

3.3. Results for double pulse application

In the previous subsection, the effects of the copper plates on the MgB_2 bulk surface and the insertion of soft iron yoke cylinder on the trapped field enhancement were clearly confirmed for the single pulse application. In this subsection, the effect of the double pulse application is presented. Figure 9(a) shows the trapped field, $B_T(2\text{nd})$, on the central surface of the composite (w/yoke) at $T_s = 20$ K, as a function of the second applied pulsed field, $B_{ex2}(\text{Hall})^{max}$, after the first pulsed field, $B_{ex1}(\text{Hall})^{max}$, of 1.20 T or 1.32 T was applied and the magnetic flux was already trapped. After the application of $B_{ex1}(\text{Hall})^{max} = 1.32$ T, the final $B_T(2\text{nd})$ value was 0.65 T, as shown in figure 8(i). For the second pulse application, $B_T(2\text{nd})$ sharply increased, took a maximum of 1.61 T at $B_{ex2}(\text{Hall})^{max} = 1.26$ T, and then decreased with increasing $B_{ex2}(\text{Hall})^{max}$. The $B_T(2\text{nd}) = 1.61$ T is a record high B_T value for an MgB_2 bulk by PFM to date. The trapped field profile 5 mm above the bulk surface was fairly

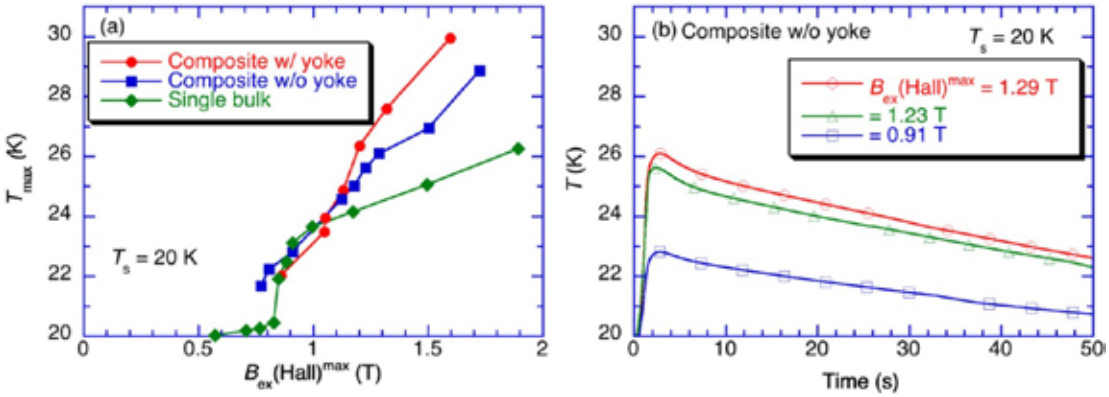

Figure 7. The maximum temperature rise, T_{max}, during PFM for each composite, as a function of B_{ex}(Hall)^{max} at 20 K. (b) An example of the time dependence of the temperature, $T(t)$, for the composite (w/o yoke) for B_{ex}(Hall)^{max} = 0.91, 1.23 and 1.29 T at 20 K.

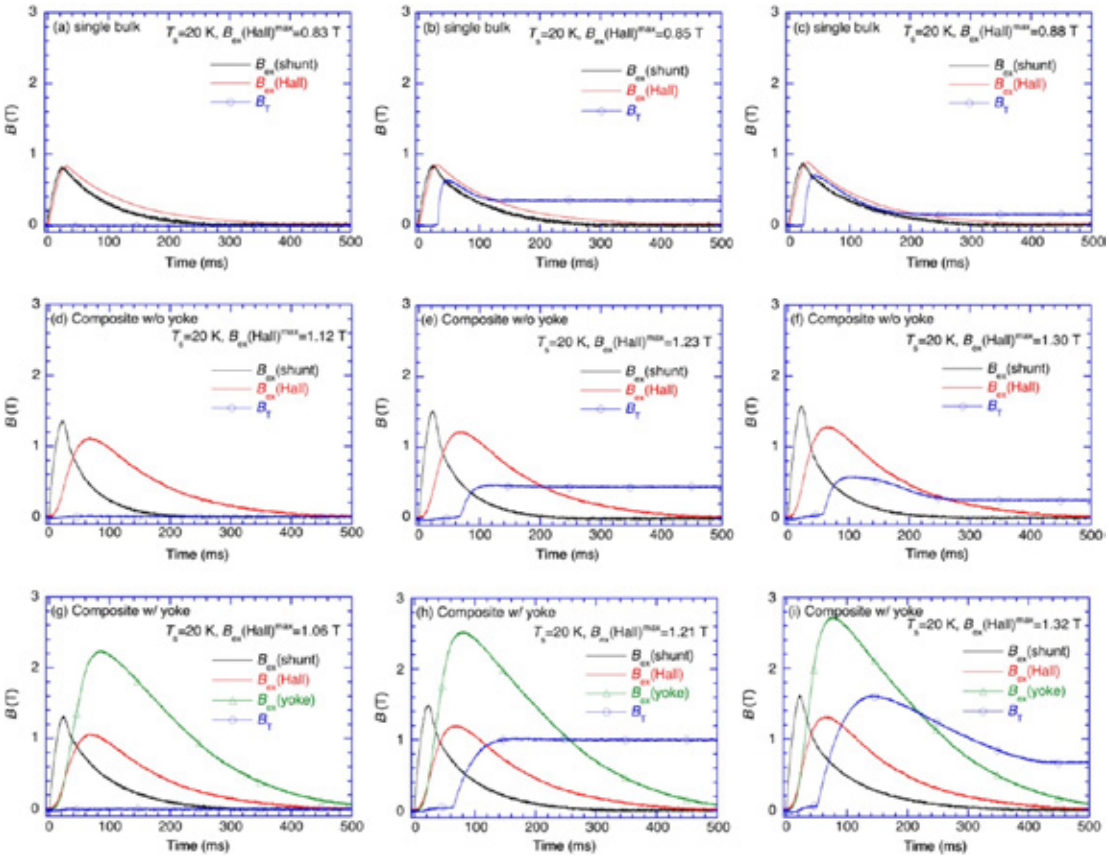

Figure 8. The time dependence of the applied fields, $B_{ex}(t)$, and the trapped field, $B_T(t)$, for single pulse application of B_{ex}(Hall)^{max} for (a)–(c) the single bulk, (d)–(f) the composite (w/o yoke), and (g)–(i) the composite (w/yoke).

cone shaped. The highest B_T value comes from the reduction of temperature rise due to the already trapped magnetic flux during the 1st magnetic pulse [17, 40]. For the case of B_{ex1}(Hall)^{max} = 1.20 T, similar B_T(2nd) vs B_{ex2}(Hall)^{max} behavior can be observed. However, the maximum B_T(2nd) value was smaller than that for B_{ex1}(Hall)^{max} = 1.32 T. These results suggest that an optimum trapped field and B_T(1st) profile exists to maximize the B_T(2nd) value. Figure 9(b) shows the maximum temperature rise, T_{max}, of the composite (w/yoke) at T_s = 20 K, as a function of second applied pulsed field, B_{ex2}(Hall)^{max}. T_{max} for the single pulse application of the composite (w/yoke) at T_s = 20 K is also shown, which was presented in figure 7(a). It should be noted that T_{max} after the second pulse application is about 2 K smaller than that for the single

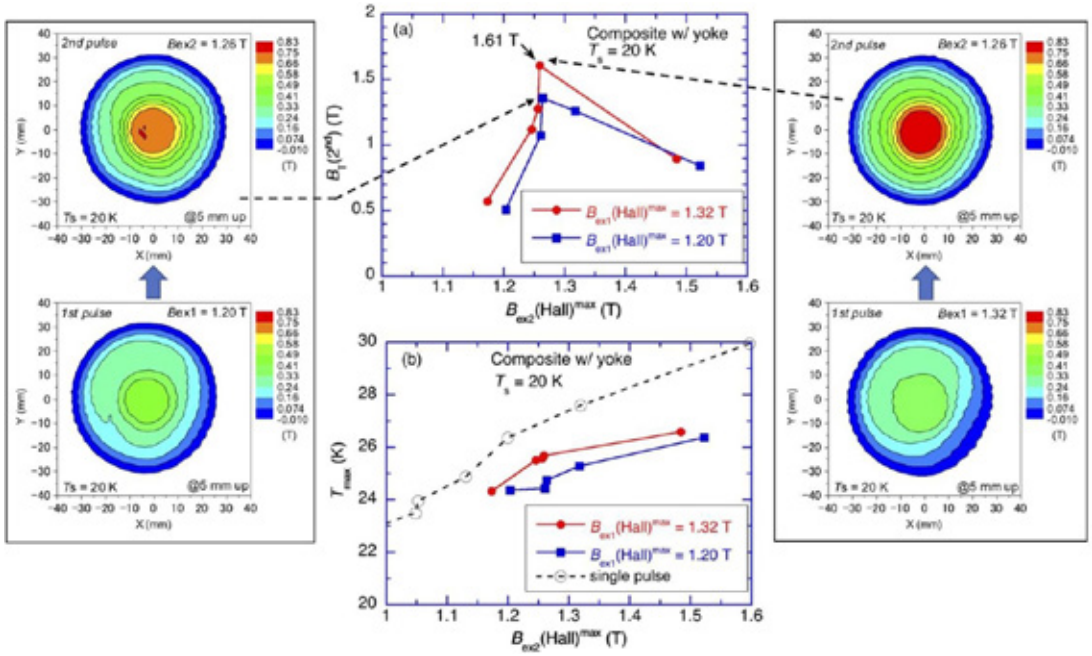

Figure 9. (a) The trapped field, B_T(2nd), on the central surface of the composite (w/yoke) at $T_s = 20$ K, as a function of the second applied pulsed field, B_{ex2}(Hall), after the first pulsed fields, $B_{ex1}(\text{Hall})^{max}$, of 1.20 T and 1.32 T were applied. The trapped field profiles of the composite (w/yoke) measured 5 mm above the bulk surface at 20 K, for which the maximum B_T(2nd) was achieved for $B_{ex1}(\text{Hall})^{max} = 1.20$ T and 1.32 T. (b) The maximum temperature rise, T_{max}, of the composite (w/yoke) at $T_s = 20$ K, as a function of $B_{ex2}(\text{Hall})^{max}$. T_{max} for the single pulse application for the composite (w/yoke) at $T_s = 20$ K is also shown.

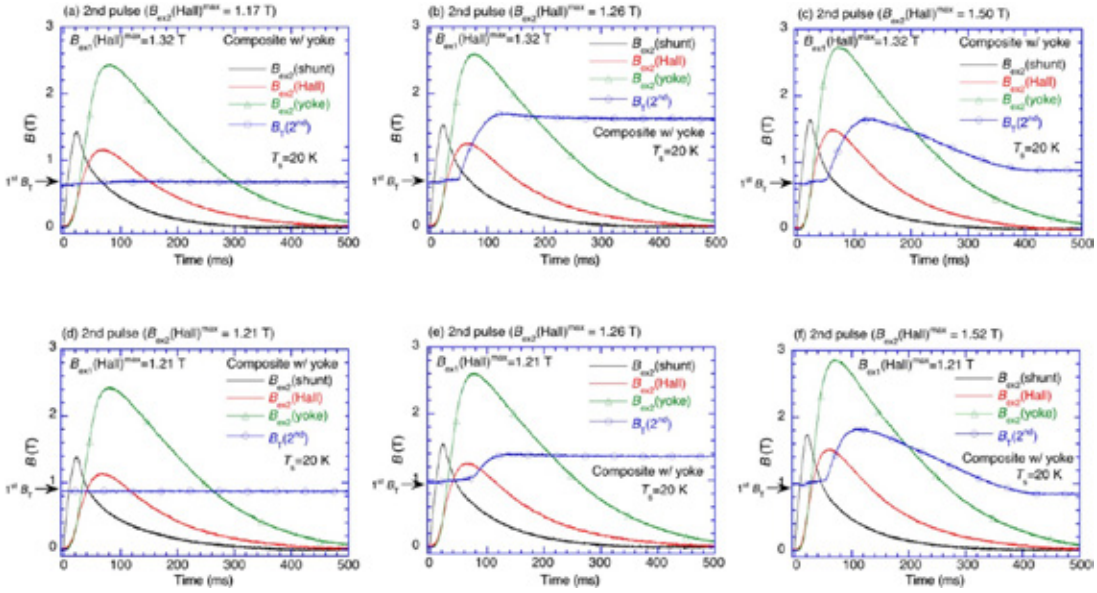

Figure 10. The time dependence of the applied fields, $B_{ex2}(t)$, and the trapped field, B_T(2nd)(t) for the second pulse application, $B_{ex2}(\text{Hall})^{max}$, after the first pulse application of (a)–(c) $B_{ex1}(\text{Hall})^{max} = 1.32$ T and (d)–(f) $B_{ex1}(\text{Hall})^{max} = 1.21$ T at $T_s = 20$ K.

pulse application. The reduction of temperature rise results in the enhancement of B_T after the second pulse.

Figures 10(a)–(c), respectively, show the time dependence of the applied fields, B_{ex2}(shunt)(t), B_{ex2}(Hall)(t) for w/o yoke and B_{ex2}(yoke)(t) for w/yoke, and the trapped field, B_T(2nd)(t), at $T_s = 20$ K for $B_{ex2}(\text{Hall})^{max} = 1.17$, 1.26 and 1.50 T, after the first pulse of $B_{ex1}(\text{Hall})^{max} = 1.32$ T was applied. The time dependence of B_T(1st)(t) for $B_{ex1}(\text{Hall})^{max} = 1.32$ T was shown in figure 8(i), in which B_T(1st) = 0.65 T was trapped. For $B_{ex2}(\text{Hall})^{max} = 1.26$ T, the maximum B_T(2nd) of 1.61 T

was achieved. Figures 10(d)–(f), respectively, show the time dependence of applied fields and the trapped field, B_T(2nd)(t), at $T_s = 20$ K for B_{ex2}(Hall)$^{max} = 1.21$, 1.26 and 1.52 T, after the first pulse of B_{ex1}(Hall)$^{max} = 1.20$ T was applied. The time dependence of B_T(1st)(t) for B_{ex1}(Hall)$^{max} = 1.21$ T was shown in figure 8(h), in which B_T(1st) = 1.00 T was trapped.

As shown in figure 9(a), a similar trend can be seen after the B_{ex1}(Hall)^{max} application of 1.32 and 1.20 T, although a slight difference in the maximum value of B_T(2nd) exists. However, the $B_T(t)$ behavior was different after the identical B_{ex2}(Hall)$^{max} = 1.26$ T application, as shown in figures 10(b) and (e). In the case of B_{ex1}(Hall)$^{max} = 1.32$ T, which was higher than the optimum B_{ex1}(Hall)^{max} shown in figure 6, B_T(1st) was as low as 0.65 T. For the 2nd pulse application of B_{ex2}(Hall)$^{max} = 1.26$ T, a clear B_T(2nd)(t) enhancement up to 1.61 T can be observed. On the other hand, in the case of B_{ex1}(Hall)$^{max} = 1.20$ T, which was the optimum B_{ex1}(Hall)^{max} shown in figure 6, B_T(1st) was 1.00 T. For the 2nd pulse application of B_{ex2}(Hall)$^{max} = 1.26$ T, the B_T(2nd)(t) enhancement was relatively small. These results suggest that the enhancement of B_T(2nd) is sensitive to the trapped field profile in the bulk after the 1st pulse application. A similar trend in the enhancement of B_T(2nd) was observed in the results from the MMPSC method for the GdBaCuO bulk in [17].

4. Conclusion

We have investigated the pulsed field magnetization (PFM) of three types of MgB_2 bulk modules (single ring bulk, composite (w/o yoke) and composite (w/yoke)) using a split-type coil (also inserting a soft iron yoke) at $T_s = 20$ K. The composite (w/o yoke) consisted of two MgB_2 ring bulks sandwiched by thin oxygen-free copper ring plates, which were then stacked. The composite (w/yoke) module included a soft iron yoke cylinder that was inserted in the composite (w/o yoke). We also studied the effect of the copper plates and soft iron yoke to enhance the trapped field, B_T. The important results and conclusions are summarized as follows.

(1) The copper plates delayed the rise time of magnetic pulse due to the flow of the eddy currents. The inserted soft iron yoke attracted the magnetic flux and enhanced the trapped field due to its large permeability. Both parts contribute to the magnitude and shape of the effective pulsed field, B_{ex}.
(2) The trapped field was enhanced from $B_T = 0.34$ T for the single MgB_2 ring bulk without both the copper plates and soft iron yoke to $B_T = 0.44$ T for the composite (w/o yoke) and, finally to $B_T = 1.00$ T for the composite (w/yoke). The inserted soft iron yoke can be exploited to enhance the trapped field because the intrinsic B_T of the single MgB_2 ring bulk was smaller than the saturation field of the yoke.
(3) Using the optimized second pulse application after appropriate flux trapped, B_T(1st), by the first pulse, B_{ex1}, the trapped field was enhanced considerably to B_T(2nd) = 1.61 T, which is a record-high trapped field for MgB_2 bulk by PFM to date.
(4) The combination of the longer magnetic pulse by the copper plates, the enhancement of the effective applied field by the inserted soft iron yoke and the double pulse application using the split-type coil is an effective technique to enhance the trapped field in the MgB_2 bulk using PFM. This composite structure with copper plates and an iron yoke may also be applicable to REBaCuO bulk trapped field magnets magnetized by PFM.

Acknowledgments

The authors thank Dr Mark D Ainslie of University of Cambridge for his valuable discussions and suggestions. This research is supported by Adaptable and Seamless Technology transfer Program through Target-driven R&D (A-STEP) from Japan Science and Technology Agency (JST), Grant No. VP30218088419 and by JSPS KAKENHI Grant No. 19K05240.

ORCID iDs

Tatsuya Hirano https://orcid.org/0000-0003-1658-914X
Sora Namba https://orcid.org/0000-0001-7268-5326
Tomoyuki Naito https://orcid.org/0000-0001-7594-3466
Hiroyuki Fujishiro https://orcid.org/0000-0003-1483-835X

References

[1] Weinstein R, Parks D, Sawh R-P, Carpenter K and Davey K 2016 *J. Appl. Phys.* **119** 133906
[2] Zou J, Ainslie M D, Fujishiro H, Bhagurkar A G, Naito T, Hari Babu N, Fagnard J-F, Vanderbemden P and Yamamoto A 2015 *Supercond. Sci. Technol.* **28** 075009
[3] Fujishiro H, Mochizuki H, Naito T, Ainslie M D and Giunchi G 2016 *Supercond. Sci. Technol.* **29** 034006
[4] Fujishiro H, Tateiwa T, Fujiwara A, Oka T and Hayashi H 2006 *Physica* C **445–8** 334
[5] Zhou D, Izumi M, Miki M, Felder B, Ida T and Kitano M 2012 *Supercond. Sci. Technol.* **25** 103001
[6] Bhagurkar A G, Yamamoto A, Anguilano L, Dennis A R, Durrell J H, Hari B N and Cardwell D A 2016 *Supercond. Sci. Technol.* **29** 035008
[7] Yamamoto A, Ishihara A, Tomita M and Kishio K 2014 *Appl. Phys. Lett.* **105** 032601
[8] Fujishiro H, Ujiie T, Mochizuki H, Yoshida T and Naito T 2015 *IEEE Trans. Appl. Supercond.* **25** 6800104
[9] Hirano T, Fujishiro H, Naito T, Ainslie M D and Shi Y-H 2019 *IEEE Trans. Appl. Supercond.* **29** 6801705
[10] Fujishiro H, Naito T and Oyama M 2011 *Supercond. Sci. Technol.* **24** 075015
[11] Kambara M, Babu N H, Sadki E S, Cooper J R, Minami H, Cardwell D A, Campbell A M and Inoue I H 2001 *Supercond. Sci. Technol.* **14** L5
[12] Bhagurkar A G, Yamamoto A, Wang L, Xia M, Dennis A R, Durrell J H, Aljohani T A, Babu N H and Cardwell D A 2018 *Sci. Rep.* **8** 13320
[13] Fujishiro H, Ujiie T, Naito T, Albisetti A F and Giunchi G 2014 *J. Phys.: Conf. Ser.* **507** 032016
[14] Naito T, Yoshida T and Fujishiro H 2015 *Supercond. Sci. Technol.* **28** 095009
[15] Huang K Y *et al* 2020 *Supercond. Sci. Technol.* **33** 02LT01

[16] Hayashi H, Tsutsumi K, Saho N, Nishijima N and Asano K 2003 *Physica* C **392–6** 745–8
[17] Zhou D, Shi Y-H, Dennis A R, Cardwell D A and Durrell J H 2020 *Supercond. Sci. Technol.* **33** 034001
[18] Fujishiro H, Tamura T, Arayashiki T, Oyama M, Sasaki T, Naito T, Giunchi G and Albisetti A F 2012 *Jpn. J. Appl. Phys.* **51** 103005
[19] Nakamura T, Tamada D, Yanagi Y, Itoh Y, Nemoto T, Utumi H and Kose K 2015 *J. Magn. Reson.* **259** 68–75
[20] Oka T *et al* 2019 *IEEE Trans. Appl. Supercond.* **29** 6802606
[21] Zhou D, Ainslie M D, Srpčič J, Huang K-Y, Shi Y-H, Dennis A R, Cardwell D A, Durrell J H, Boll M and Filipenko M 2018 *Supercond. Sci. Technol.* **31** 105005
[22] Fujishiro H, Tateiwa T, Kakehata K, Hiyama T and Naito T 2007 *Supercond. Sci. Technol.* **20** 1009–14
[23] Gotoh S, Murakami M, Fujimoto H and Koshizuka N 1992 *J. Appl. Phys.* **72** 2404–10
[24] Ainslie M D, Fujishiro H, Ujiie T, Zou J, Dennis A R, Shi Y-H and Cardwell D A 2014 *Supercond. Sci. Technol.* **27** 065008
[25] Werfel F N, Floegel-Delor U, Rothfeld R, Riedel T, Goebel B, Wippich D and Schirrmeister P 2012 *Supercond. Sci. Technol.* **25** 014007
[26] Fuchs G, Häßler W, Nenkov K, Scheiter J, Perner O, Handstein A, Kanai T, Schultz L and Holzapfel B 2013 *Supercond. Sci. Technol.* **26** 122002
[27] Ikuta H, Ishihara H, Yanagi Y, Itoh Y and Mizutani U 2002 *Supercond. Sci. Technol.* **15** 606
[28] Durrell J H *et al* 2014 *Supercond. Sci. Technol.* **27** 082001
[29] Miyazaki T, Fukui S, Ogawa J, Sato T, Oka T, Scheiter J, Hasler W, Kulawansha E, Yuanding Z and Yokoyama K 2017 *IEEE Trans. Appl. Supercond.* **27** 6800504
[30] Ida T *et al* 2004 *Physica* C **412–4** 638–45
[31] Fujishiro H, Hiyama T, Miura T, Naito T, Nariki S, Sakai N and Hirabayashi I 2009 *IEEE Trans. Appl. Supercond.* **19** 3545–8
[32] Ainslie M D, Zhou D, Fujishiro H, Takahashi K, Cardwell D A and Durrell J H 2018 *IEEE Trans. Appl. Supercond.* **28** 6800207
[33] Ogino A, Naito T and Fujishiro H 2017 *IEEE Trans. Appl. Supercond.* **27** 6800905
[34] Sander M, Sutter U, Koch R and Klaser M 2000 *Supercond. Sci. Technol.* **13** 841
[35] Fujishiro H, Kaneyama M, Yokoyama K, Oka T and Noto K 2005 *Jpn. J. Appl. Phys.* **44** 4919–25
[36] Durrell J H, Dancer C E J, Dennis A, Shi Y, Xu Z, Campbell A M, Hari N, Todd R I, Grovenor C R M and Cardwell D A 2012 *Supercond. Sci. Technol.* **25** 112002
[37] Ainslie M D, Fujishiro H, Mochizuki H, Takahashi K, Shi Y-H, Namburi D K, Zou J, Zhou D, Dennis A R and Cardwell D A 2016 *Supercond. Sci. Technol.* **29** 074003
[38] Ogawa K, Nakamura T, Terada Y, Kose K and Haishi T 2011 *Appl. Phys. Lett.* **98** 234101
[39] Fujishiro H, Mochizuki H, Ainslie M D and Naito T 2016 *Supercond. Sci. Technol.* **29** 084001
[40] Yanagi Y, Itoh Y, Yoshikawa M, Oka T, Hosokawa T, Ishihara H, Ikuta H and Mizutani U 2000 *Advances in Superconductivity* vol 12 (Tokyo: Springer) pp 470

9. (H-8) K. Takahashi, H. Fujishiro and M. D. Ainslie,
"A conceptual study of a high gradient trapped field magnet (HG-TFM) providing toward a quasi-zero gravity space on Earth",
Supercond. Sci. Technol. **34** (2021) 035001 (13 pages) (No. 283 paper)

OPEN ACCESS
IOP Publishing
Superconductor Science and Technology
Supercond. Sci. Technol. **34** (2021) 035001 (13pp)
https://doi.org/10.1088/1361-6668/abd386

A conceptual study of a high gradient trapped field magnet (HG-TFM) toward providing a quasi-zero gravity space on Earth

Keita Takahashi[1], **Hiroyuki Fujishiro**[1] and **Mark D Ainslie**[2]

[1] Department of Physical Science and Materials Engineering, Faculty of Science and Engineering, Iwate University, Morioka 020-8551, Japan
[2] Bulk Superconductivity Group, Department of Engineering, University of Cambridge, Cambridge CB2 1PZ, United Kingdom

E-mail: s3119004@iwate-u.ac.jp and fujishiro@iwate-u.ac.jp

Received 23 September 2020, revised 18 November 2020
Accepted for publication 14 December 2020
Published 25 January 2021

Abstract

In this work, we propose a new concept of a high gradient trapped field magnet (HG-TFM). The HG-TFM is made from (RE)BaCuO bulk superconductors, in which slit ring bulks (slit-TFMs) are tightly stacked with TFM cylinders (full-TFMs), and state-of-the-art numerical simulations were used to investigate the magnetic and mechanical properties in detail during and after magnetization. A maximum value of the magnetic field gradient product of $B_z \cdot \mathrm{d}B_z/\mathrm{d}z = 6040\ \mathrm{T}^2\ \mathrm{m}^{-1}$ was obtained after conventional field cooled magnetization (FCM) with an applied field, B_{app}, of 10 T of the HG-TFM with 60 mm in outer diameter and 10 mm in inner diameter. This value may be the highest value ever reported compared to any other magnetic sources. The $B_z \cdot \mathrm{d}B_z/\mathrm{d}z$ value increased with decreasing inner diameter of the HG-TFM and with increasing B_{app} during FCM. The electromagnetic stress in the HG-TFM during the FCM process mainly results from the hoop stress along the circumferential direction. The simulations suggested that there is no fracture risk of the bulk components during FCM from 10 T in a proposed realistic configuration of the HG-TFM where both TFM parts are mounted in Al-alloy rings and the whole HG-TFM is encapsulated in a steel capsule. A quasi-zero gravity space can be realized in the HG-TFM with a high $B_z \cdot \mathrm{d}B_z/\mathrm{d}z$ value in an open space outside the vacuum chamber. The HG-TFM device can act as a compact and cryogen-free desktop-type magnetic source to provide a large magnetic force and could be useful in a number of life/medical science applications, such as protein crystallization and cell culture.

Keywords: bulk superconductors, trapped field magnets, high gradient magnets, finite element method, magnetic levitation, quasi-zero gravity

(Some figures may appear in colour only in the online journal)

1. Introduction

Zero gravity in space is known to be a characteristic condition in scientific research fields. Up to now, some experimental research has been carried out exploiting quasi-zero gravity conditions in the International Space Station as an environmental parameter, which focuses positively on applications related to life/medical sciences, such as protein crystallization [1] and cell culture [2] without natural convection caused by the gravitational force of the Earth. The so-called 'space biology' resulting from this research is an important developing field that could contribute significantly to the sustainable development goals.

A large magnetic field in combination with a large field gradient can provide a repulsive force against gravity on the Earth and achieve a counter-balance situation for any diamagnetic materials such as water, common metals and even cells of the human body. In 1990, magnetic levitation of diamagnetic materials such as water and plastics was first demonstrated by Beaugnon *et al* using a hybrid-type superconducting magnet (HM), in which a magnetic field gradient product, $B_z \cdot \mathrm{d}B_z/\mathrm{d}z$, as high as -1923 T^2 m^{-1} was applied along the vertical direction against gravity on Earth [3].

Superconducting technologies have satisfied several demands for high magnetic fields including magnetic levitation. Nikolayev *et al* summarizes the specification of existing superconducting magnets worldwide, where the highest $B_z \cdot \mathrm{d}B_z/\mathrm{d}z = -3000$ T^2 m^{-1} with a record-high magnetic field of 30 T has been ever achieved in a HM and superconducting coil magnet (SM) [4]. Cryo-cooled superconducting magnets without liquid helium that can generate $B_z \cdot \mathrm{d}B_z/\mathrm{d}z$ up to -400 T^2 m^{-1} with magnetic fields up to 10–12 T are now used practically at the laboratory scale.

The magnetic force, F_m, acting on a material increases in proportional to the magnetic field, B_z, and the magnetic field gradient, $\mathrm{d}B_z/\mathrm{d}z$, along the z-axis (upper direction) as follows,

$$F_m \propto B_z \cdot \frac{\mathrm{d}B_z}{\mathrm{d}z}. \quad (1)$$

To enhance F_m, there are some trends related to the magnet design, i.e. the improvement of B_z and/or $\mathrm{d}B_z/\mathrm{d}z$. One example is the gradient-type superconducting magnet developed for protein crystallization, in which an inverse coil made from Nb_3Sn was placed on the hybrid coil, consisting of an inner Nb_3Sn coil and outer NbTi coils. As a result, the magnet can generate a $B_z \cdot \mathrm{d}B_z/\mathrm{d}z$ as large as -1500 T^2 m^{-1} around the boundary of both coils [5]. The most significant issue is that such a comparatively large $B_z \cdot \mathrm{d}B_z/\mathrm{d}z$ value has been realized only in a specialized facility [4]. For practical use of a magnetic quasi-zero gravity condition on ground, it is desirable for the magnetic source to be lightweight, mobile, and cost-effective as a desktop-type apparatus, and preferably cryogen-free, i.e. operating without the need for any coolant such as liquid helium.

Large, single-grain (RE)BaCuO bulk superconductors (RE: rare earth element or *Y*) can be utilized as a compact and strong, quasi-permanent magnet [6]. Magnetic flux is trapped in bulk superconductors by a supercurrent flowing with zero-resistivity due to electromagnetic induction after applying and removing a large magnetizing field. Such (RE)BaCuO bulks with a critical temperature, T_c, over 90 K are the most promising materials to be utilized as a trapped field magnet (TFM) in a compact and desktop-type magnetic source. The record-high trapped field, 17.6 T, was achieved at the center of a two-stack GdBaCuO bulk pair magnetized by field-cooled magnetization (FCM) at 26 K using outer shrink-fit stainless steel (SS) rings [7] as well as at 23 K using SS laminations [8]. Regarding the validity of bulk TFMs magnetized by FCM, Vakaliuk *et al* indicated that the reproducibility of the trapped field can be verified experimentally under the applied field of 10 T at 50 K, but might not be proved for higher fields over $B_\mathrm{app} = 14$ T [9]. The exploration of practical use of such strong TFMs can be classified into three phases: fabrication, magnetization, and applications [6, 10]. Such experimental work has showed the significant potential of such TFMs as a powerful magnetic source. However, its configuration would not be appropriate for practical use in applications, which sometimes require the large magnetic field and/or gradient product to be provided in an open space inside or outside vacuum chamber.

Recently, the authors proposed a new concept of the hybrid TFM lens (HTFML), consisting of two bulk parts: an inner bulk lens and outer bulk cylinder [11]. The diamagnetic lens effect of the inner bulk lens can concentrate the trapped field generated from the outer bulk TFM cylinder after magnetization. It was predicted numerically that an HTFML consisting of a GdBaCuO bulk lens and GdBaCuO TFM cylinder can generate a concentrated magnetic field of $B_\mathrm{c} = 11.4$ T at 20 K that is higher than the external magnetic field of $B_\mathrm{app} = 10$ T, quasi-permanently without any additional power consumption [12]. Experimental validation has proved the feasibility of the HTFML, exploiting an inner GdBaCuO bulk lens and outer MgB_2 TFM cylinder, in which $B_\mathrm{c} = 3.5$ T was achieved for $B_\mathrm{app} = 2.0$ T at 20 K [13]. This HTFML device suggests a new pathway to enhance the trapped field from the viewpoint of the magnetizing method in contrast to conventional approaches that depend on the superconducting properties of the bulk itself.

Additionally, in the case of the HTFML using a GdBaCuO bulk lens and GdBaCuO TFM cylinder, we showed that a magnetic field gradient product as high as $B_z \cdot \mathrm{d}B_z/\mathrm{d}z = -3000$ T^2 m^{-1} could be generated inside the bulk annuli under the concentrated trapped field of $B_\mathrm{c} = 11.4$ T at 20 K, which allows for a quasi-zero gravity environment in a cost-effective and efficient way [12]. However, the HTFML device has some challenges in its construction and the magnetizing process. The temperature of the GdBaCuO bulk lens and the GdBaCuO TFM cylinder must be controlled individually during zero field-cooled magnetization (ZFCM) for the lens part and FCM for the TFM part. A special technique is required in order to control the temperature separately and the magnetization process can take several hours. Moreover, it is quite difficult to realize a room temperature bore for practical applications exploiting the advantages of the HTFML because of a narrow bore less than 10 mm in diameter in the GdBaCuO lens, which is also encapsulated in a SS holder. This does limit the effective size for practical scientific experiments.

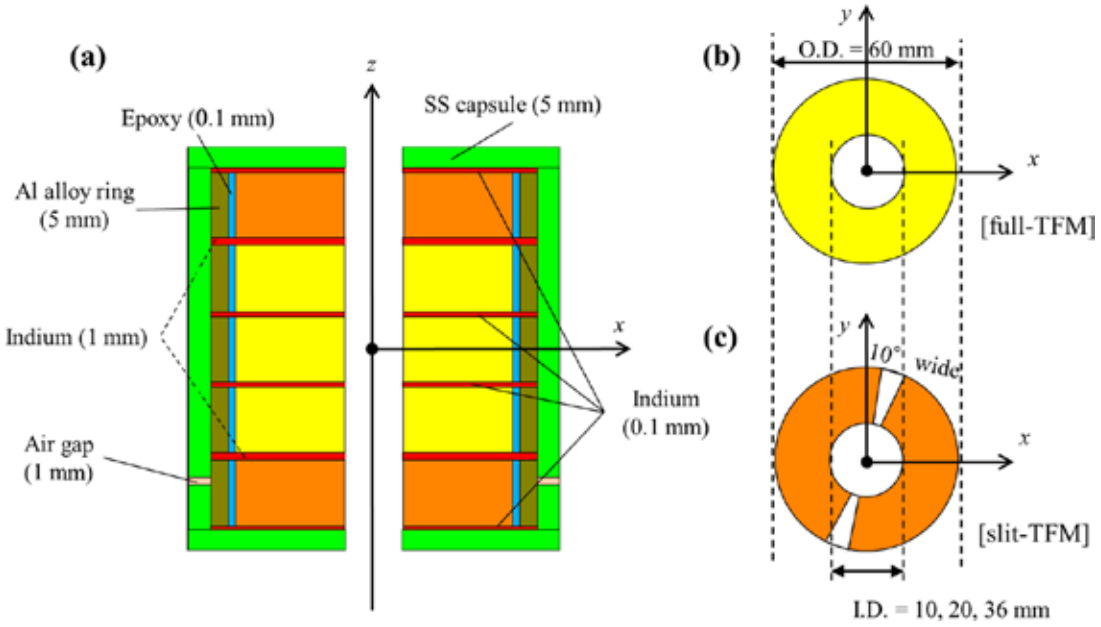

Figure 1. (a) Cross-sectional schematic of the three-dimensional numerical model of the HG-TFM, in which a conventional ring-shaped TFM cylinder, labelled 'full-TFM' (yellow), is sandwiched by two TFM cylinders with slits 10 deg. wide in the diagonal direction, labelled 'slit-TFM' (orange). The top views of the full-TFM and slit-TFM are also shown in (b) and (c), respectively.

In this study, we propose a new high gradient TFM (hereafter referred to as HG-TFM) to realize a quasi-zero gravity environment, in which slit ring bulks are combined with bulk TFM cylinders, and the magnetic properties were investigated in detail during and after magnetization using state-of-the-art numerical simulations. A maximum value of $B_z \cdot \mathrm{d}B_z/\mathrm{d}z = -6040$ T^2 m^{-1} was obtained after conventional FCM from $B_{\mathrm{app}} = 10$ T at 40 K for an HG-TFM with 10 mm in inner diameter, which may be the highest value ever reported compared to any other magnetic sources. The mechanical properties of the HG-TFM were also investigated to propose a realistic configuration of the HG-TFM device reinforced by a metal support structure that is essential to prevent mechanical fracture of the bulk superconducting material during the FCM process due to its brittle, ceramic nature.

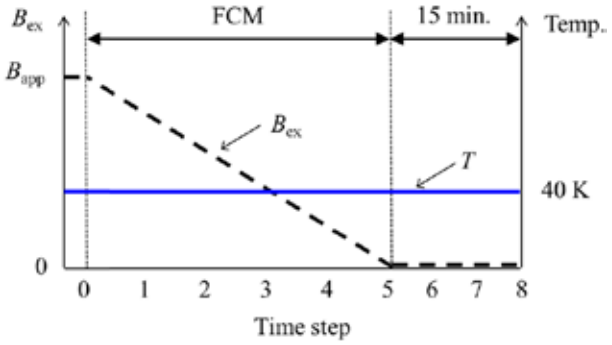

Figure 2. Magnetizing sequence for FCM of the HG-TFM, which is the same as that for a conventional TFM. The external field, B_{ex}, is decreased linearly at a ramp rate of -0.222 T min^{-1} from $B_{\mathrm{app}} = 3$, 5 or 10 T at a constant temperature at 40 K.

2. Numerical modeling procedure

Focusing on magnetic force applications for magnetic levitation [14–16], a higher magnetic field gradient product, $B_z \cdot \mathrm{d}B_z/\mathrm{d}z$, is desirable in the system as indicated by equation (1). The magnetic field gradient ($\mathrm{d}B_z/\mathrm{d}z$) term should be highly considered, as well as the trapped field (B_z) term, to improve the value of $B_z \cdot \mathrm{d}B_z/\mathrm{d}z$ overall.

Figure 1(a) presents a cross-sectional schematic of the three-dimensional numerical model of the HG-TFM, in which a conventional ring-shaped TFM cylinder, labeled 'full-TFM', is sandwiched by two TFM cylinders with slits 10 deg. wide in the diagonal direction, labeled 'slit-TFM'. Figures 1(b) and (c) show the top views of the full-TFM and slit-TFM, respectively. The outer diameter (O D) of the HG-TFM is 60 mm and the inner diameter (I D) is assumed to be either 10, 20 or 36 mm for both TFM components. The height (H) of the full-TFM is 48 mm, for which three ring-shaped bulks 16 mm in H are stacked, and each of the slit-TFMs are 16 mm in H. In the model, the height of the full-TFM is determined so that the trapped field capability to be 10 T for the HG-TFM with wider I D = 36 mm and is fixed temporarily for the comparison with various I D cases. The number of layers of the full-TFM can be reduced within the capability required in the device. Each bulk is mounted separately in an Al-alloy ring 5 mm in thickness (O D = 70 mm, I D = 60 mm, $H = 16$ mm) adhered by a thin layer of epoxy resin. A thin indium sheet layer (0.1 or 1 mm in thickness) is inserted between each bulk to reproduce the boundary condition between each bulk in the realistic HG-TFM. A

Table 1. Numerical fitting parameters for the assumed $J_c(B)$ characteristics of the GdBaCuO bulk used in equation (3), where the β value is adjusted to reproduce the experimental result for the trapped field [12].

T (K)	J_{c1} (A m^{-2})	B_L (T)	J_{c2} (A m^{-2})	B_{max} (T)	α	β
40	3.5×10^9	0.9	2.7×10^9	6.0	0.8	0.50

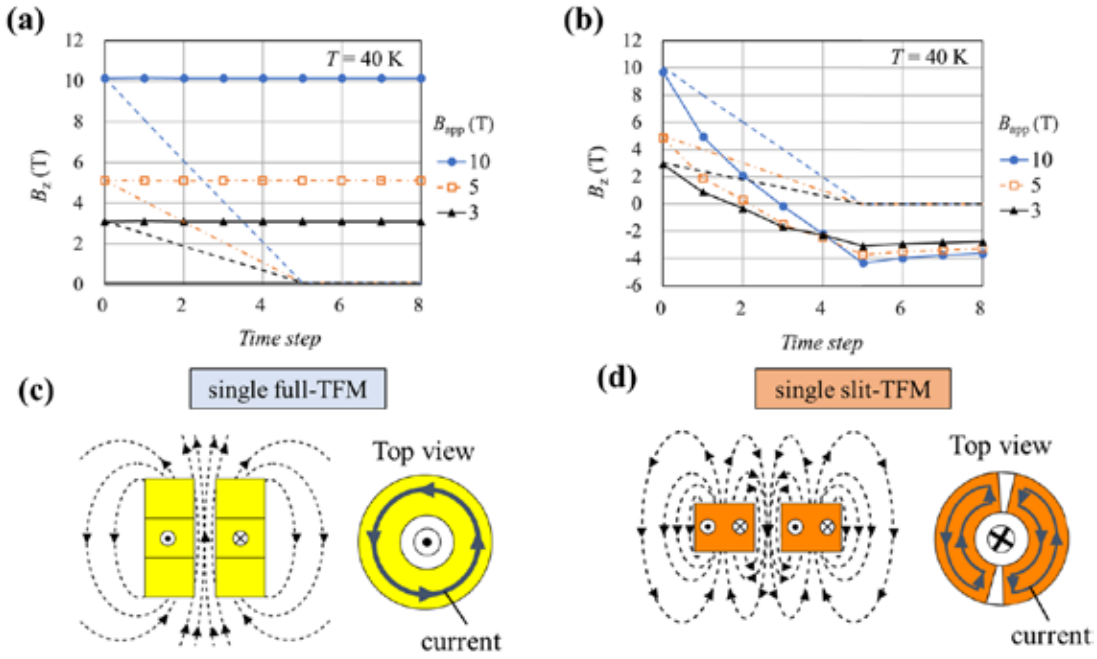

Figure 3. The time step dependence of the magnetic field, B_z, during FCM from $B_{app} = 3$, 5 and 10 T at 40 K at the center of (a) the single full-TFM (I D = 10 mm, O D = 60 mm, $H = 48$ mm) and (b) the single slit-TFM (I D = 10 mm, O D = 60 mm, $H = 16$ mm, slit 10 deg. wide). The schematic view of the magnetic flux distribution and induced current direction in (c) the single full-TFM and (d) the single slit-TFM.

solenoid coil of 170 mm in O D, 120 mm in I D and 200 mm in H is used to apply the magnetic field for the magnetization process (not shown in figure 1). As described earlier, appropriate mechanical reinforcement must be considered for the bulks due to their brittle, ceramic nature for improving the reliability of the magnetization process and the device itself. Several studies have investigated the fracture behavior of the bulk TFMs, which has a high risk of occurring under FCM from applied fields over 10 T at temperatures lower than 50 K, in particular [17–19]. As shown in figure 1(a), the model represents a realistic experimental setup for the mechanical reinforcement of the bulk magnets, which will be performed in the near future, employing outer Al-alloy rings and an outer SS capsule of 5 mm in thickness that can provide a compressive stress over −100 MPa when cooling from room temperature to the operating temperature to perform FCM. The mechanical reinforcement could endure up to $B_{app} = 10$ T in actual FCM experiments [20, 21].

Figure 2 presents the magnetizing sequence for FCM of the HG-TFM, which is the same as that for a conventional TFM. The external field, B_{ex}, is decreased linearly at a ramp rate of −0.222 T min^{-1}. from $B_{app} = 3$, 5 or 10 T at a constant temperature at 40 K. Once the external field is ramped down to 0 T for step 5, the static magnetic field 15 min later (for step 8) is then referred to as the trapped field value, B_T. Only the z-component is considered for magnetic levitation because gravity acts along the z direction. The electromagnetic phenomena of the bulk superconductor during the magnetization process are analyzed using the commercial software, PhotoEDDY (Photon Ltd, Japan).

The nonlinear electrical property of the bulk superconductor is derived from the E–J power law as follows,

$$E = E_c \left(\frac{J}{J_c}\right)^n, \tag{2}$$

where $E_c = 10^{-4}$ V m^{-1} is the characteristic electrical field, $n = 20$ is an appropriate power-law exponent for GdBaCuO bulk, and J_c is the critical current density. The realistic $J_c(B)$ characteristics, including the fish-tail effect under certain magnetic fields, can be represented by the following equation proposed by Jirsa *et al* [22],

$$J_c(B) = \beta \cdot \left\{ J_{c1} \exp\left(-\frac{B}{B_L}\right) + J_{c2} \frac{B}{B_{max}} \exp\left[\frac{1}{\alpha}\left(1 - \left(\frac{B}{B_{max}}\right)^{\alpha}\right)\right] \right\}, \tag{3}$$

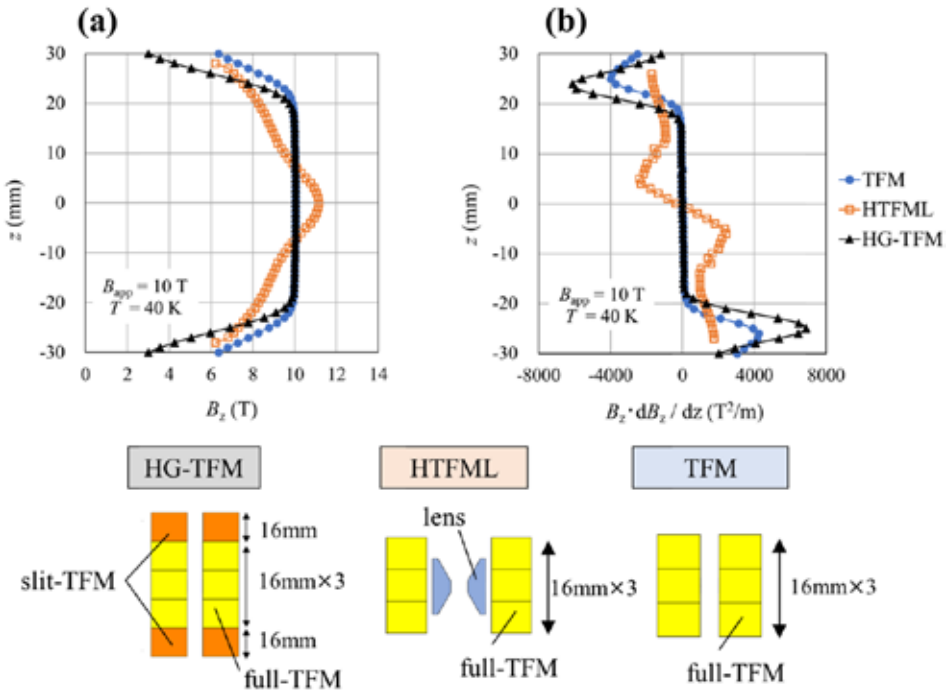

Figure 4. Numerical results for (a) the magnetic field, B_z, and (b) the magnetic field gradient product, $B_z \cdot dB_z/dz$, after magnetization with $B_{app} = 10$ T at 40 K along the z-axis inside the bulk annuli, comparing three types of TFMs: the HG-TFM, the HTFML and a conventional ring-shaped TFM (single full-TFM).

where each relevant parameter, J_{c1}, B_L, J_{c2}, B_{max}, and α are fitted from the experimental results for a GdBaCuO bulk reported by Kii *et al* [23]. The fitting coefficient, β, is employed so as to modify the deviation from the actual trapped field value (obtained experimentally) after FCM, particularly at temperatures lower than 50 K [12]. The parameters assumed for the GdBaCuO bulk material for equation (3) are summarized in table 1.

3. Electromagnetic analysis results

Before describing the mechanism of the HG-TFM in detail, the electromagnetic properties of each key component of the HG-TFM—the single full-TFM and the single slit-TFM—were investigated. Figures 3(a) and (b), respectively, show the time step dependence of the magnetic field, B_z, during FCM from $B_{app} = 3$, 5 and 10 T at 40 K at the center of the single full-TFM (I D = 10 mm, O D = 60 mm, $H = 48$ mm) and the single slit-TFM (I D = 10 mm, O D = 60 mm, $H = 16$ mm, slit 10 deg. wide). For the single full-TFM case shown in figure 3(a), the final trapped field, B_T, after FCM was almost equivalent to each B_{app} because of partial magnetization within the full capability of the full-TFM, which also enables the generation of a comparatively homogeneous magnetic field inside the bulk bore. Such a high field is realized by an induced supercurrent flowing inside the full-TFM as depicted. Nowadays, it is estimated that the trapped field capability for a disk-shaped bulk pair (O D = 24 mm, $H = 24$ mm) could be over 20 T, based on current state-of-the-art $J_c(B, T)$ characteristics [8]. The schematic view of the magnetic flux distribution and induced current direction in the single full-TFM is shown in figure 3(c), in which the conventional magnetic flux lines can be seen.

In the single slit-TFM case shown in figure 3(b), when B_{ex} decreased linearly, the B_z steeply decreased and became a negative value. Finally, the B_z value took a negative maximum at step 5 and then slightly recovered to the final B_T value because of the non-linear electrical property of bulk superconductor (see equation (2)). At step 8, $B_T = -2.8$, -3.3, -3.6 T values were obtained at the center of the single slit-TFM for $B_{app} = 3$, 5 and 10 T, respectively. Figure 3(d) also shows the schematic view of the magnetic flux distribution and induced current direction in the single slit-TFM. An induced current flows counterclockwise in each piece separated by the slits, which is the same direction with the full-TFM. However, the downward ($-z$-direction) magnetic flux would penetrate through the slit gap and exist even inside the central bore to build the magnetic loop in each piece of the slit-TFMs, which becomes the opposite direction to that generated by the single full-TFM ($+z$-direction). The HG-TFM then provides a large magnetic field gradient around the interface between the full-TFM with upward magnetic flux lines and the slit-TFM with downward magnetic flux lines.

Figures 4(a) and (b), respectively, show a comparison of the numerical results for the magnetic field, B_z, and the magnetic field gradient product, $B_z \cdot dB_z/dz$, after magnetization with $B_{app} = 10$ T at 40 K along the z-axis inside the bulk annuli, comparing three types of TFMs: the HG-TFM, the HTFML

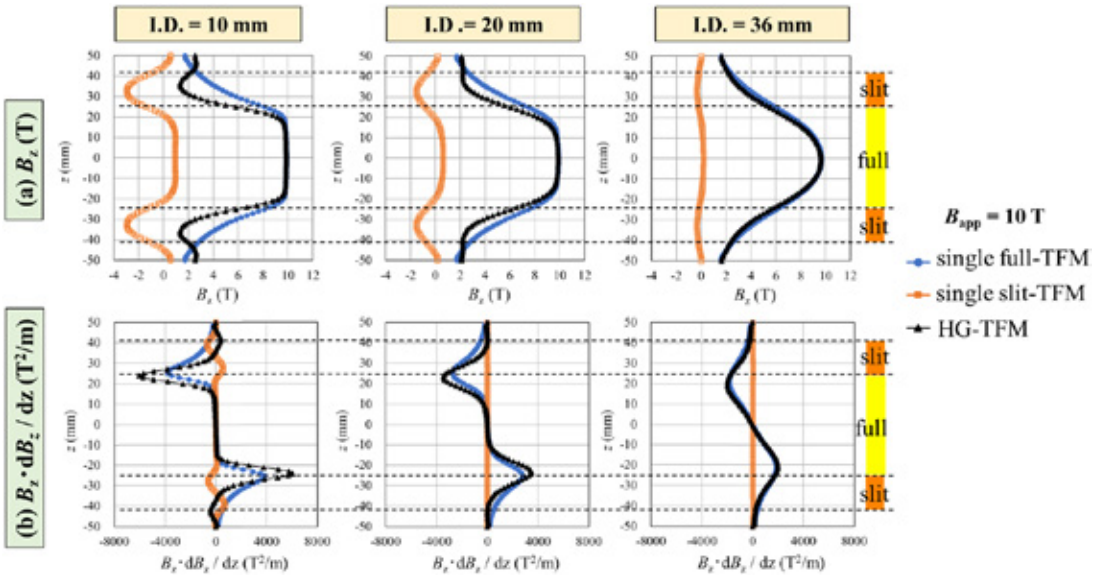

Figure 5. (a) The magnetic field, B_z, and (b) the magnetic field gradient product, $B_z \cdot \mathrm{d}B_z/\mathrm{d}z$, profiles of the HG-TFM with inner bores of I D = 10, 20 and 36 mm along the z-direction inside the bulk bore after FCM from $B_{app} = 10$ T at 40 K, compared with those of a single full-TFM (-24 mm $\leqslant z \leqslant 24$ mm) and single slit-TFM pair ($\pm z = 25 \sim 41$ mm).

and a conventional ring-shaped TFM (single full-TFM). The dimensions of each TFM are shown in the figure, where the dimensions of the full-TFM part were assumed to be identical for each case (I D = 10 mm, O D = 60 mm, $H = 48$ mm). The dimensions of the magnetic lens for the HTFML can be referred to elsewhere [12]. In figure 4(a), the trapped field, B_z, at the center ($z = 0$ mm) of the HG-TFM and full-TFM should be comparable with the applied field of $B_{app} = 10$ T. On the other hand, for the HTFML exploiting the diamagnetic lens effect, B_z can be concentrated into the bulk annuli, in which a concentrated trapped field of $B_c = 11.0$ T was achieved at 40 K at $z = 0$ mm. In figure 4(b), the HG-TFM shows the highest $B_z \cdot \mathrm{d}B_z/\mathrm{d}z$ value of -6040 T^2 m^{-1} at the boundary between each TFM part, $z = 24$ mm, which is remarkably superior than the other two types of TFM. In this sense, to improve the magnetic force efficiently, it would be more desirable to control the magnetic field gradient ($\mathrm{d}B_z/\mathrm{d}z$) profile by focusing on the gradient itself rather than improving the trapped field (B_z). One significant advantage of the HG-TFM is that its superior magnetic properties could be realized using a conventional FCM process at one temperature and without any additional costs, except for the slit-TFM. Note again that figure 4 is an example assuming a narrow 10 mm bore in inner diameter for each system. The magnetic properties of the HG-TFM would change depending on the shape of the bulk material (O D, I D, H, slit angle and so on) and the conditions of the magnetization process, such as the magnetizing temperature and B_{app}.

Figures 5(a) and (b), respectively, show the magnetic field, B_z, and the magnetic field gradient product, $B_z \cdot \mathrm{d}B_z/\mathrm{d}z$, profiles of the HG-TFM with inner bores of I D = 10, 20 and 36 mm along the z-direction inside the bulk bore after FCM from $B_{app} = 10$ T at 40 K, compared with those of a single full-TFM (-24 mm $\leqslant z \leqslant 24$ mm) and single slit-TFM pair ($\pm z = 25 \sim 41$ mm). In figure 5(a), the slit-TFM pair with a narrower bore of I D = 10 mm generates a higher negative trapped field ($= -3$ T) over a wider area at $\pm z = 20 \sim 40$ mm, which is effective for improving the HG-TFM performance with a larger magnetic field gradient. The negative trapped field of the single slit-TFM pair decreased with increasing I D value and there is no remarkable negative value for I D = 36 mm. On the other hand, for the cases of the full-TFM and HG-TFM, the B_z profile becomes broad with increasing I D value and the shape of the trapped field profile no longer varies between the full-TFM and HG-TFM with I D = 36 mm. Since B_z decays significantly with distance outside of the TFM, i.e. at $\pm z \geqslant 24$ mm, there is less, or no magnetic flux controlled in the HG-TFM with wider I D = 36 mm.

In figure 5(b), for the HG-TFM, the peak value of $B_z \cdot \mathrm{d}B_z/\mathrm{d}z$ was enhanced with decreasing I D at the boundary position between each TFM around $\pm z = 24$ mm due to the presence of the slit-TFM. A maximum $B_z \cdot \mathrm{d}B_z/\mathrm{d}z$ value of 6040 T^2 m^{-1} was achieved for I D = 10 mm, which is larger than that for the full-TFM (-3790 T^2 m^{-1}). It should be noted that a $B_z \cdot \mathrm{d}B_z/\mathrm{d}z$ value as large as -1400 T^2 m^{-1} along the $+z$-direction of the vertical magnet is required to levitate a diamagnetic water drop in air [24]. In this sense, the effective volume for magnetic levitation can be estimated to be $+z$ = 19–30, 17–30 and 13–27 mm inside the bore of the HG-TFM with I D = 10, 20 and 36 mm, respectively. For protein crystallization in a diamagnetic solution, a larger $B_z \cdot \mathrm{d}B_z/\mathrm{d}z$ value of -4450 T^2 m^{-1} is required to realize an apparent zero-gravity condition without buoyancy flow, which is much higher than that estimated numerically [25]. For realizing a higher field gradient product, the HG-TFM with a narrower inner bore is desirable, leading to a trade-off between field gradient product and effective volume.

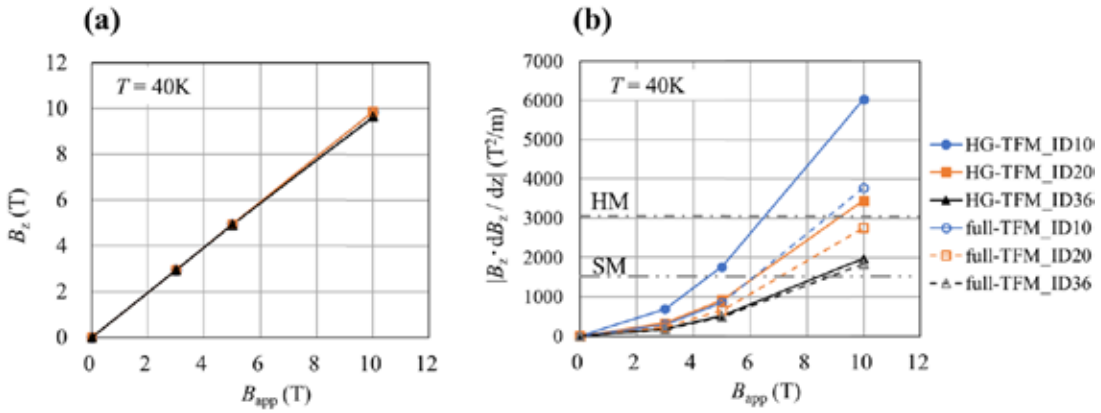

Figure 6. (a) The final trapped field, B_T ($= B_z$ at step 8), at the center ($x = y = z = 0$) and (b) the maximum field gradient product, $|B_z \cdot dB_z/dz|$, at the boundary position between the full and slit-TFMs of the HG-TFM, as a function of B_{app} for various I D cases. The results are compared to that of the full-TFM cases and other large-scale magnets: superconducting magnets (SM), and hybrid-type superconducting magnets (HM).

Figures 6(a) and (b) summarize the final trapped field, B_T ($= B_z$ at step 8), at the center ($x = y = z = 0$) and the maximum field gradient product, $|B_z \cdot dB_z/dz|$, around the boundary position between the full and slit-TFMs of the HG-TFM, as a function of B_{app} for various I D cases. The results for the full-TFM cases are also shown for reference. In figure 6(a), the trapped field capability is equivalent for all cases; thus, the relation $B_T = B_{app}$, is established based on the typical FCM process. However, for the magnetic field gradient product shown in figure 6(b), the HG-TFM would work more effectively for B_{app} higher than 5 T and for narrower bores smaller than I D = 20 mm compared to the full-TFM. Table 2 summarizes the maxima of the magnetic properties for each case including the HG-TFM, HTFML and full-TFM, extracted from figures 4 and 6. The HG-TFM with I D = 10 mm would provide a maximum $|B_z \cdot dB_z/dz| = 6040$ T m^{-2} when $B_T = 10$ T at 40 K, which may be the record-high value compared to that of other large-scale magnets: SM $\sim$ 1500 T m^{-2}, and HM $\sim$ 3000 T m^{-2} using liquid helium, shown in figure 6(b) [4, 26].

In most related studies, based on apparatus using a permanent magnet with a magnetic field $\sim$1 T, the magneto-Archimedes method must be exploited to reduce the required magnetic force using a paramagnetic medium solution [27, 28]. The HG-TFM no longer needs such a method, and consequently, can provide simpler, medium-free operation with air or water. These advantages of the HG-TFM can provide the versatility of a quasi-zero gravity space as a desktop-type magnetic source for magnetic levitation processing, which enables the suppression of gravity-induced convection in a wide range of potential industrial applications such as protein crystallization and cell culture [1, 2]. It should be noted that $B_z \cdot dB_z/dz$ values of 1980 and 2760 T^2 m^{-1} can be achieved after FCM from $B_{app} = 10$ T even for the single full-TFM with I D = 36 and 20 mm (without the slit-TFM), respectively, as shown in table 2, which are higher than that achieved by SMs [4]. These results suggest that the single full-TFM can be also applicable for quasi-zero gravity in the open space outside the vacuum chamber with a range of 15–30 mm in diameter. There is a limit for the enlargement of the space in the bore because it is difficult to fabricate good quality bulks >60 mm in O D, resulting in a narrower bore compared to that of SMs.

In our previous work [12], where the mechanism of magnetic levitation in the quasi-zero gravity space is explained in detail, it was highlighted that a large magnetic field gradient product up to 3000 T^2 m^{-1} of that particular HTFML design could be highly applicable to magnetic separation. Regarding the effectiveness of the magnetic force for crystal growth, it is shown elsewhere that the magnetic force affects several features: the magnetic field orientation, convection control, reduction of sedimentation and so on [14]. However, there are no theoretical rules yet regarding how the magnetic force works during the process and it differs between the target materials used. Thus, appropriate design of the I D of the HG-TFM needs to be explored as related to the particular application, where the magnetic force profile in the HG-TFM could be correlated with the quality of the resultant crystallization.

4. Mechanical stress analysis results

The mechanical fracture of bulk superconductors has been reported in several studies, where a crack might occur along the circumferential direction mainly due to the hoop stress induced during FCM from applied fields over 10 T at temperatures below 50 K [17–19]. To date, to prevent such mechanical fracture during magnetization, mechanical reinforcement has been usefully applied using glass fiber reinforced epoxy resin [29] or shrink-fit steel [7]. We also proposed a new hat structure of an outer metal reinforcement ring based on the results of mechanical stress simulations, in which a large (RE)BaCuO ring-shaped bulk (I D = 36 mm, O D = 60 mm, $H = 20$ mm) was experimentally confirmed to endure FCM from 10 T without fracture [20]. For the HTFML consisting of a (RE)BaCuO lens and (RE)BaCuO TFM cylinder,

Table 2. Numerical results of maxima of the magnetic properties for each case including the HG-TFM, HTFML and full-TFM magnetized at 40 K, extracted from figures 4 and 6.

	HG-TFM			HTFML
Bulk I D (mm)	10	20	36	10
B_z (B_{app}) (T)	10 (10)	10 (10)	9.8 (10)	11 (10)
$\lvert B_z \cdot dB_z/dz \rvert$ (T^2 m^{-1}) (single full-TFM)	6040 (3790)	3460 (2760)	1980 (1850)	2430 (1850)
Magnetization		FCM		ZFCM + FCM
Temperature (K)		40		

the mechanical properties have been analyzed during the magnetizing process from $B_{app} = 10$ T [30], in which the necessity of adequate mechanical reinforcement was strongly suggested, at least for the GdBaCuO TFM cylinder, but possibly the magnetic lens as well. It is also necessary to investigate the mechanical properties of the present HG-TFM as well during FCM, where the full-TFM part is tightly sandwiched by the slit-TFM pair.

After calculating the trapped field profile shown in the previous section, the nodal force was then imported into another software package, Photo-ELAS (Photon Ltd., Japan), for calculating the electromagnetic stress on each mesh element of the bulk TFMs during magnetization, which enables us to assess the reliability of the HG-TFM in terms of the mechanical reinforcement method.

Elastic behavior in an isotropic material can be expressed by Hooke's law, in which the stress tensor, σ_{ij}, is linearly proportional to the strain tensor, ε_{ij}, as follows

$$\sigma_{ij} = \lambda \cdot \varepsilon_{kk} \cdot \delta_{ij} + 2G \cdot \varepsilon_{ij}, \tag{4}$$

$$\lambda = \frac{E \cdot \nu}{(1+\nu)(1-2\nu)}, \tag{5}$$

$$G = \frac{E}{2(1+\nu)}, \tag{6}$$

where λ and G represent Lame's constants, δ_{ij} is the Kronecker delta function, E_Y is the Young's modulus, and ν is the Poisson ratio. The mechanical parameters, E_Y and ν, for each component of the HG-TFM are summarized in table 3, which are assumed in the simulation to be isotropic and in the elastic region. Note that all components, including the epoxy resin, indium and air gap, as shown in figure 1, were included in the modeling of the HG-TFM, which should be considered for the accurate prediction of the mechanical behavior [31].

Figures 7(a) and (b) show a contour map of the Von Mises stress, σ_{VM}, and the electromagnetic hoop stress along the y-direction, σ_{YY}, respectively, calculated for the full-TFM part of the HG-TFM with inner diameters of I D = 10, 20 and 36 mm, just after FCM from 10 T (step 5). In figure 7(a), the σ_{VM} value, which is a scalar quantity, represents the total value of the mechanical stresses including all directions. Compared with the maximum σ_{YY} value shown in figure 7(b), which is close to the maximum σ_{VM} value of 90 MPa around the inner periphery of the full-TFM part, it was found that the

Table 3. Assumed mechanical parameters (E_Y:Young's modulus and ν: Poisson ratio) for numerical stress analysis of the HG-TFM shown in figure 1 [20, 31].

	E_Y (GPa)	ν
(RE)BaCuO bulk	100	0.33
Epoxy resin	3.0	0.37
Al alloy (A7075-T6)	78	0.34
Indium	12.7	0.45
SS 304	193	0.28

main component of the electromagnetic stress results from the hoop stress along the y-direction in the full-TFM part. The maximum σ_{YY} value was almost independent of the bore size because the trapped field is equivalent for each HG-TFM with different bore sizes as shown in figure 6(a). These numerical results for the stress profile are similar to that reported for the annular (RE)BaCuO bulk magnet system (full-TFM) for an NMR spectrometer [21], in which an electromagnetic hoop stress about 100 MPa was generated at the inner peripheral region of the annular bulks reinforced by a similar structure. This means that the present reinforcement technique would work even for the present HG-TFM system. Considering the compressive stress of −100 MPa from the reinforcement by the Al-alloy rings and the SS capsule during the cooling process before FCM, the maximum total stress would be less than the fracture strength of typical Ag-doped (RE)BaCuO bulks of 50–70 MPa [32]. As a result, the full-TFM part should be appropriately reinforced and not break [21].

Figures 8(a)–(c) show the contour map of the Von Mises stress, σ_{VM}, the electromagnetic hoop stress along the y-direction, σ_{YY}, and the electromagnetic radial stress along the x-direction, σ_{XX}, respectively, for the slit-TFM pair of the HG-TFM with inner diameters of I D = 10, 20 and 36 mm, just after FCM from 10 T. For the case of I D = 10 mm, a maximum Von Mises stress of $\sigma_{VM} = 54$ MPa exists at the surfaces of the slit-TFM pair facing the full-TFM part. The σ_{XX} profile for each I D, as shown in figure 8(c), is similar to that for σ_{VM}. On the other hand, the σ_{YY} contribution to the Von Mises stress, as shown in figure 8(b), is relatively small. These results suggest that the main component of the electromagnetic stress results from the electromagnetic radial stress along the x-direction, σ_{XX}, in the case of I D = 10 mm and I D = 20 mm. However, for the wider I D = 36 mm, the electromagnetic stress mainly results from the hoop stress along the y-direction, σ_{YY}. Since an induced current flows in two regions

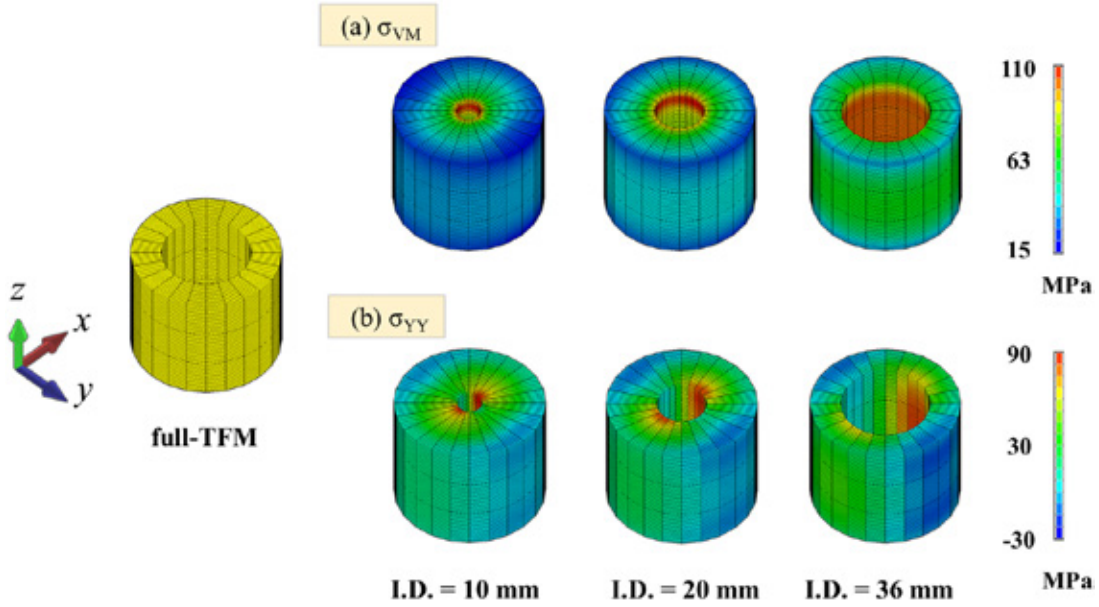

Figure 7. Contour map of (a) the Von Mises stress, σ_{VM}, and (b) the electromagnetic hoop stress along the y-direction, σ_{YY}, calculated for the full-TFM part of the HG-TFM with inner diameters of I D = 10, 20 and 36 mm, at step 5 just after FCM from 10 T.

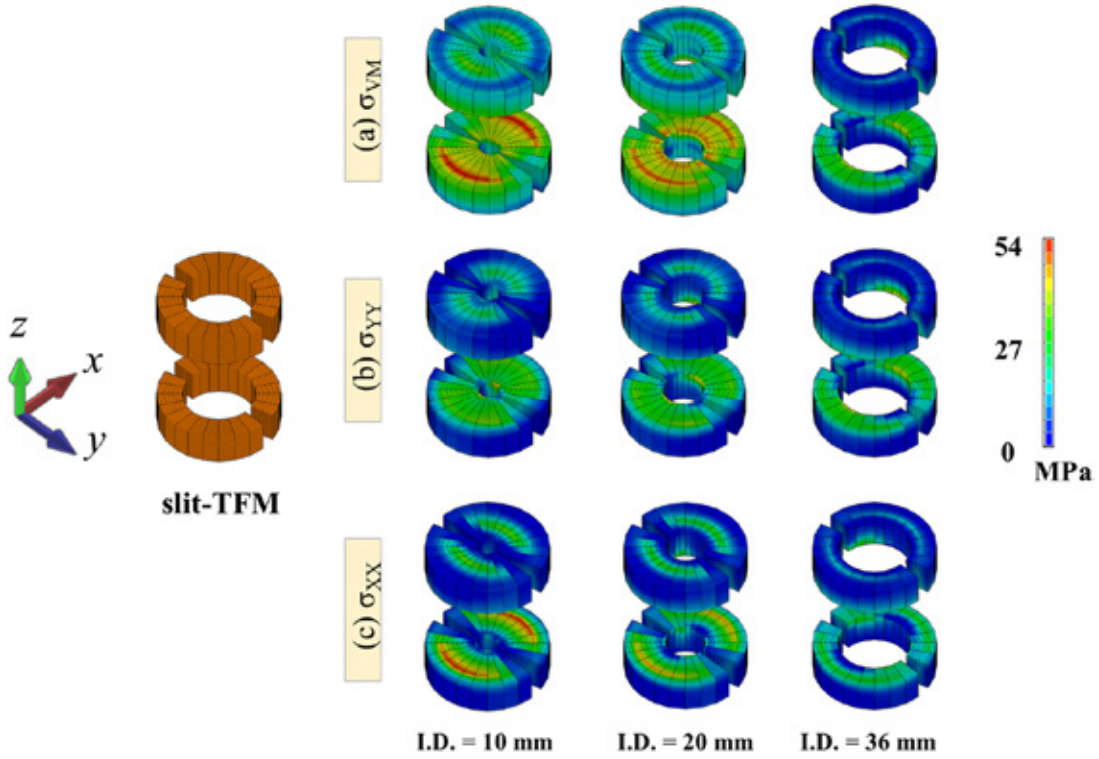

Figure 8. Contour map of (a) the Von Mises stress, σ_{VM}, (b) the electromagnetic hoop stress along the y-direction, σ_{YY}, and (c) the electromagnetic radial stress along the x-direction, σ_{XX}, for the slit-TFM pair of the HG-TFM with inner diameters of I D = 10, 20 and 36 mm, just after FCM from 10 T.

in the slit-TFM independently due to the existence of slits, the resultant trapped field and the mechanical stress become lower, compared to the full-TFM, even if the slit-TFM is magnetized by FCM from 10 T.

During the magnetization of the HG-TFM exploiting slit-TFMs stacked on the full-TFM, an extra stress component may be generated due to the repulsive force between each TFM part. Figure 9(a) shows a cross-sectional contour map

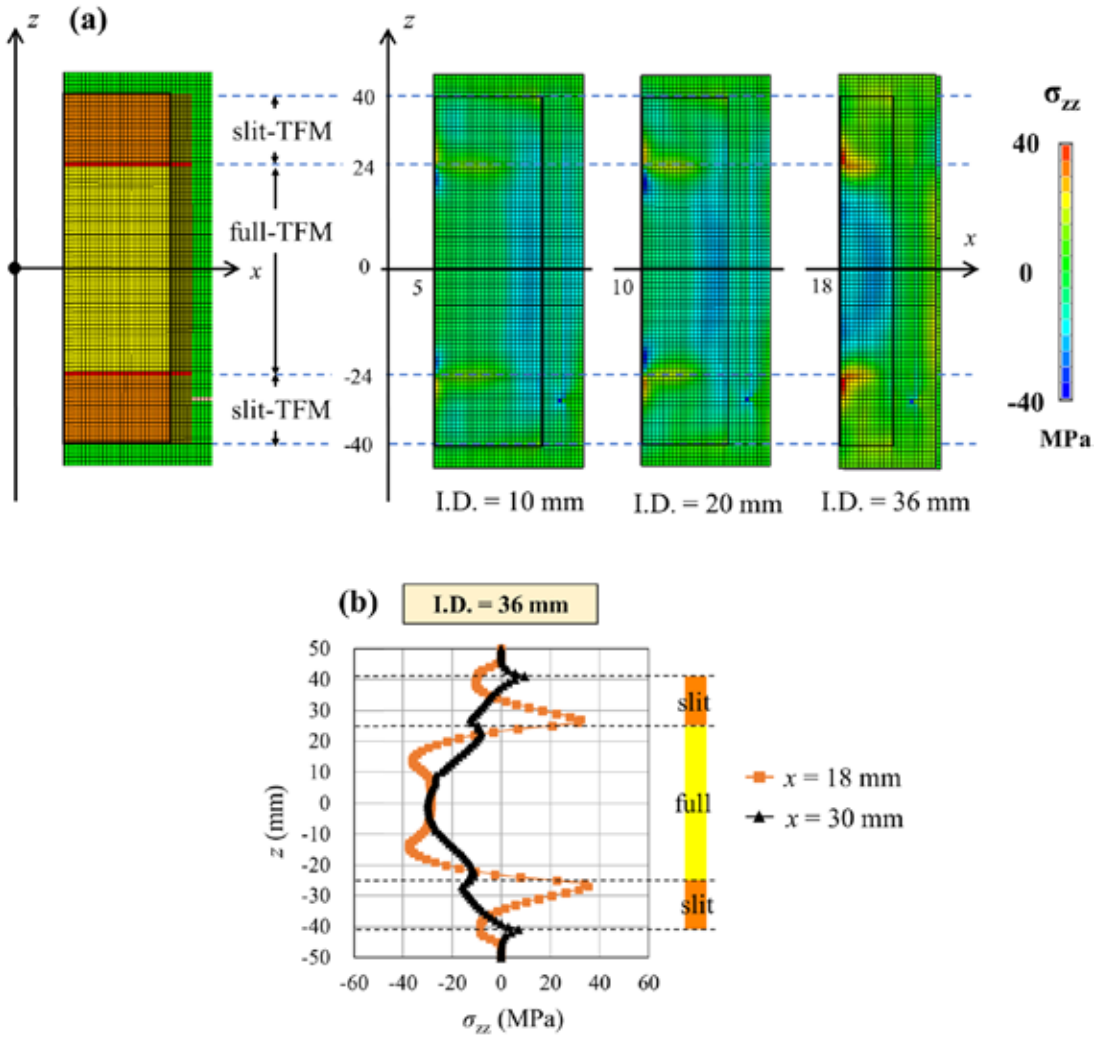

Figure 9. (a) Cross-sectional contour map of the electromagnetic stress along the vertical direction, σ_{ZZ}, for the HG-TFM with various inner diameters, just after the FCM process from 10 T. (b) The σ_{ZZ} distribution along the z-direction at the inner periphery ($x = 18$ mm) and at the outer periphery ($x = 30$ mm) for the HG-TFM with I D = 36 mm, extracted from (a).

of the electromagnetic stress along the vertical direction, σ_{ZZ}, for the HG-TFM with various inner diameters, just after the FCM process from 10 T. The positive σ_{ZZ} value is concentrated mainly in the inner periphery of the slit-TFM facing the full-TFM, and the magnitude of σ_{ZZ} increases with increasing I D These results suggest that a repulsive force exists in this region. However, the positive σ_{ZZ} region vanishes at the outer interface of the slit-TFM facing the full-TFM ($z = \pm 24$ mm, $-15 \leqslant x \leqslant 30$ mm for I D = 36 mm case), which indicates the possibility of an attractive force or very small repulsive force there. Figure 9(b) shows the σ_{ZZ} distribution along the z-direction at the inner periphery ($x = 18$ mm) and at the outer periphery ($x = 30$ mm) for the HG-TFM with I D = 36 mm, which were extracted from figure 9(a). At the inner periphery, the σ_{ZZ} value changes from positive to negative around the interface ($z = \pm 24$ mm). These results indicate that a repulsive force exists at the inner interface. On the other hand, at the outer periphery, the σ_{ZZ} value is negative and continuous for both the slit-TFM and full-TFM, suggesting that an attractive magnetic force might exist at the outer interface. Similar trends were also observed for the HG-TFM for I Ds = 10 and 20 mm.

Figure 10(b) shows a contour map of the final trapped field, B_T, of the HG-TFM with I D = 20 mm after FCM from 10 T. It should be noted that a trapped field along the $+z$-direction exists at the periphery of the slit-TFM (region A), which has a similar B_T strength of 10 T as for the full-TFM. These results suggest that 'region A' is magnetically attracted to the magnetized full-TFM. On the other hand, there exists little field trapped downward along the z-direction in the inner periphery region of the slit-TFM ('region B'). These results indicate that a repulsive magnetic force exists in the counter side in the full-TFM, which can be understood well from the schematic view of the magnetic flux lines in figure 10(a).

Figure 10(a) shows a schematic view of the magnetic flux profile for the HG-TFM after FCM. To understand the

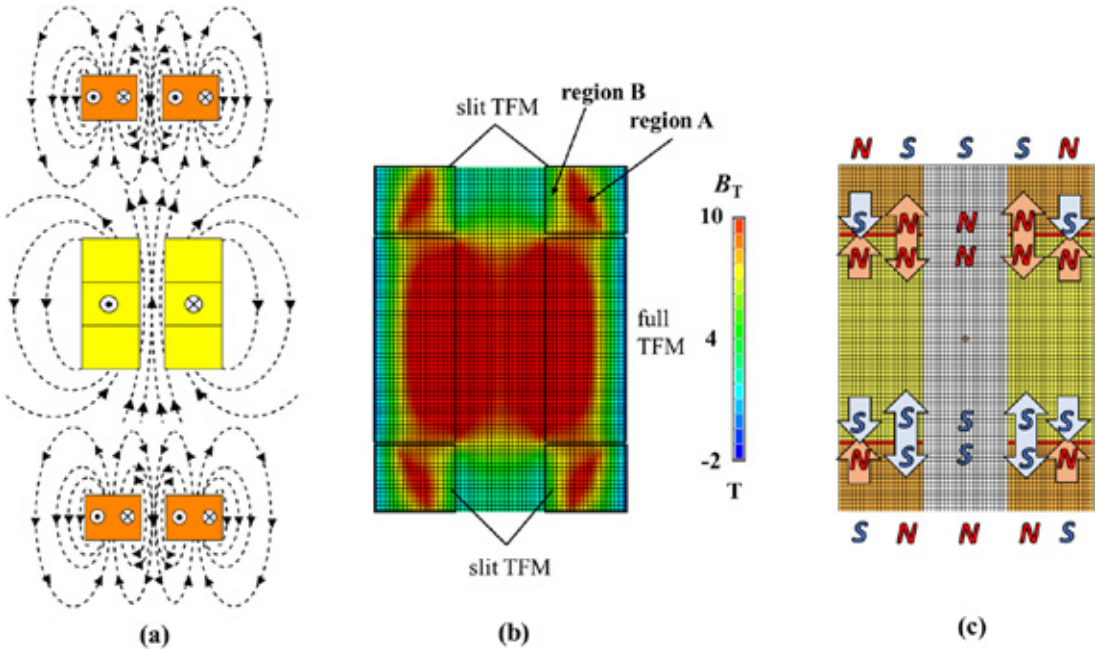

Figure 10. (a) Schematic view of the magnetic flux profile for the HG-TFM after FCM. (b) Contour map of the final trapped field, B_T, of the HG-TFM with I D = 20 mm after FCM from 10 T. (c) The effective magnetic poles of the HG-TFM after FCM. The outer periphery region (region A) and inner periphery region (region B) of the slit-TFM can be considered as opposing magnetic poles.

distribution of the magnetic flux lines at the interface visually, the full-TFM and the slit-TFM pair are placed at a distance. It can be confirmed visually that the magnetic flux lines co-exist at the interface and form the superposition of the magnetic fields that is destructive around the central bore or constructive around the bulk periphery.

Let us describe these results using a magnetic pole model. Figure 10(c) shows the effective magnetic poles of the HG-TFM after FCM, which presents the mechanism of the larger magnetic gradient of the HG-TFM. The outer periphery region (region A) and inner periphery region (region B) of the slit-TFM can be considered as opposing magnetic poles. As a result, region A is attractive (an N–S or S–N pair) and region B is repulsive (N–N or S–S pair) with respect to the magnetized full-TFM at the interface. Since both TFM parts are mounted in an Al-alloy ring and the whole HG-TFM is encapsulated in an SS capsule, σ_{ZZ} acts as a compressive stress, and that maxima is around 50 MPa for the full-TFM and 35 MPa for slit-TFM in the HG-TFM with I D = 36 mm. However, in the narrower bore cases, I D = 10 and 20 mm, σ_{ZZ} decreases despite the superior $B_z \cdot \mathrm{d}B_z/\mathrm{d}z$ performance. In any case, there is little fracture risk due to the compressive stress for the HG-TFM during FCM from 10 T, since the compressive fracture strength of (RE)BaCuO bulk is about one order of magnitude higher than the tensile mechanical strength [33].

5. Conclusion

We have proposed a new concept of a HG-TFM. The HG-TFM is made from (RE)BaCuO bulk superconductors to realize a quasi-zero gravity space using magnetic force, in which a slit ring bulk (slit-TFM) was tightly stacked with a TFM cylinder (full-TFM). State-of-the-art numerical simulations were used to investigate the magnetic and mechanical properties detail during and after magnetization. The important results and conclusions in this study are summarized as follows.

(a) A maximum value of the magnetic field gradient product of $B_z \cdot \mathrm{d}B_z/\mathrm{d}z = -6040$ T^2 m^{-1} was obtained after conventional FCM from $B_{app} = 10$ T of the HG-TFM with a 60 mm outer diameter and 10 mm inner diameter. This value may be the highest ever reported compared to any other magnetic sources. The superiority of the HG-TFM is the easier magnetization process including a single temperature and a simpler construction without any additional cost, but also the higher $B_z \cdot \mathrm{d}B_z/\mathrm{d}z$ can be provided in an open space outside the vacuum chamber.

(b) The $B_z \cdot \mathrm{d}B_z/\mathrm{d}z$ value increased with decreasing inner diameter of the HG-TFM and with increasing applied field, B_{app}, during FCM. Even if the inner diameter of the HG-TFM is 36 mm, a $B_z \cdot \mathrm{d}B_z/\mathrm{d}z$ value of 1980 T^2 m^{-1} can be achieved, which is slightly higher than 1850 T^2 m^{-1} for the single full-TFM case.

(c) The electromagnetic stress during the FCM process was also investigated to analyze the mechanical behavior of HG-TFM device. The electromagnetic stress in the HG-TFM device during the FCM process mainly results from the hoop stress along the y-direction, σ_{YY}, for the full-TFM.

(d) The outer and inner periphery regions of the slit-TFM can be considered as opposing magnetic poles. The outer

periphery region is attractive (N–S or S–N pair) and the inner periphery region is repulsive (N–N or S–S pair) with respect to the magnetized full-TFM at the interface. However, it was confirmed that there is little fracture risk for the bulks during FCM from 10 T in the proposed realistic configuration of the HG-TFM, where both TFM parts are mounted in Al-alloy rings and the whole HG-TFM is encapsulated in an SS capsule.

(e) A quasi-zero gravity space can be realized using the HG-TFM with its large $B_z \cdot \mathrm{d}B_z/\mathrm{d}z$ value in an open space outside the vacuum chamber even without the magneto-Archimedes method. The HG-TFM device is a compact and cryogen-free desktop-type magnetic source to provide a large magnetic force and can be applicable to scientific research, such as in the life/medical sciences for protein crystallization and cell culture.

Acknowledgments

This research is supported by JSPS KAKENHI Grant No. 19K05240 and by Adaptable and Seamless Technology transfer Program through Target-driven R&D (A-STEP) from Japan Science and Technology Agency (JST), Grant Nos. VP30218088419 and JPMJTM20AK. M D Ainslie would like to acknowledge financial support from an Engineering and Physical Sciences Research Council (EPSRC) Early Career Fellowship, EP/P020313/1. All data are provided in full in the results section of this paper.

ORCID iDs

Keita Takahashi https://orcid.org/0000-0002-8278-2688
Hiroyuki Fujishiro https://orcid.org/0000-0003-1483-835X
Mark D Ainslie https://orcid.org/0000-0003-0466-3680

References

[1] McPherson A and DeLucas L J 2015 Microgravity protein crystallization *NPJ Microgravity* **1** 15010
[2] Imura T, Nakagawa K, Kawahara Y and Yuge L 2018 Stem cell culture in microgravity and its application in cell-based therapy *Stem Cells Dev.* **27** 1298–302
[3] Beaugnon E and Tournier R 2003 Levitation of organic materials *Nature* **349** 470
[4] Nikolayev V S, Chatain D, Beysens D and Pichavant G 2011 Magnetic gravity compensation *Microgravity Sci. Technol.* **23** 113–22
[5] Wada H *et al* 2012 Application of high-field superconducting magnet to protein crystallization *Phys. Procedia Technol.* **36** 953–7
[6] Durrell J H, Ainslie M D, Zhou D, Vanderbemden P, Bradshaw T, Speller S, Filipenko M and Cardwell D A 2018 Bulk superconductors: a roadmap to applications *Supercond. Sci. Technol.* **31** 103501
[7] Durrell J H *et al* 2014 A trapped field of 17.6 T in melt-processed, bulk Gd-Ba-Cu-O reinforced with shrink-fit steel *Supercond. Sci. Technol.* **27** 082001
[8] Huang K *et al* 2020 Composite stacks for reliable >17 T trapped fields in bulk superconductor magnets *Supercond. Sci. Technol.* **33** 02LT01
[9] Vakaliuk O, Werfel F, Jaroszynski J and Halbedel B 2020 Trapped field potential of commercial Y-Ba-Cu-O bulk superconductors designed for applications *Supercond. Sci. Technol.* **33** 095005
[10] Ainslie M D and Fujishiro H 2019 *Numerical Modelling of Bulk Superconductor Magnetization. IOP Expanding Physics* (Bristol: IOP Publishing)
[11] Takahashi K, Fujishiro H and Ainslie M D 2018 A new concept of a hybrid trapped field magnet lens *Supercond. Sci. Technol.* **31** 044005
[12] Takahashi K, Fujishiro H and Ainslie M D 2020 Simulation study for magnetic levitation in pure water exploiting the ultra-high magnetic field gradient product of a hybrid trapped field magnet lens (HTFML) *J. Appl. Phys.* **127** 185106
[13] Namba S, Fujishiro H, Naito T, Ainslie M D and Takahashi K 2019 Experimental realization of a hybrid trapped field magnet lens using a GdBaCuO magnetic lens and MgB_2 bulk cylinder *Supercond. Sci. Technol.* **32** 12LT03
[14] Yin D-C 2015 Protein crystallization in a magnetic field *Prog. Cryst. Growth Charact. Mater.* **61** 1–26
[15] Kobayashi T, Mori T, Akiyama Y, Mishima F and Nishijima S 2017 Study on separation of structural isomer with magneto-Archimedes method *J. Phys.: Conf. Ser.* **897** 012018
[16] Miura O, Yamagishi K and Yamamoto D 2018 Magneto-Archimedes levitation of precious metals under a high magnetic field gradient *J. Phys.: Conf. Ser.* **1054** 012086
[17] Ren Y, Weinstein R, Liu J, Sawh R P and Foster C 1995 Damage caused by magnetic pressure at high trapped field in quasi-permanent magnets composed of melt-textured Y-Ba-Cu-O superconductor *Physica* C **251** 15–26
[18] Yanagi Y, Yoshikawa M, Itoh Y, Oka T, Ikuta H and Mizutani U 2004 Generation of extremely strong magnetic fields in open space by using metal-ring-reinforced 60 mmφ Sm-Ba-Cu-O superconducting bulk *Physica* C **412–414** 744–9
[19] Miyamoto T, Nagashima K, Sakai N and Murakami M 2000 Direct measurements of mechanical properties for large-grain bulk superconductors *Physica* C **340** 41–50
[20] Fujishiro H, Naito T, Yanagi Y, Itoh Y and Nakamura T 2019 Promising effects of a new *hat structure* and double metal ring for mechanical reinforcement of a REBaCuO ring-shaped bulk during field-cooled magnetization at 10T without fracture *Supercond. Sci. Technol.* **32** 065001
[21] Fujishiro H, Takahashi K, Naito T, Yanagi Y, Itoh Y and Nakamura T 2018 New proposal of mechanical reinforcement structures to annular REBaCuO bulk magnet for compact and cryogen-free NMR spectrometer *Physica* C **550** 52–56
[22] Jirsa M, Pust L, Dlouhý D and Koblischka M R 1997 Fishtail shape in the magnetic hysteresis loop for superconductors: interplay between different pinning mechanisms *Phys. Rev.* B **55** 3276–84
[23] Kii T *et al* 2012 Low-temperature operation of a bulk HTSC staggered array undulator *IEEE Trans. Appl. Supercond.* **22** 4100904

[24] Ikezoe Y, Kaihatsu T, Sakae D, Uetake H, Hirota N and Kitazawa K 2002 Separation of feeble magnetic particles with magneto-Archimedes levitation *Energy Convers. Manage.* **43** 417–25
[25] Ramachandran N and Leslie F W 2005 Using magnetic fields to control convection during protein crystallization-analysis and validation studies *J. Cryst. Growth* **274** 297–306
[26] Yan E-K, Zhang C-Y, He J and Yin D-C 2016 An overview of hardware for protein crystallization in a magnetic field *Int. J. Mol. Sci.* **17** 1906
[27] Zhao P, Xie J, Gu F, Sharmin N, Hall P and Fu J 2018 Separation of mixed waste plastics via magnetic levitation *Waste Manag.* **76** 46–54
[28] Mirica K A, Shevkoplyas S S, Phillips S T, Gupta M and Whitesides G M 2009 Measuring densities of solids and liquids using magnetic levitation: fundamentals *J. Am. Chem. Soc.* **131** 10049–58
[29] Tomita M and Murakami M 2003 High-temperature superconductor bulk magnets that can trap magnetic fields of over 17 Tesla at 29 K *Nature* **421** 517–20
[30] Namba S, Fujishiro H, Ainslie M D, Takahashi K, Namburi D K, Zhou D and Naito T 2019 Design optimization of a hybrid trapped field magnet lens (HTFML) *IEEE Trans. Appl. Supercond.* **29** 6801605
[31] Namba S, Fujishiro H, Naito T, Ainslie M D and Huang K Y 2019 Electromagnetic strain measurements and two-directional mechanical stress estimation for a REBaCuO ring bulk reinforced by a metal ring during field-cooled magnetization *Supercond. Sci. Technol.* **32** 125001
[32] Katagiri K, Murakami A, Shoji Y, Teshima H, Sawamura M, Iwamoto A, Mito T and Murakami M 2004 Tensile and bending mechanical properties of bulk superconductors at room temperature *Physica* C **412–414** 633–7
[33] Kan R, Katagiri K, Murakami A, Kasaba K, Shoji Y, Noto K, Sakai N and Murakami M 2004 Deformation and fracture behavior of SM123 bulk superconductors by compressive loading at room temperature *IEEE Trans. Appl. Supercond.* **14** 1114–7

10. (H-9) K. Takahashi, H. Fujishiro, S. Namba and M. D. Ainslie,
"Experimental realization of an all-(RE)BaCuO hybrid trapped field magnet lens generating a 9.8 T concentrated magnetic field from a 7 T external field",
Supercond. Sci. Technol. **34** (2021) 05LT02 (9 pages) (No. 284 paper)

OPEN ACCESS
IOP Publishing
Letters
Superconductor Science and Technology
Supercond. Sci. Technol. **34** (2021) 05LT02 (9pp)
https://doi.org/10.1088/1361-6668/abeb01

Letter

Experimental realization of an all-(RE)BaCuO hybrid trapped field magnet lens generating a 9.8 T concentrated magnetic field from a 7 T external field

Keita Takahashi[1,*], Hiroyuki Fujishiro[1], Sora Namba[1] and Mark D Ainslie[2]

[1] Department of Physical Science and Materials Engineering, Faculty of Science and Engineering, Iwate University, Morioka 020-8551, Japan
[2] Bulk Superconductivity Group, Department of Engineering, University of Cambridge, Cambridge CB2 1PZ, United Kingdom

E-mail: s3119004@iwate-u.ac.jp and fujishiro@iwate-u.ac.jp

Received 11 December 2020, revised 12 February 2021
Accepted for publication 1 March 2021
Published 19 March 2021

Abstract

In this work, we have verified experimentally an all-(RE)BaCuO hybrid trapped field magnet lens (HTFML) using only one cryocooler and a special technique named the 'loose contact method'. In the experimental setup, only the inner magnetic lens was tightly connected to the cold stage and cooled at all times, and the outer trapped field magnet (TFM) cylinder was loosely connected to the cold stage before the magnetizing process by introducing a gap between the outer TFM and cold stage of the cryocooler. As a result, the superconducting state for zero-field cooled magnetization of the inner magnetic lens and the non-superconducting (normal) state for field-cooled magnetization of the outer TFM cylinder can co-exist at the same time. A maximum concentrated field of $B_c = 9.8$ T was achieved for the magnetizing process with an applied field of $B_{app} = 7$ T in the present HTFML, consistent with the numerical estimation in our previous conceptual study. These results validate the HTFML concept as a compact and desktop-type magnet device that can provide 10 T-class magnetic field enhancement from the viewpoint of the magnetizing method. However, during magnetization with a higher B_{app} of 10 T, thermal instability of the outer stacked TFM cylinder caused flux jumps to occur, resulting in mechanical fracture of multiple bulks. These results suggest that the further development of a practical cooling method that can realize a stable and controllable

* Author to whom any correspondence should be addressed.

cooling process for each part of the HTFML is necessary based on fundamental studies relating to the thermal stability of the large stacked TFM cylinder.

Keywords: hybrid trapped field magnet lens, bulk superconductors, trapped field magnets, magnetic lens, vortex pinning effect, magnetic shielding effect, loose contact method

(Some figures may appear in colour only in the online journal)

1. Introduction

To provide a higher magnetic field in more cost-effective way, large single-grain bulk superconductors such as the (RE)BaCuO (RE: rare earth elements or Y) family of materials are known to be a promising for generating magnetic fields of several Tesla or more as so-called trapped field magnets (TFMs). This TFM can provide the trapped field quasi-permanently without any additional current source once it is magnetized by exploiting the 'vortex pinning effect', and only needs to be cooled below a superconducting transition temperature, T_c. To date, the highest trapped field of $B_T = 17.6$ T has been achieved in a two-stack GdBaCuO bulk pair magnetized by field-cooled magnetization (FCM) [1, 2]. According to Bean's critical state model, where the critical current density of the bulk, J_c, is assumed to be field-independent, the trapped field of a disc-shaped TFM by FCM increases in proportional to its diameter and J_c. Hence, many of conventional approaches for the trapped field enhancement have focused on the crystallization process, resulting in a higher and uniform J_c of the bulk material [3, 4]. In this sense, it is expected that these compact and strong bulk magnets would replace a conventional magnetic field source in applications such as rotating machines [5], Lorentz force velocimetry [6] and nuclear magnetic resonance apparatus [7]. On the other hand, the magnetic lens utilizing the same bulk material exploits its 'diamagnetic shielding effect' nature to concentrate a magnetic field from an external coil magnet. Zhang *et al* achieved a concentrated field of $B_c = 13$ T at 20 K using a GdBaCuO bulk lens by zero-field cooled magnetization (ZFCM) with an external applied field of 7 T [8].

In 2018, the authors proposed a new concept of a hybrid TFM lens (HTFML), in which the inner bulk magnetic lens can concentrate the trapped field provided from the outer TFM cylinder, resulting in a concentrated trapped field higher than the external magnetizing field required for magnetization that persists even after removal of the external field [9]. In the paper, a higher trapped field of $B_c = 13.49$ T was predicted at 20 K for the applied field of $B_{app} = 10$ T using inner (RE)BaCuO lens and the outer (RE)BaCuO TFM cylinder, and $B_c = 4.73$ T was predicted at 20 K for $B_{app} = 3$ T using inner (RE)BaCuO lens and the outer MgB_2 TFM cylinder. This concept was first verified experimentally using different bulk materials, i.e. an inner GdBaCuO lens ($T_c = 92$ K) and an outer MgB_2 TFM cylinder ($T_c = 39$ K) and exploiting the difference in T_c. For this design, a maximum concentrated field of $B_c = 3.55$ T was achieved reliably with an applied field of $B_{app} = 2$ T at 20 K [10]. In the case of the HTFML using an inner (RE)BaCuO lens and outer (RE)BaCuO cylinder, a special technique must be used to control the temperature of each bulk part individually, such as the use of two cryocoolers, a thermal (heater) method or a mechanical switch [11]. Hence, the magnetizing sequence of the HTFML includes two magnetizing methods: ZFCM for the inner magnetic lens and FCM for the outer TFM cylinder. As a first step, we have realized the HTFML based on the same (RE)BaCuO bulk material for both parts using liquid nitrogen, in which the inner magnetic lens and outer TFM cylinder were housed in separate containers with liquid nitrogen poured into each container sequentially according to the corresponding magnetizing sequence. As a result, $B_c = 1.83$ T was obtained at 77 K after magnetization with $B_{app} = 1.80$ T [12]. However, to best exploit the trapped field capability of the outer (RE)BaCuO cylinder and realize a higher B_c over 10 T, the all-(RE)BaCuO HTFML should be cooled to a lower temperature below 50 K and magnetized, where the $J_c(B, T)$ characteristics have a higher value under higher magnetic fields. Furthermore, if the HTFML device can be realized using one cold stage of a cryocooler, the whole system would be more cost-effective, and provide both a higher magnetic field and magnetic field gradient in an open bore space outside the vacuum chamber [13].

In this work, we have verified experimentally an all-(RE)BaCuO HTFML magnetized under 50 K using only one cryocooler by a special technique, in which only the inner magnetic lens was tightly connected to the cold stage and cooled at all times, and the outer TFM cylinder was loosely connected to the cold stage before the magnetizing process by introducing a gap between the outer TFM cylinder and cold stage. During the cooling process before magnetization, the outer TFM cylinder then cooled much slower than the inner magnetic lens. As a result, the non-superconducting (normal) state for the outer TFM cylinder and the superconducting state for the inner magnetic lens can be simultaneously realized. A maximum concentrated field of $B_c = 9.8$ T was achieved for the magnetizing process from $B_{app} = 7$ T in the present HTFML, consistent with the numerical estimation in our previous conceptual study [9]. The concentrated field values are compared for other HTFML devices reported. These results validate the HTFML as a compact and desktop-type magnet device that can provide 10 T-class magnetic field enhancement from the viewpoint of the magnetizing method.

2. Experimental setup and magnetizing sequence

Figure 1(a) presents the experimental setup of the HTFML, in which the inner magnetic lens and the outer TFM cylinder are encapsulated in a stainless steel (SS) holder for mechanical

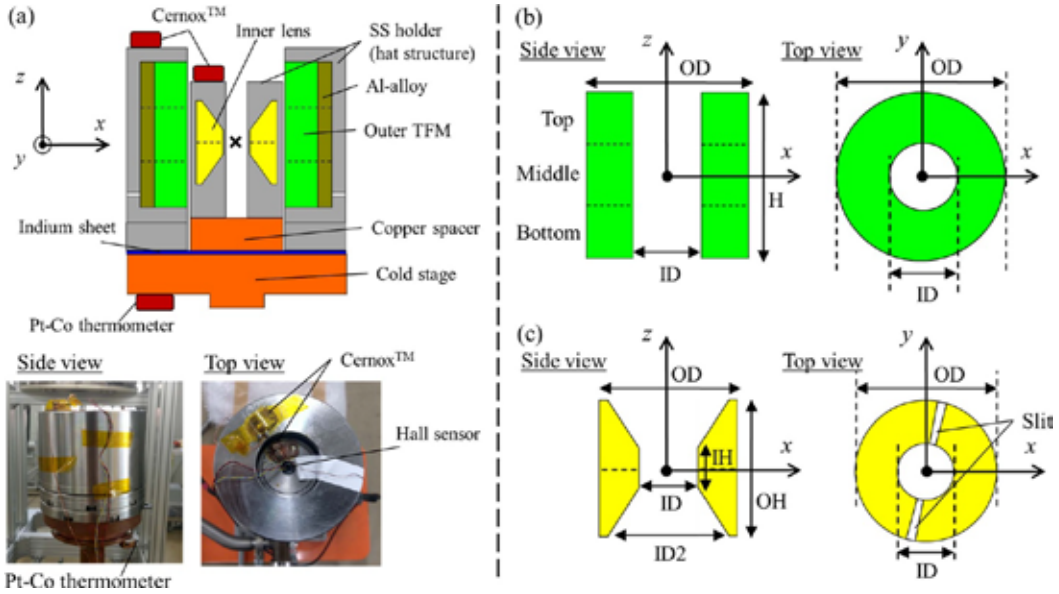

Figure 1. (a) Experimental setup of the HTFML, in which the inner magnetic lens and outer TFM cylinder, both made from (RE)BaCuO, are encapsulated in a stainless steel (SS) holder for mechanical reinforcement. The side and top views of the actual setup are also presented in the photographs. Schematic views of (b) the outer TFM cylinder and (c) the inner magnetic lens.

reinforcement. Side and top views of the actual setup are also presented in the photographs. Figures 1(b) and (c), respectively, show the side and top views of each bulk component of the outer TFM cylinder and the inner magnetic lens. All of the bulks were fabricated by the QMG^{TM} method (Nippon Steel Corporation, Japan) [14]. The outer TFM cylinder was constructed using three stacked EuBaCuO ring bulks (top bulk, middle bulk and bottom bulk). The dimensions of the EuBaCuO cylinder are a 60 mm outer diameter (OD), 36 mm inner diameter (ID) and 54 mm height (H). Each of the EuBaCuO ring bulks was reinforced by an Al alloy ring 5 mm in thickness (OD = 70 mm, ID = 60 mm) adhered by a thin layer of epoxy resin. These bulks were also encapsulated in the SS holder with a 'hat structure' 5 mm in thickness for mechanical reinforcement against the Lorentz force generated during magnetization. Such mechanical reinforcement is necessary to avoid fracture of the bulks, particularly for applied fields as high as 10 T. The effect of the 'hat structure' of the outer SS holder on the mechanical reinforcement was investigated by numerical simulation, which can provide a compressive stress around 100 MPa from the cooling process due to the difference in the thermal expansion coefficient between the bulk material and SS holder [15]. The effect was experimentally confirmed to avoid fracture of a ring bulk for FCM from $B_{app} = 10$ T in [16]. As shown in figure 1(c), the inner magnetic lens (OD = 36 mm, ID = 10 mm, ID2 = 26 mm, IH = 8 mm, OH = 30 mm) was constructed using two pieces of conical-shaped GdBaCuO bulks, in which a slit with 200 μm width is inserted in the diagonal direction so that the magnetic flux can be concentrated into the central bore through the slit. The TFM cylinder and magnetic lens are the same used in the previous experiment at 77 K [12]. Note that only the inner lens component, including the SS holder and a copper spacer, was tightly connected to the cold stage through a thin indium sheet. The temperature of the TFM cylinder, magnetic lens and the cold stage of the GM-cycle helium cryocooler was monitored by two Cernox^{TM} thermometers and a Pt–Co thermometer, as shown in figure 1(a). The whole device was enclosed in a vacuum chamber. A cryocooled 10 T superconducting magnet (JASTEC, JMTD-10T100) was utilized to ramp up/down the external magnetizing field. The concentrated field was monitored at the center of the lens by an axial-type Hall sensor (F.W. Bell, BHA921), and the external magnetic field was calculated by measuring the electric current through a shunt resistor.

Figure 2 shows the time sequence of the temperature for both bulk parts—the inner magnetic lens, T_L, and the outer TFM cylinder, T_T—and the external field, B_{ex}, and the concentrated magnetic field, B_c, at the center of the HTFML, which has been revised for these experiments in comparison to the original conceptual study [9]. To delay the cooling rate of the outer TFM cylinder quasi-independently even using one cold stage of the cryocooler, a special technique named the 'loose contact method' has been designed. Figure 3 shows the conceptual view of the 'loose contact method', exploiting two kinds of experimental configurations of the HTFML in the vacuum chamber, aligned in (a) the horizontal direction during the cooling process and (b) the vertical direction during magnetizing process. In the initial preparation of the experimental setup of the HTFML on the cold stage, the outer TFM cylinder was loosely connected to the cold stage—with a 1 mm gap—by screws and then installed in the vacuum chamber. During

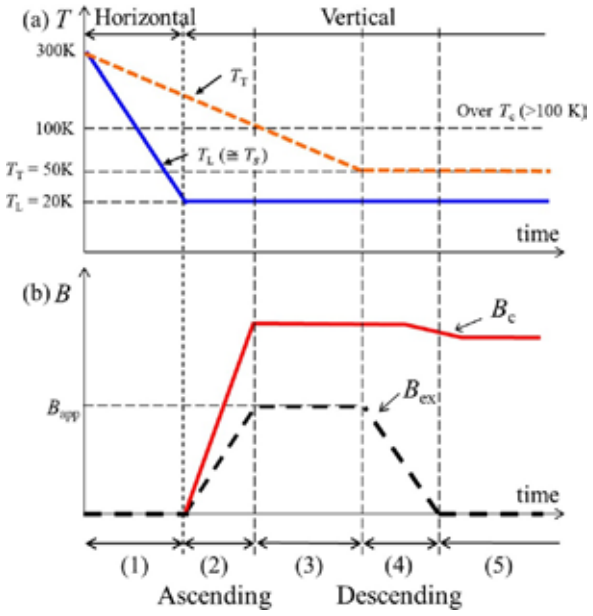

Figure 2. Time sequence of (a) the temperature T (the outer TFM cylinder, T_T, and the inner magnetic lens, T_L) and (b) the magnetic field B (external field, B_{ex}, and concentrated magnetic field, B_c at the center of the present HTFML using all-(RE)BaCuO bulks) during the magnetizing process divided into steps from (1) to (5). The magnetizing applied field, B_{app}, corresponds to the maximum value of B_{ex}.

the cooling stage of (1) in figure 2, the cooling process was started, and several hours later, the whole HTFML device was tilted 90° along the horizontal direction using a hand-held rod attached to the bottom of the apparatus. In this stage, as shown in figure 3(a), a non-uniform gap, i.e. 0–1 mm, was introduced at the interface between the TFM cylinder and the cold stage due to its own weight. This method worked sufficiently as to delay the cooling rate of the TFM cylinder in contrast to that of the inner magnetic lens, which is connected to the stage tightly without a gap. Before proceeding to the magnetization in the ascending stage of (2) in figure 2, the whole HTFML device was aligned vertically, where the gap between the TFM cylinder and the cold stage would be ≅0 mm and the TFM cylinder would contact loosely with the cold stage by its own weight, as shown in figure 3(b). At stage (2), the inner magnetic lens is in the superconducting state ($T_L < T_c$) and ZFCM is performed, but the outer TFM cylinder must be in the normal state ($T_T > T_c$). As mentioned before, the inner lens component was tightly connected to the cold stage and the temperature can be precisely controlled. In the magnetizing process, the whole HTFML device in the vacuum chamber was lifted up and inserted into the bore of the superconducting magnet as shown in figure 3(c).

In figure 2, the magnetizing applied field, B_{app}, corresponds to the maximum value of B_{ex}. The magnetizing sequence was constructed from the following process from (1) to (5), which is special for the HTFML exploiting the gap for the outer TFM cylinder.

(1) During the cooling process, where the whole HTFML device is aligned in the horizontal direction: the temperature of the inner magnet lens, T_L, (as well as that of the cold stage, T_s) is lowered from 300 K to the lowest temperature as possible (roughly, a minimum of $T_L \cong 20$ K in the present experiment). At the end of this stage, the inner magnet lens is in the superconducting state, but the outer TFM cylinder is in the normal state ($>T_c$) due to its delayed cooling speed.
(2) Ascending stage of the magnetizing process (while the cooling process proceeds), where the whole HTFML device is stood upright and aligned in the vertical direction, and then inserted in the superconducting magnet: the external magnetic field, B_{ex}, is ramped up linearly to B_{app} at a certain rate (+0.1 T min^{-1}. in the present experiment), which corresponds to the ascending stage of ZFCM for the inner magnetic lens. The magnetic field is concentrated in the bore of the magnetic lens, which would be higher than B_{app} because of the shielding effect by the magnetic lens. The temperature of the outer TFM cylinder should be kept over T_c until B_{app} completely penetrates the outer TFM cylinder. It is desirable that the difference in temperature between the outer TFM cylinder, T_T, and T_L, ΔT ($=T_T - T_L$), be over 50–100 K just before magnetization, which enables the separation of the magnetization processes of ZFCM for the magnetic lens and FCM for the TFM cylinder in the later stage.
(3) Cooling process in a static magnetic field: T_T is then decreased gradually to the lowest $T_T \cong 50$ K, below T_c but higher than T_L, due to the imperfect thermal contact to the cold stage through the gap ≅0 mm. The B_c value can be maintained reliably if T_L is kept at 20 K.
(4) Descending stage of the magnetizing process at the lowest temperature: B_{ex} is decreased linearly down to zero at a certain rate (−0.1 T min^{-1}, or −0.002 T min^{-1}. for higher B_{app} over 7 T, in the present study). During this process, the outer TFM cylinder is magnetized by FCM and a magnetic field is trapped inside the TFM cylinder within its trapped field capability based on its $J_c(B, T)$ characteristics (if this can be done successfully without the occurrence of large flux jumps caused by the resultant heat generation and/or mechanical fracture of the bulk material).
(5) As a result, the HTFML can reliably generate B_c higher than the trapped field of the single cylindrical TFM, as well as B_{app}, even after $B_{ex} = 0$.

Figure 4 shows the typical experimental results for the cooling process of the present HTFML exploiting the 'loose contact method', in which the HTFML device set in the vacuum chamber was reclined up after $t = +11$ h, from the horizontal direction to the vertical direction. The maximum $\Delta T \cong 100$ K was obtained at $t = +8$ h after beginning the cooling process.

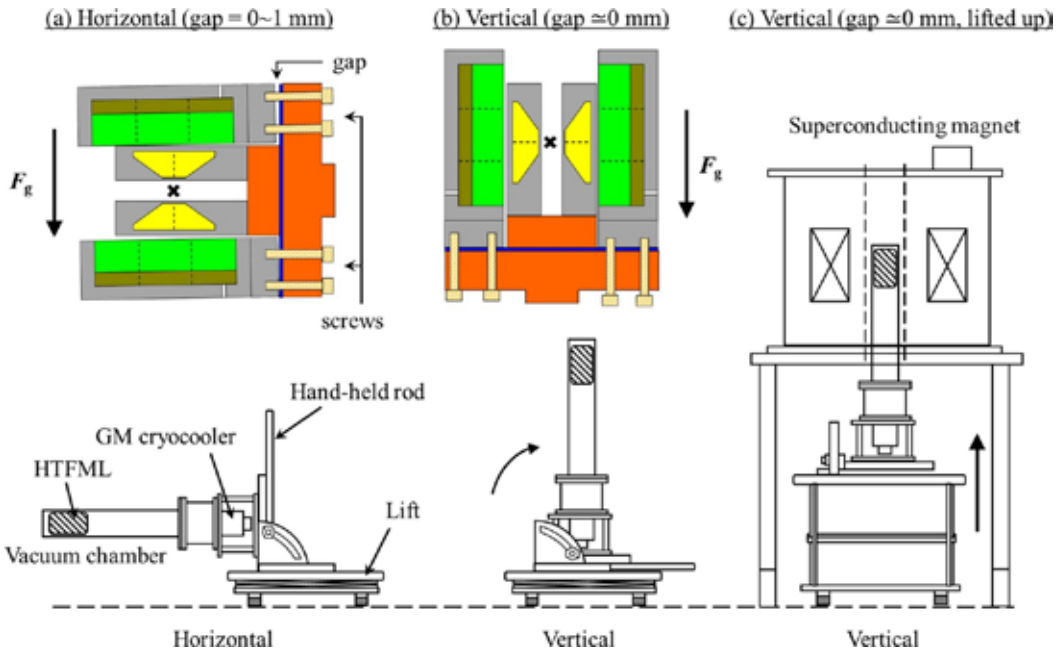

Figure 3. Conceptual view of the 'loose contact method', exploiting two kinds of experimental configurations of the HTFML in the vacuum chamber, aligned in (a) the horizontal direction during the cooling process and (b) the vertical direction during magnetizing process. (c) The whole HTFML device in the vacuum chamber lifted up and inserted into the bore of the superconducting magnet in the magnetizing process.

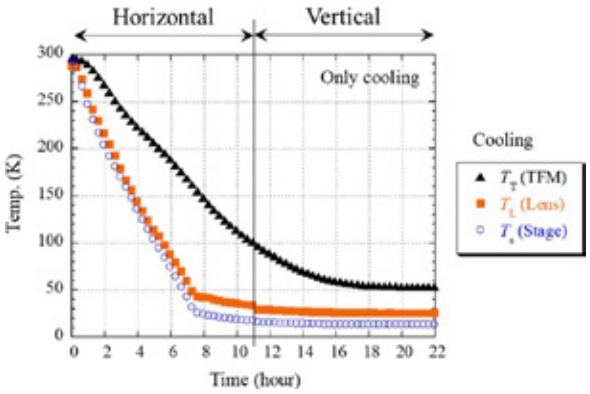

Figure 4. Typical experimental results of cooling process of the present HTFML exploiting the 'loose contact method', in which the HTFML device set in the vacuum chamber was reclined up at $t = +11$ h from the horizontal direction to the vertical direction.

It was also confirmed that ΔT would change depending on the degree of inhomogeneous contact through the gap. The lowest temperatures were $T_T = 54$ K, $T_L = 24$ K and $T_s = 14$ K for each point on the outer TFM cylinder, inner magnetic lens and under the cold stage, respectively.

3. Experimental results

Figure 5 shows the time dependence of the temperatures measured at each position—the inner magnetic lens, T_L, the outer TFM cylinder, T_T, and the cold stage, T_s—and the concentrated field, B_c, and the external field, B_{ex}, during magnetization with several applied fields, B_{app}, of (a) 3 T, (b) 5 T and (c) 7 T, respectively. The lowest value of T_L and T_T for magnetization process is included in the bottom panel of each figure. In the case of $B_{app} = 3$ T, as shown in figure 5(a), the B_{ex} value was ramped up at $t = +8.5$ h, when the maximum temperature difference $\Delta T \geqslant 100$ K was obtained reliably after cooling to $T_L = 40$ K and $T_T = 150$ K. The lowest temperatures were, respectively, $T_L = 24$ K for ZFCM and $T_L = 57$ K for FCM. Resultantly, $B_c = 5.5$ T was achieved with little flux creep caused by the non-linear electrical property of the bulk material, even well after FCM process at $t = +24$ h. Compared with the higher B_{app} cases of 5 T and 7 T, as shown in figures 5(b) and (c), it was confirmed that the ΔT value varied in the range of 50–100 K, and the lowest temperatures of T_L and T_T were not consistent because the non-uniform thermal contact through the gap during the initial cooling stage is not controllable precisely. It is also noteworthy that the present system does not require the precise adjustment of the temperature, but only needs the outer TFM cylinder to be kept above its T_c until the ascending stage of ZFCM for the inner magnetic lens is completed. Higher B_c values of 7.9 T and 9.8 T were achieved for $B_{app} = 5$ T and 7 T, respectively. These experimental results successfully verified the numerical estimations for the 10 T-class HTFML, up to $B_{app} = 7$ T, for the first time [9]. These values will be compared with conventional HTFMLs at the end of this section. It should be noted that the experimental T_T value was not constant and gradually increased due to the heat generation caused by the movement

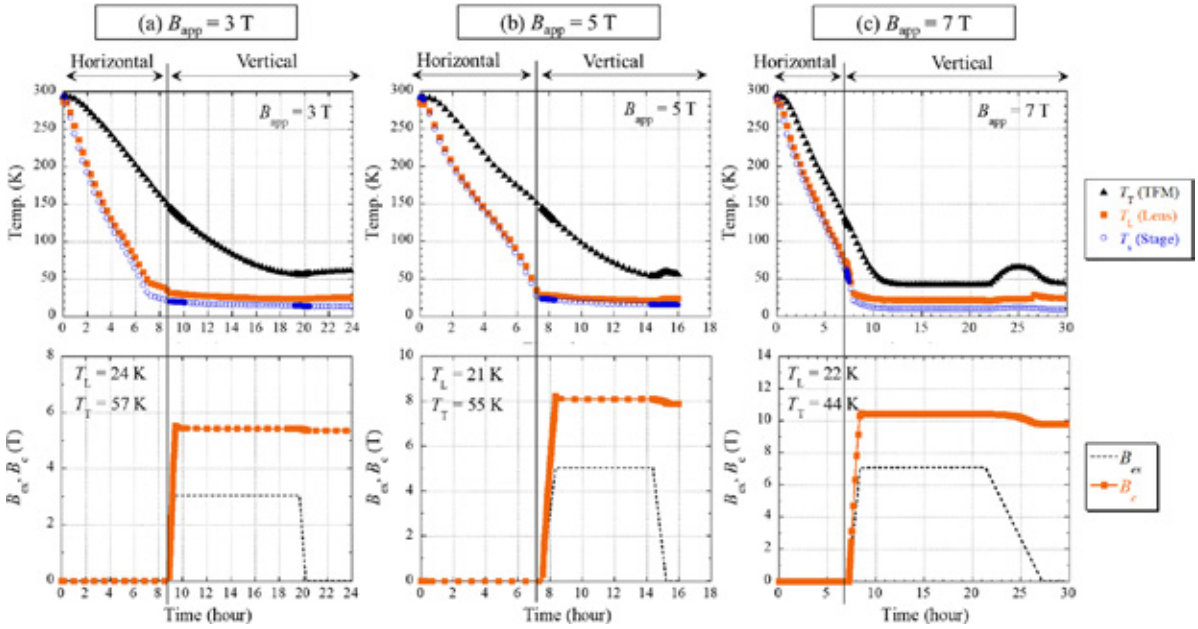

Figure 5. Time dependence of the temperatures measured at each position—the outer TFM cylinder, T_T, the inner magnetic lens, T_L, and the cold stage, T_s—and the concentrated field, B_c, and the external field, B_{ex}, during magnetization with several applied fields, B_{app}, of (a) 3 T, (b) 5 T and (c) 7 T, respectively.

of magnetic flux during FCM of the outer TFM cylinder, which was remarkably large for higher B_{app}. This thermal instability might come from the possibility of larger heat generation in the stacked TFM cylinder, as well as the slower cooling speed and efficiency of the loose contact method in the present setup.

Figures 6(a) and (b), respectively, show similar results of the time dependence of the temperature and magnetic field during magnetization with an applied field of $B_{app} = 10$ T. During the ZFCM process until $t = +14$ h, $B_c = 13.9$ T was generated at the center of the HTFML device with a background field of $B_{ex} = 10$ T, which means that the maximum of B_c might be over 13 T, if the outer TFM cylinder could replace external magnetizing magnet after the FCM process. Unfortunately, during the descending stage of the FCM process, the T_T value increased and stayed as high as 68 K, and then the B_c value suddenly dropped at $B_{ex} = 5$ T due to the occurrence of a large flux jump at $t = +18$ h, at which the temperatures also abruptly increased to above T_c. After that, the B_c gradually decreased with decreasing B_{ex} and the final B_c value became negative. Such a negative B_c value is typically obtained in the case for the single magnetic lens, in which the magnetic flux is trapped in a part of magnetic lens after completing the conventional ZFCM process [8]. These results indicate that the thermal instability of the outer TFM cylinder could result in a flux jump during FCM and/or the mechanical fracture of the bulk material. To realize a B_c value over 10 T, further investigations are required relating to the following issues: thermal stability of the large, stacked TFM cylinder, and development of a more practical cooling method that can achieve a stable and controllable cooling process for each part of HTFML.

Figure 7 summarizes the magnetization curves of the HTFML magnetized from $B_{app} = 3$, 5, 7 and 10 T, which can compare the difference of the lens effect during the ascending stage, and the flux creep and the final B_c value in the descending stage. In the ascending stage, for every B_{app} value, the $B_c - B_{ex}$ relation shows an identical trend, which indicates the good reliability of the shielding effect by the magnetic lens. However, in the descending stage for B_{app} values of 7 T and 10 T, the flux creep seems clearly due to the large temperature rise during FCM (up to 68 K) in the stacked TFM cylinder. In the case of $B_{app} = 10$ T, a flux jump occurred during the descending stage that may be of mechanical or thermal nature, which will be discussed later. If this flux jump did not occur under a constant and stable temperature during magnetization from $B_{app} = 10$ T, it is expected that $B_c = 13$ T would be achieved.

To find out whether mechanical fracture occurred after the magnetization of the HTFML from $B_{app} = 10$ T, the inner magnetic lens and outer TFM cylinder were magnetized separately again. Figure 8 shows the magnetization curve of the magnetic lens by itself during the ascending stage of ZFCM with $B_{app} = 3$ T and $T_L = 30$ K, after the occurrence of the flux jump during the magnetization of the HTFML from $B_{app} = 10$ T (labeled 'After'). A similar result before the flux jump is shown for comparison (labeled 'Before'; see figure 5(a)). The measured B_c was enhanced (with respect to B_{ex}) by the magnetic lens and increased in proportional to B_{ex}, consistent with the 'Before' results. This result clearly shows that there was no fracture in the inner magnetic lens after the flux jump.

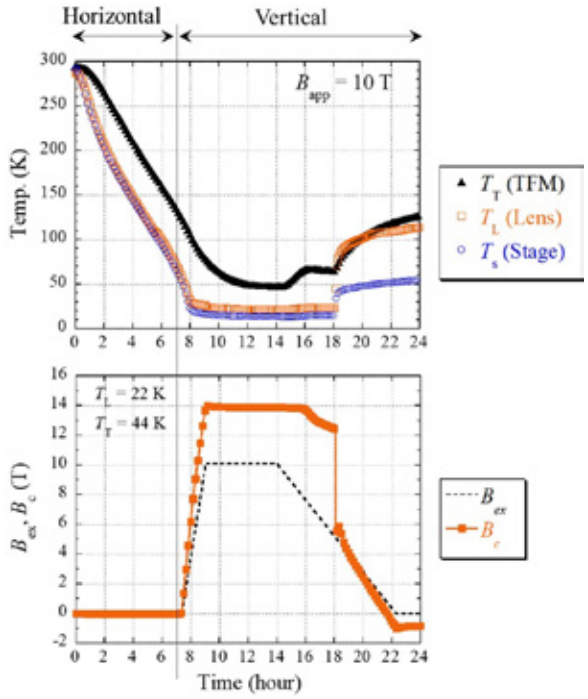

Figure 6. Time dependence of the temperatures measured at each position—the outer TFM cylinder, T_T, the inner magnetic lens, T_L, and the cold stage, T_s—and the concentrated field, B_c, and the external field, B_{ex}, during magnetization with an applied field, $B_{app} = 10$ T.

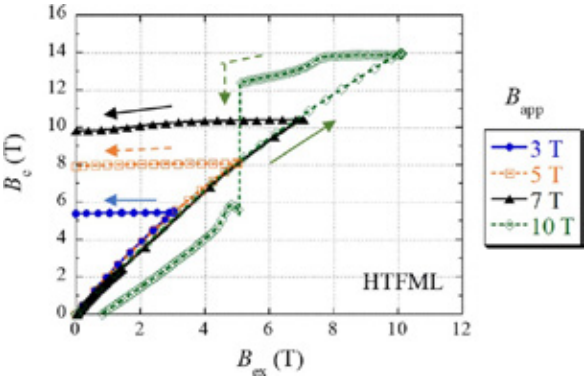

Figure 7. Magnetization curves of the HTFML magnetized with applied fields, $B_{app} = 3$, 5, 7 and 10 T. The lens effect during the ascending stage, and the flux creep and the final trapped field in the descending stage are compared.

Figure 9 shows the trapped field profiles for the (a) top surfaces and (b) bottom surfaces of each TFM ring bulk (top bulk, middle bulk, and bottom bulk), magnetized by FCM from $B_{app} = 1$ T in liquid nitrogen after the flux jump, in which the trapped field value was measured 3 mm above the surfaces of each ring bulk. Photographs of each bulk were also taken after the measurement. The fracture point can be seen in the

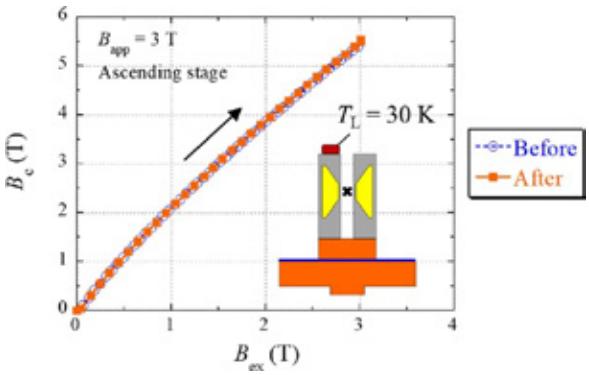

Figure 8. Magnetization curve of the single magnetic lens during the ascending stage of ZFCM with the applied field of $B_{app} = 3$ T, after the happening of the flux jump during the magnetization of the HTFML from $B_{app} = 10$ T, labeled as 'After'. The result before the flux jump is referred as 'Before' from figure 5(a).

top surface view of the bottom bulk, in which the crack penetrates along the 10 o'clock direction as depicted. In addition, it was confirmed that there is an identical trace of burning at the interface between the top surface of the bottom bulk and the bottom surface of the middle bulk, as marked in each picture. The degree of fracture behavior was determined from the results of the trapped field profile into three-levels: not broken (top bulk), partially broken (middle bulk), and completely broken (bottom bulk), respectively. The bottom bulk, in which the crack destroyed the circumferential current, showed the so-called 'C-shaped' magnetic field profile on both surfaces of the bulk and there is no longer the remnant trapped field inside the central region, i.e. $B_T = 0$ T. In contrast, only the top bulk showed a comparative, uniform field profile with a peak value of $B_T = \pm 0.32$ T at the center of both surfaces. This profile might deserve to be described as 'not broken'. In the middle bulk, evaluated as 'partially broken', the bulk showed an inhomogeneous trapped field profile that is not identical for each surface, and the trapped magnetic field is as small as $B_T = \pm 0.02$ T at the center. These results offer evidence that the thermal instability of the stacked TFM cylinder caused a flux jump during the FCM process, which resulted in the mechanical fracture of multiple bulks at the same time, even though the mechanical reinforcement using the SS support with the 'hat structure' was applied. It is therefore recommended that the stacked bulk cylinder should be kept at a constant temperature with adequate cooling to avoid flux jumps when it is magnetized with higher $B_{app} \cong 10$ T. In this sense, fundamental studies related to the suppression of the thermal instability of the HTFML should be performed in more detail.

Finally, figure 10 summarizes the concentrated field, B_c, at the center of the HTFML, as a function of B_{app}, compared with previously reported experimental results [10, 12]. Since 2018, the feasibility of the HTFML has been proved particularly for lower B_{app} up to 3 T for two cases: (a) exploiting an inner GdBaCuO bulk lens and outer MgB_2 TFM cylinder, in which a maximum concentrated field of $B_c = 3.55$ T was achieved for $B_{app} = 2$ T at 20 K, and (b) replacing the outer

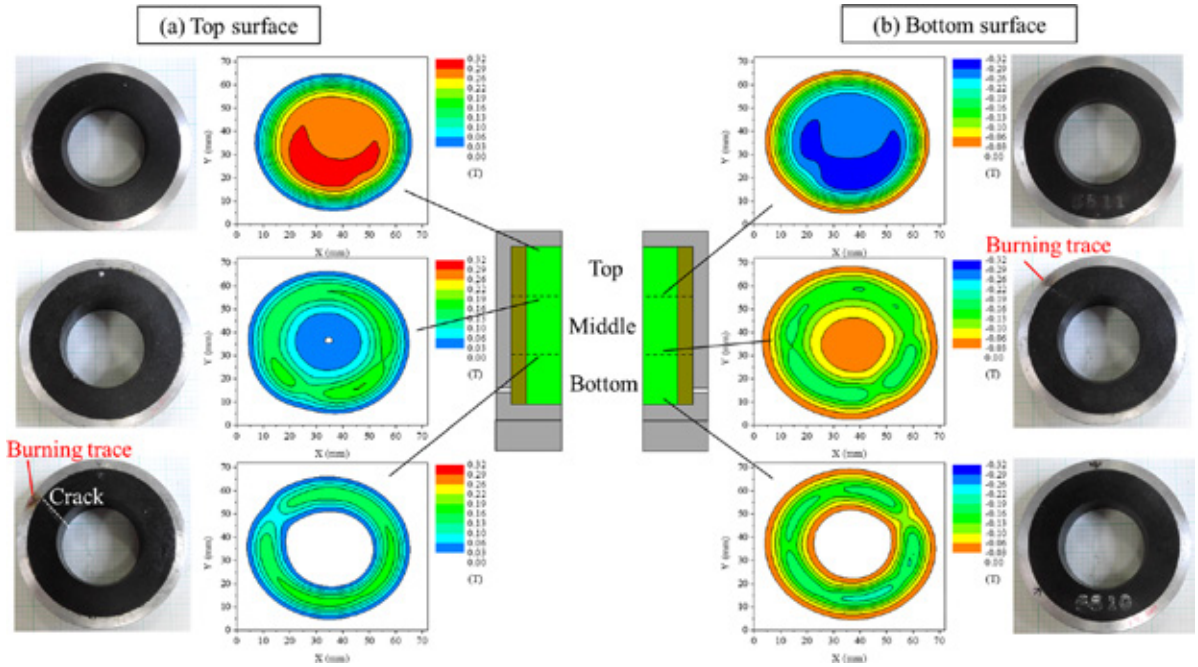

Figure 9. Trapped field profiles for (a) the top and (b) the bottom surface of each TFM ring bulk (top bulk, middle bulk, and bottom bulk), magnetized by FCM with the applied field of $B_{app} = 1$ T in liquid nitrogen after the happening of the flux jump. The trapped field value was measured 3 mm above the surfaces. Photographs of each bulk were also taken after the measurement.

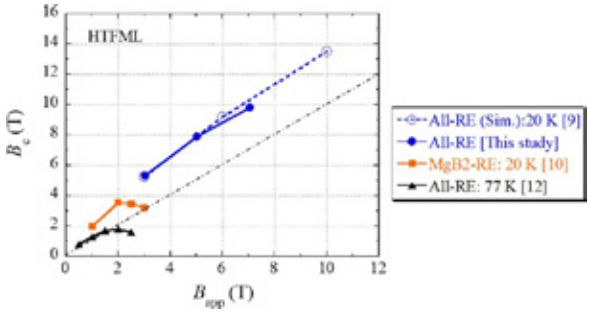

Figure 10. The concentrated field, B_c, at the center of the HTFML (labelled 'All-RE [This study]'), as a function of B_{app}, compared with previously reported experimental results. In the previous experiments, the HTFMLs were constructed with the combination of an outer MgB_2 TFM cylinder and inner GdBaCuO magnetic lens (labeled 'MgB_2-RE: 20 K') [10], as well as an all-(RE)BaCuO design at 77 K (labeled 'All-RE: 77 K') [12]. The numerical estimations for the HTFML with all-(RE)BaCuO bulks are also included (labeled 'All-RE (Sim.): 20 K') [9].

MgB_2 cylinder with an EuBaCuO one, in which $B_c = 1.83$ T was achieved for $B_{app} = 1.80$ T at 77 K. However, these configurations are not appropriate for magnetization with higher B_{app} over 3 T, because of (a) the inferior $J_c(B, T)$ characteristics of the MgB_2 bulk and (b) the operating temperature of 77 K. An original concept of the HTFML that could generate over $B_c = 10$ T requires that both the inner and outer (RE)BaCuO bulks are utilized at lower temperatures below 50 K [9]. In this study, the HTFML exploiting the 'loose contact method' using one cold stage of a cryocooler realized such a realistic configuration which could work in a range of B_{app} from 3 T to 7 T. A maximum $B_c = 9.8$ T value was achieved successfully when magnetizing with $B_{app} = 7$ T, although the flux creep was larger compared to that of lower B_{app} values. The $B_c - B_{app}$ relation obtained from this experiment is consistent with our numerical estimations (indicated by the dotted line), but not for higher B_{app} due to the larger flux creep for B_{app} over 7 T and the mechanical fracture of the bulk materials over 10 T. This issue would be resolved by use of a more practical cooling method that can provide proper individual cooling of each part of the HTFML using one (or two) cold stages, combined with a switch that would work based on its thermal property and/or mechanical function. Furthermore, fundamental studies to understand and improve the thermal and mechanical stability of the stacked TFM cylinder during its magnetization would have an important role in improving the practical design of the HTFML.

4. Conclusion

We have verified experimentally an all-(RE)BaCuO HTFML magnetized under 50 K, using only one cryocooler and a special technique named the 'loose contact method', where the outer TFM was loosely connected to the cold stage before magnetizing process by introducing a gap between the cold stage. A maximum concentrated field of $B_c = 9.8$ T was achieved after magnetization with an applied field of

$B_{app} = 7$ T, which is twice as superior as the other HTFML devices to date. The experimental B_c values, as a function of B_{app}, were consistent with the numerical estimation reported in our previous conceptual study. These results validate the HTFML concept as a compact and desktop-type magnet device that can provide 10 T-class magnetic field enhancement from the viewpoint of the magnetizing method.

However, during magnetization with a higher B_{app} of 10 T, the B_c value suddenly dropped due to the occurrence of a large flux jump that resulted in the mechanical fracture of the bottom bulk in the stacked TFM cylinder, even though mechanical reinforcement using the SS support with the 'hat structure' was applied. If the flux jump did not occur during magnetization from $B_{app} = 10$ T, it is predicted that $B_c = 13$ T would be achieved. To realize a B_c value of over 10 T, further investigations are needed relating to the thermal stability of the stacked TFM cylinder and the development of a more practical cooling method that can achieve a stable and controllable cooling process for each part of HTFML.

Acknowledgments

The authors thank Mr Y Yanagi of IMRA Material R&D Co., Ltd, Japan, and Mr Y Takeda of Iwate University for their valuable experimental supports. This research is supported by JSPS KAKENHI Grant No. 19K05240, and by Adaptable and Seamless Technology transfer Program through Target-driven R&D (A-STEP) from Japan Science and Technology Agency (JST), Grant Nos. VP30218088419 and JPMJTM20AK. M D Ainslie would like to acknowledge financial support from an Engineering and Physical Sciences Research Council (EPSRC) Early Career Fellowship, EP/P020313/1. All data are provided in full in the results section of this paper.

ORCID iDs

Keita Takahashi https://orcid.org/0000-0002-8278-2688
Hiroyuki Fujishiro https://orcid.org/0000-0003-1483-835X
Sora Namba https://orcid.org/0000-0001-7268-5326
Mark D Ainslie https://orcid.org/0000-0003-0466-3680

References

[1] Durrell J H, Ainslie M D, Zhou D, Vanderbemden P, Bradshaw T, Speller S, Filipenko M and Cardwell D A 2018 Bulk superconductors: a roadmap to applications *Supercond. Sci. Technol.* **31** 103501

[2] Durrell J H *et al* 2014 A trapped field of 17.6 T in melt-processed, bulk Gd–Ba–Cu–O reinforced with shrink-fit steel *Supercond. Sci. Technol.* **27** 082001

[3] Zhai W, Shi Y-H, Durrell J H, Dennis A R, Zhang Z and Cardwell D A 2015 Processing and properties of bulk Y–Ba–Cu–O superconductors fabricated by top seeded melt growth from precursor pellets containing a graded CeO_2 composition *Cryst. Growth Des.* **15** 907–14

[4] Namburi D K, Shi Y-H, Zhai W, Dennis A R, Durrell J H and Cardwell D A 2015 Buffer pellets for high-yield, top-seeded melt growth of large grain Y–Ba–Cu–O superconductors *Cryst. Growth Des.* **15** 1472–80

[5] Zhang Y, Zhou D, Ida T, Miki M and Izumi M 2016 Melt-growth bulk superconductors and application to an axial-gap-type rotating machine *Supercond. Sci. Technol.* **29** 044005

[6] Vakaliuk O V, Ainslie M D and Halbedel B 2018 Lorentz force velocimetry using a bulk HTS magnet system: proof-of-concept *Supercond. Sci. Technol.* **31** 084003

[7] Ogawa K, Nakamura T, Terada Y, Kose K and Haishi T 2011 Development of a magnetic resonance microscope using a high T_c bulk superconducting magnet *Appl. Phys. Lett.* **98** 234101

[8] Zhang Z Y, Matsumoto S, Teranishi R and Kiyoshi T 2013 Improving the properties of GdBaCuO magnetic lenses by adopting a new design and resin impregnation *Supercond. Sci. Technol.* **26** 045001

[9] Takahashi K, Fujishiro H and Ainslie M D 2018 A new concept of a hybrid trapped field magnet lens *Supercond. Sci. Technol.* **31** 044005

[10] Namba S, Fujishiro H, Naito T, Ainslie M D and Takahashi K 2019 Experimental realization of a hybrid trapped field magnet lens using a GdBaCuO magnetic lens and MgB_2 bulk cylinder *Supercond. Sci. Technol.* **32** 12LT03

[11] Li M, Li L and Xu D 2017 A mechanical thermal switch for conduction-cooled cryogenic system *J. Phys. Conf. Ser.* **897** 012016

[12] Namba S, Fujishiro H, Hirano T, Naito T and Ainslie M D 2020 Optimized performance of an all-REBaCuO hybrid trapped field magnet lens (HTFML) with liquid nitrogen cooling *Physica* C **575** 1353690

[13] Takahashi K, Fujishiro H and Ainslie M D 2020 Simulation study for magnetic levitation in pure water exploiting the ultra-high magnetic field gradient product of a hybrid trapped field magnet lens (HTFML) *J. Appl. Phys.* **127** 185106

[14] Morita M, Sawamura M, Takebayashi S, Kimura K, Teshima H, Tanaka M, Miyamoto K and Hashimoto M 1994 Processing and properties of QMG materials *Physica* C **235–240** 209–12

[15] Fujishiro H, Takahashi K, Naito T, Yanagi Y, Itoh Y and Nakamura T 2018 New proposal of mechanical reinforcement structures to annular REBaCuO bulk magnet for compact and cryogen-free NMR spectrometer *Physica* C **550** 52–56

[16] Fujishiro H, Naito T, Yanagi Y, Itoh Y and Nakamura T 2019 Promising effects of a new *hat structure* and double metal ring for mechanical reinforcement of a REBaCuO ring-shaped bulk during field-cooled magnetization at 10 T without fracture *Supercond. Sci. Technol.* **32** 065001